

Doctoral Dissertation from the Faculty of Physics at the
Ludwig-Maximilians-Universität München



**Searches for Supersymmetric Top Squarks
and Higgsinos in Single-Lepton Final States
with the ATLAS Detector**

Presented by
Paola Arrubarrena Tame
born in Mexico City

Munich, May 27th, 2021

First referee: PD. Dr. Alexander Mann

Second reviewer: Prof. Dr. Thomas Kuhr

Date of oral exam: July 23rd, 2021

Zusammenfassung

Supersymmetrie (SUSY) ist eine Erweiterung des Standardmodells (SM) der Teilchenphysik, die für jedes Teilchen des SM einen supersymmetrischen Partner vorhersagt. Diese neuen Teilchen würden einige der Probleme des Standardmodells lösen. Natürliche SUSY-Szenarien sagen leichte skalare Top-Quarks (Top-Squarks) und Higgsinos vorraus. Diese Arbeit präsentiert zwei Suchen mit einem isolierten Elektron oder Myon im Endzustand, eine für die direkte Top-Squark-Produktion und eine für die direkte Higgsino-Produktion. Die Analysen werden unter Verwendung von Daten aus Proton-Proton-Kollisionen mit integrierter Luminosität von 139 fb^{-1} durchgeführt, die vom Large Hadron Collider bei einer Schwerpunktsergie von $\sqrt{s} = 13 \text{ TeV}$ bereitgestellt und vom ATLAS-Detektor innerhalb der entsprechenden Jahre 2015 bis 2018 aufgezeichnet wurden.

Wenn R -Parität erhalten ist, ist das leichteste supersymmetrische Teilchen (LSP) stabil und ein potenzieller Kandidat für dunkle Materie. SUSY-Modelle mit R -Paritätsverletzung (RPV) sind ebenfalls motiviert und weisen weniger experimentelle Einschränkungen auf als viele R-Paritätserhaltende Modelle (RPC). Bei der ersten Suche wird RPC mit einem bestimmten Top-Squark-Zerfall angenommen, bei dem die Massendifferenz zwischen dem Top-Squark und dem LSP kleiner ist als die Masse des W -Bosons, sodass jedes Top-Squark über einen Vier-Körper-Zerfall zu einem Bottom-Quark, zwei verschiedenen leichten Fermionen und einem LSP zerfällt. Die zweite Analyse sucht nach RPV SUSY mit einer direkten Higgsino-Paar-Produktion, die prompt in SM-Teilchen zerfallen und durch hohe Jet- und b -Jet-Multiplizitäten im Endzustand gekennzeichnet sind.

In beiden Suchen wird keine signifikante Abweichung von den erwarteten Standardmodell-Ereignissen beobachtet, daher werden Ausschlussgrenzen bei 95% Vertrauensniveau in Bezug auf das supersymmetrische Modell bestimmt. Für das RPC-Top-Squark-Modell wird die Ausschlussgrenze im Vergleich zu den vorherigen Ergebnissen um 240 GeV erweitert. Für die Higgsino-RPV-Analyse werden Higgsino-Massen bis zu 320 GeV ausgeschlossen.

Abstract

Supersymmetry (SUSY) is an extension of the Standard Model (SM) of particle physics which predicts a supersymmetric partner for each particle in the SM. These new particles would solve some of the problems in the Standard Model. Natural SUSY scenarios favor light scalar top quarks (stops) and higgsinos. This dissertation presents two searches with an isolated electron or muon in the final state, one for direct stop production and another for direct higgsino production. The analyses are performed using data from proton-proton collisions delivered by the Large Hadron Collider at a center-of-mass energy of $\sqrt{s} = 13$ TeV and recorded by the ATLAS detector within the years 2015 to 2018, corresponding to an integrated luminosity of 139 fb^{-1} .

If R -parity is conserved, the lightest supersymmetric particle (LSP) is stable and a potential dark matter candidate. SUSY models with R -parity violating (RPV) scenarios are also motivated, with fewer experimental constraints than many R -parity conserving (RPC) models. The first search assumes RPC with a particular stop decay where the mass difference between the stop and the LSP is smaller than the W boson mass, resulting in each stop decaying via a four-body process into a b quark, two different light fermions, and the LSP. The second analysis searches for RPV SUSY with direct higgsino pair production decaying promptly into SM particles characterized by high jet and b -jet multiplicities in the final state.

In both searches, no significant excess over the Standard Model expectation is observed. Exclusion limits at 95% confidence level are derived for the decay scenarios. For the RPC stop model, the exclusion limit from the previous results is extended by 240 GeV, excluding stop masses up to 640 GeV for an LSP of 590 GeV. For the higgsino RPV analysis, higgsino masses up to 320 GeV are excluded.

Contents

1. Introduction	1
2. Theoretical Background	3
2.1. The Standard Model	3
2.1.1. Particle Content	3
2.1.2. The Standard Model as Gauge Theory	6
2.1.3. Spontaneous Symmetry Breaking and Higgs Field	11
2.1.4. Limitations of the SM	14
2.2. Supersymmetry	18
2.2.1. Minimal Supersymmetric Standard Model (MSSM)	19
2.2.2. Neutralinos and Charginos	23
2.2.3. Scalar Top Quarks	23
2.2.4. Natural SUSY	24
2.2.5. <i>R</i> -Parity	26
3. Experimental Apparatus	30
3.1. Large Hadron Collider	30
3.2. The ATLAS Detector	31
3.2.1. Coordinate System	32
3.2.2. Inner Detector	33
3.2.3. Calorimeters	35
3.2.4. Muon Spectrometer	36
3.2.5. Magnet System	38
3.2.6. Luminosity Detector	39
3.2.7. Trigger and Data Acquisition System	39
4. Data and Simulation	41
4.1. Data Acquisition in LHC Run 2	41
4.1.1. Luminosity measurement	41
4.1.2. Triggers	42
4.2. Monte Carlo Simulation	44
4.2.1. Event Generation	44
4.2.2. Simulated Samples	46
5. Event Reconstruction	49
5.1. Object Definitions	49
5.1.1. Tracks, Primary Vertex Reconstruction and Topo Clusters	49

5.1.2. Electrons	51
5.1.3. Muons	52
5.1.4. Jets	54
5.1.5. b -tagging	55
5.1.6. Overlap removal	56
5.1.7. Missing Transverse Momentum	56
5.2. Event Cleaning	58
6. Search Strategies	59
6.1. RPC stops and RPV higgsinos search strategies	59
6.1.1. RPC stops strategies	59
6.1.2. RPV higgsinos strategies	60
6.2. Signal models	61
6.2.1. Simplified models	62
6.3. Background events	64
6.3.1. Discriminating variables	66
6.3.2. Background estimation	67
6.3.3. Systematic uncertainties	69
6.3.4. Statistical treatments	72
6.3.5. Previous results	76
7. Search for top squark pair production in the 4-body decay mode	79
7.1. Event preselections	79
7.2. Signal region	84
7.3. Background estimation	89
7.3.1. Control and validation regions	89
7.4. Uncertainties	101
7.4.1. Theoretical uncertainties results	101
7.5. Results	103
8. Search for R-parity violating supersymmetry in events with multiple jets and one lepton	109
8.1. Analysis Strategy	109
8.2. Background Estimation	110
8.2.1. Jet Multiplicity Prediction	110
8.2.2. b -Jet Multiplicity Prediction	113
8.3. Shape Analysis	114
8.3.1. Machine Learning	114
8.3.2. Adversarial Neural Network	116
8.4. Results	120
8.4.1. ANN	120
8.4.2. Distance Correlation	123

9. Search for Mono-Top Signatures in Compressed SUSY Scenarios	126
9.1. Motivation	126
9.1.1. Region to Target	127
9.1.2. Mono-top Cross-sections	129
9.2. Signal Regions Optimization	131
9.2.1. Leptonic Final State	132
9.2.2. Hadronic Final State	133
9.3. Conclusions	135
10. Discussion	138
11. Conclusion	140
Appendices	149
A. bffN b-tag High Negative Event Weights in WCR Selection	150
B. Additional plots for the theoretical systematic uncertainties	154
B.1. Signal	154
B.2. $t\bar{t}$	154
B.3. W +jets	155
C. Choice of the ANN Decision Metric Parameters	158
D. Metric Plots	162
E. Mono-Top Discriminating Variables	165

1. Introduction

With the discovery of the Higgs boson by the ATLAS and CMS collaborations at the Large Hadron Collider in 2012 [1, 2], the successful history of finding experimental evidence for the fundamental building blocks of nature continued. It was the last undiscovered particle of the Standard Model (SM) of particle physics, a theory developed throughout the second half of the 20th century that has become one of the most successful theories to date [3–6]. The SM explains many experimental results with remarkable precision.

As the experimental results improved, some observations that cannot be explained by the SM have appeared. For example, the existence of dark matter (DM) is strongly supported by astronomical observations [7–11], but no SM particle satisfies the postulated properties of DM. There are four forces that interact between particles: the weak, strong, electromagnetic, and gravitational forces. The SM framework summarizes the former three forces but does not contain the gravitational force. There is a huge gap between the energy scale of gravity and the mass of the Higgs boson, which seems to be unnatural, and it is difficult to explain within the regime of the SM. This huge gap may affect the mass of the Higgs boson and the stability of the electroweak vacuum due to quantum loop corrections.

Many particle physicists are trying to solve these problems by finding new physics beyond the standard model. It is strongly believed that an extension of the SM can account for the unexplained phenomena in the SM framework. Many theories could explain these mysteries, but none of them has been experimentally confirmed. *Supersymmetry* (SUSY) [12–17] is one of the main candidates for a unified theory beyond the SM. It introduces a symmetry between fermions and bosons, so the number of elementary particles will be roughly doubled. SUSY was proposed in the 1970s based on the quantum field theory, and it is now a well-established concept in particle physics though no evidence of SUSY has been found yet.

The search for SUSY is intensively performed at the European Organization for Nuclear Research (CERN) where the Large Hadron Collider (LHC) is located and collides protons with a center of mass energy of 13 TeV. In these high energetic reactions many other particles can be created, possibly also supersymmetric particles. A natural choice for SUSY parameters (naturalness [18, 19]) makes the SUSY partners of the top (stop) and the Higgs (higgsino) to be not much heavier than the lightest SUSY particle, being potentially within the reach of the LHC. This calls vividly for searching them at the LHC. Experimental evidence of at least one of these new particles as an excess over the

prediction of the SM processes in data would indicate the existence of new physics.

In many SUSY models, a conserved quantity, R -parity ¹ [20], is often introduced to avoid rapid proton decay. Conserved R -parity renders the lightest supersymmetric particle (LSP) stable and only interacting weakly with ordinary matter, making it a potential DM candidate [21, 22]. The vast majority of SUSY searches assume R -parity conservation (RPC) which typically comes with large missing transverse momentum (with the magnitude referred to as E_T^{miss}) that results from the two undetected LSPs. The requirement of large E_T^{miss} is a powerful strategy for separating the SUSY signal from SM processes. However, it also sacrifices sensitivity to a variety of beyond-SM models with no or little E_T^{miss} . Complementary to the E_T^{miss} -based SUSY searches are the R -parity violating (RPV) SUSY searches providing an excellent coverage of phase space [23, 24].

This thesis presents the search for supersymmetry through two models focusing on events with one isolated electron or muon in the final state. The first one assumes RPC searching for direct stop pair production [25] in a particular region where the mass difference between the stop and the LSP is smaller than the W boson mass. This is the main target of this dissertation because a complete high-energy physics analysis was performed. Each stop would decay via a four-body process into a LSP, and low momentum objects such as a b quark and two different fermions. A large amount of E_T^{miss} , low momentum b -jets, and a low momentum electron or muon are expected in the final state. In this search, the sensitivity of the signal model is improved by utilizing the shape differences of the signal model and the dominant standard model background in the distributions of the most discriminating kinematic variables.

The second analysis presents a search for RPV SUSY with a direct higgsino production decaying promptly via an RPV coupling to SM particles [26]. The final states are characterized by high jet and b -jet multiplicities and one isolated muon or electron. The analysis strategy relies on machine learning techniques aiming to reach higgsino sensitivity.

The theoretical framework of the SM and SUSY is reviewed in Chapter 2. The LHC and ATLAS' experimental apparatus are described in Chapter 3. The data and Monte Carlo simulation used in the searches are explained in Chapter 4. In Chapter 5, the standard reconstruction algorithms used in ATLAS are documented. The general analysis strategy of the RPC stops and RPV higgsinos searches is presented in Chapter 6. The RPC stops analysis is described in Chapter 7. Chapter 8 presents the RPV higgsinos search. The results of both analyses are discussed in Chapter 10. Finally, conclusions are presented in Chapter 11. An extra analysis is shortly mentioned in Chapter 9 showing preliminary studies for a new SUSY process named the supersymmetric Monotop.

¹A multiplicative quantum number, referred to as R -parity, is introduced in SUSY models in order to jointly conserve baryon and lepton (B-L) number. R -parity is 1 (-1) for all SM (SUSY) particles.

2. Theoretical Background

Particle physics main goal is to describe nature at the smallest observable scales, governed by quantum mechanics and special relativity. Experimental observations are interpreted in the context of the Standard Model (SM), a quantum field theory with specific gauge structure and matter content. It describes the electromagnetic, weak, and strong forces, and the field interactions. The structure and parameters of the theory are encoded in a Lagrangian density, from which experimental predictions may be calculated. This chapter will describe the structure of the SM and some known limitations.

2.1. The Standard Model

Since the discovery of the electron in 1897 by J. J. Thomson [27], elementary particle physics has made extraordinary progress in understanding the fundamental processes in the universe. The Standard Model (SM) of particle physics is a relativistic quantum field theory that incorporates three (out of four) fundamental interactions in nature: electromagnetic, weak, and strong interactions. Experimental results can be accurately described by the Standard Model. From a theoretical point of view, the SM unified the electromagnetic and the weak force, and it successfully included the strong force. As a consequence, it leads to its current formulation as described in more detail in [28].

2.1.1. Particle Content

The SM includes four types of particles with an integer spin number¹ that follow the Bose-Einstein statistics and are called gauge bosons, plus a Higgs boson that follows the same statistics but with spin 0. It also includes twelve particles with half-integer spin number that follow the Dirac-Fermi statistics called fermions.

Fundamental forces are described by a quantum field theory. Quantum electrodynamics (QED) is the theory that explains electromagnetism by the exchange of photons (γ) between charged particles. The second fundamental force is the weak nuclear force, mediated by the Z and W bosons. The W and Z bosons are massive, carriers of the weak charge, and self-interacting particles. The W boson is electrically charged and exists in two variants, the positive (W^+) and the negative (W^-), and the Z boson is electrically neutral (Z^0). The unification of the weak force with QED, forming the electroweak theory, was developed by S.L. Glashow, S. Weinberg and A. Salam [29–31]. Finally,

¹Using the common convention in high energy physics $c = \hbar = 1$.

Table 2.1.: Bosonic particle content of the SM. The spin and mass values were taken from reference [32] and are rounded to three significant digits.

Particle	Electric charge	Spin	Mass
gluon (g)	0	1	0
photon (γ)	0	1	0
W^\pm	± 1	1	80.4 GeV
Z	0	1	91.2 GeV
Higgs (H)	0	0	125.1 GeV

Table 2.2.: Basic properties of the twelve fundamental fermions separated into leptons and quarks. All listed particles have a spin of 1/2. The masses are taken from reference [32] and are rounded to three significant digits, if known to this precision. Neutrinos also have masses, though they are very small. In the SM they are treated as completely massless.

Generation	Quarks	Q [e]	Mass	Leptons	Q [e]	Mass
1	up (u)	+2/3	2.2 MeV	neutrino (ν_e)	0	≈ 0
	down (d)	-1/3	4.7 MeV	electron (e)	-1	0.511 MeV
2	charm (c)	+2/3	1.28 GeV	neutrino (ν_μ)	0	≈ 0
	strange (s)	-1/3	95 MeV	muon (μ)	-1	106 MeV
3	top (t)	+2/3	173 GeV	neutrino (ν_τ)	0	≈ 0
	bottom (b)	-1/3	4.18 GeV	tau (τ)	-1	1.78 GeV

the strong nuclear force is mediated by gluons (g) which, like the photon, are assumed to be massless and its respective quantum theory is quantum chromodynamics (QCD). Gluons carry color charge² which can take three values: red, blue and green³. They can interact with themselves, as the weak bosons, explained in more detail in [33] and in the following section.

The mediators of the fundamental interactions in the SM are shown in Table 2.1. In the case of gravity, a complete quantum field theory has to be developed, nevertheless, it is assumed to be too weak to play a significant role in particle physics. Unlike the gauge bosons, the Higgs boson is a massive spinless particle which is the only elementary scalar particle discovered in nature. The Higgs boson is essential to formulate a theory explain-

²Gluons are mixtures of different color-anticolor combinations [33].

³Plus anti-red, anti-blue, and anti-green.

ing the mass of the gauge bosons, known as the Brout-Englert-Higgs mechanism [34, 35] explained in Section 2.1.3. The Higgs boson is the excited state⁴ of the Higgs field from this mechanism.

Fermions are the building blocks of matter and classified into leptons and quarks. They can be further classified into three generations containing two particles each. In total, there are twelve particles with half-integer spin number as seen on Table 2.2. In this table, the anti-particle content is not taken into account, but there exists an anti-particle for every fermion listed with the same mass and opposite charge; this is a consequence of the Dirac equation of relativistic quantum mechanics describing the fermion dynamics.

The first group of fundamental fermions are the quarks. They are six: up (u), down (d), charm (c), strange (s), top (t), and bottom (b), as shown in Table 2.2. Each generation contains a doublet of particles with electric charge $+2/3$ (up-type) and $-1/3$ (down-type). Unlike leptons, quarks carry an additional quantum number, the color charge [33]. Isolated quarks cannot be observed due to a phenomenon known as confinement. Moreover, they can only be found as bound states referred to as hadrons. Hadrons are color-neutral, either as a meson (quark-antiquark system) or as a baryon (quark-quark-quark system). Anti-quarks have the same mass and spin as their corresponding quarks but opposite electric and color charges. The formation of hadrons out of quarks and gluons is called hadronization, and can give rise to cascades of hadrons or other particles, referred to as jets. Quarks, which have color-, weak-, and electromagnetic-charge, interact with each other through all three forces incorporated in the SM.

Leptons do not take part in the strong interaction and they constitute the second group of fundamental fermions. They can be subdivided in two classes: charged leptons and neutral leptons. The electron (e), muon (μ) and tau (τ) are massive and have an electric charge of $-e$ (1.602×10^{-19} C [32]), and interact via both electromagnetic and weak interactions. The neutrinos (ν_e, ν_μ, ν_τ) are taken to be massless in the SM⁵ and are electrically neutral, therefore, only interact via the weak interaction. As a consequence, the W boson is the mediator in the conversion from a charged lepton to its neutrino and vice-versa. The muon and tau have the same properties as the electron except for their masses and lifetime.

⁴In quantum mechanics, an excited state of a system is any quantum state that has a higher energy than the ground state (i.e. more energy than the absolute minimum) [36].

⁵The observation of neutrino oscillations shows that the neutrinos should have a small mass [32].

2.1.2. The Standard Model as Gauge Theory

The SM can be described as a non-Abelian Yang-Mills gauge theory based on the symmetry group:

$$\mathrm{SU}(3)_C \otimes \mathrm{SU}(2)_L \otimes \mathrm{U}(1)_Y \quad (2.1)$$

with $\mathrm{SU}(2)_L \otimes \mathrm{U}(1)_Y$ representing the underlying symmetry of the electroweak theory, and $\mathrm{SU}(3)_C$ three colored degrees of freedom. The hypercharge is represented by Y and explained in more detail in the following subsections. $\mathrm{SU}(2)_L$ is the symmetry group of the weak interaction which only couples via the weak isospin to left-handed (L) particles and right-handed (R) antiparticles. Gauge theories build the mathematical foundation to describe interactions in the SM. A basic concept of the Lagrangian formalism will be presented because it is essential for the understanding of the relationship between particles and forces. Detailed descriptions may be found in references [37, 38].

In this framework, particles are not treated as a discrete mass point but as a continuous system represented by a field $\phi(\vec{x}, t)$. The main mechanism is taken from classical mechanics where a Lagrangian $L(q, \dot{q}, t)$ describes a system in motion and dependent on the generalized coordinates q_i with their time derivatives (velocities) \dot{q}_i . Analogously to a field theory, a Lagrangian with density $\mathcal{L}(\phi, \partial_\mu \phi)$ is a function of the fields ϕ_i , and their time derivatives with respect to the space-time coordinates $x^\mu = (t, x^1, x^2, x^3)$. Incorporating the fields ϕ with the action S :

$$S = \int L dt = \int \mathcal{L}(\phi, \partial_\mu \phi) d^4x \quad (2.2)$$

By the principle of least interaction δS , the Euler-Lagrange equations are obtained and describe the dynamics of a system. If \mathcal{L} has more than one field ϕ , the Euler-Lagrange equation acts separately on each field ϕ_i , leading to [37]:

$$\partial_\mu \left(\frac{\partial \mathcal{L}}{\partial (\partial_\mu \phi_i)} \right) - \frac{\partial \mathcal{L}}{\partial \phi_i} = 0 \quad (2.3)$$

The advantage of the Lagrangian formulation is that all resulting expressions are Lorentz invariant. According to Noether's theorem, the invariance of physics laws under a continuous transformation is related to a conservation law [37, 39]. For example, the symmetry under translations in time results in the conservation of energy. Similarly, the conservation of electric charges originates from the invariance of Quantum Electrodynamics (QED) under gauge transformations. As an example, the Dirac Lagrangian of a free fermion described by the four-component complex spinor field $\psi(x)$ and mass m looks like

$$\mathcal{L} = \bar{\psi}(x)(i\gamma^\mu \partial_\mu - m)\psi(x) \quad (2.4)$$

where γ^μ denotes the Dirac matrices⁶. The hermitian adjoint of the field $\bar{\psi}$ is defined as $\bar{\psi} = \psi^\dagger \gamma^0$. The Lagrangian density \mathcal{L} has a global U(1) symmetry under transformations of the form:

$$\psi(x) \rightarrow e^{-iQ\alpha} \psi(x) \quad (2.5)$$

with Q as the fermion charge and α an arbitrary real number. However, \mathcal{L} is not *gauge invariant*, i.e. is not invariant under local transformations with a space-time dependent $\alpha(x)$. To achieve gauge invariance, ∂_μ in equation 2.4 is substituted by the covariant derivative D_μ

$$D_\mu = \partial_\mu + iQ A_\mu(x) \quad (2.6)$$

Here, A_μ represents a massless vector field that interacts with the fermion field. The strength of the interaction is proportional to Q . The A_μ field transforms like:

$$A_\mu(x) \rightarrow A_\mu(x) - \frac{1}{Q} \partial_\mu \alpha(x) \quad (2.7)$$

With this, \mathcal{L} becomes the Lagrangian of QED:

$$\mathcal{L}_{QED} = \bar{\psi} (i\gamma^\mu D_\mu - m) \psi - \frac{1}{4} F_{\mu\nu} F^{\mu\nu} \quad (2.8)$$

with $\frac{1}{4} F_{\mu\nu} F^{\mu\nu}$ as the kinetic term, which is already invariant under U(1) transformations and contains the field strength tensor of electromagnetism:

$$F_{\mu\nu} = \partial_\mu A_\nu - \partial_\nu A_\mu \quad (2.9)$$

and it is invariant under transformations of A_μ . Equation 2.9 represents the photon field (A_μ).

The steps to achieve gauge invariance in QED can be generalized to non-abelian gauge groups like SU(N), which describe special unitary matrices of dimension N with a unit determinant. QED is based on a U(1) symmetry group, leading to a single vector field formalism, while a Yang-Mills theory has as many gauge bosons as there are generators in the underlying group. The symmetry group SU(N) has $N^2 - 1$ generators. Therefore, a Yang-Mills theory based on the group SU(2) has three, while for SU(3) there are eight associated gauge fields. In addition to the coupling to fermions, Yang-Mills' theories also allow for self-interactions of gauge fields with triple and quartic couplings.

Quantum chromodynamics SU(3) \mathcal{C}

The strong nuclear force acts between colored particles. It is described by Quantum Chromodynamics (QCD) [37, 40]. Instead of a positive and a negative charge like in QED, the strong interaction couples to the color-charge which is only carried by quarks

⁶The Dirac matrices notation follows $\gamma^5 = i\gamma^0\gamma^1\gamma^2\gamma^3 = \begin{pmatrix} 0 & I \\ I & 0 \end{pmatrix}$ with I the identity matrix.

and gluons. Gluons carry one color and one anti-color each, leading to a *color-octet*. There are eight gluon states that correspond to a combination of color and anti-color, and as they carry color charge, they can interact with each other. The corresponding gluon singlet⁷ is not realized in nature because it would be a color-neutral particle freely propagating allowing for long-range strong interactions, which has not been observed [41]. Mathematically, the strong interaction is equal to a SU(3) gauge group with eight generators, due to the eight gluons. It is referred to as a $SU(3)_C$ gauge group due to the color charge interaction, where the subscript C indicates that the strong force only acts on particles with color charge.

As previously described, local gauge invariance is satisfied by introducing a covariant derivative:

$$D_\mu = \partial_\mu - ig_s \frac{\lambda^a}{2} G_\mu^a \quad (2.10)$$

where g_s is the strong coupling constant usually defined by $\alpha_s = g_s^2/4\pi$ analogous to the fine-structure constant. The SU(3) generators are represented by λ^a as the Gell-Mann matrices. The index a runs from 1 to 8. New vector fields G_μ^a are introduced which correspond to eight massless gluon fields. The gluon field tensor strength is given by

$$G_{\mu\nu}^a = \partial_\mu G_\nu^a - \partial_\nu G_\mu^a + g_s f^{abc} G_\mu^b G_\nu^c \quad (2.11)$$

with f^{abc} as the structure constants of the SU(3) symmetry. The QCD Lagrangian is obtained as:

$$\mathcal{L}_{QCD} = \sum_q \bar{q}(i\gamma^\mu D_\mu - m)q - \frac{1}{4} G_{\mu\nu}^a G^{a,\mu\nu} \quad (2.12)$$

The quark field is represented by \bar{q} and q where the sum runs over six different quark flavors. The last term in Equation 2.12 represents the kinetic term of the gluon fields which is responsible for the non-Abelian nature of QCD and describes the self-interaction of gluons. Apart from quark-gluon interactions, the gluon fields can also undergo self-interacting with triple and quartic vertices. This gluon-gluon self-interaction induces important features of QCD, as additional bosonic loops which are possible [42]. As a consequence, the coupling strength becomes dependent of the momentum scale ($\alpha_s(q^2)$), meaning that α_s decreases with increasing momentum scale. Therefore, quarks and gluons act as free particles at short distances. This QCD property is known as *asymptotic freedom*. In this regime, QCD processes can be calculated using perturbation theory. However, at large distances QCD becomes non-perturbative and quarks and gluons are confined in color-neutral states, referred to as color confinement [37]. This is the reason why quarks and gluons are not seen as free particles. Instead, they can only be found as bound states referred to as hadrons as explained in section 2.1.1.

⁷ $(|rr\rangle + |b\bar{b}\rangle + |g\bar{g}\rangle)/\sqrt{3}$.

Electroweak unification $SU(2)_L \otimes U(1)_Y$

In the SM, the electromagnetic and weak interactions are described in a common theory of electroweak interactions, based on the symmetry group $SU(2)_L \times U(1)_Y$. It was shown by the Wu experiment [43] and polarization studies [44] that fermions produced in weak interactions are polarized⁸. Particles can be left handed⁹ or right handed¹⁰. Nevertheless, the weak force does not conserve parity, meaning that fermions that participate in weak interactions are only left handed¹¹ in the limit when the mass of the fermion $m_f \rightarrow 0$.

The transformations of the $SU(2)_L \times U(1)_Y$ group act differently on left and right-handed fermion fields. Chirality is introduced to distinguish left- and right-handed fermions, for a Dirac fermion is defined through the operator γ^5 with eigenvalues ± 1 . Any Dirac field can thus be projected into its left- or right-handed component with the projection operators P_L and P_R ¹² as

$$\psi_L = P_L \psi, \quad \psi_R = P_R \psi \quad (2.13)$$

$SU(2)_L$ represents the weak isospin group. The conserved quantum number of the weak interaction is the weak isospin I where I_3 is the z -component of I . The states are labeled in terms of I and I_3 leading to an isospin symmetry [37]. Each doublet has a weak total isospin of $I = 1/2$, and individually, the upper components of the doublet have $I_3 = +1/2$ and the down components $I_3 = -1/2$. The weak isospin doublets consist of an up-type and a down-type quark, or of a charged lepton and its associated neutrino:

$$\left(\begin{array}{c} \nu_e \\ e^- \end{array} \right)_L, \left(\begin{array}{c} \nu_\mu \\ \mu^- \end{array} \right)_L, \left(\begin{array}{c} \nu_\tau \\ \tau^- \end{array} \right)_L, \left(\begin{array}{c} u \\ d' \end{array} \right)_L, \left(\begin{array}{c} c \\ s' \end{array} \right)_L, \left(\begin{array}{c} t \\ b' \end{array} \right)_L \quad (2.14)$$

with the subscript L appended to the group name. Transformations of the weak isospin group proceed always within the same doublet. For leptons, the doublets are identical to the mass eigenstates of a given generation. This means that a charged lepton ℓ could transform into its corresponding neutrino ν_ℓ and vice-versa through the weak interaction. However, this is not the case for quarks, hence a prime symbol is appended to the down-type quarks in the definition from 2.14 [37].

An up-type (down-type) quark will still predominantly transform into the corresponding down-type (up-type) quark of its generation. It is also possible, with a smaller probability, that it goes into a down-type (up-type) quark of another generation. For example, charm quarks decay mostly into strange quarks, but transitions into a down or bottom quark can occur, too. This is indicated by s' . The different quark-transition probabilities are given by the magnitude squared elements of the Cabibbo-Kobayashi-

⁸Depending on their velocity $\beta = v/c$ [44].

⁹When the particle spin points in opposite direction of their momentum vector.

¹⁰When the spin of the particle points in the same direction as the momentum vector.

¹¹And right-handed antifermions.

¹² $P_L = \frac{1}{2}(1 - \gamma_5)$ and $P_R = \frac{1}{2}(1 + \gamma_5)$

Maskawa (CKM) matrix.

Right-handed fermions fields are singlets and do not participate in the weak interactions, so they have an isospin of 0. As a result, right-handed particle states do not couple to the gauge bosons of the $SU(2)_L$ symmetry. A $SU(2)_L$ singlet consist only of a quark or a charged lepton, as there are no right-handed neutrinos in the SM.

For the $U(1)$ group, the charge operator needs to produce the same eigenvalues for members of each left-handed fermion doublet. Such charge should be related to the electric charge Q and the third component of the isospin I_3 in the form called *hypercharge* (Y) defined by the Gell-Mann-Nishijima relation [45]:

$$Y = \frac{Q - I_3}{2} \quad (2.15)$$

The unitary group is denoted $U(1)_Y$ because the expression from equation 2.15 introduces a weak hypercharge invariant under the isospin construction.

The procedure to form a gauge invariant theory is the same as shown before for QED. Local gauge invariance for $SU(2)_L$ and $U(1)_Y$ symmetries are satisfied by introducing the covariant derivative for left- and right-handed fermion fields as:

$$D_\mu^L = \partial_\mu - ig_2 \frac{\sigma^a}{2} W_\mu^a + ig_1 \frac{Y}{2} B_\mu \quad (2.16)$$

$$D_\mu^R = \partial_\mu + ig_1 \frac{Y}{2} B_\mu \quad (2.17)$$

with three generators of the $SU(2)$ symmetry σ^a written in terms of the Pauli matrices¹³. The $U(1)_Y$ coupling constant is g_1 , and g_2 is the coupling constant of $SU(2)_L$. Three new gauge fields W_μ^a (with $a = 1, 2, 3$) are introduced. The hypercharge Y is described in equation 2.15 and B_μ is the fourth bosonic field introduced in the electroweak model. The gauge field W_μ^a couples with strength g_2 , while the gauge field B_μ couples through g_1 with different strength to left- and right-handed fermions¹⁴.

The Lagrangian density for the electroweak (EWK) model results:

$$\mathcal{L}_{\text{EWK}} = \sum_f \bar{\psi}_L^f i\gamma^\mu D_\mu^L \psi_L^f + \sum_f \bar{\psi}_R^f i\gamma^\mu D_\mu^R \psi_R^f - \frac{1}{4} W_{\mu\nu}^a W^{a,\mu\nu} - \frac{1}{4} B_{\mu\nu} W^{\mu\nu} \quad (2.18)$$

The sum over f represents the fermion content, including left- and right-handed states. The terms $W_{\mu\nu}^a$ and $B_{\mu\nu}$ are the field strength tensors related to the respective gauge

¹³Where $\sigma^a = \{\sigma^1, \sigma^2, \sigma^3\}$ and $\sigma^1 = \begin{pmatrix} 0 & 1 \\ 1 & 0 \end{pmatrix}$, $\sigma^2 = \begin{pmatrix} 0 & -i \\ i & 0 \end{pmatrix}$, $\sigma^3 = \begin{pmatrix} 1 & 0 \\ 0 & -1 \end{pmatrix}$.

¹⁴Proportional to the hypercharge Y , as described in more detail in reference [49].

fields as:

$$B_{\mu\nu} = \partial_\mu B_\nu - \partial_\nu B_\mu \quad (2.19)$$

$$W_{\mu\nu}^a = \partial_\mu W_\nu^a - \partial_\nu W_\mu^a - g_2 \epsilon^{abc} W_\mu^b W_\nu^c \quad (2.20)$$

Here, ϵ^{abc} is the structure constant of SU(2) resulting in gauge self-interactions given by the antisymmetric Levi-Civita tensor.

At this stage all gauge and fermion fields are predicted to be massless. This is obviously a contradiction with the experimental observations. In the SM, the mass terms are obtained by introducing a Higgs field and the concept of spontaneous symmetry breaking to the theory, explained in Section 2.1.3.

2.1.3. Spontaneous Symmetry Breaking and Higgs Field

The Higgs sector in the SM is composed of an isospin doublet with complex scalar fields [34, 35]:

$$\phi(x) = \begin{pmatrix} \phi^+ \\ \phi^0 \end{pmatrix} \quad (2.21)$$

where ϕ^+ has an electric charge of +1 and ϕ^0 is electrically neutral. The field ϕ has $Y = 1$ with $I = 1/2$. Consequently the same covariant derivative (D_μ) for the left handed fermion fields, as in equation 2.16, is applied to ϕ . The scalar field contributes to the SM Lagrangian as

$$\mathcal{L}_H = (D^\mu \phi)^\dagger (D_\mu \phi) - V(\phi) \quad (2.22)$$

The Hermitian conjugate of a four-component particle state is denoted by the dagger symbol (\dagger) as $\phi^\dagger = (\phi^*)^T$. $V(\phi)$ represents the potential whose ground state follows different symmetries than the system, represented by:

$$V(\phi) = -\mu^2 \phi^\dagger \phi + \frac{\lambda}{4} (\phi^\dagger \phi)^2 \quad (2.23)$$

where λ and μ are two real free parameters, and λ is positive. In the ground state of the theory (or vacuum state) $V(\phi)$ should be minimal. The potential has a Mexican-hat shape as seen on Figure 2.1 and has a minimum for field configurations satisfying $\phi^\dagger \phi = 2\mu^2/\lambda$. The vacuum expectation value, v , of the scalar field ϕ corresponds to the minimum of the potential $V(x)$ chosen as the expectation value of ϕ ($\langle \phi \rangle$) as:

$$\langle \phi \rangle = \frac{1}{\sqrt{2}} \begin{pmatrix} 0 \\ v \end{pmatrix} \quad \text{where} \quad v = \frac{2\mu}{\sqrt{\lambda}} \approx 246 \text{GeV} \quad (2.24)$$

The choice of the minimum breaks the symmetry of the Lagrangian \mathcal{L}_H spontaneously. From the formula relating v with the Fermi constant G_F , $v = (\sqrt{2}G_F)^{-1/2}$, v was found

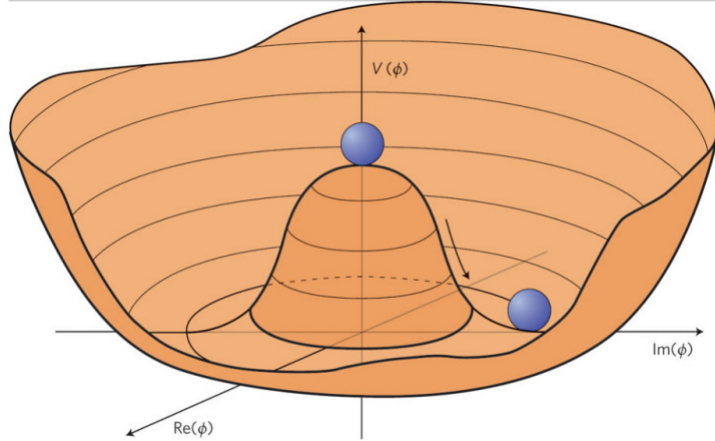


Figure 2.1.: Illustration of the Mexican hat shaped Higgs potential $V(\phi)$ with $\mu^2 > 0$ (as in Equation 2.23 the μ is chosen to have a negative coefficient). The blue spheres represent the state of the system at the point of spontaneous symmetry breaking in the ground state ϕ_0 . In this figure one could have two possibilities of fluctuations around the ground state: around the azimuthal angle and the radius [50].

to have the value of ≈ 246 GeV, determined from muon decay measurements [46–48]. This relation describes the effective coupling constant of a four-fermion interaction in the Fermi’s weak decay theory obtained from muon lifetime measurements.

The Higgs field ϕ can be expanded around the vacuum expectation value

$$\phi = \frac{1}{\sqrt{2}} \begin{pmatrix} \phi_1(x) + i\phi_2(x) \\ v + H(x) + i\chi(x) \end{pmatrix} \quad (2.25)$$

where H , χ , ϕ_1 and ϕ_2 are newly introduced scalar fields. The Higgs potential becomes:

$$V = \mu^2 H^2 + \frac{\mu^2}{v} H(H^2 + \chi^2 + \phi_1^2 + \phi_2^2) + \frac{\mu^2}{4v^2} (H^2 + \chi^2 + \phi_1^2 + \phi_2^2)^2 \quad (2.26)$$

In equation 2.26, the H represents a neutral scalar particle with mass $m_H = \sqrt{2}\mu$. No mass terms exist for the other three fields χ , ϕ_1 and ϕ_2 . This agrees with the Nambu-Goldstone theorem [51], which postulates the existence of a massless particle for every spontaneously broken continuous symmetry. They can be removed from \mathcal{L} with a suitable gauge transformation.

The kinematic term $(D_\mu\phi)^\dagger(D_\mu\phi)$ of \mathcal{L}_H in Equation 2.22, leads to a coupling of H with the gauge fields and mass terms of the gauge bosons as

$$\mathcal{L}_H = \propto \frac{v^2}{8} [g_2^2(W_\mu^1)^2 + g_2^2(W_\mu^2)^2 + (-g_2 W_\mu^3 + g_1 B_\mu)^2] \quad (2.27)$$

through which W_μ^a and B_μ acquire mass. The physical charged bosons are defined as the superposition of the first two components by

$$W_\mu^\pm = \frac{1}{\sqrt{2}}(W_\mu^1 \mp iW_\mu^2) \quad (2.28)$$

and the neutral boson defined as the third component $W_\mu^0 = W_\mu^3$. The neutral gauge fields W_μ^3 and B_μ mix to form the physical states A_μ and Z_μ , which are associated with the photon and the Z^0 boson, defined by the electroweak mixing angle θ_W ¹⁵:

$$A_\mu = B_\mu \cdot \cos \theta_W + W_\mu^3 \cdot \sin \theta_W \quad (2.29)$$

$$Z_\mu = -B_\mu \cdot \sin \theta_W + W_\mu^3 \cdot \cos \theta_W \quad (2.30)$$

The invariance under local $SU(2)_L \otimes U(1)_Y$ transformations leads to the existence of the W^\pm , Z^0 and the photon (γ)¹⁶.

The A_μ corresponding to the photon field of the electromagnetic symmetry group $U(1)_{EM}$ remains massless. The masses of the bosons are given by

$$m_W = \frac{g_2}{2}v, \quad m_Z = \frac{\sqrt{g_1^2 + g_2^2}}{2}v, \quad m_A = 0. \quad (2.31)$$

and are related to the electroweak coupling constant with

$$\cos \theta_W = \frac{g_2}{\sqrt{g_1^2 + g_2^2}} = \frac{m_W}{m_Z} \quad (2.32)$$

To summarize, the bosons of the weak interaction acquire their masses through the Brout-Englert-Higgs mechanism when the symmetry gets spontaneously broken with a non-zero vacuum expectation value.

Fermions also get their masses through the Brout-Englert-Higgs mechanism by gauge-invariant Yukawa interactions with the Higgs field. The Lagrangian describing the Yukawa interaction is represented by

$$\mathcal{L}_{Yukawa} = -\lambda_\ell \bar{L}_L \phi \ell_R - \lambda_d \bar{Q}_L \phi d_R - \lambda_u \bar{Q}_L \phi^c u_R + \text{h.c.} \quad (2.33)$$

¹⁵Also named the Weinberg angle.

¹⁶While the W boson only couples to left-handed fermions, the coupling of the photon is the same for any handedness.

where L_L and Q_L are the left-handed lepton and quark doublets with the Yukawa couplings for the corresponding fermion type given by λ_ℓ , λ_d , and λ_u . The leptonic right-handed fields are denoted by ℓ_R , while d_R and u_R indicate the up-type and down-type right-handed fields. The term ϕ^c specifies the charge conjugate of the Higgs field. The last term, h.c. stands for hermitian conjugate of the previous three terms. Extra quark coupling terms could be added mixing quark-generations. The Cabibbo-Kobayashi-Maskawa matrix V_{ij} [52, 53] describes them where the off-diagonal entries represent the probability of transition between one quark generation and another in the weak interaction. No transitions between lepton generations in the SM are achieved due to the absence of right-handed neutrinos [37]. The mass of a fermion f is given by

$$m_f = \lambda_f \frac{v}{\sqrt{2}} \quad (2.34)$$

The vacuum expectation value v of the Higgs field gives rise to the mass of the fermion m_f . Equation 2.34 shows that the higher the mass of the fermion is, the stronger is its coupling strength to the Higgs field.

2.1.4. Limitations of the SM

The SM successfully provides with accurate precision the known phenomena in high energy physics. It describes the known elementary particles and their electromagnetic, weak, and strong interactions. However, it still leaves some open questions. Because of some of the SM limitations presented in this subsection, one of the most pressing issues in particle physics today is to find a suitable beyond-the-Standard-Model (BSM) theory.

Hierarchy and Fine-Tuning Problem

At the LHC energy scale, gravity does not play an important role. Nevertheless, at a reduced Planck scale $M_P = (8\pi G_{Newton})^{-1/2} = 2.4 \times 10^{18}$ GeV, quantum gravitational effects become important and the forces are expected to become alike [17]. The electromagnetic and weak forces become unified at the electroweak energy scale M_W defined by the vacuum expectation value of the Higgs field in the order of 10^2 GeV. M_W and the M_P scale differ by 16 orders of magnitude in energy. The fact that the ratio M_P/M_W is so high is considered unnatural and a good motivation to search for new physics beyond the SM. This big discrepancy between the two energy scales is often referred to as the *hierarchy problem*.

Taking into account higher orders in Feynman diagrams, the parameters μ^2 and λ from the Higgs potential are corrected by loop diagrams from each particle that couples to the Higgs field¹⁷. These corrections are proportional to the coupling λ_f^2 to a fermion f and therefore proportional to the mass of the fermion m_f^2 as shown in Figure 2.2 (a). This leads to a squared Higgs mass m_H^2 correction. To get the experimental Higgs mass,

¹⁷With a 125 GeV Higgs mass, the parameters are taken to be $\mu = -(92.9 \text{ GeV})$ and $\lambda = 0.126$ [17].

a cancellation between this correction and the bare Higgs mass squared should happen. This cancellation requires incredible *fine-tuning* of the bare Higgs squared mass violating the naturalness [42] principle. As a fermion f couples to the Higgs boson with a term in the Lagrangian $-\lambda_f H f \bar{f}$, the mass of the Higgs boson should be modified by quantum corrections caused by virtual loop diagrams by [17]:

$$\Delta m_H^2 = -\frac{|\lambda_f|^2}{8\pi^2} \Lambda_{UV}^2 + \dots \quad (2.35)$$

where λ_f is the coupling strength of the fermion to the Higgs boson and Λ_{UV}^2 is an ultraviolet momentum cutoff. It should be interpreted as the least energy scale where new physics phenomena could alter the high-energy behavior of the theory. For example, if Λ_{UV}^2 is taken to be in the order of M_P , the Higgs squared mass parameter μ^2 is about 30 orders of magnitude in energy higher than measured. This is a direct problem, not only to the Higgs squared mass corrections, but for all the SM particle masses which are obtained by the vacuum expectation value of the Higgs field, so that the entire mass spectrum of the SM is directly or indirectly sensitive to the cutoff Λ_{UV} [17]. This amount of tuning is not considered *natural* in the theory.

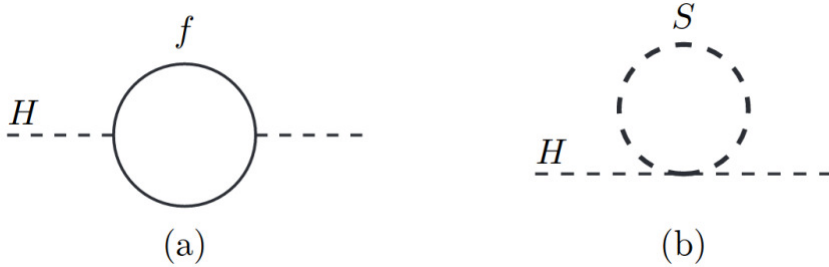


Figure 2.2.: Loop corrections to the Higgs squared parameter m_H^2 due to (a) a fermion f and (b) a scalar boson S . [17]

A scalar boson S can be introduced as shown in Figure 2.2 (b), as a solution to this problem as it also couples to the Higgs field via a term $-\lambda_S |H|^2 |S|^2$ in the Lagrangian. The quantum corrections of these new particles could cancel out the loop integrals induced by the known SM particles. Supposing there exists S with mass m_S , such scalar particle would induce a further quantum correction to m_H as:

$$\Delta m_H^2 = \frac{\lambda_S}{16\pi^2} \Lambda_{UV}^2 + \dots \quad (2.36)$$

The term λ_S represents the coupling between the scalar particle and the Higgs field. By comparing Equations 2.35 and 2.36, it seems that fermions and bosons can relate by the relative minus sign between fermion loop and boson loop contributions to m_H^2 . Under this assumption, each of the quarks and leptons of the SM would be accompanied with two complex scalars $|\lambda_f|^2 = \lambda_S$, then Λ_{UV}^2 contribution will be nicely canceled. This is a very elegant solution independent on the cutoff scale which has as a consequence a

stable Higgs mass, giving rise to a bosonic and fermionic symmetry.

Dark Matter

Cosmological observations have revealed that visible matter observed by telescopes is not enough to account for the estimations of matter in the universe. It has been known for decades that the largest fraction of mass in the entire universe is non-luminous. The invisible matter is called dark matter (DM). Fritz Zwicky studied in 1933 nebulae clusters [54]. The clusters appeared to be gravitationally bound, but all the luminous material inside them did not add up to the sufficient mass to retain the fast-moving galaxies. He found that the average density in the Coma system needed to be at least 400 times larger than the results derived from luminous matter observations, leading to the conclusion that dark matter should be present in a larger amount than luminous matter and that most of the clusters' mass is not visible. Figure 2.3 shows another piece of evidence for DM: the rotation velocity of the galaxy M33 [55]. The expected rotation velocity from the visible disk around the galaxy should have a peak at a certain distance from the center (R), and then decrease as a function of R . The rotation velocity of the galaxy M33 did not follow the classical expectations given by the shape of the luminous contributions. On the contrary, the rotation velocity seemed quite flat at larger distances away from R . This would indicate that there is more matter than expected. The rotation velocity was also observed using the 21 cm line emitted from hydrogen atoms indicating additional invisible material around the galaxy in the shape of a halo.

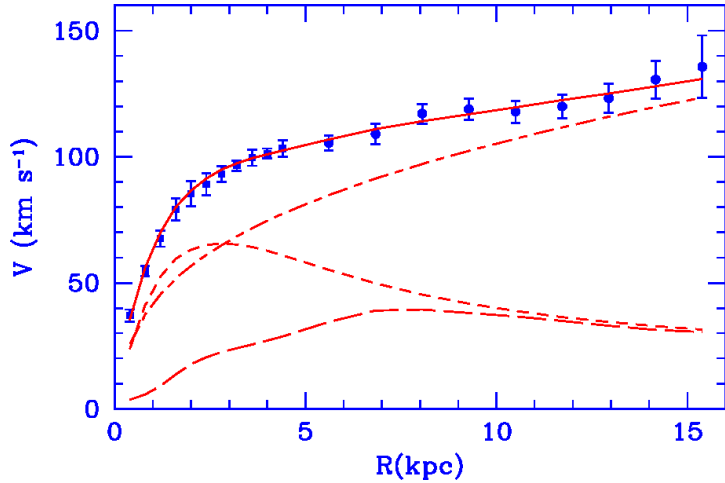


Figure 2.3.: The rotation velocity of the galaxy M33 as a function of the distance from the center of the galaxy [55]. The points show the observed M33 rotation curve with the best fit model (solid line). The contribution of the halo (dashed-dotted line), stellar disk (short dashed line) and gas (long dashed line) are shown together.

Another evidence of the existence of dark matter was given by gravitational lensing effects [56]. According to the general relativity theory, space is bent by gravity. By

this principle, if light emitted by a distant source would pass by a very massive object it should deviate from its straight path. Consequently, the massive object will act as an optical lens and it will bend light proportional to the mass of this massive object. This effect was first observed in 1919 during the solar eclipse in front of Hyades star cluster, whose stars appeared to be displaced as they passed close to the sun [57] giving experimental verification of general relativity. The lensing effect presented results that required concentrations of unseen matter more massive than expected from the plasma [58].

Unification of Forces

The coupling constants of the presented forces are very different. However, the gauge couplings are not a fixed value but dependent on the energy scale. The unified description of the electromagnetic and the weak forces gave rise to a possible unified theory. The extrapolation of the coupling constants of the electromagnetic, weak, and strong interactions at high energies and scales is shown in Figure 2.4 left. In the SM description, the coupling constants run into each other but do not reach the same value at the same energy. While the SM description must unify the electromagnetic and the weak forces, it is not possible to unify the electroweak and the strong force [37]. When extrapolating the coupling constants behavior to high energies within the SM, a unifying value is not obtained. In Figure 2.4 right, new particles at a TeV scale have been introduced making the unification of the three forces possible. For this to happen a new physics model would be needed.

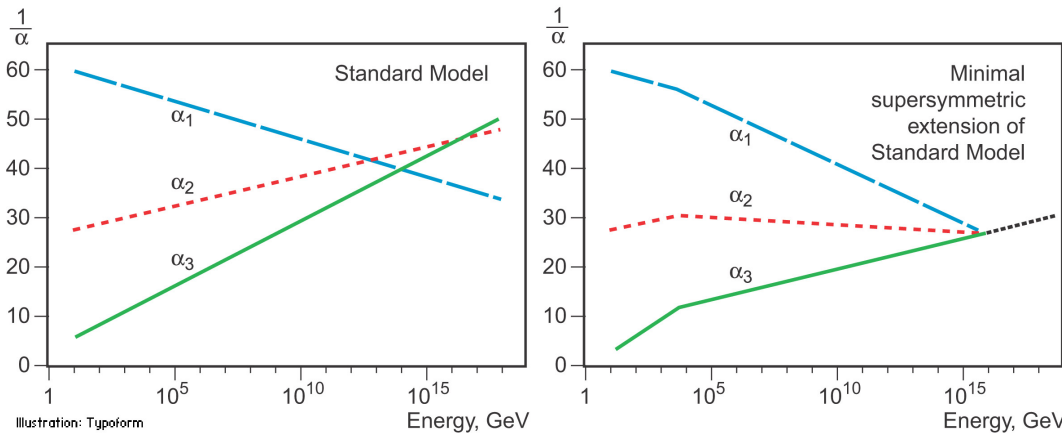


Figure 2.4.: Left plot: Extrapolation to high energies of the inverse gauge couplings ($\frac{1}{\alpha}$) of the electromagnetic (α_1), weak (α_2) and strong (α_3) interactions as in the SM. On the right plot the illustration of the extrapolation in a minimal supersymmetric extension of the SM chosen to meet at some point around the Planck scale in a logarithmic scale [59].

2.2. Supersymmetry

An extension to the SM is needed to solve the problems presented in the previous section. Supersymmetry (SUSY) is one of the best-studied candidates to do so. SUSY establishes a symmetry between bosons and fermions, which provides boson partners to fermion particles of the SM and vice versa. In this way, the SM particle content is roughly doubled. Each known SM particle is associated to a supersymmetric partner differing by 1/2 in their spin and keeping all the other quantum numbers. The superpartners of fermions are denoted by the same name of the SM only adding a *s* in the front (i.e., the electron superpartner is the *selectron*), and the superpartners of bosons have the suffix -ino to the name (i.e., *W* bosons becomes *wino*). SUSY particles are then marked with a tilde (i.e., *e* becomes \tilde{e}). Simply speaking, a supersymmetric transformation turns a bosonic state into a fermionic one and vice versa. In terms of operators, the operator Q that generates such transformation must be an anti-commuting spinor as [17]:

$$Q|\text{Boson}\rangle = |\text{Fermion}\rangle, \quad Q|\text{Fermion}\rangle = |\text{Boson}\rangle \quad (2.37)$$

Spinors are complex objects, so the hermitian conjugate of the operator Q is Q^\dagger and also a symmetry generator in the Weyl representation¹⁸. Q and Q^\dagger are fermionic operators carrying spin angular momentum of 1/2. The operator Q satisfies the following anti-commutation and commutation relations:

$$\{Q, Q^\dagger\} = P^\mu \quad (2.38)$$

$$\{Q, Q\} = \{Q^\dagger, Q^\dagger\} = 0 \quad (2.39)$$

$$[P^\mu, Q] = [P^\mu, Q^\dagger] = 0, \quad (2.40)$$

where P^μ represents the four-momentum generator of space-time and thus, the SUSY algebra extends the ordinary space-time to super-space. Equation 2.38 introduces a connection between SUSY and the space-time translations, and equation 2.39 points that supersymmetric transformations are independent of the space-time positions. All quantum numbers, with the exception of the spin, should match their SM partners. The third equation 2.40, indicates that Q is exchangeable with $m^2 = P^\mu P_\mu$, resulting in the operator Q not changing mass. Hence, fermion and boson partners, for example the electron in the SM and its supersymmetric partner, have the same mass [17].

Such supersymmetric partners have not been discovered yet; for example, there is no supersymmetric partner of the electron, which is a boson with $m_e = 0.511$ MeV. Supersymmetry should be broken so that fermion and boson partners have different masses to account for the fact. The quantum numbers related to SUSY particles are identical to the SM ones, and the pair has the same coupling constants. The SUSY breaking

¹⁸Weyl spinors describe particles with 1/2 of spin and a given chirality. Each left and right handed spinors has two components. The component with left (right) chirality is denoted by $\psi_\alpha = \psi_L$ ($\bar{\psi}^\alpha = \psi_R$). The matrices $\epsilon_{\alpha\beta} = i\sigma_2$ and $\epsilon^{\alpha\beta} = -i\sigma_2$ are used to raise and lower the spinorial indices α and β with σ_i denoting the Pauli matrices [60].

could happen by introducing soft breaking terms into the SUSY Lagrangian [61]. By a soft breaking, the superpartners should acquire more mass than the SM particles but the masses of the supersymmetric particles should not be too large [17]. For this reason there is still a good motivation to find supersymmetry at the LHC at CERN.

2.2.1. Minimal Supersymmetric Standard Model (MSSM)

The Minimal Supersymmetric Standard Model (MSSM) is a supersymmetric extension that includes the minimum amount of new particles [62, 63]. The particles in the MSSM are listed in Table 2.3. Each SM particle has a supersymmetric partner with a spin which is shifted by 1/2. A representation of the SUSY algebra is given by the construction of *supermultiplet* states. A supermultiplet state is an irreducible representation combining fermion and boson states. A particle and its superpartner form a supermultiplet. A supermultiplet has the same number of fermionic and bosonic degrees of freedom $n_F = n_B$.

Two types of supermultiplets can be constructed. The first one is called *chiral* supermultiplet (i.e., whose left- and right-handed pieces transform differently under the gauge group). It contains a Weyl fermion of spin 1/2 and its superpartner, which is represented by a complex scalar field of spin 0. This Weyl fermion has two helicity states $n_F = 2$ while the complex scalar field has its real and imaginary part. It contains two scalar fields described in a single complex scalar field [60] where each one yield $n_B = 1$. Q contains the $SU(2)_L$ doublets $(\tilde{u}_L, \tilde{d}_L)$ and (u_L, d_L) . The supermultiplet \bar{u} and \bar{d} denote the associated $SU(2)_L$ singlets $\tilde{u}_R^*, u_R^\dagger$ and $\tilde{d}_R^*, d_R^\dagger$. Likewise L contains the lepton and slepton doublets. The quark and lepton multiplets come, as usual, in three generations. Table 2.3 shows only the first generation.

The Higgs sector in the MSSM consists of two chiral supermultiplets H_u and H_d with weak hypercharge $Y = +1/2$ and $-1/2$ respectively. They contain complex scalar fields arranged as $SU(2)_L$ doublets labeled $H_u = (H_u^+, H_u^0)$ and $H_d = (H_d^-, H_d^0)$. To guarantee the cancellation of gauge anomalies [17], at least two Higgs supermultiplets are required with $Y = \pm 1/2$. The Higgs boson in the SM would then correspond to a linear combination of H_u^0 and H_d^0 . The higgsinos, the fermionic superpartners to the Higgs scalars, are arranged as Weyl spinor fields as $SU(2)_L$ doublets denoted $(\tilde{H}_u^+, \tilde{H}_u^0)$ and $(\tilde{H}_d^-, \tilde{H}_d^0)$.

The second representation is the *gauge* supermultiplet, also shown in Table 2.3. The field is obtained by a massless gauge boson with spin 1 together with a spin 1/2 fermionic superpartner called *gaugino* [63]. They consist of gluons and their fermionic superpartner, the *gluino*; the W^\pm , W^0 , and B^0 with their spin 1/2 superpartners called *winos* and *bino*. Both have two possible helicity states therefore $n_F = n_B = 2$.

Table 2.3.: The chiral and gauge supermultiplets in the minimal supersymmetric extension of the Standard Model (MSSM). Chiral multiplets are defined in terms of left-handed Weyl spinors so that the conjugates of the right-handed quarks and leptons appear in the table. For quarks, leptons, squarks, and sleptons, only the first generation is listed. Table adapted from [17].

		names	spin 0	spin 1/2
chiral	squarks, quarks	Q	$(\tilde{u}_L, \tilde{d}_L)$	(u_L, d_L)
		\bar{u}	\tilde{u}_R^*	u_R^\dagger
		\bar{d}	\tilde{d}_R^*	d_R^\dagger
	sleptons, leptons	L	$(\tilde{e}_L, \tilde{\nu})$	(e_L, ν)
		\bar{e}	\tilde{e}_R^*	e_R^\dagger
	Higgs, higgsinos		H_u (H_u^+, H_u^0)	$(\tilde{H}_u^+, \tilde{H}_u^0)$
		H_d (H_d^-, H_d^0)	$(\tilde{H}_d^-, \tilde{H}_d^0)$	
		names	spin 1	spin 1/2
gauge	gluon, gluino		g	\tilde{g}
	W boson, wino		W^\pm, W^0	$\tilde{W}^\pm, \tilde{W}^0$
	B boson, bino		B^0	\tilde{B}^0

Table 2.4.: Particles predicted by the MSSM which have not been discovered yet (except for h^0 . The mixing in the first two generations is assumed to be negligible [17].

	Name	Spin	Gauge Eigenstates	Mass Eigenstates
squarks		0	$\tilde{u}_L, \tilde{u}_R, \tilde{d}_L, \tilde{d}_R$	$\tilde{u}_L, \tilde{u}_R, \tilde{d}_L, \tilde{d}_R$
			$\tilde{c}_L, \tilde{c}_R, \tilde{s}_L, \tilde{s}_R$	$\tilde{c}_L, \tilde{c}_R, \tilde{s}_L, \tilde{s}_R$
			$\tilde{t}_L, \tilde{t}_R, \tilde{b}_L, \tilde{b}_R$	$\tilde{t}_1, \tilde{t}_2, \tilde{b}_1, \tilde{b}_2$
sleptons		0	$\tilde{e}_L, \tilde{e}_R, \tilde{\nu}_e$	$\tilde{e}_L, \tilde{e}_R, \tilde{\nu}_e$
			$\tilde{\mu}_L, \tilde{\mu}_R, \tilde{\nu}_\mu$	$\tilde{\mu}_L, \tilde{\mu}_R, \tilde{\nu}_\mu$
			$\tilde{\tau}_L, \tilde{\tau}_R, \tilde{\nu}_\tau$	$\tilde{\tau}_1, \tilde{\tau}_2, \tilde{\nu}_\tau$
Neutralinos		1/2	$\tilde{B}^0, \tilde{W}^0, \tilde{H}_u^0, \tilde{H}_d^0$	$\tilde{\chi}_1^0, \tilde{\chi}_2^0, \tilde{\chi}_3^0, \tilde{\chi}_4^0$
Charginos		1/2	$\tilde{W}^\pm, \tilde{H}_u^+, \tilde{H}_d^-$	$\tilde{\chi}_1^\pm, \tilde{\chi}_2^\pm$
Gluinos		1/2	\tilde{g}	\tilde{g}
Higgs Bosons		0	$H_u^0, H_d^0, H_u^+, H_d^-$	h^0, H^0, A^0, H^\pm

SM fermions have different interactions depending if they are left- or right-handed (L or R) [63]. In SUSY, the left- and right-handed should belong to different supermultiplets and have distinct spartners. The \tilde{f}_R and \tilde{f}_L are different, even though the concept of handedness does not have any meaning for a scalar particle with helicity = 0. The L and R indexes refer to the chirality of their superpartners to indicate their couplings. For example, a right-handed slepton $\tilde{\ell}_R$ does not couple to a W boson while the left-handed slepton $\tilde{\ell}_L$ does.

It will be useful in the following to introduce a function describing all the non-gauge interactions with the chiral superfields called *superpotential* (W). For the MSSM it is written as [17]:

$$W_{\text{MSSM}} = \bar{u}\mathbf{y}_u Q H_u - \bar{d}\mathbf{y}_d Q H_d - \bar{e}\mathbf{y}_e L H_d + \mu H_u H_d \quad (2.41)$$

with objects \bar{u} , \bar{d} , \bar{e} , Q , L , H_u , and H_d making reference to the chiral superfields corresponding to the chiral supermultiplets in Table 2.3. The terms \mathbf{y}_u , \mathbf{y}_d , and \mathbf{y}_e are the dimensionless Yukawa coupling parameters represented by 3×3 matrices in the family space. The μ term is the supersymmetric version of the Higgs boson mass in the SM. Roughly speaking, μ parametrizes the mass in the Higgs sector of the MSSM and is consequently referred to as higgsino mass parameter.

Soft SUSY Breaking

The particles in the supermultiplets are massless until the gauge symmetry is spontaneously broken. A conserved and unbroken supersymmetry would imply that the masses of the supersymmetric particles are identical with their SM counterparts, but this has been found to be not the case, since no SUSY particles have been discovered. Hence, supersymmetry must be broken and as a consequence the supersymmetric particles must be heavier than the SM particles. The Lagrangian of the MSSM can be split into two parts as

$$\mathcal{L}^{\text{MSSM}} = \mathcal{L}_{\text{SUSY}}^{\text{MSSM}} + \mathcal{L}_{\text{soft}}^{\text{MSSM}} \quad (2.42)$$

where the first part $\mathcal{L}_{\text{SUSY}}^{\text{MSSM}}$ describes the properties of the SUSY particles that are the same as the ones of the SM particles [17]. The second part $\mathcal{L}_{\text{soft}}^{\text{MSSM}}$ describes the soft breaking terms of the MSSM, which are essential when discussing the phenomenology of the MSSM particles. As the exact nature of SUSY breaking is not known, all possible terms that break SUSY softly are explicitly added to the Lagrangian in the MSSM. In a general way, the soft Lagrangian can be expanded to

$$\begin{aligned} \mathcal{L}_{\text{soft}}^{\text{MSSM}} = & -\frac{1}{2} \left(M_3 \tilde{g} \tilde{g} + M_2 \tilde{W} \tilde{W} + M_1 \tilde{B} \tilde{B} + \text{c.c.} \right) \\ & - \left(\tilde{\bar{u}} \mathbf{a}_u \tilde{Q} H_u - \tilde{\bar{d}} \mathbf{a}_d \tilde{Q} H_d - \tilde{\bar{e}} \mathbf{a}_e \tilde{L} H_d + \text{c.c.} \right) \\ & - \tilde{Q}^\dagger \mathbf{m}_Q^2 \tilde{Q} - \tilde{L}^\dagger \mathbf{m}_L^2 \tilde{L} - \tilde{\bar{u}} \mathbf{m}_u^2 \tilde{\bar{u}}^\dagger - \tilde{\bar{d}} \mathbf{m}_d^2 \tilde{\bar{d}}^\dagger - \tilde{\bar{e}} \mathbf{m}_e^2 \tilde{\bar{e}}^\dagger \\ & - m_{H_u}^2 H_u^* H_u - m_{H_d}^2 H_d^* H_d - (b H_u H_d + \text{c.c.}) \end{aligned} \quad (2.43)$$

Here \bar{u} , \bar{d} , and \bar{e} are supermultiplets of right handed fermions, and \tilde{Q} and \tilde{L} are left-handed supermultiplets, as shown before in Table 2.3. The terms \tilde{Q} and \tilde{L} have tildes because they represent their corresponding scalar field. The first line on equation 2.43 represents the gaugino masses. The masses of the gluino, wino, and bino are given by M_3 , M_2 , M_1 , respectively corresponding to $SU(3)$, $SU(2)$, and $U(1)$ gauge groups. The second line shows the trilinear scalar couplings parameters included in 3×3 matrices in family space \mathbf{a}_u , \mathbf{a}_d , and \mathbf{a}_e , where left-handed and right-handed scalar particles are involved. The coupling parameters correspond to squark, slepton and Higgs fields (Higgs-squark-squark and Higgs-slepton-slepton) and are proportional to the Yukawa coupling parameters. On the third line the mass terms of the squarks and sleptons appear as \mathbf{m}_Q^2 , \mathbf{m}_L^2 , $\mathbf{m}_{\bar{u}}^2$, $\mathbf{m}_{\bar{d}}^2$, and $\mathbf{m}_{\bar{e}}^2$. They are complex 3×3 matrices corresponding to the particles. The last line corresponds to the SUSY breaking contributions to the Higgs potential in the MSSM with $m_{H_u}^2$, $m_{H_d}^2$ and b .

Before the introduction of the soft supersymmetry breaking Lagrangian $\mathcal{L}_{\text{soft}}$, there was only one free parameter in the theory which is not present in the SM, the mass parameter μ . The $\mathcal{L}_{\text{soft}}$ introduces 104 additional free parameters (+ 19 free parameters in the SM), making the experimental searches for supersymmetric particles rather challenging with 124 free parameters in total.

In the MSSM, the electroweak breaking mechanism is generalized to account for the two Higgs doublets (H_u^0 and H_d^0) in the theory. Similarly as in the SM, each doublet acquires their vacuum expected values by $v_u = \langle H_u^0 \rangle$ and $v_d = \langle H_d^0 \rangle$. The ratio between these will give

$$\tan \beta = \frac{v_u}{v_d} \quad (2.44)$$

which represents an important parameter that governs the phenomenology as seen in the following sections with $v^2 = v_u^2 + v_d^2$. In the MSSM, the masses and CKM mixing angles of the quarks and leptons are determined not only by the Yukawa couplings of the superpotential but also by the parameter $\tan \beta$, as shown in Equation 2.44. The top, charm and up quark mass matrix is proportional to $v_u = v \sin \beta$; and the bottom, strange, down quarks, and the charge leptons get masses proportional to $v_d = v \cos \beta$.

When the electroweak symmetry is spontaneously broken, the two complex Higgs doublets contain in total 8 degrees of freedom, the mechanism uses 3 degrees of freedom to give masses to the two W bosons (\pm) and to the Z boson. This leaves five Higgs scalar mass eigenstates [17]:

- h^0 , H^0 , one light and one heavy neutral Higgs under even- CP ¹⁹ transformations. With $m_{h^0} < m_{H^0}$ by definition
- A^0 , a neutral CP -odd Higgs

¹⁹Charge conjugation and Parity symmetry.

- H^+ , H^- , two charged Higgs

The scalar discovered at 125 GeV may then be identified with h^0 .

2.2.2. Neutralinos and Charginos

The electroweak gauginos and higgsinos mix with each other and form mass eigenstates. The four neutral particles (\tilde{H}_u^0 , \tilde{H}_d^0 , \tilde{W}^0 , and \tilde{B}^0) form *neutralinos* with four mass eigenstates $\tilde{\chi}_1^0$, $\tilde{\chi}_2^0$, $\tilde{\chi}_3^0$, $\tilde{\chi}_4^0$, as shown in Table 2.4. The charged states (\tilde{H}_u^+ , \tilde{H}_d^- , and \tilde{W}^\pm) form two charged mass eigenstates named *charginos* $\tilde{\chi}_1^\pm$, $\tilde{\chi}_2^\pm$. In these expressions, the numbers in the subscript of $\tilde{\chi}$ are assigned in ascending order of their masses. The mass matrix of the neutralinos is given by

$$\mathbf{M}_{\tilde{N}} = \begin{pmatrix} \tilde{\chi}_1^0 \\ \tilde{\chi}_2^0 \\ \tilde{\chi}_3^0 \\ \tilde{\chi}_4^0 \end{pmatrix} = \begin{pmatrix} M_1 & 0 & -c_\beta s_W m_Z & s_\beta s_W m_z \\ 0 & M_2 & c_\beta s_W m_Z & -s_\beta s_W m_z \\ -c_\beta s_W m_Z & c_\beta c_W m_Z & 0 & -\mu \\ s_\beta s_W m_Z & -s_\beta c_W m_Z & -\mu & 0 \end{pmatrix} \begin{pmatrix} \tilde{B} \\ \tilde{W}^3 \\ \tilde{H}_d^0 \\ \tilde{H}_u^0 \end{pmatrix} \quad (2.45)$$

with $s_\beta = \sin \beta$, $c_\beta = \cos \beta$, $s_W = \sin \theta_W$, and $c_W = \cos \theta_W$. The electroweak mixing angle is denoted by θ_W . The masses of the neutralinos are obtained by diagonalizing the mass matrix $\mathbf{M}_{\tilde{N}}$. Similarly, the mass matrix for charginos is given by

$$\mathbf{M}_{\tilde{C}} = \begin{pmatrix} \mathbf{0} & \mathbf{X}^T \\ \mathbf{X} & \mathbf{0} \end{pmatrix} \quad (2.46)$$

with

$$\mathbf{X} = \begin{pmatrix} M_2 & \sqrt{2} s_\beta m_W \\ \sqrt{2} c_\beta m_W & \mu \end{pmatrix} \quad (2.47)$$

The mass eigenstates are related to the gauge eigenstates by two unitary 2×2 matrices \mathbf{U} and \mathbf{V} as

$$\begin{pmatrix} \tilde{\chi}_1^+ \\ \tilde{\chi}_2^+ \end{pmatrix} = \mathbf{V} \begin{pmatrix} \tilde{W}^+ \\ \tilde{H}_u^+ \end{pmatrix}, \quad \begin{pmatrix} \tilde{\chi}_1^- \\ \tilde{\chi}_2^- \end{pmatrix} = \mathbf{U} \begin{pmatrix} \tilde{W}^- \\ \tilde{H}_d^- \end{pmatrix} \quad (2.48)$$

The exact diagonalized form of the mass mixing matrices are quite complex [64], for this reason, the mass eigenstates typically refer to the component that dominates them. Neutralinos with a dominant bino, wino, or higgsino component are called bino-, wino-, or higgsino-like. Likewise, charginos are wino- or higgsino-like.

2.2.3. Scalar Top Quarks

Similar to the neutralinos' and charginos' mixing, the right- and left-handed squarks mix too. A large mixing could happen for the stop due to the large Yukawa coupling of

the top, while the mixing is negligible for the first and second generation squarks. The Lagrangian of the stop mass term is given as

$$\mathcal{L}_{\text{stop}}^{\text{mass}} = \begin{pmatrix} \tilde{t}_L^* & \tilde{t}_R^* \end{pmatrix} \mathbf{m}_t^2 \begin{pmatrix} \tilde{t}_L \\ \tilde{t}_R \end{pmatrix} \quad (2.49)$$

with the stop mass matrix

$$\mathbf{m}_t^2 = \begin{pmatrix} m_{Q_3}^2 + m_t^2 + \Delta_{\tilde{u}_L} & v(A_t^* \sin \beta - \mu y_t \cos \beta) \\ v(A_t \sin \beta - \mu^* y_t \cos \beta) & m_{\tilde{u}_3}^2 + m_t^2 + \Delta_{\tilde{u}_R} \end{pmatrix} \quad (2.50)$$

The matrix elements $\Delta_{\tilde{u}_L} = (\frac{1}{2} - \frac{2}{3} \sin^2 \theta_W) \cos(2\beta) m_Z^2$ and $\Delta_{\tilde{u}_R} = (\frac{2}{3} \sin^2 \theta_W) \cos(2\beta) m_Z^2$. A_t is the trilinear coupling and v the vacuum expectation value in the SM related as $v^2 = v_u^2 + v_d^2$ from Equation 2.44. The mass eigenstates of the stop are obtained by diagonalizing the mass matrix

$$\begin{pmatrix} \tilde{t}_1 \\ \tilde{t}_2 \end{pmatrix} = \begin{pmatrix} c_{\tilde{t}} & -s_{\tilde{t}^*} \\ s_{\tilde{t}} & c_{\tilde{t}^*} \end{pmatrix} \begin{pmatrix} \tilde{t}_L \\ \tilde{t}_R \end{pmatrix} \quad (2.51)$$

where the condition $|s_{\tilde{t}}|^2 + |c_{\tilde{t}}|^2 = 1$ is fulfilled. The off-diagonal terms of the stop mass matrix tend to induce a large mixing. Because of this, the mass of the \tilde{t}_1 is typically light, and many models predict that \tilde{t}_1 is the lightest squark.

In this thesis, only the top squark is studied, although a very similar analysis can be performed for the rest of the third-generation sfermions with their respective gauge-eigenstate bases $(\tilde{b}_L, \tilde{b}_R)$ and $(\tilde{\tau}_L, \tilde{\tau}_R)$ [17].

2.2.4. Natural SUSY

The mass of the Z boson at lowest order (“tree level”) in the MSSM can be written in terms of large $\tan \beta$, m_{H_u} , and the supersymmetric μ parameter [17, 66] as:

$$m_Z^2 = -2(|\mu|^2 + m_{H_u}^2) \quad (2.52)$$

In the natural SUSY scenario, the right term on equation 2.52 should not be too large compared to the left side, otherwise a large cancellation between the terms on the right side would be needed. Equation 2.52 also provides guidance towards understanding which superparticles are required to be light, defining the minimal spectrum for *Natural SUSY*. The masses of the superpartners with the closest ties to the Higgs must not be too far above the weak scale. In particular, the higgsinos should not be too heavy because their mass is controlled by μ , as shown in Equation 2.41. The stop mass correcting $m_{H_u}^2$ at one-loop order, also cannot be too heavy. Hence, $m_{H_u}^2$ and μ must be adjusted in a way to get the m_Z .

The m_{H_u} term can be split into the tree level and radiation correction as $m_{H_u}^2 = m_{H_u}^2|_{\text{tree}} + m_{H_u}^2|_{\text{rad}}$ [65]. The radiative corrections to $m_{H_u}^2$ proportional to the top Yukawa

coupling λ_t are given by

$$m_{H_u}^2 |_{rad} = -\frac{\lambda_t^2}{8\pi^2} (m_{Q_3}^2 + m_{U_3}^2 + |A_t|^2) \ln \left(\frac{\Lambda}{m_{\tilde{t}}} \right) \quad (2.53)$$

Here m_{Q_3} and m_{U_3} are soft supersymmetry breaking masses for the third-generation squark doublet. The term Λ denotes the scale at which SUSY breaking effects are mediated generating massless SUSY particles [66]. To avoid large radiative corrections, m_{Q_3} and m_{U_3} should not be too large compared to m_Z . The expected mass spectrum from the natural SUSY requirement is summarized in Figure 2.5.

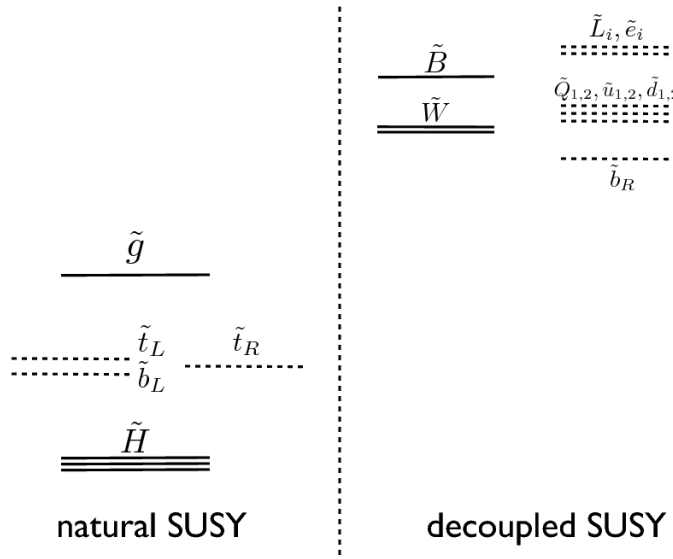


Figure 2.5.: Mass spectrum with naturalness constraints in the MSSM [66]. The particles on the left side are considered to be light in natural SUSY models, while the SUSY particle on the right side can be heavy.

The discovery of the Higgs boson indicates that a too light stop is not favored. The mass of the Higgs boson also provides information on the SUSY particles. The Higgs mass is described as

$$m_h^2 \sim m_Z^2 \cos^2 2\beta + \frac{3}{4\pi^2} \frac{m_t^4}{v^2} \left\{ \ln \frac{m_{\tilde{t}}^2}{m_t^2} + \frac{X_t^2}{m_{\tilde{t}}^2} \left(1 - \frac{X_t^2}{12m_{\tilde{t}}^2} \right) \right\} \quad (2.54)$$

with $X_t^2 = A_t - \mu \cot \beta$ as the stop mixing parameter [66]. At tree level, the observed Higgs boson with a mass of 125 GeV cannot be achieved by the term $m_Z^2 \cos^2 2\beta$. Hence, the second term in equation 2.54 must be large enough to account for the observed mass. In the case of heavy stops, the first term in the braces in equation 2.54 positively contributes to the Higgs mass. The second term becomes a maximum when $|X_t| = \sqrt{6}m_{\tilde{t}}$,

which is called the *maximal mixing* case. Figure 2.6 shows the Higgs mass calculated with Suspect [67] and FeynHiggs [68] packages. If the stop mixing is zero, the observed Higgs mass cannot be explained with a light stop below a few TeV, but the maximal mixing scenario gives a solution where a light stop below 1 TeV is actually possible.

Generally speaking, Natural SUSY assumes that the first and second generations of squarks are decoupled as seen in Figure 2.5, greatly decreasing the total SUSY cross-section.

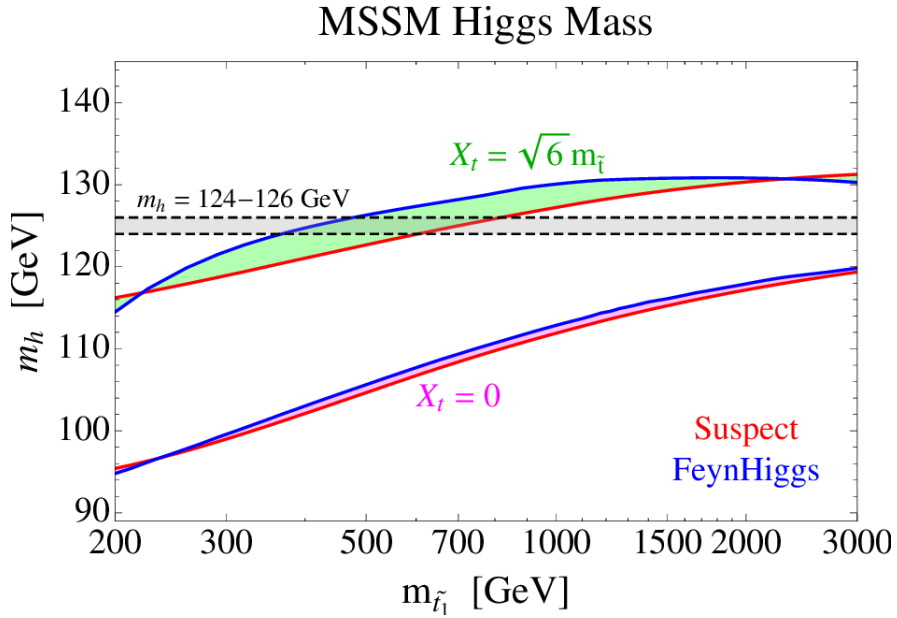


Figure 2.6.: The Higgs mass as a function of the lightest stop mass in the MSSM [69]. Two calculation packages are used: Suspect in red lines and FeynHiggs in blue. The maximal and zero stop mixing parameters are shown. The green (pink) area shows the difference between the Suspect and FeynHiggs calculations at the maximal (zero) stop mixing.

2.2.5. *R*-Parity

It is possible to add terms that violate either lepton number (L) or baryon number (B) conservation to the superpotential introduced in Equation 2.41. These terms are also gauge-invariant and renormalizable, and can be written as [17]:

$$W_{\Delta L=1} = \frac{1}{2} \lambda^{ijk} L_i L_j \bar{e}_k + \lambda'^{ijk} L_i Q_j \bar{d}_k + \mu^i L_i H_u \quad (2.55)$$

$$W_{\Delta B=1} = \frac{1}{2} \lambda''^{ijk} \bar{u}_i \bar{d}_j \bar{d}_k \quad (2.56)$$

where the color indexes have been suppressed and the letters i, j, k denote fermion-generation. The chiral supermultiplets carry lepton number assignments $L = +1$ for L_i , $L = -1$ for \bar{e}_i , and $L = 0$ for the rest. The total baryon number assignments are $B = +1/3$ for Q_i , $B = -1/3$ for \bar{u}_i and \bar{d}_i , and $B = 0$ for all of the others. Therefore, the terms in Equation 2.55 violate the total lepton number by 1 unit (as well as the individual lepton flavors) and those in Equation 2.56 violate baryon number by 1 unit. The μ and various λ factors are the coupling strengths of their corresponding interactions.

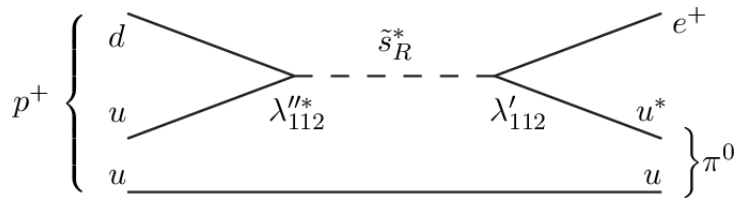


Figure 2.7.: Diagram of a proton decay via $p^+ \rightarrow e^+ \pi^0$ if R -parity is violated by both $\Delta B = 1$ and $\Delta L = 1$ interactions [17]. In this example, the decay is mediated by a strange squark.

Some theories consider these violating terms to be small. If both couplings λ' and λ'' were present and unsuppressed, then the lifetime of the proton would be extremely short as shown in Figure 2.7. For example, the proton decay via $p^+ \rightarrow e^+ \pi^0$, which is constrained by lower limits on the proton lifetime from experimental results of $> 10^{32}$ years [17]. Therefore, at least one of λ'^{ijk} and λ''^{11k} couplings in Figure 2.7, for each of $i = 1, 2$, $j = 1, 2$, and $k = 2, 3$ must be extremely small. In the MSSM a new symmetry is added, which has the effect of eliminating the possibility of B and L violating terms. This new symmetry is called *R-parity* defined as

$$P_R = (-1)^{3(B-L)+2s} \quad (2.57)$$

where s is the spin of the particle. Therefore, particles within the same supermultiplet do not have the same *R*-parity. The value of P_R is +1 for SM particles and -1 for SUSY particles. The conservation on *R*-parity in each vertex of a Feynman diagram has some implications. First, it predicts the existence of a lightest supersymmetric particle (LSP) which is stable making the LSP a leading candidate for DM. From the cosmological constraints, DM cannot have a color or an electric charge; thus, the LSP can be considered as one of the neutral SUSY particles. Like neutrinos, the LSP would escape detection in collider experiments. The second implication of *R*-parity conservation is that SUSY particles are produced in pairs at colliders, and decay (except the LSP) into particles in which an odd number of SUSY particles are included.

R-parity conservation is well-motivated in the MSSM as previously presented. It provides a good DM candidate and agrees with the non-observation of proton decay. The *R*-parity conservation requirement could be relaxed by allowing only lepton or baryon number violating terms but not both to avoid a potential proton decay. Such *R*-parity

violating models [70] exhibit a different phenomenology and are the basis for complementary SUSY searches. In this thesis, two SUSY models are presented, one conserving R -parity and another one violating it.

2.2.5.1. R -Parity Violation

The phenomenology for R -parity conserving (RPC) and R -parity violating (RPV) SUSY models is very different. For RPC scenarios, the stable LSP does not interact with the detector and escapes without depositing any energy. The presence of the LSPs, however, can be inferred by examining the imbalance in the transverse momentum in an event, which due to the negligible transverse momentum of the initial colliding particles, should be zero in events without LSPs or neutrinos. Thus, the imbalance in the transverse momentum in an event provides a powerful handle for discriminating a SUSY signal and SM background. Most RPC analyses search for signatures that include significant amounts of this imbalance. In the RPV models, however, the LSP is not stable and decays to SM particles, which does not produce any of these missing momentum signatures. Although this disfavor the LSP as a dark matter candidate, it allows RPV models to evade the constraints from RPC searches and cover a different phase space.

In the MSSM, the RPV terms for the superpotential can be written as $W_{\text{RPV}} = W_{\Delta L=1} + W_{\Delta B=1}$, summing Equations 2.55 and 2.56 [70]. While there is no fundamental theoretical reason forbidding R -parity violation, there are significant constraints on these interactions, specifically on the lepton number violating (LNV) couplings, λ and λ' , and the baryon number violating (BNV) coupling λ'' [71].

The most stringent of these constraints is from proton decay previously mentioned. Proton decay, however, requires both a lepton number and baryon number violating coupling. This constraint can be avoided if a mechanism exists that makes one of these couplings zero or negligibly small. Additionally, there are strong limits on the individual LNV and BNV couplings coming from neutron oscillation and muon-to-electron decay measurements. Thus, for any mechanism to evade these constraints, it must also motivate smaller couplings for the lighter generations.

Minimal Flavor Violating Supersymmetry

To avoid the constraints placed on the RPV couplings, a model is constructed following the structure of minimal flavor violation (MFV) [72]. The MFV hypothesis [73, 74] establishes that the Yukawa couplings are the source of irreducible flavor violation in BSM. In these MFV SUSY models, the RPV couplings are related to the SM Yukawa couplings. As a consequence, the third generation RPV couplings are large and the first two generations couplings are small.

The size of the small R -parity violating terms is determined by the flavor parameters,

such as the lepton and quark chiral supermultiplets (L , \bar{e} , Q , \bar{u} , \bar{d}). Some MFV models assume the absence of neutrino masses, leading to only one renormalizable R -parity violating interaction inferred from Equation 2.55 and 2.56: the baryon-number violating $\bar{u}\bar{d}\bar{d}$ coupling [72, 75]. This coupling is small for the first two generations meeting the necessary criteria to evade experimental constraints on RPV couplings. Some other MFV models assume neutrinos acquiring a Majorana mass term [76], having LNV couplings but tuned by the tiny neutrino masses. The RPV model studied in this thesis assumes only a BNV $\bar{u}\bar{d}\bar{d}$ coupling.

One of the outstanding problems of the SM and the MSSM is the issue of baryonic asymmetry. It is seen that there is predominance of matter over antimatter in the universe [77]. In MFV SUSY, the appearance of the λ'' BNV operator, opens new explanations for this imbalance. A violation of baryon number is an essential ingredient for the creation of an asymmetry of matter over antimatter in a symmetrical Universe that emerged from the Big Bang [78, 79]. This is a strong motivation to search for models with BNV.

3. Experimental Apparatus

Physicists probe the fundamental structure of the universe at the European Organization for Nuclear Research (CERN). It is located at the border of France and Switzerland, near the city of Geneva [80]. At CERN, the discovery of various fundamental particles took place, contributing to a better understanding of the SM. The aim of the Large Hadron Colider (LHC) [81] is to test the predictions of different theories of particle physics, including measuring the properties of the Higgs boson (experimentally discovered in 2012 [1, 2]), and searching for new physics beyond the SM.

3.1. Large Hadron Collider

The Large Hadron Collider (LHC) is a proton–proton accelerator consisting of a 27 kilometer ring. The CERN accelerator complex is shown in Figure 3.1, where the LHC is one part of it. The proton acceleration starts from an injection of hydrogen atoms into the Linear accelerator 2 (Linac 2). At the beginning of Linac 2, hydrogen gas passes through an electric field to strip off the electrons, and only protons are injected into Linac 2. In Linac 2, pulses of protons are generated and accelerated to an energy of 50 MeV. The accelerated pulse of protons is extracted from Linac 2 and injected into the Proton Synchrotron Booster (PSB). Here, protons are accelerated to 1.4 GeV for the injection into the Proton Synchrotron (PS). The Booster enhances the number of protons injected into the PS by accelerating protons in advance. The PS takes the protons to the energy of 25 GeV in its ring with a circumference of 628 m.

The next step is the Super Proton Synchrotron (SPS). The SPS was originally used as the main ring to collide proton and antiproton beams, and it was the historical place where the W and Z bosons were discovered in 1983. Today, the SPS is used as the last part of the supply chain before the LHC and accelerates protons to 450 GeV in its nearly 7 km circumference. The LHC is the main ring of the complex and uses the same tunnel built for the LEP accelerator. Two proton beams with opposite directions are injected from the SPS and accelerated to an energy of 6.5 TeV. The proton beams are accelerated through radiofrequency cavities and bent to a circular orbit with 1232 superconducting dipole magnets, which are cooled down to 1.9 K with superfluid helium. They provide a maximum magnetic field of 8.33 T. Apart from dipole magnets, the LHC comprises different quadrupole and correction magnets to focus the beams. The LHC has four interaction points where the major detectors are: ATLAS, CMS, ALICE, and LHCb. The protons travel through the LHC in a vacuum with a nominal bunch spacing of 25 ns. Each beam contains 2808 bunches with about 10^{11} protons in each bunch.

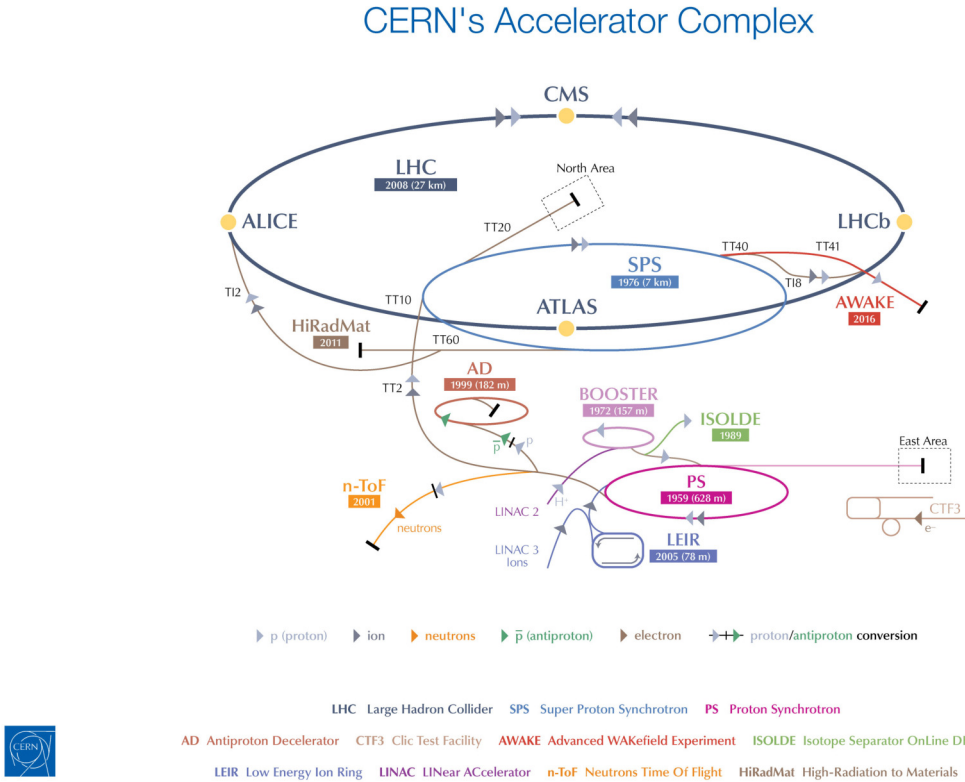


Figure 3.1.: The accelerator complex at CERN [82].

3.2. The ATLAS Detector

The ATLAS detector is a multi-purpose particle detector designed to cover a broad physics programs at the LHC, including the Higgs boson search, new physics searches, and precision measurements of the SM. Figure 3.2 shows a sketch of the ATLAS detector. It has a cylindrical shape, and the size of the detector is 44 m in length and 25 m in diameter. The center of the cylindrical shape is called the *barrel*, and the ends on each side are called *endcaps*.

The ATLAS detector consists of several subsystems. A tracking system is found in the most inner part of the ATLAS detector. It consists of the silicon pixel detector, the silicon strip tracker (SCT), and the Transition Radiation Tracker (TRT). These detectors are used to provide charged-particle trajectories, called *tracks*. The tracking subsystem is surrounded by a solenoid magnet, providing a magnetic field for the tracking detectors to measure the momenta of tracks using the track curvature. The next outer subsystem are the calorimeters, which consist of electromagnetic and hadronic calorimeters. The

energies of jets, electrons, and photons are measured by the calorimeters. The outermost part of the detector is the muon spectrometer (MS). Together with the muon spectrometer, toroid magnets are installed in both the barrel and endcap regions to provide the magnetic field to improve the measurement of the muons momentum. The details of the subsystems are described in the following sections.

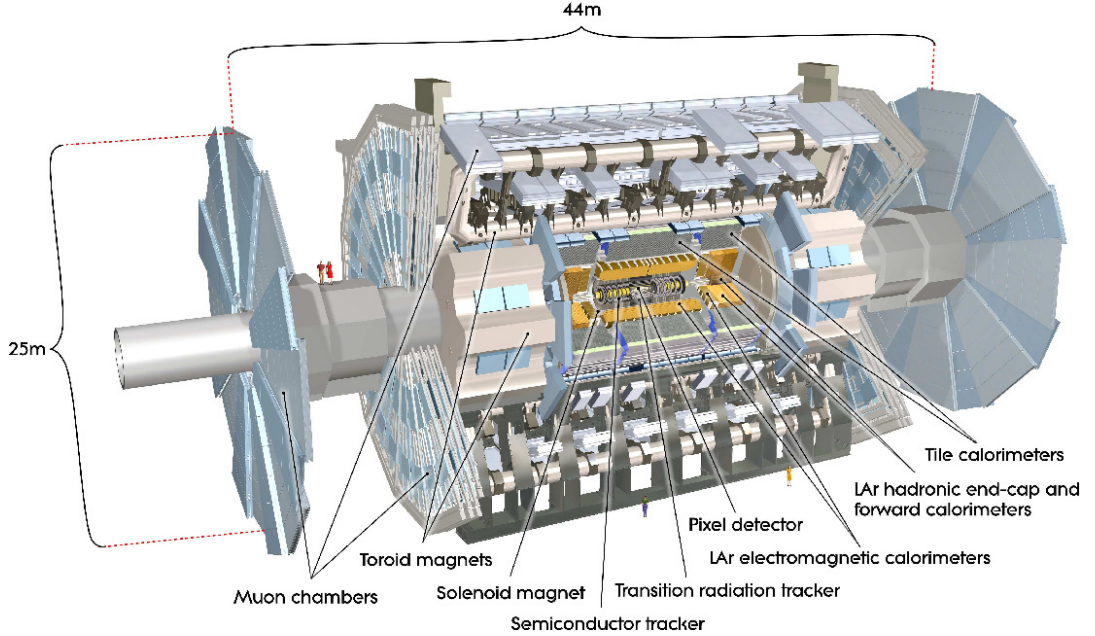


Figure 3.2.: A schematic drawing of the ATLAS detector and its subsystems [83].

3.2.1. Coordinate System

A right-handed coordinate system is used in ATLAS. The interaction point (IP) at the center of the ATLAS detector denotes the origin of the coordinate system. The x -axis points from the IP to the center of the LHC ring, the y -axis upwards, and the z -axis along the beamline, as shown in Figure 3.3. Polar coordinates are also useful to describe the detector parts and particles' momenta with respect to the IP. The polar angle ϕ is defined as the angle in the $x - y$ plane (transverse plane) starting from the positive x -axis. The azimuthal angle θ is defined as the angle from the positive z -axis to the negative z -axis. In collider experiments, the pseudorapidity η is often used instead of θ [84] as

$$\eta = -\ln \left(\tan \frac{\theta}{2} \right). \quad (3.1)$$

In Figure 3.3 the pseudorapidity is zero along the y -axis and it approaches infinity along the z -axis. It is used to give a description of the trajectories of massless objects.

For massive objects the rapidity difference is an invariant under a boost along the z -axis and is defined as [84]:

$$y = \frac{1}{2} \ln \left(\frac{E + p_z}{E - p_z} \right) \quad (3.2)$$

In the collisions, quantities such as energy and momentum are conserved effectively in the $x - y$ plane, transverse to the beam axis because their initial quantities in this plane are known to be zero. Some kinematic variables are defined in the transverse plane, such as transverse momentum p_T and transverse energy E_T . In order to describe the distance of two positions in the $\eta - \phi$ plane

$$\Delta R = \sqrt{\Delta\eta^2 + \Delta\phi^2} \quad (3.3)$$

is often used, where $\Delta\eta$ and $\Delta\phi$ are the differences between the two positions in the η and ϕ coordinates, respectively.

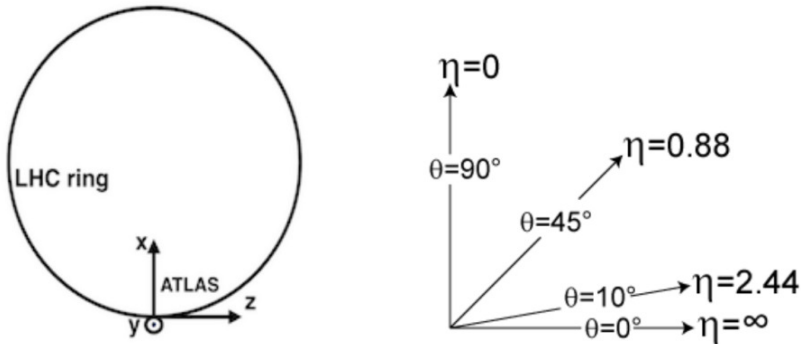


Figure 3.3.: The ATLAS Cartesian coordinate system (left). Values of pseudorapidity η for different polar angles θ [85].

3.2.2. Inner Detector

The detector system closest to the beam line is the inner detector (ID). It is placed in a 2 T magnetic field generated by a superconducting solenoid. The magnetic field is parallel to the beam axis, so that charged particles are bent in the transverse plane. Charged particles travel through the ID in curved tracks bent by the Lorentz force. The charge of the particle and its momentum is inferred by the direction and strength of the track-curvature. The inner detector consists of three trackers: Pixel detector, Silicon Strip Tracker (SCT), and Transition Radiation Tracker (TRT). The layout of the ID is shown in Figure 3.4. In each tracker, different shapes of the layers are used in the barrel and endcap regions to provide tracking information in the range of $|\eta| < 2.5$.

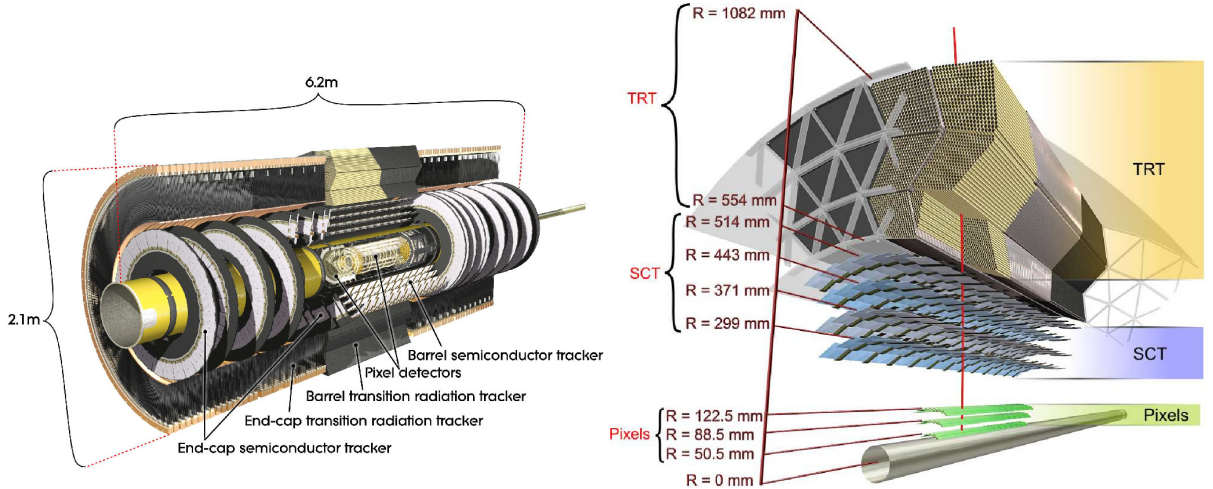


Figure 3.4.: An illustration of the Inner Detector on the left side. Both barrel and endcap regions are shown. On the right side, the positions of the Pixel, SCT, and TRT layers in the barrel region are shown. A typical track crosses one IBL, three pixel and eight SCT layers, as well as 36 TRT tubes [83].

Insertable B-Layer (IBL)

The IBL is a single pixel layered detector located at 33 mm from the beamline. It was installed during the LHC shutdown between LHC Run 1 (2011–2013) and Run 2 (2015–2018) to improve the tracking performance.

Pixel Detector

The pixel detector provides the hit position of charged-particle tracks with high precision covering the $|\eta| < 2.5$ region. With its pixel structure, a 2D hit position is measured on each layer. The hit position measurement on the pixel detector is more important than in the outer layers in terms of reconstruction of primary vertices and b -tagging. Typically three layers of the pixel detector are crossed by each track in both barrel and endcap regions. In total, 80.4 M readout channels are used in the pixel detector. The nominal size of the pixel is $50 \times 400 \mu\text{m}$, and the thickness of the sensors is $250 \mu\text{m}$.

Semiconductor Tracker (SCT)

The SCT is a semiconductor detector with a stripe structure. One SCT layer provides a 1D hit position. Two layers attached in a module are not placed in parallel but inclined by 40 mrad, with this the SCT module can provide 2D hit positions by combining the 1D information from the stereo and nominal SCT layers. Each track typically crosses eight layers. The intrinsic accuracy of hit positions on the SCT modules is $17 \mu\text{m}$ in both barrel and endcap ($R - \phi$), and $580 \mu\text{m}$ for z (R) direction in the barrel (endcap).

Transition Radiation Tracker (TRT)

The TRT [86] contains proportional drift tubes (straws) with a diameter of 4 mm. It provides continuous tracking in $|\eta| < 2.0$. The straw tube wall is made of Kapton coated with aluminum and graphite-polyamide. Tungsten wires plated with gold are used as anodes and supported at the ends of the straw tubes. The straws are filled with a Xe based gas mixture. The TRT has the ability to identify electrons by exploiting photons from the transition radiation. An estimated 36 hits produced per track in the straw tubes, combine with a longer measured track length compensating its lower precision compared to the pixel and SCT systems. The system provides $R - \phi$ information with an intrinsic accuracy of $130 \mu\text{m}$ per straw.

3.2.3. Calorimeters

The calorimeters were designed to measure the energy contained in the showers induced by electrons, photons and hadrons. They also play an important role in measuring missing transverse energy. The electromagnetic calorimeter is surrounded by the hadron calorimeter, as shown in Figure 3.5.

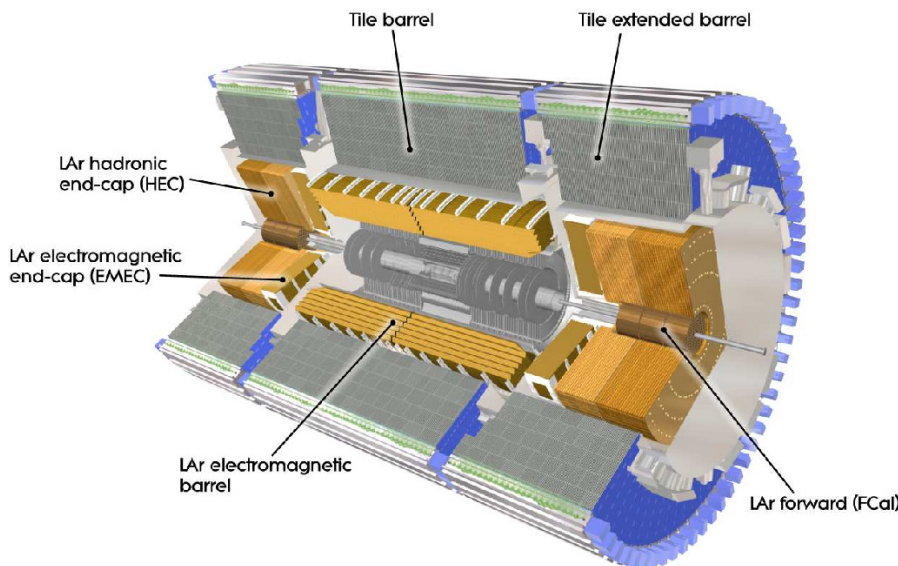


Figure 3.5.: Cut-away view of the ATLAS calorimeter system [83]. The electromagnetic calorimeters are surrounded by the hadronic calorimeters. The calorimeter covers $|\eta| < 4.9$.

Electromagnetic Calorimeter

The electromagnetic (EM) calorimeter is important to perform precise measurements and particle identification of photons and electrons. It covers the barrel ($|\eta| < 1.475$) and endcap ($1.375 < |\eta| < 3.2$) regions. It is a sampling calorimeter in which liquid Ar

(LAr) is used as an active material, and lead as absorber plates. The lead absorber has an accordion shape in the barrel region, as shown in Figure 3.6, to cover the full range in ϕ without azimuthal cracks.

Hadronic Calorimeter

The hadronic calorimeter is divided into three parts: the tile calorimeter ($|\eta| < 1.0$), the LAr hadronic endcap calorimeter (HEC) located behind the endcap EM calorimeter, and the LAr forward calorimeter (FCal) between $3.1 < |\eta| < 4.9$. The tile calorimeter is a sampling calorimeter with scintillating tiles as active material and steel as absorbers, as shown in Figure 3.6 right. The HEC and FCal are sampling calorimeters using liquid argon as active medium. The absorbers are copper (copper-tungsten) plates in the HEC (FCal). Tungsten was used in the outer FCal modules to minimize the lateral spread of hadronic showers.

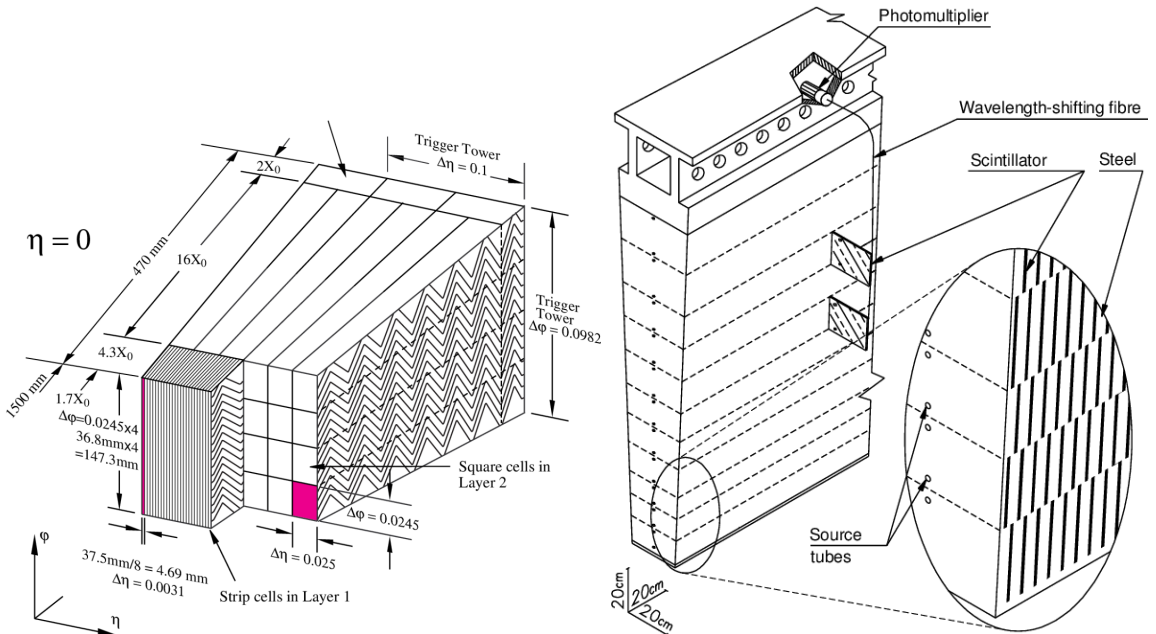


Figure 3.6.: Illustrations of the LAr EM calorimeter (left) and tile calorimeter (right) in the barrel region [83]. The LAr EM calorimeter has three layers with different sizes of segments in $\Delta\eta \times \Delta\phi$. In the tile hadron calorimeter, signals in the scintillators are read by photomultipliers installed at the edge of the detector.

3.2.4. Muon Spectrometer

Muons can pass through the EM and hadronic calorimeters, so a muon spectrometer (MS) is needed to improve the identification and the momentum resolution. It is the outermost sub-detector system of the ATLAS detector, as appreciated in Figure 3.7.

Like the ID, the MS measures momenta by bending the muons trajectories in a magnetic field in $|\eta| < 2.7$.

Four detectors are divided into two types depending to their purposes. The Monitored Drift Tubes (MDT) and Cathode Strip Chambers (CSC) are detectors used for precise measurements of the muon momentum. The Resistive Plate Chambers (RPC) and Thin Gap Chambers (TGC) are mainly used for the trigger decision. The trigger chambers contribute to determine the second coordinate in the muon reconstruction to complement the MDT's 1D measurements in the bending direction. The MS is designed to provide a transverse momentum resolution of 10% for 1 TeV muon tracks. The muon chambers in the barrel are placed in three concentric cylindrical shells around the beam axis at $R = 5, 7.5$, and 10 m. The chambers in the endcaps that form wheels are placed at $|z| = 7.4, 10.8, 14$, and 21.5 m.

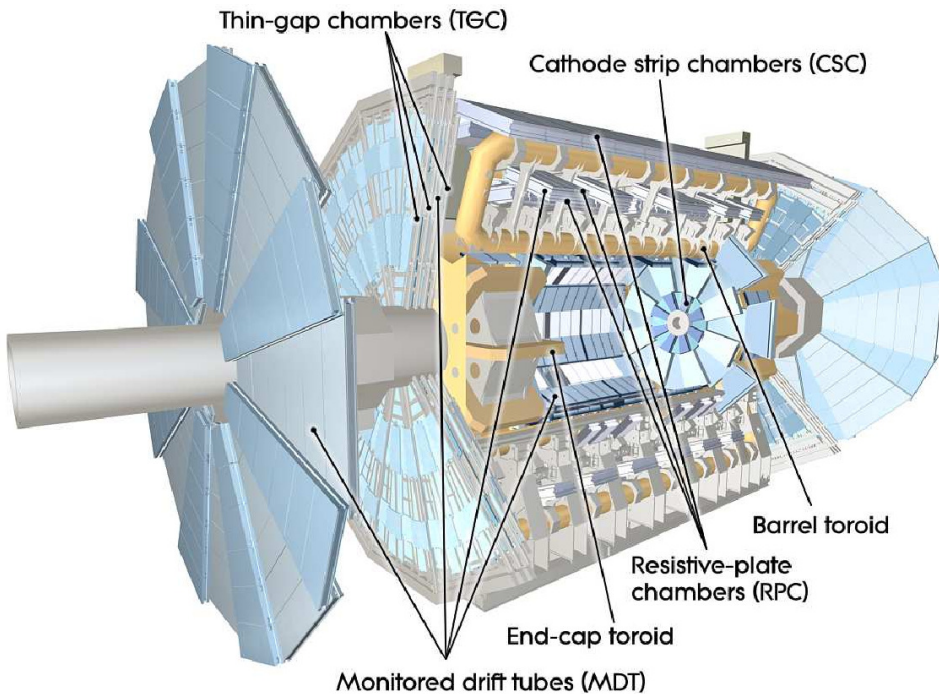


Figure 3.7.: ATLAS muon spectrometers: MDT, CSC, RPC, and TGC [83]. The toroid magnets are shown in yellow.

Monitored Drift Tubes (MDTs)

MDTs are used in both barrel and endcap regions to provide high-precision tracking for muons. The spatial resolution of the track position in the z -direction is $35\ \mu\text{m}$. The MDT system consists of three to eight layers of drift tubes, each with a diameter of 3 cm and filled with Ar (93%) and CO₂ (7%) at 3 bar. At the center of the tubes, a tungsten-rhenium wire is used as an anode of the drift chamber.

Cathode Strip Chambers (CSCs)

CSCs are used as precision muon trackers in the innermost forward region ($2 < |\eta| < 2.7$) instead of MDTs, as CSCs provides better tracking performance than MDTs in the high-hit-rate environment. The CSCs system consists of a set of multi-wire proportional chambers. The cathode plane is divided into strips in the direction orthogonal to the wires to provide 2D hit positions. The resolution of the CSCs is of $40 \mu\text{m}$ in the bending plane and 5 mm in the transverse plane.

Resistive Plate Chambers (RPCs)

RPCs act as trigger chambers in the barrel ($|\eta| < 1.05$) region. The RPCs are gaseous parallel electrode-plate detectors with a 2 mm distance between the two electrodes. The electrodes are separated by PET foils. The readout strips on both sides are placed in the orthogonal direction, so that 2D information of the hit position is available.

Thin Gap Chambers (TGCs)

In the endcap region ($1.05 < |\eta| < 2.4$), TGCs provide muon track information for the trigger decision. The TGCs are made up of multi-wire proportional chambers with a 2.8 mm gap between graphite coated FR4 plates, as the name suggests. Copper strips on the other side of the plate provide azimuthal position measurements. In the middle of the gap, anode wires have a wire-to-wire distance of 1.8 mm. A highly quenching gas mixture of $\text{CO}_2/\text{n-pentane}$ is used to prevent continuous current.

3.2.5. Magnet System

The ATLAS detector has solenoid and toroid magnets, as mentioned in the ID and muon spectrometer, respectively. The solenoid magnet provides a 2 T magnetic field for the ID, while the toroid magnet provide approximately 0.5 T and 1 T for the muon detectors in the barrel and endcap regions. The solenoid magnet is between the ID and EM calorimeter in the barrel, and the inner and outer radii are 2.46 m and 2.56 m, respectively. The nominal operating current is 7.7 kA, which corresponds to the stored energy of 40 MJ. The solenoid is designed to be as thin as possible to reduce material in front of the calorimeters. An Al-stabilized NbTi superconductor surrounding a single-layer coil. The barrel toroid consists of eight coils installed between the muon detectors. The endcap toroid is found between the inner and middle layers of the endcap muon wheels.

3.2.6. Luminosity Detector

The luminosity determination for ATLAS in Run 2 was performed by the LUCID-2 detector (LUMinosity Cherenkov Integrating Detector) [87]. It consists of several Cherenkov detectors installed in the forward region. On each side of the ATLAS detector, 16 photomultiplier tubes (PMT) are installed surrounding the beam pipe at approximately $z = \pm 17$ m and detect Cherenkov light produced in the quartz window of the PMTs. Four additional PMTs are installed on the muon shielding to record Cherenkov light from quartz fibers situated around the beam pipe as a Cherenkov medium. Hit counts in the detectors are then converted into an interaction rate per bunch crossing which is proportional to the instantaneous luminosity.

3.2.7. Trigger and Data Acquisition System

With a spacing time of 25 ns, the proton bunches collide up to 40 million times per second corresponding to 40 MHz bunch crossings. Since it is not possible to record all data due to the huge collision rate, the ATLAS trigger system performs an online selection of the collision data in two steps: the Level 1 (L1) and High-Level Trigger (HLT). An overview of the trigger and data acquisition system is shown in Figure 3.8. The L1 trigger is a hardware-based trigger, which reduces the trigger rate from 40 MHz to about 100 kHz. The trigger decision information comes from the calorimeters and muon trigger detectors (RPCs and TGCs). If an event satisfies a certain trigger requirement, an L1 Accept signal is issued by the Central Trigger Processor (CTP), and the data is transferred downstream. The HLT is a software-based trigger system, which reduces the trigger rate from 100 kHz to about 1 kHz. The events selected by the HLT trigger processor are then recorded in the storage.

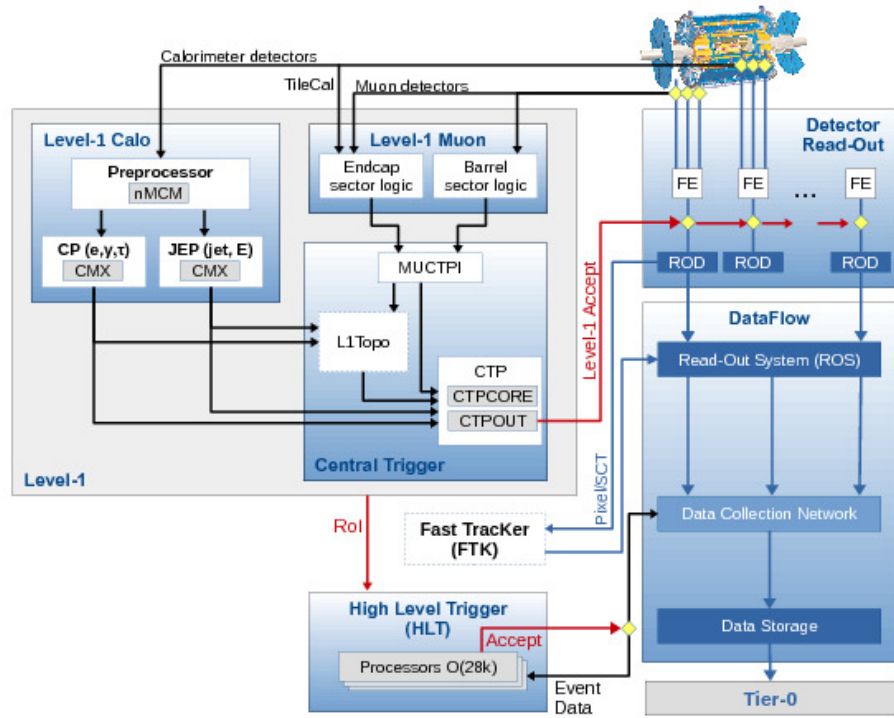


Figure 3.8.: The ATLAS trigger and data acquisition system [88]. The trigger system consists of two stages: Level-1 and HLT. The hardware-based Level-1 trigger uses information from the calorimeter and muon detectors, and issues Level-1 Accept providing information of a region of interest (ROI) to the HLT. The software-based HLT issues the accepted signals to record events using offline-like reconstruction algorithms.

4. Data and Simulation

4.1. Data Acquisition in LHC Run 2

The presented thesis uses pp collisions at a center-of-mass energy of $\sqrt{s} = 13$ TeV recorded with the ATLAS detector during LHC Run 2 in 2015–2018. The total integrated luminosity delivered by the LHC was of 156 fb^{-1} of which ATLAS recorded 147 fb^{-1} . Figure 4.1 shows the evolution of the integrated luminosity in Run 2. The total data with all the component working in 2015–2018 corresponded to 139 fb^{-1} .

Particle detectors at the LHC are challenged by the high pp collision rate and beam intensity. The intensity of the beams needs to be high enough to create multiple interactions per bunch crossing so the processes of interest occur at a reasonable rate. Figure 4.2 shows the profile of the mean number of interactions per bunch crossing (pile-up), as recorded by the ATLAS detector during Run 2. The profile underlines the busy environment in which the data taking took place, with up to 70 simultaneous collisions in some of the LHC fills in 2017 due to special fill conditions. Overall, on average the ATLAS detector recorded $\langle \mu \rangle = 33.7$ interactions per bunch crossing during Run 2. The LHC Run 2 started with low instantaneous luminosity in 2015, but it increased as the LHC and ATLAS operation became stable.

4.1.1. Luminosity measurement

The LUCID 2 detector [87, 89] measures a visible interaction rate per bunch crossing μ_{vis} . The instantaneous luminosity per bunch is

$$\mathcal{L}_b = \frac{\mu_{\text{vis}} f_r}{\sigma_{\text{vis}}} \quad (4.1)$$

where f_r is LHC’s revolution frequency (11246 Hz) defined as the ratio of the speed of light to the circumference of the LHC. The visible cross-section σ_{vis} is a calibration constant specific to the luminosity calibration algorithm. In Equation 4.1, $\mathcal{L}_b \sigma_{\text{vis}}$ corresponds to the visible number of pp collisions given by a bunch crossing pair. A per-bunch instantaneous luminosity with the LHC parameters is given by

$$\mathcal{L}_b = \frac{f_r n_1 n_2}{2\pi \sum_x \sum_y} \quad (4.2)$$

with n_1 and n_2 as the numbers of protons in each bunch of the two colliding beams. Σ_x (Σ_y) is the horizontal (vertical) convoluted beam width measured by the van de Meer (vdM) method [91], in which the beam position in the transverse plane is scanned in a special vdM run once per year. The factor $n_1 n_2$ is determined based on the measurement of beam-gas event rates by the LHCb experiment [92].

4.1.2. Triggers

In the following, *online* refer to triggers measured during the data-taking, while *offline* refers to the reconstruction performed on the recorded dataset and on Monte Carlo (MC) samples. The triggers are simulated for all MC samples of the analysis, so that both data and MC are required to pass the listed triggers. Scale factors were applied to the simulated event samples, in order to correct for differences in the trigger efficiencies between data and simulated samples. The triggers presented are at HLT level, meaning that events passing the L1 requirement are subsequently analyzed by the software algorithms of the high-level trigger (HLT), as explained in the previous Subsection 3.2.7.

In the direct RPC stops search in Chapter 7, the dataset was recorded with a type of trigger requiring a large amount of missing transverse momentum, denoted as E_T^{miss} triggers. At the L1 trigger stage, the trigger algorithm is based on the vectorial sum of energy deposits in the calorimeters, while a more refined computation is done at the HLT, which is based on the vector sum of all calorimeter cells above a particular noise level. The thresholds of the triggers at HLT level are summarized in Table 4.1 and were raised during the period of data taking as the instantaneous luminosity increased. The same trigger conditions were implemented in the simulation. The trigger is fully efficient for an offline calibrated transverse momentum imbalance above 230 GeV, which is applied on the analysis [25].

For the RPV higgsinos scenario described in Chapter 8, an event selection was applied requiring at least one offline identified electron or muon. The full dataset collected by electron or muon triggers at HLT level are summarized in Table 4.1. For electron or muon triggers a matching criteria is applied, which requires that an offline electron or muon is geometrically matched to the object reconstructed by the trigger algorithm. The muon and lepton triggers satisfied the identification criteria similar to those used in the offline reconstruction and isolation criteria in references [93, 94]. Electrons or muons in the final event had to satisfy a transverse momentum (p_T) > 27 GeV condition, in order to be above the trigger threshold [26].

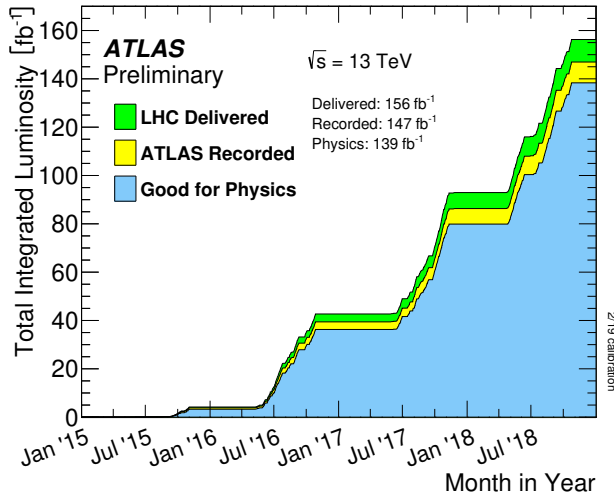


Figure 4.1.: Total integrated luminosity of pp collisions at the LHC during Run 2 (2015–2018). The plot shows the luminosity values delivered by the LHC, the luminosity fraction recorded by ATLAS and the luminosity fraction, where ATLAS was fully operational and stable data-taking conditions were maintained (“Good for Physics”). The size of the dataset taken under these conditions corresponds to an integrated luminosity of 139 fb^{-1} . Figure taken from Ref. [90].

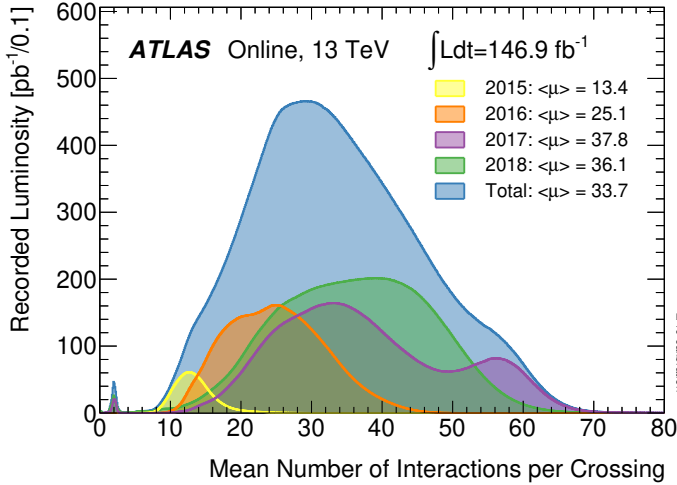


Figure 4.2.: The mean number of interactions per bunch crossing (pile-up) during Run 2, as recorded with the ATLAS detector. The plot shows the profiles of pile-up conditions in the four years of operation. A characteristic double-peak structure is observed for 2017 as the filling scheme of the LHC was adjusted. Figure taken from Ref. [90].

Table 4.1.: Overview of online trigger thresholds at HLT level in each year. The E_T^{miss} triggers were used in the RPC stops search and the lepton triggers in the RPV higgsinos analysis. For the electron and muon triggers only events selected by one of the triggers are used in the event selection. The trigger thresholds were raised as the instantaneous luminosity increased each year.

RPC direct stops		RPV direct higgsinos	
Year	E_T^{miss} (GeV)	electron p_T (GeV)	muon p_T (GeV)
2015	70	24, 70, 120	20, 50
2016	90–110	26, 60, 140	26, 50
2017	90–110	26, 60, 140	26, 50
2018	110	26, 60, 140	26, 50

4.2. Monte Carlo Simulation

Monte Carlo (MC) simulation is of great importance in collider experiments in many aspects. Simulated events are compared with the recorded data and used to estimate the shape and strength of the signal in the data. Moreover, it is common to base estimations of the contributions from SM processes on simulation that are then used for instance as background estimations in searches. In this way, comparisons to simulations are essential to make reliable interpretations from the recorded data. The ATLAS simulation chain follows three steps which are event generation, then detector simulation (including digitization step), and event reconstruction. The event generation has different components such as modeling the parton density functions inside the proton, the pp hard-scattering process, parton showering and hadronization, and detector response [95]. In this section, the steps of MC simulation for SM background and SUSY signal processes are explained.

4.2.1. Event Generation

The simulation of pp collisions is split into two parts in terms of the energy scale of the process. Processes at high energy scales are calculated in the perturbation theory at a fixed order of the strong coupling constant (α_s). Processes at low-energy scale are described by models tuned to data. Models parameterized by experimental results are used because calculating low-energy QCD processes is difficult due to non-perturbative effects with large α_s . A cross-section for a process with a final state n is described as [95]:

$$\sigma = \sum_{a,b} \int dx_a dx_b \int f_a^{p_1}(x_a, \mu_F) f_b^{p_2}(x_b, \mu_F) d\hat{\sigma}_{ab \rightarrow n}(\mu_F, \mu_R) \quad (4.3)$$

with

$$d\hat{\sigma}_{ab \rightarrow n}(\mu_F, \mu_R) = d\Phi_n \frac{1}{2\hat{s}} |\mathcal{M}_{ab \rightarrow n}|^2(\Phi_n; \mu_F, \mu_R) \quad (4.4)$$

The parton distribution function (PDF) is denoted by $f_a^{p_i}(x_a, \mu_F)$ and it describes the quark and gluon distributions in an incoming proton p_i ($i = 1, 2$). The choice of the PDF has an influence on the cross-section as well as on the event shape. In equation 4.3, the PDF is a function of the x_a , which is the fraction of the total proton momentum carried by parton a . The PDF also depends on a factorization scale μ_F , which is an energy scale splitting the low- and high-energy for the PDF and perturbative calculation. The factor $\hat{\sigma}_{ab \rightarrow n}(\mu_F, \mu_R)$ describes the parton-level cross-section of initial partons a and b to a final state n with μ_R as a renormalization scale.

The parton flux is indicated by the factor $1/(2\hat{s}) = 1/(2x_a x_b s)$ with \hat{s} as the parton level center-of-mass energy squared, and Φ_n the phase space of the final state n . $\mathcal{M}_{ab \rightarrow n}$ represents the matrix element (ME) of $ab \rightarrow n$ processes, which corresponds to a sum of Feynman diagrams and depends on μ_F and μ_R . Finally, the total cross-section σ is obtained by summing over all the initial partons in proton p_1 and p_2 , and integrating over the phase space of the final state n together with the momentum fraction of the partons a and b .

There are a large variety of PDF sets provided by specialized groups. Figure 4.3 shows an example of the PDFs of the gluon and the quark sea of the proton at two different energy scales provided by the NNPDF group [96]. The calculations correspond to a precision of the PDF at the next-to-next-to-leading order (NNLO) of perturbation theory. As seen in the figure, the PDFs depend on the energy scale and the momentum fraction x of the partons that contribute to the total momentum.

A schematic view of pp collisions can be seen in Figure 4.4 indicating the different elements with a color code. The ME calculation does not account for low-energy scales to avoid divergence in low-momentum and collinear limits. *Parton showers* (PS) perform an evolution from the energy scale of initial and final state partons towards a hadron confinement scale at an order of 1 GeV, taking into account all effects at higher orders [96]. Below that scale reached after the evolution of the PS, the perturbation theory does not work.

The low-energy non-perturbation treatment is performed by the *hadronization*. It describes the confinement of QCD to generate colorless hadrons from colored partons. Many of the hadrons produced in the hadronization process are unstable resonances. These decay into lighter hadrons with a lifetime long enough to reach and interact with the detector material. As the incoming hadrons are complex bound states, parton shower algorithms handle the evolution down to the hadronization scale. Such contributions are soft and often do not lead to additional reconstructed objects. Instead, they increase the overall scattered energy in the event and increase the amounts of particles at hadronization level.

Additional contributions to the total event structure come from the *underlying event*. It represents a final state component that does not originate from the original hard process and the associated initial or final state radiation. Electromagnetic radiation can be present at all stages of the event generation where charged particles are involved. Commonly it is modeled by shower algorithms working similar to the parton shower.

The models describing the parton shower, underlying event and hadronization introduce a large number of free parameters that cannot be constrained from theoretical principles. Hence, these are derived (tuned) by parameter optimization with respect to experimental data [97]. Several tuning approaches are available [98], and a variety of tunes have been derived from early LHC data.

4.2.2. Simulated Samples

Two sets of samples were used for this thesis. The first is referred to as **SetA** summarized in Table 4.2 and was used in the analysis searching for direct RPC stops processes. The second set, **SetB** in Table 4.3, was used for the RPV direct higgsinos searches. In **SetB** only $t\bar{t}$ and signal samples were used for the studies presented.

The $t\bar{t}$ samples in **SetA** and **SetB** were generated with PowhegBox [100] with the NNPDF3.0 PDF at next-leading order (NLO) accuracy. Events were interfaced to PYTHIA 8 [101] for PS. The $t\bar{t}$ cross-sections were calculated at next-to-next-to-leading order (NNLO) with the resummation of soft gluon emission at next-to-next leading-logarithm (NNLL) accuracy. Single-top samples in **SetA** were generated using the same generator setup as described for $t\bar{t}$. For **SetB** additional $t\bar{t}$ samples were generated with MADGRAPH5_aMC@NLO [102] using the NNPDF3.0 set of PDFs interfaced with PYTHIA 8, and PowhegBox interfaced with HERWIG7 [103] using MMHT2014lo PDF [104], for modeling comparisons and evaluation of systematic uncertainties.

The production of W - and Z -bosons in association with jets ($V+jets$) were generated with SHERPA 2.2.1 [105] for **SetA** at NLO, and the cross sections were calculated up to NNLO [105]. The multiboson samples were generated with SHERPA 2.2.1–2.2.2, and merged with SHERPA PS [106]. The cross sections of the multiboson processes were calculated at NLO. The SHERPA samples used COMIX [107] and OPENLOOPS [108] and were merged with SHERPA PS using the ME+PS@NLO prescription [109].

SUSY signals in **SetA** were generated with MADGRAPH 2.6.2 [110] and PYTHIA 8 PS. MADSPIN [111] was used in the stop four-body decay samples, and the cross-sections were calculated approximately at NNLO+NNLL. SUSY signals in **SetB** were generated with MADGRAPH5_aMC@NLO interfaced to PYTHIA 8. Direct higgsinos were generated with up to two additional partons in the ME. The samples were produced separately for $\tilde{\chi}_1^0 \tilde{\chi}_1^\pm$, $\tilde{\chi}_2^0 \tilde{\chi}_1^\pm$, and $\tilde{\chi}_1^0 \tilde{\chi}_2^0$. Production modes which do not contain leptons in the final

state were not generated, such as $\tilde{\chi}_1^\pm \tilde{\chi}_1^\pm$ because $\tilde{\chi}_1^\pm$ will not decay into a top quark. The cross-sections for higgsino production were calculated at NLO+NLL.

The secondary scattering interactions from the beam remnants were tuned with P2012 [112] and A14 [113] for underlying events (UE) using PYTHIA 8 PS for most of the samples as seen in Tables 4.2 and 4.3. With **SetA**, the dedicated set of tuned parton-shower parameters developed by the SHERPA authors was used. In **SetB**, the events interfaced with HERWIG used the H7UE [114] set of tuned parameters. The GEANT 4 [115] simulation framework was used to describe the interaction of the particles with the ATLAS detector [116]. In the SUSY signal samples, the fast simulation algorithm [115] was used for the shower evolution in the calorimeters.

Process	ME event generator	PDF	PS and and hadronization	UE Tune	Cross-section calculation
$t\bar{t}$	POWHEG-BOX v2	NNPDF3.0	PYTHIA 8	A14	NNLO+NNLL [117–122]
Single top:					
t -channel	POWHEG-BOX v1	NNPDF3.0	PYTHIA 8	A14	NNLO+NNLL [123]
s - and Wt -channel	POWHEG-BOX v2	NNPDF3.0	PYTHIA 8	A14	NNLO+NNLL [124, 126]
$W/Z+jets$	SHERPA 2.2.1	NNPDF3.0	SHERPA	SHERPA default	NNLO [105]
Multiboson	SHERPA 2.2.2-2.2.1	NNPDF3.0	SHERPA	SHERPA default	NLO
$t\bar{t} + V$	AMC@NLO	NNPDF2.3	PYTHIA 8	A14	NLO
SUSY Signal	MADGRAPH 2.3.3	NNPDF2.3	PYTHIA 8	A14	NNLO+NNLL [126, 127]

Table 4.2.: Overview of the MC samples (**SetA**) used in the RPC direct stop search (Chapter 7).

Process	ME event generator	PDF	PS and and hadronization	UE Tune	Cross-section calculation
$t\bar{t}$	POWHEG-BOX v2	NNPDF3.0	PYTHIA 8	A14	NNLO+NNLL [100, 128, 129]
$t\bar{t}$ (*)	MG5_aMC 2.6.0	NNPDF3.0	PYTHIA 8	A14	NNLO+NNLL [102]
$t\bar{t}$ (*)	POWHEG-BOX v2	MMHT2014	HERWIG7	H7UE	NNLO+NNLL [103, 104, 114]
SUSY Signal	MG5_aMC	NNPDF3.0	PYTHIA 8	A14	NNLO+NNLL [130–135]

Table 4.3.: Overview of the MC samples (**SetB**) used in the RPV direct higgsino search (Chapter 8). The samples marked with (*) are alternative samples used to validate the background estimation method or to assess systematic uncertainties on the modeling. The abbreviation MG5_aMC is used to label the MADGRAPH5_aMC@NLO generator.

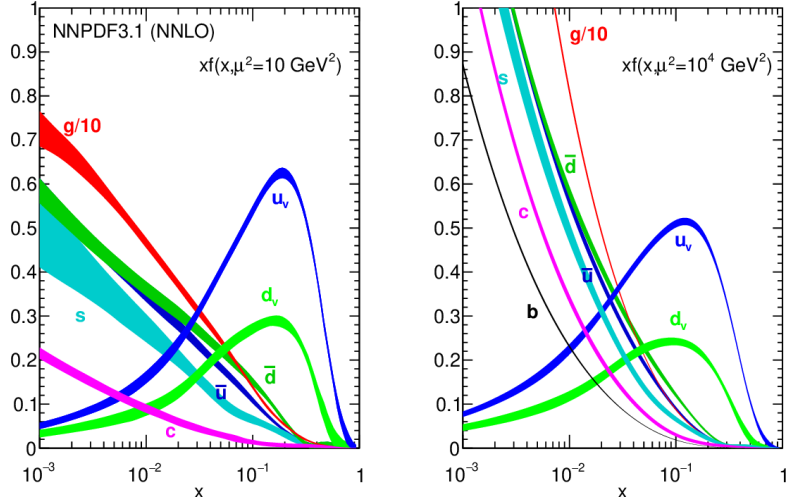


Figure 4.3.: Parton distribution functions (PDFs) of the gluon and valence sea quarks of the proton obtained in the NNLO NNPDF3.1 global analysis [96]. The left plot corresponds to hadronic scales ($\mu^2 = 10 \text{ GeV}^2$) and the right plot corresponds to higher scales as present at the LHC ($\mu^2 = 10^4 \text{ GeV}^2$) [99].

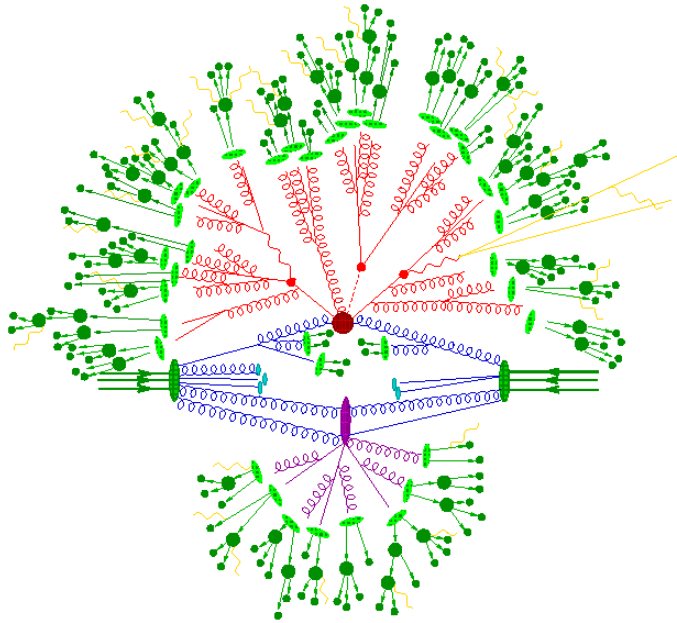


Figure 4.4.: Schematic representation of a top-antitop-Higgs ($t\bar{t}H$) event [110]. Protons collide coming from the left and right sides. The big red blob points to the hard-scatter interaction emitting outgoing particles of the hard process. Initial (final) state radiation is shown in curly blue (red) lines produced below (above) the hard process blob. The hadronization of final-state partons are represented by the light green ellipses while dark green circled blobs are hadrons produced in the hadronization step. The big purple blob shows the underlying event (secondary interaction) generated by the proton remnants. QED radiation is shown by yellow lines.

5. Event Reconstruction

As discussed in Chapter 3, the reconstruction of analysis objects combines information of different parts of the ATLAS detector, by building particle candidates from the measured energy deposits and tracks pointing to the studied particles. However, the object reconstruction is not perfect and miss identifications can occur. To mitigate this, certain quality criteria are introduced to identify the analysis objects.

Not all reconstructed particle types are relevant for every analysis. Different signal models predict certain objects in the events, so additional selection criteria are applied to different variables to reject events outside the phase space of interest. These criteria include, for example, restrictions on the number of reconstructed particles of a certain type. Objects that pass this looser set of criteria are named *baseline* objects. Afterwards, some more sophisticated criteria are required to obtain the event selection, so the remaining particles are the *signal* objects. Only signal objects are considered as a potential outcome of SUSY processes. Either way, baseline objects are needed for the background estimation. In this thesis, the analyses select final states with exactly one electron (e) or muon (μ). For the RPC stop searches in Chapter 7 a large amount of missing transverse energy (E_T^{miss}) is required. On the contrary, the RPV higgsino search selects no or little E_T^{miss} and multiple jets.

5.1. Object Definitions

In this section, how the physics objects are reconstructed from the measured detector signals is explained. The object selection consists of overlap removal (OR) and signal selection. The OR ensures that there is no double-counting of objects as explained in the following. The objects that pass the OR are selected as signal objects. Baseline leptons that pass the OR but fail at least one signal criterion are named loose leptons.

5.1.1. Tracks, Primary Vertex Reconstruction and Topo Clusters

ID tracks are trajectories of charged particles reconstructed from hit information in the ID [136]. Tracks are not used directly in the analyses presented, but they are basic objects for higher-level reconstruction such as b -tagging and the reconstruction of lepton candidates. Reconstructed track parameters are: p_T , η , ϕ , d_0 , z_0 , and the charge of tracks. These are measured using the track curvature caused by the magnetic field provided by the solenoid magnet. The d_0 and z_0 are the transverse and longitudinal

impact parameters. They are defined as the distances from the beam spot to the perigee of the track in the transverse plane and z -direction.

The tracking algorithm starts with the Pixel clustering and SCT hits to define three-dimensional coordinates (space points) in each layer of the tracker. On the Pixel detector layers, the adjacent hits are assembled and a point in space is obtained. The SCT layer contains two sensor layers on both sides of the SCT module that estimate a 3D position. From 3D space points created in the clustering, track seeds are formed. A set of criteria is applied to limit the number of track seeds and increase the track purity. The track seeds are extended by incorporating additional space points on the IBL, the Pixel, and the SCT using Kalman filter [137, 138], in this way track candidates are reconstructed. In this step, the track collection contains an overlap of incorrectly assigned track candidates. The ambiguity is solved by using a score in a reward/penalty scheme considering the properties of the track candidates, such as the shared hits and holes in the ID sensors are taken into account.

The track candidates still need to satisfy basic quality criteria as a p_T threshold of > 500 MeV, $|\eta| > 2.5$, and impact parameters. A high-resolution fit is then applied to the track candidates that pass the ambiguity process to measure the track parameters precisely. The high-resolution fit uses all available information, such as the position and uncertainty of clusters of hits determined by an artificial neural network (NN). The NN also identifies merged clusters that are formed by multiple particles. Finally, the track candidates found in the silicon detectors are extended into the TRT, which are then used in the high-level reconstruction algorithms, as explained in the following sections.

The interaction points of the pp collisions are obtained from the reconstructed tracks [139, 140]. The vertex is reconstructed by the adaptive vertex fitter [141], using the beam spot as a seed position in the transverse plane. The vertex position resolution is about $30 \mu\text{m}$ in the longitudinal direction and of the order of $10 \mu\text{m}$ in the transverse plane. The vertex with the highest sum of squared p_T of tracks is selected as hard-scattering vertex. This hard-scattered vertex is considered as the origin of the physics process of interest. In the following, the hard-scatter vertex is referred to as the primary vertex (PV), and the other vertices of pp collisions are referred to as pileup vertices.

Topological clusters (topo-clusters) are formed when the energy deposits in the calorimeters are clustered collecting the measured energies from neighboring cells [142, 143]. The reconstruction of topo-clusters uses the three-dimensional distribution of energy deposits in the calorimeter cells. The energy and direction of an input particle are calculated by summing all the energies in these cells. Topo-clusters are formed based on the cell signal significance $\zeta_{\text{cell}}^{\text{EM}}$, which is defined as the measured energy $E_{\text{cell}}^{\text{EM}}$ in the calorimeter cell divided by the average level of the noise in the cell $\sigma_{\text{noise},\text{cell}}^{\text{EM}}$ as

$$\zeta_{\text{cell}}^{\text{EM}} = \frac{E_{\text{cell}}^{\text{EM}}}{\sigma_{\text{noise},\text{cell}}^{\text{EM}}} \quad (5.1)$$

Both energies are measured on the electromagnetic energy scale. This scale reconstructs the energy deposited by electrons and photons. The calorimeter signal is converted to energy for electrons and photons (EM scale). The hadron energy is different from the EM scale due to different responses between the EM showers and hadron showers.

The reconstruction of topo-clusters starts with the reconstruction of *proto-clusters*. First, a seed cell with $\zeta_{\text{cell}}^{\text{EM}} > 4$ is reconstructed as a proto-cluster. If the neighboring cells have significant energy above a certain threshold, they are added to the proto-cluster. Finally, if a cell in the new proto-cluster has $\zeta_{\text{cell}}^{\text{EM}} > 2$, the neighboring cells are checked to have $\zeta_{\text{cell}}^{\text{EM}} > 0$ to be added too. Topo-cluster formation is a sequence of seed and collect steps, which are repeated until all topologically connected cells passing the criteria described above is satisfied. The direction of a topo-cluster is calculated from the average of positions of cells in η and ϕ .

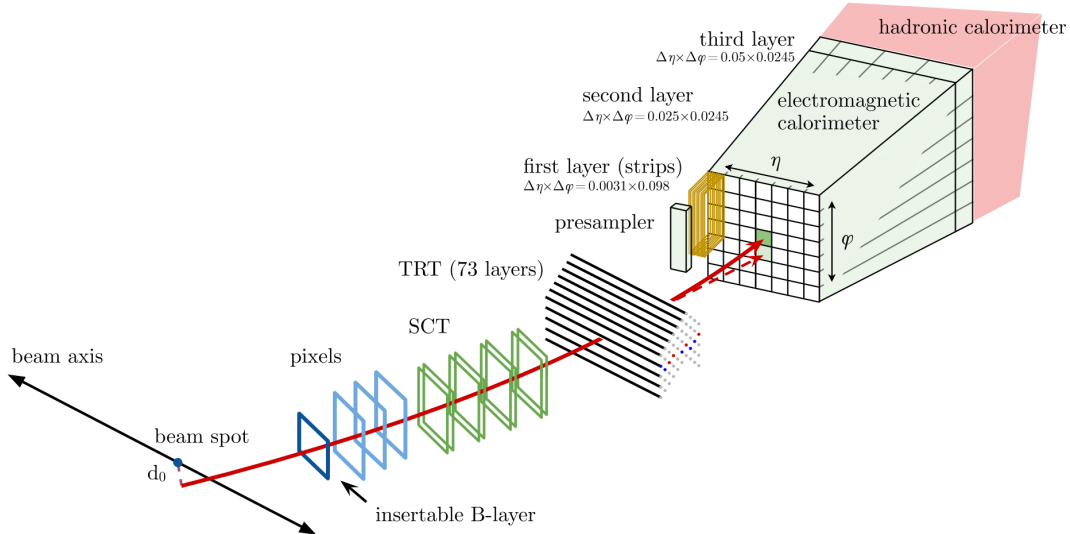


Figure 5.1.: Illustration of the trajectory of an electron through the detector. The red trajectory shows the hypothetical path of an electron, which first traverses the tracking system and then enters the electromagnetic calorimeter. The dashed red trajectory indicates the path of a photon produced by the interaction of the electron with the material in the tracking system [144].

5.1.2. Electrons

Electron candidates are reconstructed from energy clusters formed in the EM calorimeter matched to a track in the inner detector (ID). Figure 5.1 shows an illustration of an electron trajectory passing through the detector components. The reconstruction of an electron is based on track reconstruction, cluster reconstruction, and track-to-

cluster matching. Additional to the track fit presented in Section 5.1.1, another fit is performed if the first one fails. In the second fit attempt, the bremsstrahlung losses from electrons are considered by an additional degree of freedom using a Gaussian-sum filter (GSF) [145] to recover efficiency for electrons. Clusters of the calorimeter cells are reconstructed using the topo-cluster algorithm. The electron is reconstructed using the energy from the EM calorimeter cells except for the transition region ($1.37 < |\eta| < 1.63$).

The electrons in the presented analyses are identified using the `LooseAndBLayerLH` definition in [146] for the RPC stops search and `MediumLH` identification criteria [147] for the RPV higgsinos analysis. These criteria set requirements on the showers widths and energy deposits in the EM calorimeter or number of hits in the ID associated with the track. Electrons reconstructed in Monte Carlo (MC) simulation are calibrated so that their energy resolution matches the one observed in data. Baseline electrons are required to have $|\eta| < 2.47$ and are used for the OR between jets and electrons. For the RPC direct stops search a $p_T > 4.5$ GeV is required while the RPV higgsinos search selects electron candidates with $p_T > 10$ GeV and not in the transition region between the barrel and endcap calorimeters ($1.37 < |\eta| < 1.52$) [26].

To suppress electrons from secondary vertexes, signal electrons must have a transverse impact parameter with respect to the primary vertex (d_0) satisfying $|d_0|/\sigma_0 < 5$ with σ_0 as uncertainty. In addition, the primary vertex along the z_0 beam direction needs to satisfy $|z_0 \sin \theta| < 0.5$ mm. Furthermore, they must pass additional p_T -dependent isolation criteria. This improves the discrimination against semileptonic decays of hadrons and misidentified jets.

Signal electrons are required to satisfy additional criteria such as `TightLH` definition introduced in [147], which is an identification working point. Signal regions requiring low-momentum leptons, such as the RPC stop analysis, have the tighter `FCTight` isolation working point. The $p_T > 4.5$ GeV selection is also required for signal electrons in this search. The RPV search selected the isolation WP guided by the Isolation and Fake Forum group recommendations on the `PLVTight` WP [148]. The analysis selected signal electrons with $p_T > 27$ GeV. In the RPV higgsinos search, the `PLVTight` WP was found to have the best fake/non-prompt electron background rejection while keeping the signal electron efficiency reasonably high. Scale factors that take into account discrepancies between data and MC in the electron reconstruction, identification and isolation efficiency are applied to MC events.

5.1.3. Muons

Muons are reconstructed from combined objects formed in the muon spectrometer, inner detector and calorimeter. Muons are characterized by a long trajectory penetrating the detector due to their small energy losses in the calorimeters. Muons in the physics analyses are mainly prompt muons produced directly from decays of e.g. W/Z bosons or potential BSM particles. Background muons from pion or kaon decays are suppressed at

the isolation step. Several working points (WP) are provided depending on the tightness of the muon identification (Loose, Medium, Tight). For the searches in this thesis, the Medium working point was selected. The muon efficiency with the Medium WP is shown in Figure 5.2 on the right. Within the ID acceptance $|\eta| < 2.5$, the Medium WP accepts only combined (CB) and inside-out combined (IO) muons classified as follows [149, 150]

- Combined muon (CB)

Muon candidate tracks are reconstructed separately in the ID and MS. Then, the candidate tracks from each detector are used as a single muon combining the hits from the ID and MS.

- Inside-out combined muon (IO)

The ID tracks are extrapolated to the MS using a complementary *inside-out* algorithm. This algorithm searches for at least three aligned MS hits to be used in a combined track fit recovering some efficiency in limited regions.

Muons originating from heavy particles such as W/Z bosons or BSM particles are isolated, while muons from semileptonic decays of heavy hadrons (b - or c -hadrons) typically are accompanied by hadronic activity around the muon track. To reduce these background muons from hadron decays, isolation variables are defined, two of which are used in the searches presented. The first one is $p_T^{\text{varcone}30}$, the scalar p_T sum of the muon tracks with $p_T > 1$ GeV in a cone of size $\Delta R = \min(10 \text{ GeV}/p_T^{\text{muon}}(\text{GeV}), 0.3)$ around the muon track. The second variable is $E_T^{\text{topcone}20}$ which is the scalar sum of the transverse energy of topological clusters measured in the calorimeters in a cone of size $\Delta R = 0.2$ around the muon, taking into account the contribution from the muon.

Baseline muons in the RPC stop search (RPV higgsino search) are selected up to $|\eta| < 2.7$ (< 2.5) and are required to have $p_T > 4$ GeV (> 10 GeV) fulfilling the **Medium** [149] identification criteria. The left plot in Figure 5.2 shows the muon reconstruction and identification efficiencies as a function of p_T as low as 4 GeV. For muon tracks with p_T greater than 10 GeV, the efficiencies and the data/MC agreement are stable. On the contrary, the efficiencies drop significantly in the p_T region below 5 GeV, as soft muons crossing the calorimeters often do not have enough residual energy to reach the second station of precision MS chambers.

Signal muons must pass the baseline requirements and in addition have impact parameters satisfying $|d_0|/\sigma_0 < 3$ and $|z_0 \sin \theta| < 0.5$ mm in both analyses. Signal muons also satisfy the **Medium** [149] identification criteria. Like electrons, muons have similar isolation criteria but with a fixed cut on the track-based isolation energy variable for the RPC search. The RPV analysis uses the same isolation WP as in the electron criteria, the PLVTight, and signal muons with > 27 GeV p_T .

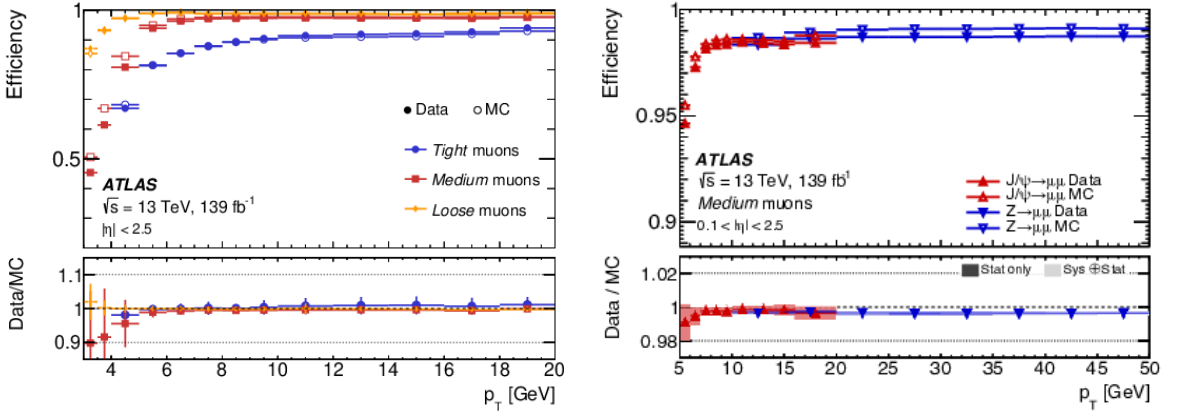


Figure 5.2.: The left plot displays the reconstruction efficiency for the Loose, Medium and Tight muons [150]. It shows the selection criteria as a function of the muon p_T (lower than 4 GeV), in the region $|\eta| < 2.5$ as obtained with $J/\psi \rightarrow \mu\mu$ events. The right plot shows the efficiencies only for the Medium muon criteria in $Z \rightarrow \mu\mu$ and $J/\psi \rightarrow \mu\mu$ events as a function of p_T in the $0.1 < |\eta| < 2.5$ region. The error bars on the efficiencies indicate the statistical uncertainty. The panel at the bottom shows the ratio of the measured to predicted efficiencies, with statistical and systematic uncertainties.

5.1.4. Jets

Jets are reconstructed from three-dimensional topological clusters in the calorimeters. The cluster reconstruction starts with a cell containing a certain energy deposit. Then, neighboring calorimeter cells that have significant energy deposits compared to the expected noise are grouped into clusters. Using such clusters, jets are reconstructed by the anti- k_t jet clustering algorithm [151] with a distance parameter of $R = 0.4$.

The reconstructed jet candidates are calibrated [152] to account for the effects from e.g. the calorimeter inhomogeneities, using calibration factors which depend on the energy and η of the jets. The calorimeters have a different response for electromagnetic and hadronic constituents of the jets. The energy losses in inactive regions and energy deposits which are below the noise threshold are not used in the jet reconstruction. In addition, particles from pileup interactions (additional pp collisions) also affect jet energies, these additional particles increase the jet-energy response and make it luminosity-dependent.

In the simulation, truth jets are formed from generator-level particles with a lifetime ≥ 10 ps produced in the fragmentation model of the MC generator. The calibration factors are derived from simulation and defined by [152]:

$$R(E, \eta) = \left\langle \frac{E_{\text{reco}}}{E_{\text{truth}}} \right\rangle \quad (5.2)$$

where E_{reco} is the reconstructed energy and E_{truth} is the jet energy at truth level. The jet energy calibration also corrects for pileup effects. The calibration is then validated with test-beam and collision data. This p_{T} and η -dependent jet calibration corrects the energy of the jet to be the same as the energy at particle level. There is also a pileup correction to the direction of the jet to point to the primary vertex, and a further correction to reduce the dependence on quark-gluon composition.

The difference between data and MC is corrected via *in situ* calibration. In the *in situ* calibration, the data and MC differences are quantified by the p_{T} ratio of a jet to other well-measured reference objects. The response $R_{\text{in situ}}$ is defined as the average ratio of jet p_{T} to the p_{T} of the reference object. The ratio of the $R_{\text{in situ}}$ between data and MC is used to correct the p_{T} of jets as a function of jet p_{T} and η . In order to utilize good reference objects balancing to the jet that is being calibrated, Z boson, photon, and multijet events are used. The uncertainties on the *in situ* mainly arise from the miss-modeling of physics effects and the kinematic measurements of the reference objects. A final residual calibration using *in situ* measurements is applied only to data in all the analyses.

The baseline jets are required to have a $p_{\text{T}} > 20$ GeV and are used to perform OR. Signal jets in the RPC (RPV) analysis are further required to have $p_{\text{T}} > 25$ (20) GeV, be within $|\eta| < 2.5$, and pass a jet vertex tagger cut [152] ($\text{JVT} > 0.59$ to suppress pileup jets) if the jet p_{T} is below 120 GeV and it resides within $|\eta| < 2.4$.

5.1.5. b -tagging

Jets containing b -hadrons can be identified as b -jets. The b -jet identification is based in general on the measure of the first and secondary vertex information. The MV2c10 algorithm is applied which uses a boosted decision tree (BDT) algorithm to discriminate b -jets from light (u , d , s -quark or gluon jets) and c -jets [153] in the RPC stops search. The BDT is trained with simulated $t\bar{t}$ events for jets with $p_{\text{T}} < 250$ GeV, while Z' events are used for the jet p_{T} above 250 GeV. The kinematic variables, p_{T} , and η , are included in the input variables for the BDT to account for their correlation with the discriminant variables. The JetFitter algorithm [153] uses variables that describe properties of the cascade decay, such as the number of vertices, the total number of tracks, and the vertex mass. The MV2c10 distributions of b -jet, c -jets, and light-flavor jets are shown in Figure 5.3. Working points are defined by selecting a certain threshold on the MV2c10 score above which jets are identified as b -jets. The WP with 77% b -tagging efficiency is used in the RPC stops search which means that the probability of a b -jet within $|\eta| < 2.5$ is b -tagged amounts to 77%. This WP yields rejection factors for the light-flavor and c -jets of 110 and 4.9, respectively.

In RPV higgsinos search, the DL1 algorithm [154] is used instead which is based on an Artificial Deep Neural Network. A WP is chosen which provides an average b -jet identification efficiency of 70%. The rejection factors for this WP are for light-flavor 130

and c -jets 10.2.

Jets passing the pileup-cleaning requirement within the b -tagging acceptance of $p_T > 20$ GeV and $\eta < 2.5$ are considered for b -tagging. The $\text{JVT} > 0.59$ is applied in the same way as in the jet selection for both analyses. Scale factors that take into account discrepancies between data and MC in tagging efficiencies are applied to the MC events.

To complement the RPC stops search, a dedicated soft b -tagging algorithm and calibration were developed [155]. The results of the default b -tagging and the soft b -tagging were combined to increase the sensitivity as seen in Section 7.5.

5.1.6. Overlap removal

Ambiguities can arise when the objects described above are reconstructed. As the object reconstruction run independently from each other the same detector signature may be used twice. For example, an electron could also be reconstructed as a jet in the calorimeters. The procedure to resolve this needs to be capable of retaining two different and close by objects. A solution for this kind of problem is the OR optimized using simulation following a scheme established in Run 1 [156].

In the OR procedure, a distance measure is employed using the rapidity y capturing better than the pseudorapidity η where the jet's p_T is located denoted by $\Delta R_y = \sqrt{(\Delta y)^2 + (\Delta\phi)^2}$ [157]. A shared track or distance between the two objects based on ΔR_y are used as matching criteria. The steps are performed in the following order, with only surviving objects participating in subsequent steps:

- if an electron and a muon share an ID track and if in addition the muon is calorimeter-tagged, the muon is removed, otherwise the electron is rejected
- if an electron and a jet (non b -tagged) are separated by $\Delta R_y < 0.2$, then the jet is discarded and the electron retained
- if a muon can be ghost-matched [159] to a jet within $\Delta R_y < 0.2$ and the jet is not b -tagged, the object is interpreted as a muon if the jet has less than 3 tracks with $p_T > 500$ MeV
- if a jet and a lepton overlap within $\Delta R < \min(0.4, 0.04 + \frac{10}{p_T/\text{GeV}})$, then the lepton is removed and the jet is retained

5.1.7. Missing Transverse Momentum

Momentum conservation implies that the total sum of transverse momenta in a pp collision should be zero. Neutral weakly interacting particles, such as neutrinos or the lightest supersymmetric particle (LSP), do not interact with any detector material and

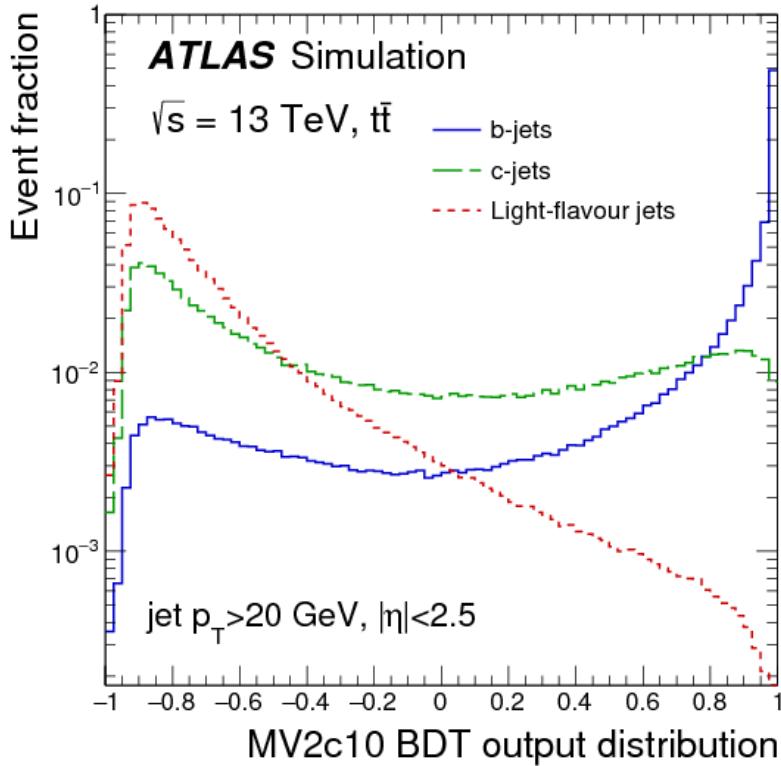


Figure 5.3.: MV2c10 distribution of b -jets, c -jets, and light-flavor jets [158]. The histograms are normalized to unity. Scores close to one are given to b -jet-like jets, while jets with low scores are less likely b -jets.

hence escape detection. As a consequence, a momentum imbalance in the transverse plane originates in an event where such particles are present, referred to as the missing transverse momentum \vec{E}_T^{miss} . Only the transverse momentum is considered because the longitudinal momenta of the partons are unknown. It is defined as the negative vector sum of all reconstructed objects in an event and its magnitude is denoted as E_T^{miss} .

The reconstruction of \vec{E}_T^{miss} contains a *hard* component from calibrated objects and a *soft* component of charged-particle tracks from the ID which are associated with the primary vertex but not related to any reconstructed object.

$$\vec{E}_T^{\text{miss}} = \vec{E}_T^{\text{miss,hard}} + \vec{E}_T^{\text{miss,soft}} \quad (5.3)$$

with

$$\vec{E}_T^{\text{miss,hard}} = - \sum_{\text{electrons}} \vec{p}_T^e - \sum_{\text{muons}} \vec{p}_T^\mu - \sum_{\text{jets}} \vec{p}_T^{\text{jet}} \quad (5.4)$$

$$\vec{E}_T^{\text{miss,soft}} = - \sum_{\text{unused tracks}} \vec{p}_T^{\text{track}} \quad (5.5)$$

In the presented analyses, E_T^{miss} is computed using baseline jets, electrons, muons as well as an extra soft term built from high quality tracks associated to the primary vertex but not to the baseline objects [160]. Photons are not considered but enter as jets, electrons or via the soft term allowing E_T^{miss} to be almost independent of pileup effects. In addition tracks that are not associated to reconstructed objects are included in the E_T^{miss} calculation. Ambiguities between close-by objects are resolved by a dedicated OR procedure [161] in the calculation, that runs independently from the one used in the analysis.

5.2. Event Cleaning

Data corruption given by detector problems, software bugs, noise bursts and other issues can happen. Before using the events for the analysis, events must pass an event cleaning resumed in some stages [162]:

- **Good Run List:** The Good Run List (GRL) is used to remove luminosity blocks (approx. 1–2 minutes of data taking) affected by detector problems.
- **Cosmic Muons:** Cosmic-ray showers produced in the atmosphere can overlap with collision events. Since ATLAS is deep underground, the particles reaching the ATLAS detector are predominantly muons [163]. To avoid this, a veto is applied in cosmic muon candidates. Criteria depending on the longitudinal and transverse impact parameters of impact with respect to the primary vertex are applied.
- **Jet Cleaning:** Jets arising from cosmic rays, beam induced backgrounds or detector noise are suppressed by applying a quality criterion named `BadLoose` described in [163]. It applies certain quality requirements depending on the signal pulse shape in the LAr calorimeter, track variables and energy ratios.

6. Search strategies

The purpose of the following chapter is to give an overview of the basic analysis strategy. Two searches are presented in this thesis. The first one studies a direct production of top squarks conserving R -parity (RPC). It is referred to as *RPC stops*. The second is a search for direct higgsinos in a R -parity violating (RPV) scenario, ergo *RPV higgsinos*. Their strategies are quite different, but their specifications are given in Chapter 7 for RPC stops, and Chapter 8 for RPV higgsinos.

6.1. RPC stops and RPV higgsinos search strategies

In the following chapters, the searches are performed by looking for excesses over the SM prediction in the collected data. To predict the SM events, we rely on the MC simulation by making use of the established knowledge of the SM.

First, signal models are considered for a specific scenario and MC events are generated for signals and backgrounds. Afterwards, discriminating variables are constructed by exploiting the kinematics of the processes. These discriminating variables separate the SUSY signal from the SM backgrounds or a specific SM background from the rest. Signal regions (SRs) are defined to maximize the sensitivity for a benchmark signal. Different selections on the discriminating variables are optimized to suppress most of the backgrounds.

6.1.1. RPC stops strategies

The search for direct stop production presented in Chapter 7 was designed with the following strategy. Two types of SRs are used in the analysis. First, a discovery scenario is defined based on counting events in a signal region to quantify the existence of potential excess. The other analysis technique, referred to as the exclusion scenario, is used in the absence of any evidence for new physics beyond the SM, in which the SR is split into multiple bins in a specific variable. The results are already public in reference [25].

SM processes that have a similar signature as the expected SUSY signal remain in the SR. It is important to have a good understanding of these processes to study their contributions to the SR. In order to estimate the background processes contaminating the SR, control regions (CRs) are defined. The CRs are designed to have a high purity

of one type of SM background process and a set of selection criteria similar to those describing the SR. The difference is that requirements are altered to retain a sufficiently large number of events from that process and reject most of the signal and other backgrounds. Kinematically the CRs should be as close as possible to the SR to have a small extrapolation from CR to the SR.

The prediction obtained from the CRs is verified by comparing it to the observed data in dedicated validation regions (VR). They are typically defined between the SR and the CR. All the SR, CRs, and VRs are required to be orthogonal to each other. Experimental and theoretical systematic uncertainties are evaluated as explained in Section 7.4.

A simultaneous fit as in Section 7.4 is performed in the SR and the associated CR. The VR is only used to cross-check the background prediction and it does not constrain the SM background events in the fit. The observed data are compared to the SM background prediction estimated from the MC with scale factors, which correct the imperfect modeling of the MC simulation. A maximum-likelihood fit is performed with all the exclusion scenario bins. The reason for this procedure is that using the signal-to-background ratios in the different bins leads to an increased sensitivity for a potential signal exclusion. Signal regions are then compared to data looking for an “excess”, in a process called *unblinding*. Hypothesis tests are performed to discover or exclude the signals.

6.1.2. RPV higgsinos strategies

The strategy for this analysis is different from conventional SUSY searches. It cannot rely fully on MC simulations due to its complex final state. This is why a data-driven method was used. More details are presented in Chapter 8.

This analysis searches for RPV SUSY with many jets and b -jets in the final state. A nominal analysis called *jet-counting* was used in the beginning. After a basic selection, no additional cuts were imposed on any other kinematic variables aside from the number of jets and b -jets. This strategy alone was not sufficient to reach sensitivity in the targeted scenario. For this reason in this thesis, a new extension of the analysis named *shape analysis* is introduced. It includes a third variable based on a neural network (NN) discriminant [26].

The NN training is performed imposing the constraint that the NN output distribution of the main background is invariant with respect to the b -jet multiplicity. This property is later exploited to estimate the background from data, as described in Section 8.2. The estimation of the dominant backgrounds is carried out by a combined fit to the jet and b -jet multiplicity. The parametrization applied is further explained in Section 8.2, and its assumptions are then validated using data and MC simulation.

6.2. Signal models

Two different signal models are presented in this thesis. The main target of this dissertation is the search of direct \tilde{t}_1 pair production in the R -parity conserved (RPC) scenario. It is the main search because a complete high-energy physics analysis was performed. Nevertheless, higgsino searches are also described using a machine learning technique in a R -parity-violating (RPV) process. The R -parity-violating analysis searches for events with at least one lepton, jets, and b -jets in the final state. This model considers directly pair-produced higgsinos decaying promptly via the RPV coupling.

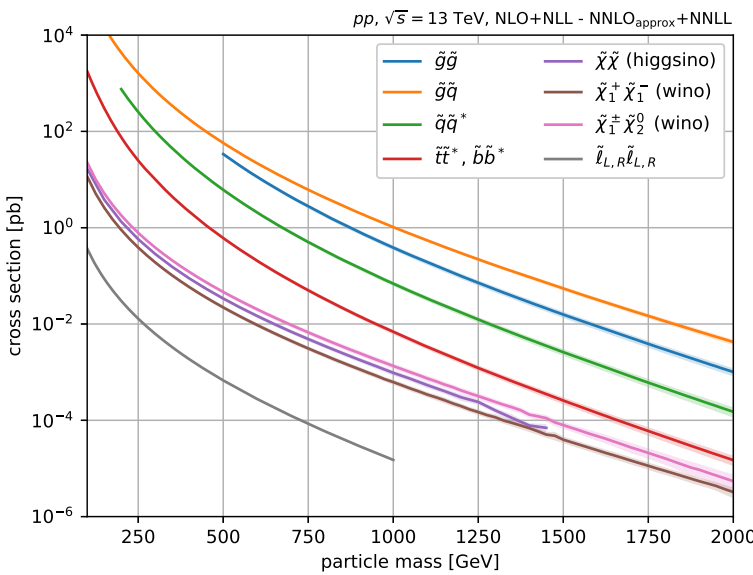


Figure 6.1.: Cross-sections of SUSY signals as a function of the mass of the particle [166]. The cross-sections are calculated approximately at the NNLO + NNLL precision for the squarks (RPC stops) and gluino productions, and the NLO+NLL precision for the electroweak (RPV higgsinos) productions. For a pair of different types of particles, the two particles are assumed to have the same mass. The colored bands show the uncertainties on the cross-sections estimated from the variation of renormalization and factorization scales and the PDF.

Figure 6.1 shows the production cross-sections of SUSY particles in pp collisions at $\sqrt{s} = 13$ TeV, where the cross-sections depend on the masses of the SUSY particles. The cross-sections are calculated at NNLO + NNLL precision for the \tilde{t} shown in the red curve used for the RPC stops model, and at NLO+NLL precision for the $\tilde{\chi}$ (higgsino) in purple used for the RPV higgsinos analysis.

6.2.1. Simplified models

The large number of free parameters in the MSSM, the huge amount of possible decay scenarios and not knowing the range of the masses of the supersymmetric particles, make the experimental searches rather challenging. However, to evaluate searches for new physics, an effective framework referred to as a simplified model is used. Simplified models are only characterized by a small number of parameters, such as particle masses or branching ratios, which are directly related to collider physics observables [164, 165]. In this thesis, the targeted simplified models set all their sparticles masses to high values except for the few sparticles involved in the decay chain of interest.

The experimental signatures can vary dramatically, depending on the spectrum of the SUSY particles. The phenomenology of each model is largely driven by the composition of its lightest supersymmetric particles. In this dissertation, for the RPC stops scenario a pure bino LSP is considered. For the RPV higgsinos a higgsino LSP hypothesis is used.

6.2.1.1. RPC pure bino LSP model

A simplified model is considered for the scenario that conserves R -parity where the only light sparticles are the stop and the lightest neutralino as shown in Figure 6.2. The decay modes depend on the mass difference between \tilde{t}_1 and $\tilde{\chi}_1^0$ ($\Delta m(\tilde{t}_1, \tilde{\chi}_1^0)$). When $\Delta m(\tilde{t}_1, \tilde{\chi}_1^0) > m_t$, the \tilde{t}_1 directly decays into the same flavor SM particle, top quark, together with the LSP $\tilde{t}_1 \rightarrow t + \tilde{\chi}_1^0$. If $\Delta m(\tilde{t}_1, \tilde{\chi}_1^0)$ is smaller than m_t and greater than $m_W + m_b$, the \tilde{t}_1 decays via a three-body decay via an off-shell top quark $\tilde{t}_1 \rightarrow bW\tilde{\chi}_1^0$. For the most compressed case where $\Delta m(\tilde{t}_1, \tilde{\chi}_1^0) < m_W + m_b$ the four-body decay mode takes place via an off-shell W boson $\tilde{t}_1 \rightarrow bff'\tilde{\chi}_1^0$, where f and f' denote fermions¹. In each model a 100% branching ratio of the respective decay mode is considered. The diagrams of these decay models are shown in Figure 6.3. The region where $m_{\tilde{t}_1} < m_{\tilde{\chi}_1^0}$ is considered as “forbidden” as the $\tilde{\chi}_1^0$ is taken to be our lightest supersymmetric particle (LSP). The main target of this dissertation is the most compressed region or the four-body decay.

6.2.1.2. RPV higgsino LSP model

This analysis considers two models of pair-produced higgsinos decaying promptly via a R -parity-violating (RPV) coupling. Under the hypothesis of R -parity conservation (RPC) as explained in Subsection 2.2.5, SUSY particles must be produced in pairs and decay to the stable lightest supersymmetric particle (LSP). The majority of SUSY searches at the LHC assume RPC because the LSP is a good dark matter candidate as explained in Chapter 2. The associated SUSY scenarios typically come with large missing transverse momentum that results from the two undetected LSPs.

¹A flavor changing decay $\tilde{t}_1 \rightarrow c\tilde{\chi}_1^0$ is not considered in this dissertation.

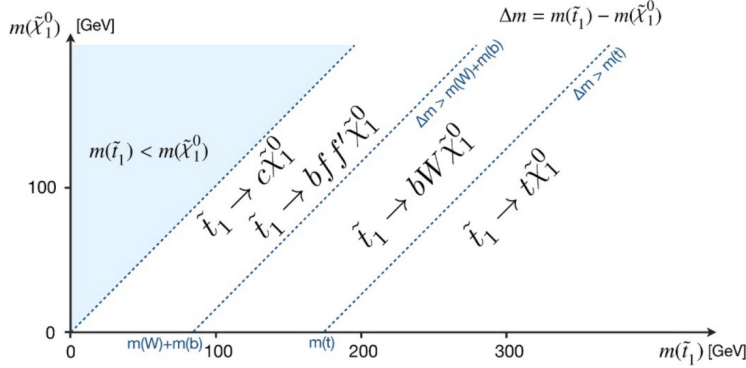


Figure 6.2.: Possible decay modes in the RPC stops simplified model. The decay modes depends on $\Delta m(\tilde{t}_1, \tilde{\chi}_1^0)$. In each region of the phase space, 100% branching ratio is assumed.

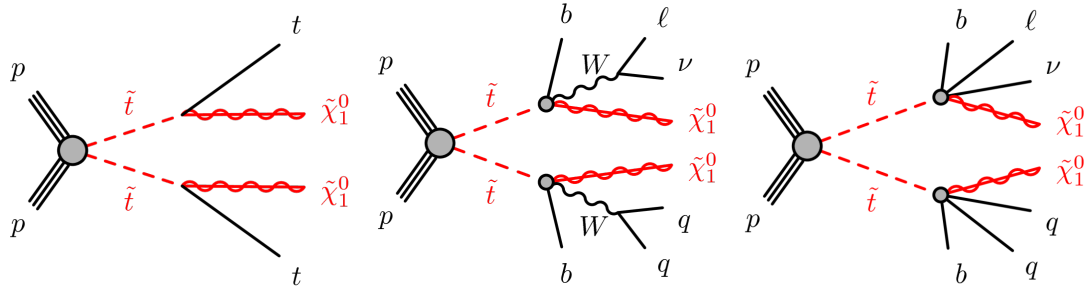


Figure 6.3.: Diagrams of \tilde{t}_1 decaying into $\tilde{\chi}_1^0$. When $\Delta m(\tilde{t}_1, \tilde{\chi}_1^0)$ is large enough to decay to an on-shell top quark, the two-body decay (left) is considered. In the three-body decay (middle), \tilde{t}_1 decays into a b -quark, an on-shell W boson and a $\tilde{\chi}_1^0$. The four-body decay (right) is the most compressed case where $\Delta m(\tilde{t}_1, \tilde{\chi}_1^0)$ is too small for the \tilde{t}_1 to decay via an on-shell W boson.

Complementary to the RPC SUSY searches are the RPV SUSY searches that require no or little missing transverse momentum. The combined search program provides an excellent coverage of unexplored regions.

A simplified model searching for SUSY via a direct higgsino production including $\tilde{\chi}_1^\pm$, $\tilde{\chi}_2^0$, $\tilde{\chi}_1^0$, and $\tilde{\chi}_2^\pm$ is presented. The charginos and neutralinos are assumed to be pure higgsino-like and they decay promptly via a RPV coupling into a variety of jets and b -jets as seen in Figure 6.4. The SUSY masses are assumed to be almost the same ($\lesssim 1$ GeV) for all the signatures $m_{\tilde{\chi}_1^0} \approx m_{\tilde{\chi}_2^0} \approx m_{\tilde{\chi}_1^\pm}$. The three signatures $\tilde{\chi}_1^0$, $\tilde{\chi}_2^0$, $\tilde{\chi}_1^\pm$, and $\tilde{\chi}_2^\pm$ are combined for the full higgsino analysis. A new technique is shown in Chapter 8 in order to gain sensitivity for these processes. Previous lower limits were defined by LEP [167–169] excluding $\tilde{\chi}_1^\pm$ masses below 103 GeV in a RPV scenario .

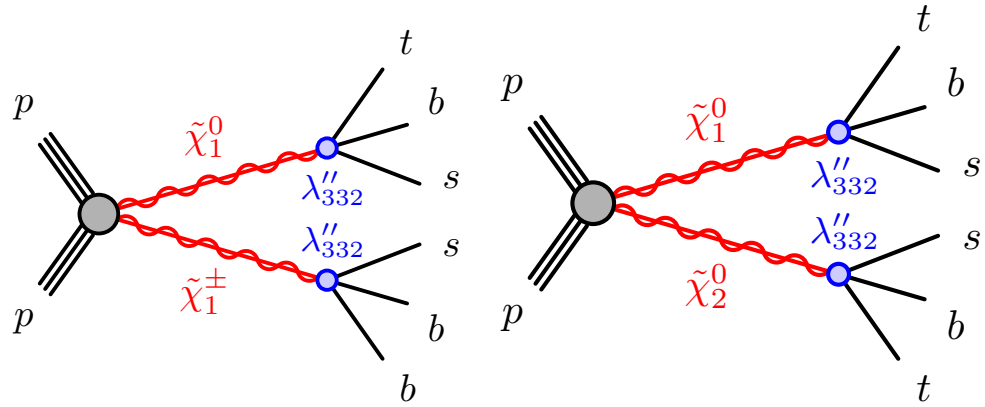


Figure 6.4.: Diagrams for the higgsino-like scenarios decaying via a RPV coupling [26]. The $\tilde{\chi}_{1,2}^0$ decay to t , b , and s quarks, while the $\tilde{\chi}_1^\pm$ to s , b , and b quarks. The process $\tilde{\chi}_2^0 \tilde{\chi}_1^\pm$ is also taken into account.

6.3. Background events

Both analyses presented in the previous section target final states containing exactly one electron or muon, which should be isolated from surrounding hadronic activity. Such prompt leptons are typically produced from the decay of a W boson. The other decay product from the leptonic W decay is a corresponding neutrino, which produces a significant amount of momentum imbalance in the detector because it escapes undetected. As a consequence, SM backgrounds with a W boson populate the same phase space as potential supersymmetric decays. The processes shown in Figure 6.5 are the most recurrent throughout the studies.

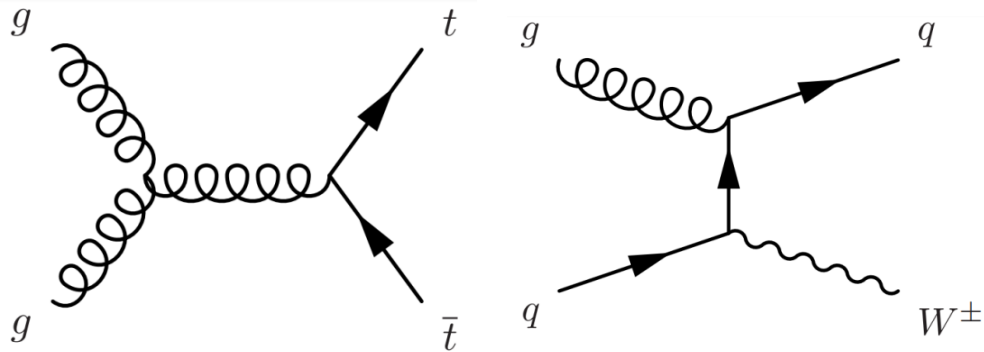


Figure 6.5.: Exemplary Feynman diagrams of the main background processes: $t\bar{t}$ (left) and $W + \text{jets}$ (right).

$t\bar{t}$

In the signal regions, the top pair production ($t\bar{t}$) is the dominant background process as its topology resembles our supersymmetric RPC stop signal. The cross-section of the $t\bar{t}$ process at $\sqrt{s} = 13$ TeV is 818 pb [170]. The $t\bar{t}$ background is classified into three categories in terms of the decay modes of the top quarks. When both top quarks decay hadronically ($t \rightarrow bW(\rightarrow qq)$), it is called *all-hadronic $t\bar{t}$* , and $t\bar{t}$ with two leptonically decaying tops ($t \rightarrow bW(\rightarrow l\nu)$) is referred to as *dileptonic $t\bar{t}$* . When one top decays hadronically and another top decays leptonically, the event is categorized as *semileptonic*.

Both semileptonic and dileptonic processes enter the RPC stops signal regions because of the high E_T^{miss} requirement, which in the background case originates from the neutrinos. Despite the exactly-one-lepton requirement, the dileptonic $t\bar{t}$ is a dominant background in some cases when one of the leptons is lost due to the inefficiency of the lepton identification or the lepton is out of acceptance.

In the higgsinos RPV model, the production of $t\bar{t}$ with additional heavy-flavor jets is the dominant background as regions with many jets and b -tagged jets are explored. In fact, it is the only background taken into account for the RPV higgsinos studies presented, but the rest of the backgrounds are also taken into account for the full analysis results.

W -jets

The W boson production associated with jets has a large cross-section at $\sqrt{s} = 13$ TeV, 190 nb [171]. A good amount of events with a leptonically decaying W boson pass the one lepton and high E_T^{miss} selections. The W -jets events are strongly suppressed by requirements of b -tagging, but the events with a gluon splitting to $b\bar{b}$ pair ($g \rightarrow b\bar{b}$) from initial or final state radiation enter the RPC stops signal region.

Single top

A process with a single top quark (or anti-top quark) is a negligible background in the RPC stop signal region. Nevertheless, the single top production in association with a W boson (Wt) gives the larger single top contribution with a cross-section of 94 pb [172].

Multiboson

Events with more than one electroweak bosons (W^\pm and Z) are not main background processes, but still these events account for some fraction of the background in the RPC

stops signal region. Large E_T^{miss} is created by neutrinos from $Z \rightarrow \nu\nu$ or leptonically decaying W bosons. Contributions are mainly from the diboson process, which has exactly two electroweak bosons.

Z+jets

The Z boson production is a minor background process in the RPC stops signal region. The $Z \rightarrow ll$ process is suppressed by the one lepton and b -tagging requirements.

ttV

In spite of a small cross-section, $t\bar{t} + V$ (V is Z or W^\pm) is a tough background process, it has not been precisely studied yet in SM measurements, which makes the estimation of this process difficult.

Multijet

Most pp collisions do not contain leptons produced via electroweak interactions, but they create quarks and gluons via QCD interactions, resulting in multijet signatures. The multijet processes do not contain isolated leptons, but some of the tracks or clusters can be misidentified as leptons. When the jet energy is miss-measured, the transverse energy is not conserved, and a non-zero E_T^{miss} is obtained. The probability of having a jet mimicking a lepton and creating large E_T^{miss} is very small.

However, events with a fake lepton are observed mainly in low E_T^{miss} regions due to the large cross-section of the QCD processes compared to the electroweak processes. The contribution of the multijet to the following analyses was found to be negligible compared to the total amount of events (in RPV higgsinos analysis), and due to the large E_T^{miss} requirement (in RPC stops).

6.3.1. Discriminating variables

The variables described are used to separate signal events from the SM background events in the RPC stops search.

- m_T : Requiring one isolated lepton (ℓ), several jets and a big amount of missing transverse energy (E_T^{miss}) selects samples enriched with semileptonic $t\bar{t}$ events and

$W+jets$ events. Both backgrounds can be reduced by implementing a transverse mass (m_T) to be above the mass of the W boson mass and defining m_T as:

$$m_T = \sqrt{2 \cdot p_T^\ell \cdot E_T^{\text{miss}} (1 - \cos \Delta\phi(\vec{\ell}, \vec{p}_T^{\text{miss}}))} \quad (6.1)$$

where the lepton p_T is p_T^ℓ and $\Delta\phi(\vec{\ell}, \vec{p}_T^{\text{miss}})$ is the azimuthal angle between the lepton and the \vec{p}_T^{miss} making the assumption that the lepton mass is negligible. After this requirement the dominant background is dileptonic $t\bar{t}$ with one miss-identified lepton. The $t\bar{t}$ products include high m_T values and two or more high p_T neutrinos resulting in a big amount of E_T^{miss} .

- $\Delta\phi(\vec{p}_T^{\text{miss}}, b\text{-jet})$: Is the azimuthal angle between the missing transverse momentum and the b -tagged jet with the largest momenta. It is very effective in suppressing $W+jets$ background due to the emission angle of the b -jets from gluon splitting which aren't correlated to other decay products. After applying this variable, the background is left mainly with $t\bar{t}$ processes.
- $p_T^\ell/E_T^{\text{miss}}$: Is the ratio of the lepton p_T and the missing transverse energy. This variable is mainly exploited in the signal region as it requires a very low lepton p_T . This is one of our main discriminating variables as seen on Chapter 7.
- C_{T2} : The leptons in the final state, originating from the off-shell W boson decay, are expected to have very low p_T . To compensate this, a high transverse momentum jet from an initial state radiation (ISR) is required to boost the system in the opposite hemisphere enhancing E_T^{miss} expected from the two LSPs, as shown in Figure 6.6. The correlation between E_T^{miss} and the ISR jet candidate ($p_T(\text{ISR})$) is taken into account to define a variable as:

$$C_{T2} = \min(E_T^{\text{miss}}, p_T(\text{ISR}) - 25 \text{ GeV})$$

where the numerical value of 25 GeV is used due to the fact that our jet preselection starts at 25 GeV. The C_{T2} variable has been used before [173] to define signal regions targeting signatures with soft final states.

6.3.2. Background estimation

This section explains the background estimation only for the RPC stops analysis because the strategy is quite different from the RPV higgsinos. The RPV higgsinos background estimation is explained in Section 8.2.

The background events in the RPC stops SRs are estimated based on MC simulation. Each SR has a CR for a dominant background process to study their modeling. Once an SR is defined with a maximum contribution of signal events, corresponding CRs are constructed with similar SR selections. Normalization factors (NF) are measured ratios

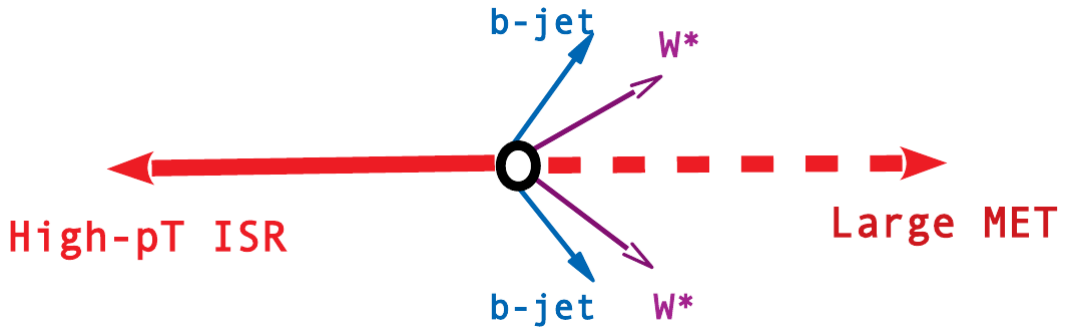


Figure 6.6.: Illustration showing the required ISR jet to boost the system and obtain the required E_T^{miss} . The resulting objects are soft (low p_T) including the soft lepton selected from the off-shell W boson.

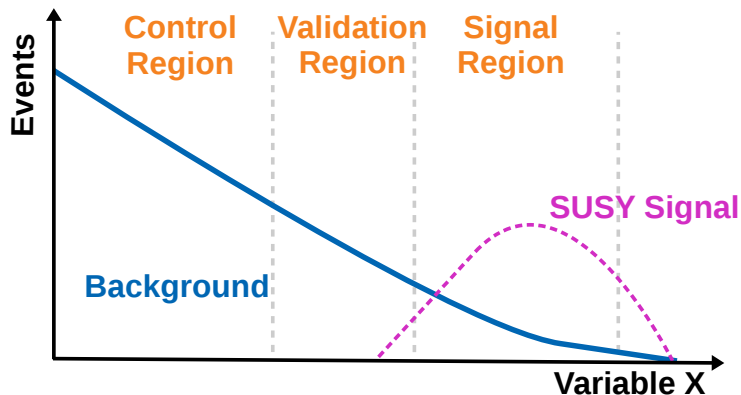


Figure 6.7.: Illustration of the background estimation strategy. The SR is defined to maximize the sensitivity to discover the signal. The CR is in a region where enough background events are available and the signal contamination is negligible. Between the SR and CR, the VR is defined to validate the extrapolation from the CR to the SR.

of data to MC in CRs. The CRs should have enough data events to minimize the statistical fluctuation of the NF. The CR selection needs to be as close as possible to the SR selection so that the normalization factor is obtained in a similar phase space. If the CR and SR have different MC modeling, the normalization factor obtained in the CR would overestimate or underestimate the background yields in the SR. It is important to design the CRs with a negligible contribution of signal events, otherwise, the NF would become large due to the signal contamination.

The CRs for all dominant backgrounds are then fitted simultaneously to obtain the NFs for each process. VRs are used to check if the NFs give a proper data/MC normalization.

The CRs and VRs need to have a good purity of the background process which they represent. To increase the purity of the process, additional requirements that enhance or suppress the others are applied. Figure 6.7 depicts how the regions are regularly defined. The NFs are applied to each background in the SRs, CRs, and VRs.

6.3.3. Systematic uncertainties

A crucial part of the background estimation is to know how accurate the results are. Statistical fluctuations systematic uncertainties can be present and increase the uncertainty in the result. The systematic uncertainties are evaluated for all background and signal samples using MC simulations. Systematic uncertainties are classified into two types: experimental and theoretical. The first one is generally associated with the calibration of physical objects, and the latter is usually caused by the imperfect modeling of the MC simulation. In this section, the details of the uncertainties are explained.

6.3.3.1. Experimental uncertainties

The experimental uncertainties associated with each object come from the uncertainties in its calibration. The variations in the number of events of the SR, CR, and VR from each uncertainty source are included in the fit as nuisance parameters, described in Section 7.4.

Jets

The jet energy scale (JES) and jet energy resolution (JER) are the main components of the uncertainty in the momentum of jets [174, 175]. As already discussed in Chapter 5, these uncertainties are associated with their calibration. The event yields are directly affected by the uncertainties from the jet p_T cuts or via indirect effects on the magnitude and direction of E_T^{miss} .

Flavor tagging

The uncertainty from the b -tagging efficiency is estimated by varying the efficiency correction factors for b and c jets together with the miss-tag rate correction factors measured in $t\bar{t}$ and dijet events [176, 177]. These uncertainties affect SR event yields if CR selections have different flavor composition of b -tagged jets.

Missing transverse momentum

The uncertainties in E_T^{miss} originating from an object with high p_T such as jets or leptons are considered. They can lead to changes in the magnitude and the direction of the missing transverse momentum. Since E_T^{miss} is determined from the physics objects in an event, E_T^{miss} is re-calculated for each systematic variation of the calibrated objects. Additionally, a soft term also contributes to the uncertainties in the scale and the resolution [178] and is evaluated in the E_T^{miss} calibration with $Z \rightarrow \mu\mu$.

Pile-up reweighting

The MC events are weighted to reproduce the distribution of the average number of interactions per bunch crossing (μ) observed in the data, referred to as “pile-up reweighting” [179]. An uncertainty in the reweighting is included accounting for the imperfect residual in the pile-up modeling of the MC simulation.

Leptons

The size of the lepton uncertainties is typically small compared to the jet measurements, nevertheless, the uncertainties in the electron and muon calibrations are considered. The scale and resolution of the lepton momentum and the isolation efficiency measurements are taken into account.

Luminosity

The uncertainty in the luminosity measurement is considered for minor backgrounds that do not have a dedicated CR. The uncertainties mainly come from the vdM scan and the calibration transfer from the scan to data. The uncertainty for the full Run 2 data is 1.7% [180].

Normalization

The uncertainties in the normalization factors of the dominant background processes are taken into account as they originated from limited data statistics in the CRs.

Monte Carlo statistics

In some cases, the background and signal MC events are limited due to a tight selection in the SR, causing a large uncertainty.

6.3.3.2. Theoretical uncertainties

Since the yields for the dominant background sources ($t\bar{t}$ and $W+jets$) are obtained in dedicated control regions, the modeling uncertainties for these processes affect only the extrapolation from the CRs into the signal region but not the overall normalization. They are given by the generator modeling, parton distribution function choice and parton shower uncertainties. In the following, the different theoretical systematic uncertainties will be explained for each background.

Transfer Factor method To extract accurate information from data, a probability density function (PDF) is used whose parameters are included in the fitting procedure. The fit performed to data is based on the CRs and SR being statistically independent. One of the key ingredients to the fit procedure are the ratios of the event counts, called *transfer factors* (TF), of each normalized background between the SR and CRs. It is defined as the ratio of the yields. For example, the $t\bar{t}$ TF which controls the number of $t\bar{t}$ events in the SR is:

$$\text{TF}_{\text{SR}}^{t\bar{t}} = \frac{N_{\text{SR}}^{t\bar{t}}}{N_{\text{TCR}}^{t\bar{t}}} \quad (6.2)$$

where $N_{\text{SR}}^{t\bar{t}}$ and $N_{\text{TCR}}^{t\bar{t}}$ are the number of $t\bar{t}$ events in the SR and CR respectively. This is calculated for the nominal (TF_{nom}) and the systematic (TF_{syst}) samples. And the double ratio (u) gives the desired systematic uncertainties:

$$u = \frac{(\text{TF}_{\text{syst}} - \text{TF}_{\text{nom}})}{\text{TF}_{\text{nom}}} \quad (6.3)$$

The advantage of this method is that by choosing more kinematically similar CRs to the SR, a greater cancellation in the systematic uncertainties is obtained in the extrapolation [181].

The statistical uncertainties (σ) are calculated as:

$$\sigma_{\text{TF}} = \text{TF} \cdot \sqrt{\left(\frac{\sigma_{\text{SR}}}{N_{\text{SR}}}\right)^2 + \left(\frac{\sigma_{\text{CR}}}{N_{\text{CR}}}\right)^2} \quad (6.4)$$

and for the double ratio u they are defined as:

$$\sigma_u = \frac{\text{TF}'}{\text{TF}} \cdot \sqrt{\left(\frac{\sigma_{\text{TF}'}}{\text{TF}'}\right)^2 + \left(\frac{\sigma_{\text{TF}}}{\text{TF}}\right)^2} \quad (6.5)$$

In equation 6.5, TF' denotes the transfer factor of the systematic sample and TF the one of the nominal sample.

Variable by variable approach This method was only used when calculating the uncertainties for the W +jets regions. When the theory uncertainties are limited due to the available statistics for alternative samples, a method called variable by variable (VBV) is used. It “boosts” the statistics by:

1. When defining the regions (SR, CR, VR), the number of events is taken separately for each main kinematic variable defined in the SR. In other words, the preselection is taken into account plus the cut of only one main kinematic variable.
2. Then the TFs are computed for one variable at a time, i.e.: $\text{TF}_{m_T} = \text{SR}_{m_T}/\text{TCR}_{m_T}$.
3. They are added variable by variable in quadrature for each systematic source. By this, the uncertainty associated to each variable is then summed in quadrature to obtain the total uncertainty estimate as

$$u_{\text{total}} = \sqrt{\sum_i^{\text{variable}} u_i^2} \quad (6.6)$$

$$\sigma_{u_{\text{total}}} = \frac{1}{\sum_i^{\text{variable}} u_i^2} \cdot \sum_i^{\text{variable}} u_i^2 \cdot \sigma_{u_i}^2 \quad (6.7)$$

The disadvantage of this method is that by boosting the statistics, the uncertainty numbers might not be entirely correct due to correlations, nevertheless, this is a valid approximation and gives fairly good results as shown in the studies.

$t\bar{t}$ modeling Hard scatter uncertainty is estimated by comparing different matrix element (ME) calculations. The nominal $t\bar{t}$ sample generated with Powheg (ME) [100] and Pythia Parton shower (PS) [101] is compared with an alternative $t\bar{t}$ sample generated with MG5 aMC@NLO (ME) [102] and Pythia (PS). The difference is the uncertainty in the hard scattering. The PS uncertainty is evaluated with an alternative sample with Powheg (ME) and Herwig (PS) [103]. Systematic uncertainties from initial- and final-state radiation are computed comparing nominal $t\bar{t}$ events with reweighted $t\bar{t}$ events using internal event weights. The internal event weights include the variation of factorization and renormalization scales and shower radiation.

$W+\text{jets}$ modeling The uncertainty on the $W+\text{jets}$ background from the MC generator is estimated by comparing the nominal Sherpa [110] sample with MadGraph (ME) [102] + Pythia (PS) sample to evaluate the uncertainty in Sherpa PS. In addition, the renormalization, factorization, and soft gluon resummation scale uncertainties are evaluated by varying these scales from 1/2 to 2 with respect to the nominal scales.

SUSY signal modeling Dedicated uncertainties in the SUSY signal acceptance due to the modeling of additional radiation, factorization, renormalization, and parton matching scales are evaluated. Besides, the SUSY signal cross-section uncertainty is taken from an envelope of cross-section predictions using different PDF sets and factorization and renormalization scales.

Minor backgrounds modeling Theoretical uncertainties on these processes have a negligible impact on the final result. Thus, flat uncertainties in the event yields are included in each region as an inclusive modeling uncertainty. Also, a conservative uncertainty on the theoretical cross-section of the respective SM background is applied.

6.3.4. Statistical treatments

For interpreting the results, a simultaneous fit of the data and MC predictions is performed in all SRs and CRs. The underlying methods of the fit are based on frequentist

statistics, in which probability is interpreted as the frequency of the outcome of a repeatable experiment under identical conditions [182, 183].

The level of agreement of the observed data with a given model is quantified using hypothesis tests. These evaluate a likelihood that describes the statistical model of the analysis, i.e. the signal and background predictions in the different SRs and CRs and the corresponding uncertainties. The `HISTFITTER` software framework [181] was used with the `HISTFACTORY` package [184] to build the likelihood and its associated probability density function (PDF). The parameters of the PDF are adjusted during the fit. The PDF contains *normalization factors* that scale the background processes correcting potential miss-modeling effects in simulations. The signal and background predictions are affected by so-called *nuisance parameters*, which describe the impact of systematic uncertainties. The nuisance parameters are included as priors in the fit and are initially determined from auxiliary measurements.

The SRs and CRs are divided (*binned*) in ranges of some variables which show a characteristic shape for certain signal or background processes. The events follow a Poisson probability distribution describing the expected event yields in each bin as [185]:

$$P(n_i|\mu s_i + b_i) = \frac{(\mu s_i + b_i)^{n_i}}{n_i!} e^{-(\mu s_i + b_i)} \quad (6.8)$$

which describes the probability to observe n_i events in bin i given a Poisson probability function with an expectation value $\nu_i = \mu s_i + b_i$. The term μ denotes the signal strength and is tested in the hypothesis test. A value of $\mu = 0$ stands for the background-only hypothesis (absence of signal) and $\mu = 1$ for the signal + background hypothesis model [186]. The shape of the PDFs are characterized by nuisance parameters describing the effect of systematic uncertainties [186] and explained in more detail in [183].

The nuisance parameters are typically modeled in a Gaussian form

$$C(\alpha) = \frac{1}{\sqrt{2\pi}} e^{-(\frac{\alpha - \alpha^0}{2})^2} \quad (6.9)$$

with α as the nuisance parameter in the search. The α term can vary around α^0 , which corresponds to a central value of a pre-fit yield. To construct the PDF for any combination of nuisance parameter values, `HISTFACTORY` uses various interpolation and extrapolation algorithms, which are further described in Ref. [184].

The likelihood for the fit function is defined as the product of the Poisson probabilities for all regions like

$$L(\mu, \eta, \alpha) = \prod_{i=1}^N P(n_i|\nu_i(\mu, \eta, \alpha)) \prod_{j=1}^M C(\alpha_j) \quad (6.10)$$

The first product runs over all N bins including the SRs and CRs bins, and the second

product over all M nuisance parameters. The terms η and α describe the sets of normalization factors and nuisance parameters used in the analysis, with $\alpha = (\alpha_1, \alpha_2, \dots, \alpha_M)$. The final likelihood built by `HISTFACTORY` also considers the statistical uncertainty of the MC samples as well as the luminosity uncertainty. In the following, η, α , the statistical uncertainties, and the luminosity uncertainty are collectively denoted by $\boldsymbol{\theta}$. The PDF built by `HISTFACTORY` is equivalent to $L(\mu, \boldsymbol{\theta})$.

Hypothesis tests In order to discover or exclude certain models like an SM-only prediction or existence of new physics beyond the SM, hypothesis tests are performed [186]. In the following, μ refers to the signal strength compared to the theoretically predicted signal yield. The test statistic for hypothesis tests is defined as a ratio of the likelihoods [182]

$$\lambda(\mu) = \frac{L(\mu, \hat{\boldsymbol{\theta}})}{L(\hat{\mu}, \hat{\boldsymbol{\theta}})} \quad (6.11)$$

where $\hat{\boldsymbol{\theta}}$ is the value of $\boldsymbol{\theta}$ that maximizes $L(\mu, \boldsymbol{\theta})$ for a given μ . The terms $\hat{\mu}$ and $\hat{\boldsymbol{\theta}}$ are the estimators of μ and $\boldsymbol{\theta}$. The ratio $\lambda(\mu)$ varies between 0 and 1. Values close to 1 mean that a good description of the observed data is given with the hypothesized μ . Usually, this is expressed by $-2 \ln \lambda(\mu)$, where higher values imply a worse compatibility between the data and μ . Normally a signal process is assumed to contribute only non-negatively $\mu \geq 0$. The estimator $\hat{\mu}$ can also take negative values for convenience. The exact definition of the test statistics depends on the application.

One case would be if the observed data shows an excess over the SM background expectations. If this happens, one would want to know and quantify how significant this excess is. A hypothesis test can be performed in which the background-only prediction constitutes the null hypothesis. This is tested against signal+background model taken as the alternative hypothesis. To claim the discovery of a positive signal, it is necessary to reject the background-only hypothesis. The test statistic is given by a $q_0 = -2 \ln \lambda(0)$, if the estimator is $\hat{\mu} \geq 0$, otherwise $q_0 = 0$. If the studied signal exists, this would lead to an increase in the SR event yields compared to the background-only expectations. Its presence will not reduce the total yield, therefore, an under-fluctuation of the data should not be used to reject the background-only hypothesis ($q_0 = 0$).

On the other hand, if the observed data is in good agreement with the SM background predictions, certain signal models can be excluded and *upper limits* can be defined on the signal strength μ . In this kind of test, the null and alternative hypothesis need to be swapped, i.e. the signal+background hypothesis must be rejected in favor of the background-only hypothesis. Similarly to q_0 , observing more events than predicted by the signal+background model should not be taken into account as an indication against this hypothesis. Therefore, the corresponding test statistic is defined by

$$q_\mu = \begin{cases} -2 \ln \lambda(\mu) & \hat{\mu} \leq \mu \\ 0 & \hat{\mu} > \mu \end{cases} \quad (6.12)$$

After the calculation of the test statistic, p -values are used to quantify the discovery or exclusion sensitivity of the performed hypothesis test. The p -value gives the probability of obtaining a result that has an equal or greater incompatibility with the tested hypothesis than the observed data. If the p -value lies below certain threshold, a given hypothesis can be excluded. For the upper limit scenario presented in Equation 6.12, the p -value is defined as

$$p_\mu = \int_{q_\mu, \text{obs}}^{\infty} f(q_\mu | \mu) dq_\mu \quad (6.13)$$

with the observed value of q_μ as $q_{\mu, \text{obs}}$, and $f(q_\mu | \mu)$ as a PDF of the associated test statistic under the assumption of signal+background hypothesis. By definition, a smaller p -value means that the hypothesis with the μ is more incompatible with the observed data.

A p -value can be also interpreted as a statistical significance $Z = \Phi^{-1}(1 - p_\mu)$. Z reflects multiples of the standard deviation σ of a Gaussian distributed variable. Φ^{-1} is the inverse of the cumulative distribution of the Gaussian distribution. In the particle physics community, a new *discovery* is claimed if $Z \geq 5\sigma$, corresponding to $p_0 \leq 2.87 \times 10^{-7}$. A 3σ is commonly considered as *evidence* for new physics. To *exclude* a signal model, the threshold $p_\mu = 0.05$ ($Z = 1.64\sigma$) is used, which is referred to a 95% confidence level (CL).

A distinction is made between observed and expected limits. The observed limit corresponds to the test results using the actually observed data, while the expected limit is defined as the limit which would be obtained from the statistical test, if the observed data is equal to the SM background expectations.

The CLs method As the exclusion test is based on the evaluation of the signal+background hypothesis, this is also referred to as the CL_{s+b} method and the associated p_μ is denoted as p_{s+b} .

If the sensitivity for a potential signal model in a dedicated SR is very low or a downward fluctuation of data compared to the prediction is observed, the results can be miss-interpreted and a potential signal could be falsely excluded. The CLs technique aims to prevent excluding signal models with low sensitivity ($b \approx s + b$). This method takes into account both p_{s+b} and p_b . The latter denotes the p -value for the alternative, i.e. background-only hypothesis of the exclusion test

$$p_b = \int_{-\infty}^{q_{\mu, \text{obs}}} f(q_\mu | \mu) dq_\mu \quad (6.14)$$

With p_{s+b} and p_b , the CLs value is defined as [187, 188] :

$$\text{CLs} = \frac{p_{s+b}}{1 - p_b} \quad (6.15)$$

The CLs denominator can only be less than or equal to unity, as a consequence, the exclusion criterion based on the CLs method is more stringent than the usual requirement for p_μ . If the signal sensitivity is very low, then p_{s+b} decreases, but $1-p_b$ as well, hence the exclusion condition of the CLs value below a certain threshold will not be satisfied. The CLs technique is a widely acknowledged procedure in the high energy physics community and used in the documented analysis to derive an exclusion limit on the signal strength. A signal is excluded at a 95% confidence level if the CLs value is smaller than 0.05 for the background+signal hypothesis.

6.3.5. Previous results

RPC top squark search Top squark searches had been a benchmark scenario at ATLAS and CMS experiments since the beginning [190–211]. Figure 6.8 shows the summary of ATLAS results as of 2017, the results from Run 1 and Run 2 in 2015–2016. In general, the searches included the full-hadronic (0L), semileptonic (1L), and dileptonic (2L) final state analyses. For the $\tilde{t}_1 \rightarrow t + \tilde{\chi}_1^0$ (2-body) decay region, the 0L and 1L analyses have strong sensitivities, while in the compressed scenario with $\tilde{t}_1 \rightarrow bW\tilde{\chi}_1^0$ / $\tilde{t}_1 \rightarrow bff'\tilde{\chi}_1^0$ (3-body / 4-body) decays, 1L and 2L analyses have comparable sensitivities. At the very compressed region of the 4-body decay, the mono-jet analysis uses a high- E_T^{miss} and a high- p_T ISR selection resulting in a high sensitivity in this area. On the contrary, the 1L and 2L analyses lose sensitivity due to the inefficiency of the lepton reconstruction.

The bottom right corner of the exclusion region with large $\Delta m(\tilde{t}_1, \tilde{\chi}_1^0)$ has been extended to a stop mass of around 1 TeV, while in the compressed region, the search sensitivities were lower due to the difficulties of the reconstruction of low p_T particles. Besides, the excluded region in the small $\Delta m(\tilde{t}_1, \tilde{\chi}_1^0)$ phase space was smaller compared to the large $\Delta m(\tilde{t}_1, \tilde{\chi}_1^0)$ region. Therefore, the search in Chapter 7 is performed targeting the stop in the 4-body region.

RPV higgsinos search The RPC SUSY scenarios usually require large E_T^{miss} accounting for the two LSPs. The requirement of large E_T^{miss} is a powerful strategy for discriminating the SUSY signal from SM background processes. However, it might sacrifice sensitivity from beyond the SM searches with small or no E_T^{miss} . Complementary to the RPC searches, the RPV scenarios are defined as a search program providing excellent coverage without a strong E_T^{miss} requirement.

The model presents a search for a natural SUSY scenario with minimum flavor violation (MFV) that predicts only the baryon-number-violating $\bar{u}d\bar{d}\bar{l}$ coupling to be non-zero [72], and is explained in more detail in Subsection 2.2.5.1. Signals with gluino and stop production were the target of the previous iteration of the analysis [214] based on

the 2015–2016 dataset. In the former searches, signals with direct higgsinos production were defined but no sensitivity was reached [214]. Therefore, the previous paper targeted the model shown in Figure 6.9 with a pair production of top squarks decaying into electroweakinos and a top or b quark. In this process, the wino and higgsino scenarios were presented as shown on the exclusion plot in Figure 6.10. For this reason, Chapter 8 describes a new Machine Learning technique aiming to reach sensitivity for direct higgsino production with the 2015–2018 dataset.

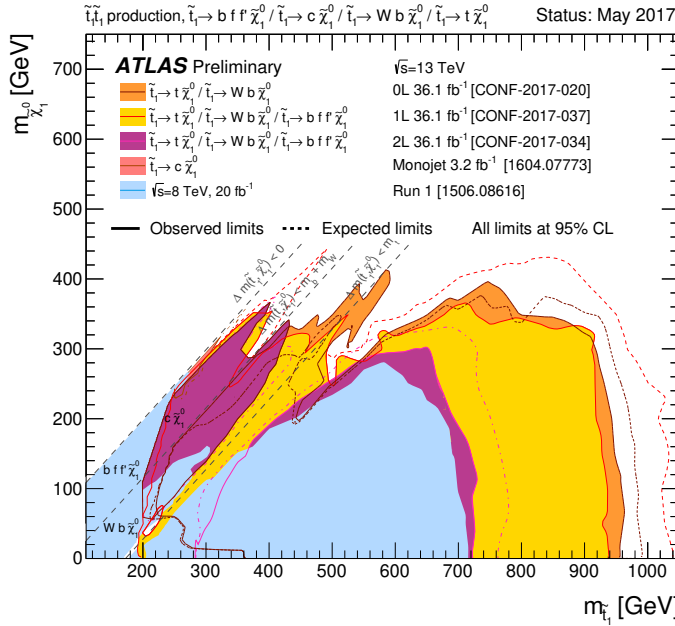


Figure 6.8.: Exclusion contours from previous searches at ATLAS [212]. The results of Run 1 analyses [190] and Run 2 analyses [189, 191–200] with the data collected in 2015–2016 are displayed. Another scenario in which \tilde{t}_1 decays into a charm quark and the LSP [213] is overlaid, but it assumes a different model with a flavor-changing neutral-current decay. The dashed lines show the expected exclusion limits while the solid lines show the observed exclusion limits. The gray dash lines separate the \tilde{t}_1 decay modes depending on the mass difference between \tilde{t}_1 and $\tilde{\chi}_1^0$. If the on-shell top decay is kinematically allowed ($\Delta m(\tilde{t}_1, \tilde{\chi}_1^0) > m_t$), $\tilde{t}_1 \rightarrow t + \tilde{\chi}_1^0$ is considered. In the diagonal region where $m_b + m_W < \Delta m(\tilde{t}_1, \tilde{\chi}_1^0) < m_t$ and $\Delta m(\tilde{t}_1, \tilde{\chi}_1^0) < m_b + m_W$, the 3-body decay ($\tilde{t}_1 \rightarrow b W \tilde{\chi}_1^0$) and 4-body decay ($\tilde{t}_1 \rightarrow b f f' \tilde{\chi}_1^0$) are presented. For each decay mode, a 100% branching ratio is considered.

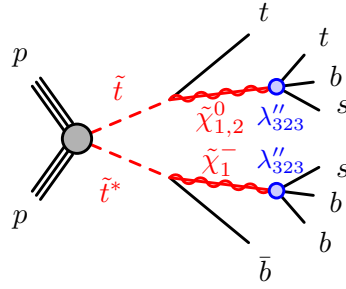


Figure 6.9.: Diagram of one of the simplified signal benchmark model considered in the previous paper iteration [214]. It involves pair production of top squarks decaying $\tilde{t}_1 \rightarrow t\tilde{\chi}_1^0$ and with LSP decays $\tilde{\chi}_1^0 \rightarrow tbs$, and $\tilde{\chi}_1^- \rightarrow sb\bar{b}$.

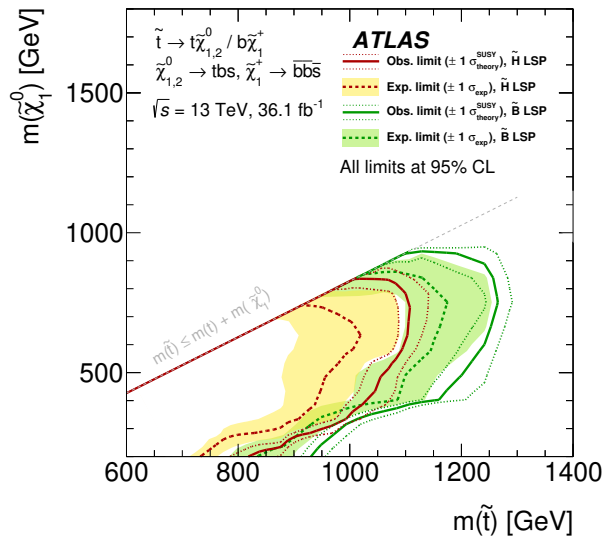


Figure 6.10.: Observed and expected exclusion contours on the \tilde{t}_1 and $\tilde{\chi}_1^0$ masses in the context of top-squark production model with RPV decays of the LSP. Limits are shown in the case of pure bino (\tilde{B}) or pure higgsino (\tilde{H}) LSPs. The contours of the band around the expected limit are the $\pm 1\sigma$ variations, including all uncertainties. All limits were computed at 95% CL. The diagonal line indicates the kinematic limit for the decays in the considered scenario [214].

7. Search for top squark pair production in the 4-body decay mode with a single lepton final state

This chapter shows the main research of my thesis. A search for top squark pair production in final states with one isolated lepton, jets, and missing transverse momentum is presented. Proton-proton collision data are recorded by the ATLAS detector over the full Run 2 of the LHC. The latest results of the analysis targeting a compressed region of the top-squark phase space are shown where the mass difference between the \tilde{t}_1 and $\tilde{\chi}_1^0$ is smaller than the sum of a b -quark and the W boson mass. In this scenario the \tilde{t}_1 decays via a 4-body process into a b -quark, two soft fermions and a $\tilde{\chi}_1^0$. A strategy to discriminate the SUSY signal from the dominant top-quark and W +jets background processes is described. The presented results have been already published [215].

7.1. Event preselections

In this analysis, the stop four-body decay ($\tilde{t}_1 \rightarrow bff'\tilde{\chi}_1^0$) with $m(\tilde{t}_1, \tilde{\chi}_1^0) = (450, 400)$ GeV signal is used as a benchmark signal to define a SR but the results for $m(\tilde{t}_1, \tilde{\chi}_1^0) = (450, 370)$ GeV are also shown. The reason was to study and optimize different Δm 's and choose the most compressed in order to better target this region. Events were selected with exactly one lepton and high E_T^{miss} . The first set of the event selection criteria (preselection) is summarized in Table 7.1. This preselection is useful in order to check the kinematic distributions considered in the analysis. All events were recorded with triggers that accepted events with E_T^{miss} above a given threshold. The E_T^{miss} triggers relied on energy measurements in the calorimeter and on several algorithms based on cells, jets or topological clusters. The triggers were fully efficient for events passing an offline-reconstruction requirement of $E_T^{\text{miss}} > 230$ GeV. Afterwards, all regions require $E_T^{\text{miss}} > 230$ GeV to ensure that the trigger was fully efficient. A jet-cleaning criteria is applied for the leading jet in order to avoid having events that mimic an ISR + high E_T^{miss} topology due to a fake high- p_T jet.

The preselection for this search uses muons with $p_T > 4$ GeV and electrons with $p_T > 4.5$ GeV. To improve the signal-to-background ratio, the leading jet p_T is required to be larger than 200 GeV to select a boosted topology with a high- p_T ISR. This helps in choosing the \tilde{t}_1 pair recoiling into the opposite hemisphere of the ISR jet.

Table 7.1.: Preselection criteria.

Selection	Preselection
Trigger	E_T^{miss} triggers
Data quality	jet cleaning
Second-lepton veto	no additional baseline leptons
Number of leptons, tightness	= 1 ‘tight’ lepton
Lepton p_T [GeV]	> 4 for μ > 4.5 for e
Number of jets	≥ 1 ($p_T > 200$ GeV)
$ \Delta\phi(j_{1,2}, p_T^{\text{miss}}) $	> 0.4
E_T^{miss} [GeV]	> 230
m_T [GeV]	> 90

The result is large E_T^{miss} from the two LSPs. In order to reduce $t\bar{t}$ and $W+\text{jets}$ events which have a leptonically decaying W boson, $m_T > 90$ GeV is required. Finally, the $|\Delta\phi|$ between the E_T^{miss} and leading jet is selected to be larger than 0.4 in order to reduce multijet contributions. These events are produced by QCD processes with a jet that is mis-reconstructed as a lepton and large E_T^{miss} created by mis-measured jets. If there is more than one jet, the same requirement is also applied to the second leading jet. The modeling of the key variables after the preselection are shown in Figures 7.1, 7.2 and 7.3. As the low lepton p_T preselection was applied, a miss modeling is seen in high lepton p_T regions in figure 7.3, for this reason the preselection was different in the other analyses using hard leptons.

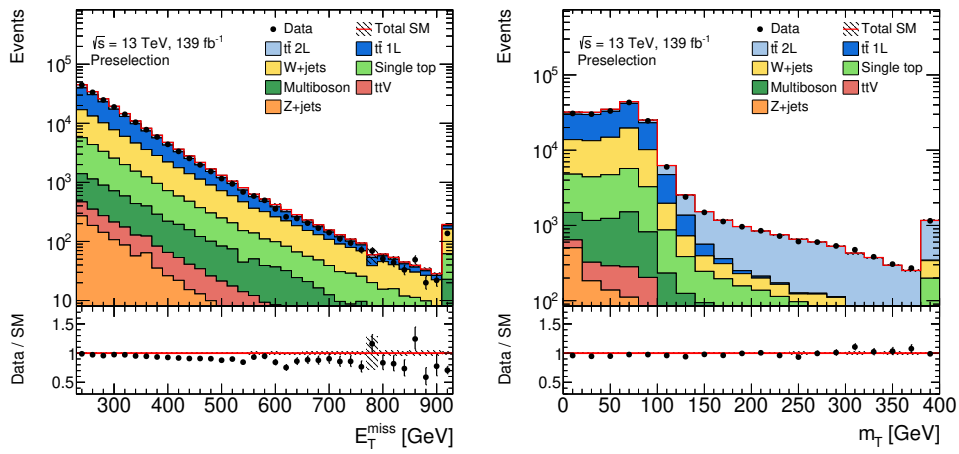


Figure 7.1.: Comparison of data and simulation for the main discriminating variables before fitting MC to data at preselection level. The preselection cuts are applied except the one on the displayed distribution. The overflow is included in the last bin.

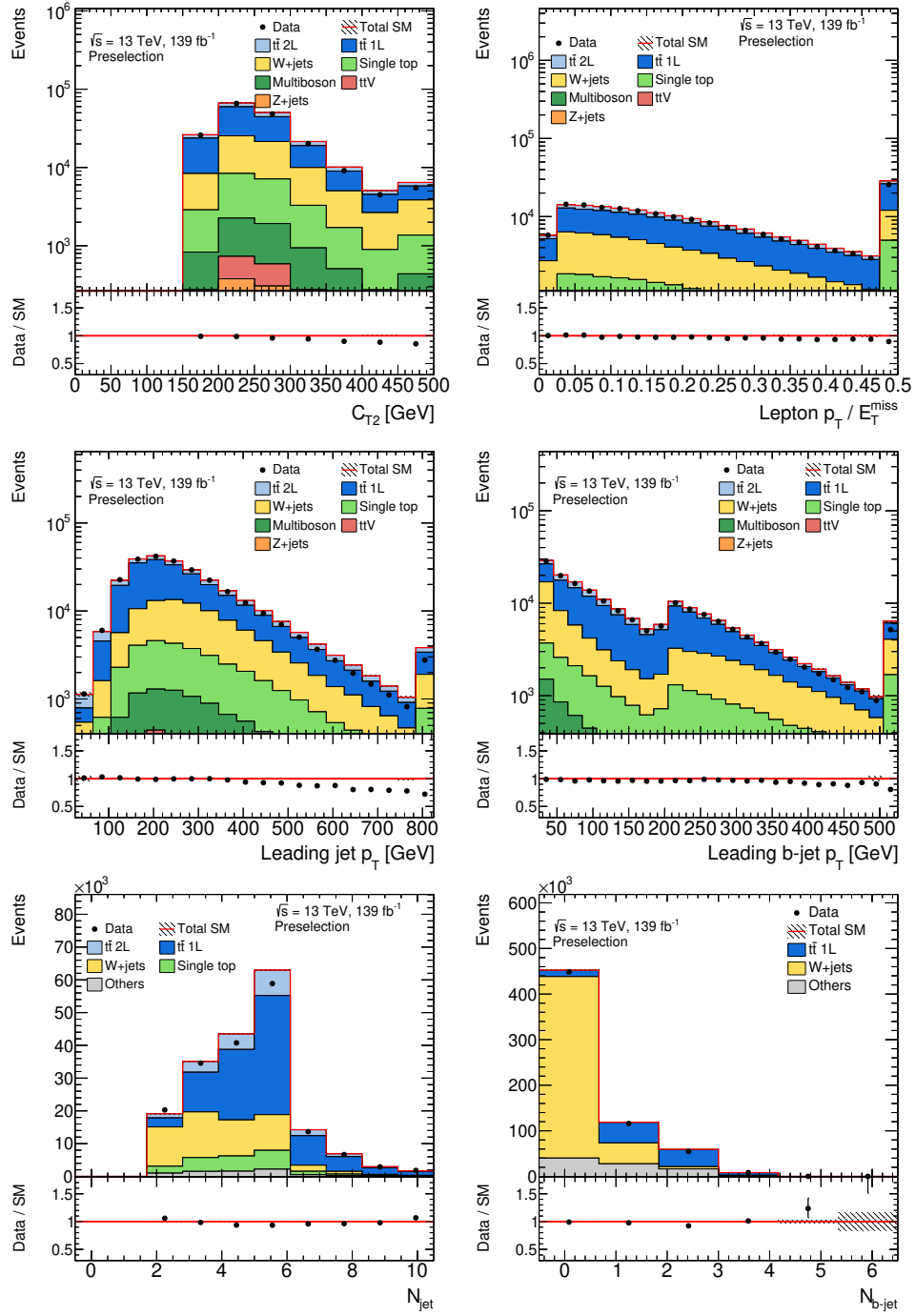


Figure 7.2.: Comparison of data and simulation for the main discriminating variables before fitting MC to data at preselection level. The preselection cuts are applied except the one on the displayed distribution. The overflow is included in the last bin.

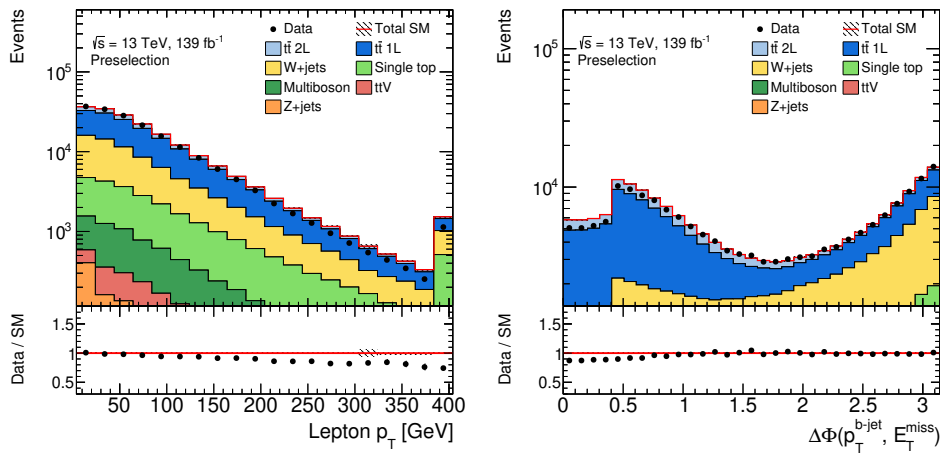


Figure 7.3.: Comparison of data and simulation for the main discriminating variables before fitting MC to data at preselection level. The preselection cuts are applied except the one on the displayed distribution. The overflow is included in the last bin.

7.2. Signal region

A signal region (SR) is an area of phase space where the SUSY signal is enhanced, as explained in more detail in Section 6.1. In this analysis, the stop four-body decay (`bffN`) with $m(\tilde{t}_1, \tilde{\chi}_1^0) = (450, 370)$ and $(450, 400)$ GeV signals are used as benchmark signals to define a SR. The stop decays via 4-body (`bffN`) to a bottom quark, two fermions, and a LSP when $\Delta m(\tilde{t}_1, \tilde{\chi}_1^0) < m_W$ is satisfied. The SR is optimized for $\Delta m = 50, 80$ GeV so the standard ATLAS b -tagging ($p_T > 20$ GeV) is used [153, 216]. This is the reason why the SR is named `bffN_btag`.

On top of the preselection, tighter selection criteria are applied to define the SR. The event selection for the `bffN_btag` SR is summarized in Table 7.2. Distributions of the variables used to define the SR are shown in Figures 7.7. Leptons and all objects in the final state, originating from the off-shell W boson, are expected to have very low p_T even after the preselection. Therefore, a high transverse momentum jet from an initial state radiation (ISR) is required for triggering. The ISR jet, which is explicitly required to be non b -tagged, tends to boost the system in the opposite hemisphere enhancing the E_T^{miss} value expected from the two neutralinos. The correlation between E_T^{miss} and the ISR jet candidate is exploited to define the C_{T2} variable explained in Subsection 6.3.1. The high $C_{T2} > 400$ GeV requirement directly affects the E_T^{miss} and the first jet p_T events towards the 400 GeV value. The b -jet in the SUSY signal is expected to have low p_T , hence a < 50 GeV selection helps to gain sensitivity. The signal events also have a low- p_T lepton (p_T^ℓ) and large E_T^{miss} . Therefore, $p_T^\ell/E_T^{\text{miss}}$ is a good estimator to separate the signal from the background.

Two types of SRs are defined: a single-bin SR targeting a discovery and a shape-fit SR for excluding signals when there is no discovery. A single-binned signal region corresponds to a simple cut-and-count analysis in which the number of events in the signal region is counted. The single-bin SR is defined with $p_T^\ell/E_T^{\text{miss}} < 0.05$ as shown in Table 7.2. In a scenario where no excess is observed, a combined `bffN_btag` exclusion region is defined by performing a 2-variable shape-fit in the `bffN_btag` signal region shown on Table 7.4. As depicted on Figure 7.5, the `bffN_btag` exclusion region contains the single-bin SR. In this way, the selection is binned in key variables to retain sensitivity to the widest possible range of \tilde{t}_1 and $\tilde{\chi}_1^0$ masses for the exclusion.

The event yields after applying the single-bin SR selection are shown in Table 7.3 for background and the benchmark signals. The fractions of the background processes before applying the normalization factors are displayed in the pie chart in Figure 7.4.

Table 7.2.: Summary of the event selections defining bffN SR with the b -tag. Preselection is applied.

Selection	bffN b -tag region
$N_{\text{jet}}, N_{b\text{-jet}}$	$\geq (2, 1)$
$C_{\text{T2}} [\text{GeV}]$	> 400
$m_{\text{T}} [\text{GeV}]$	> 90
leading b -jet p_{T} [GeV]	< 50
$\min \Delta\phi(p_{\text{T}}^{b\text{-jet}}, E_{\text{T}}^{\text{miss}})$	< 1.5
$p_{\text{T}}^{\ell}/E_{\text{T}}^{\text{miss}}$	< 0.05 (discovery)
$p_{\text{T}}^{\ell}/E_{\text{T}}^{\text{miss}}$ and $\min \Delta\phi(p_{\text{T}}^{b\text{-jet}}, E_{\text{T}}^{\text{miss}})$	as Table 7.4 (exclusion)

Table 7.3.: Pre-fit expected events in bffN_btag SR for 139 fb^{-1} . Only the statistical uncertainty of the MC samples is given.

	Process	Events
	Multiboson	1.07 ± 0.14
	Single top	0.82 ± 0.13
	$W + \text{jets}$	2.23 ± 0.54
Background	$Z + \text{jets}$	0.40 ± 0.13
	$t\bar{t} \text{ 1L}$	1.36 ± 0.17
	$t\bar{t} \text{ 2L}$	7.29 ± 0.22
	$t\bar{t}V$	0.21 ± 0.08
	Total SM	13.38 ± 0.66
Signal	$m(\tilde{t}_1, \tilde{\chi}_1^0) = 450, 370 \text{ GeV}$	34.87 ± 2.89
	$m(\tilde{t}_1, \tilde{\chi}_1^0) = 450, 400 \text{ GeV}$	36.11 ± 2.82

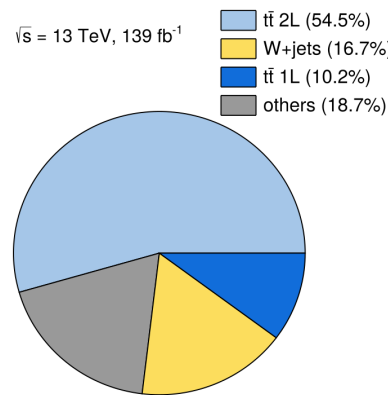


Figure 7.4.: Breakdown of the individual SM contributions to the signal region. The minor background processes are merged into the “Others” category.

Table 7.4.: Description of the 2-dimensional shape-fit for the `bffN_btag` signal region used to maximize the exclusion sensitivity.

	$p_T^\ell/E_T^{\text{miss}}$	$\min \Delta\phi(p_T^{\text{b-jet}}, E_T^{\text{miss}})$
bffN1	< 0.03,	< 0.8
bffN2	[0.03, 0.06],	< 0.8
bffN3	[0.06, 0.1],	< 0.8
bffN4	< 0.03,	[0.8, 1.5]
bffN5	[0.03, 0.06],	[0.8, 1.5]
bffN6	[0.06, 0.1],	[0.8, 1.5]

Figure 7.5.: Sketch of the 2D shapefit selection.

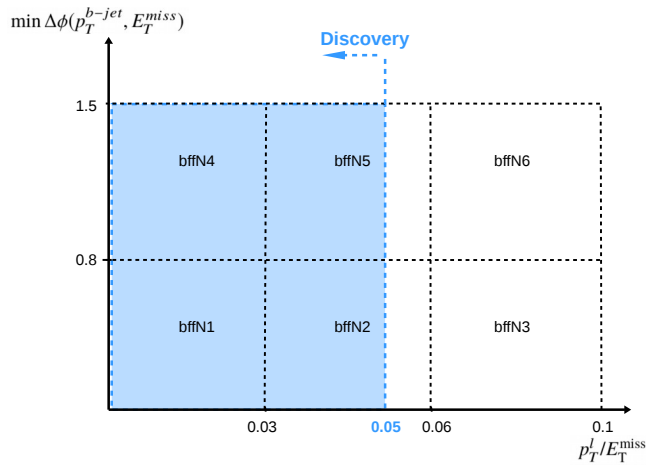
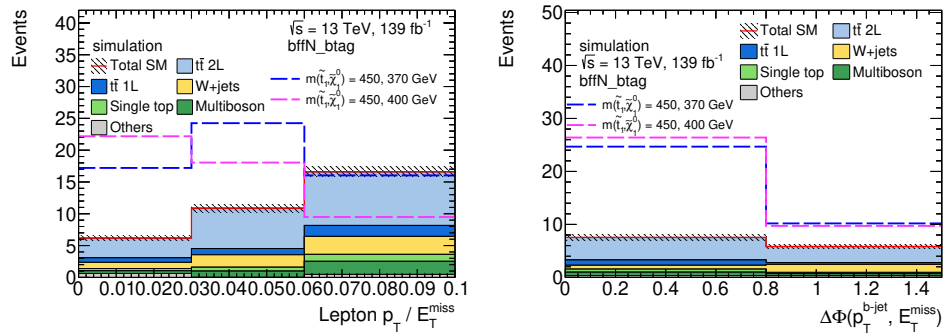


Figure 7.6.: Distribution plots of the variables chosen for the shape-fit selection with the corresponding binning. The `bffN_btag` SR cuts are applied except the one on the displayed distribution. The events are not scaled by the normalization factors, and only the statistical uncertainty is displayed. The last bin includes the overflow. The minor background processes are merged into the “Others” category



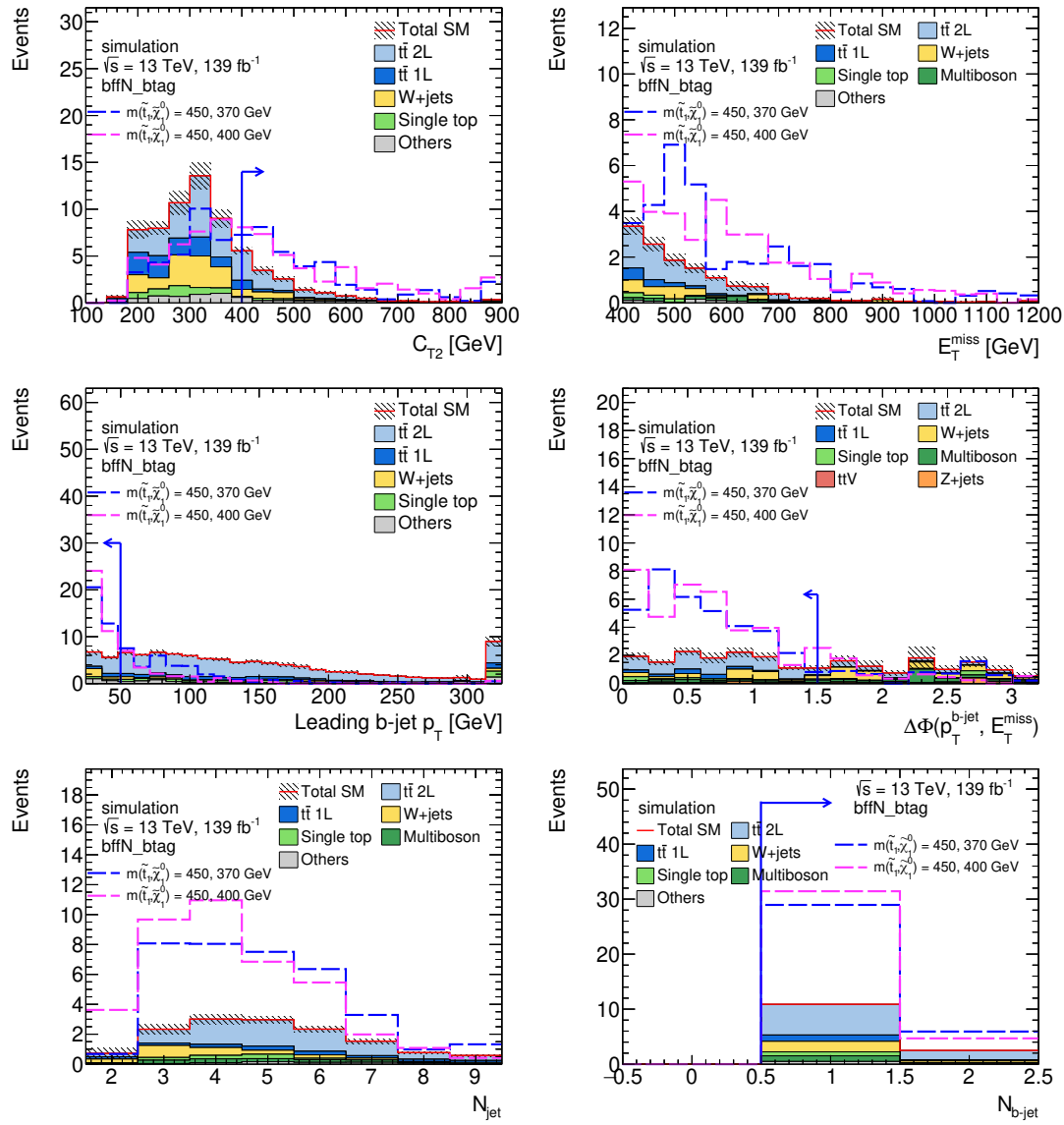


Figure 7.7.: Plots for each discriminating variable defining the `bffN_btag` single-bin SR after applying the `bffN_btag` cuts except the one on the displayed distribution. The events are not scaled by the normalization factors, and only statistical uncertainty is displayed. The last bin includes the overflow. The arrow indicates the value and points to the direction of the selection criteria. The minor background processes are merged into the “Others” category.

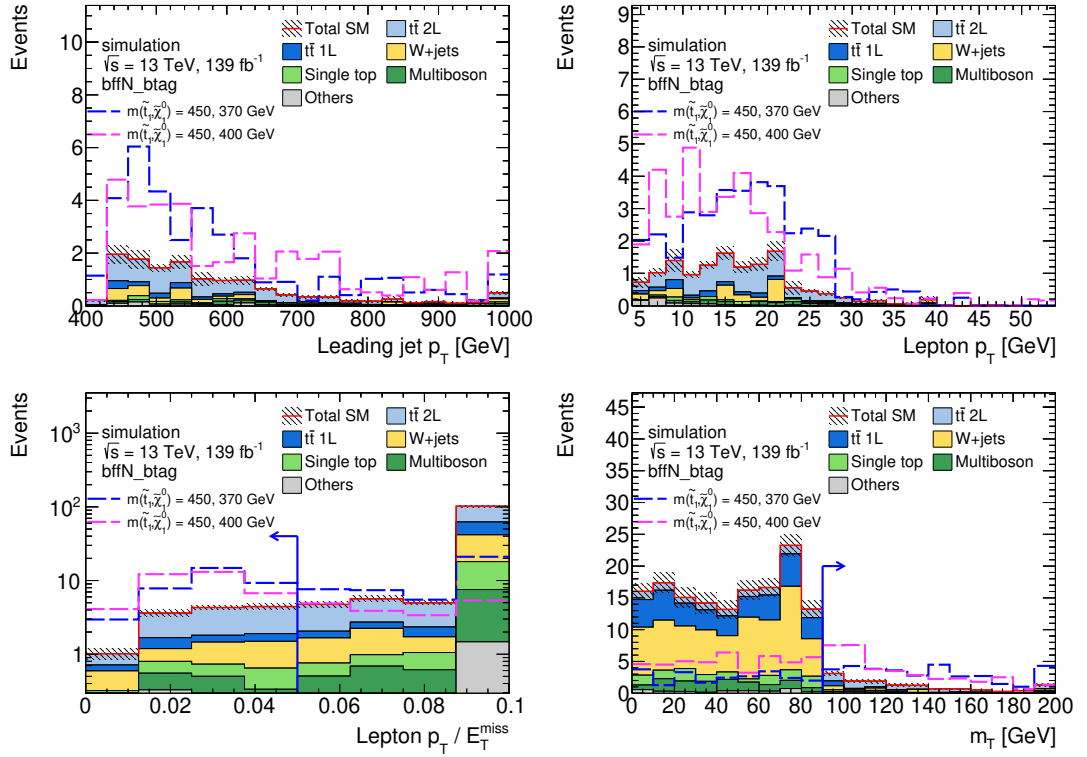


Figure 7.8.: Plots for each discriminating variable defining the `bffN_btag` single-bin SR after applying the `bffN_btag` cuts except the one on the displayed distribution. The events are not scaled by the normalization factors, and only statistical uncertainty is displayed. The last bin includes the overflow. The arrow indicates the value and points to the direction of the selection criteria. The minor background processes are merged into the “Others” category.

7.3. Background estimation

To allow conclusive statements about the significance of a potential excess in the signal selection, a reliable prediction of the SM background in the corresponding phase space is required. After defining the SR, the main SM processes left are very similar to our SUSY signal: dileptonic $t\bar{t}$ with one miss-identified lepton, and W +jets.

For the SR described in the previous section, two control regions (CRs) are defined. They are kinematically close to the SR but with a few key variable thresholds inverted to significantly reduce signal contamination and enhance the yield of a particular background. These CRs are then used in a simultaneous likelihood fit to constrain the background normalization. The CRs are defined to normalize the main backgrounds: dileptonic $t\bar{t}$ (TCR) and W +jets (WCR).

In order to validate the background estimates from the CRs, validation regions (VRs) are introduced for dileptonic $t\bar{t}$ (TVR) and W +jets (WVR). The VRs are disjoint from both the SRs and CRs. Background normalizations, referred to as normalization factors (NF), determined in the CRs are applied to the VRs and compared with the data. The VRs are not included in the final simultaneous fit, but provide a statistically independent test of the background estimates. The potential signal contamination in the VRs is required to be negligible compared to the total number of background events. If a process is not normalized via a control region then it is estimated directly from Monte Carlo simulation and theoretical cross-sections.

7.3.1. Control and validation regions

Table 7.5 summarizes the event selections for the TCR, TVR, WCR and WVR compared to the SR. The event yields of the TCR and WCR are shown in Table 7.6 and Figure 7.9. The ISR jet is the leading jet p_T with a > 200 GeV selection and it is required to not be b -tagged in every region. The CRs are defined with high $p_T^\ell/E_T^{\text{miss}}$ compared to the SR requirement to increase the background events and minimize the signal contamination.

In TCR the leading b -jet p_T is selected with a higher value than the SR to enrich the dileptonic $t\bar{t}$ background and the intermediate value is used for TVR. A higher m_T cut in the TCR and TVR regions is applied to reduce other backgrounds contributions. A b -jet p_T requirement is omitted on the W +jets regions and instead high values of $\min \Delta\phi(p_T^{b\text{-jet}}, E_T^{\text{miss}})$ are selected to enhance W +jets events. An intermediate value between SR and WCR of $\min \Delta\phi(p_T^{b\text{-jet}}, E_T^{\text{miss}})$ is selected for WVR. A positive charged lepton is required in W +jets CR and VR. The reason is that more positively charged leptons are expected in W +jets events than negative ones because of the different cross sections between $ug \rightarrow W^+d$ and $dg \rightarrow W^-u$. In the WCR selection, two events with a high negative weight were observed. Studies were performed and explained in more detail in appendix A.

Table 7.7 shows the $t\bar{t}$ and W +jets VR yields, and the breakdown is shown in Figure 7.10. Distributions of the key variables are shown in figs. 7.11 to 7.14 for $t\bar{t}$ and W +jets CRs, respectively. The data and MC distributions of variables in $t\bar{t}$ and W +jets VRs are shown in figs. 7.15 to 7.18. In all CRs and VRs, the signal contamination is found to be negligible.

In order to test the background estimation method, the NFs obtained in the CRs, are applied in the VRs and the observed number of events is compared to the predicted number of events. The $t\bar{t}$ and W +jets NFs obtained from the simultaneous fit in both CRs are summarized in Table 7.8, which are applied to the CRs and VRs plots. Table 7.9 is the summary of the post-fit yields in all CRs and VRs. The number of predicted SM events agrees with the observed data in the TVR and WVR regions within the uncertainty, meaning that the backgrounds are correctly estimated.

Table 7.5.: Overview of the event selections defining `bffN_btag` signal region and the associated control and validation regions. The maximum signal contamination with respect to the total SM background yield is shown with respect to the total number of SM background events in the region.

Variable	bffN signal	TCR	TVR	WCR	WVR
preselection					
C_{T2} [GeV]	> 400	> 400	> 400	> 400	> 400
leading b -jet p_T [GeV]	< 50	> 100	$[50,100]$	–	–
m_T [GeV]	> 90	> 110	> 110	> 90	> 90
$p_T^\ell/E_T^{\text{miss}}$	< 0.05	> 0.05	> 0.05	> 0.05	> 0.05
$\min \Delta\phi(p_T^{b\text{-jet}}, E_T^{\text{miss}})$	< 1.5	< 1.5	< 1.5	> 2.3	$> [1.5,2.3]$
lepton charge	–	–	–	> 0	> 0
Max Signal Contamination		$\sim 2\%$	$\sim 6\%$	$\sim 2\%$	$\sim 7\%$

Table 7.6.: Pre-fit expected events in `bfN_btag` TCR and WCR for 139 fb^{-1} . Only the statistical uncertainty of the MC samples is given.

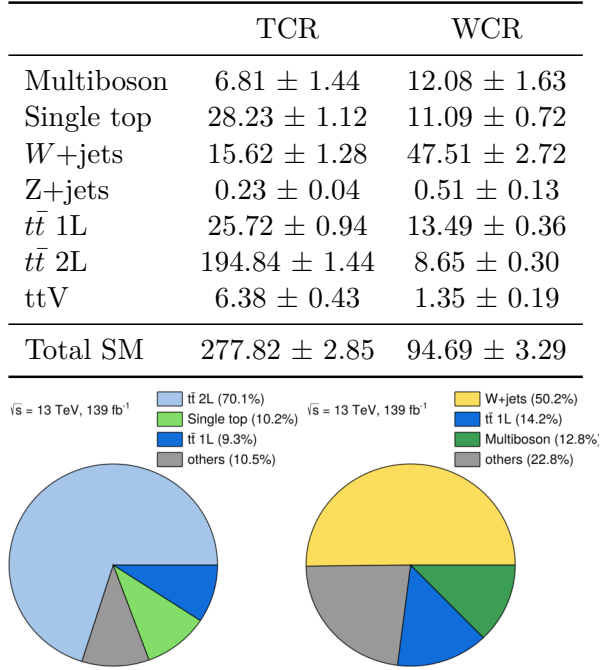


Figure 7.9.: Breakdown of the individual SM contributions to the TCR and WCR selection. The minor background processes are merged into the “Others” category.

Table 7.7.: Pre-fit expected events in `bfN_btag` TVR and WVR for 139 fb^{-1} . Only statistical uncertainty of the MC samples is given.

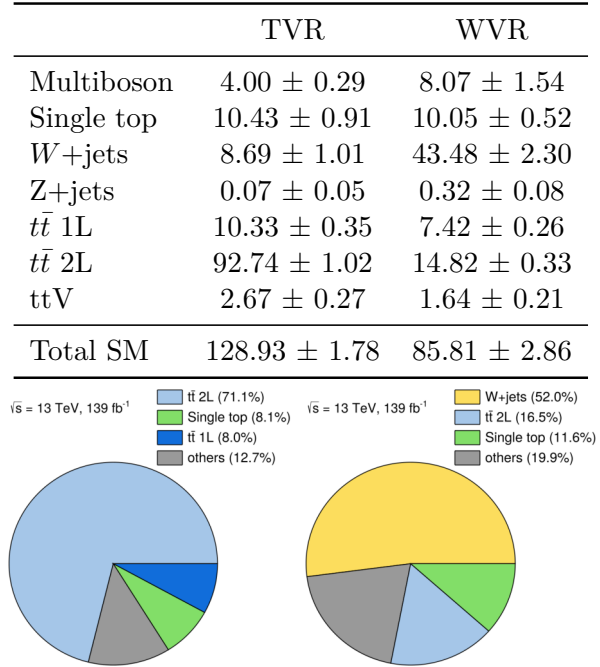


Figure 7.10.: Breakdown of the individual SM contributions to the TVR and WVR selection. The minor background processes are merged into the “Others” category.

Table 7.8.: Normalization factors obtained by the background only fit in $t\bar{t}$ and W +jets CRs. The errors of the NFs include statistical, experimental, and theoretical uncertainties.

Background process	NF
$t\bar{t}$	$0.799^{+0.088}_{-0.083}$
W +jets	$0.831^{+0.276}_{-0.280}$

Table 7.9.: Post-fit yields in the CRs and VRs.

	TCR	WCR	TVR	WVR
Observed events	231	82	108	88
Fitted background	230.88 ± 15.21	82.10 ± 9.10	106.73 ± 9.50	74.00 ± 11.39
$t\bar{t}$	176.28 ± 18.81	17.59 ± 7.18	82.34 ± 10.88	17.73 ± 4.23
W +jets	13.00 ± 5.23	39.52 ± 12.97	7.23 ± 2.89	36.20 ± 13.72
Singletop	28.22 ± 8.93	11.09 ± 3.61	10.43 ± 3.34	10.05 ± 3.23
Multiboson	6.80 ± 2.19	12.05 ± 3.93	4.00 ± 1.30	8.06 ± 2.53
ttV	6.35 ± 3.71	1.34 ± 0.79	2.66 ± 1.56	1.63 ± 0.96
Z +jets	0.23 ± 0.07	0.51 ± 0.16	0.07 ± 0.03	0.32 ± 0.10

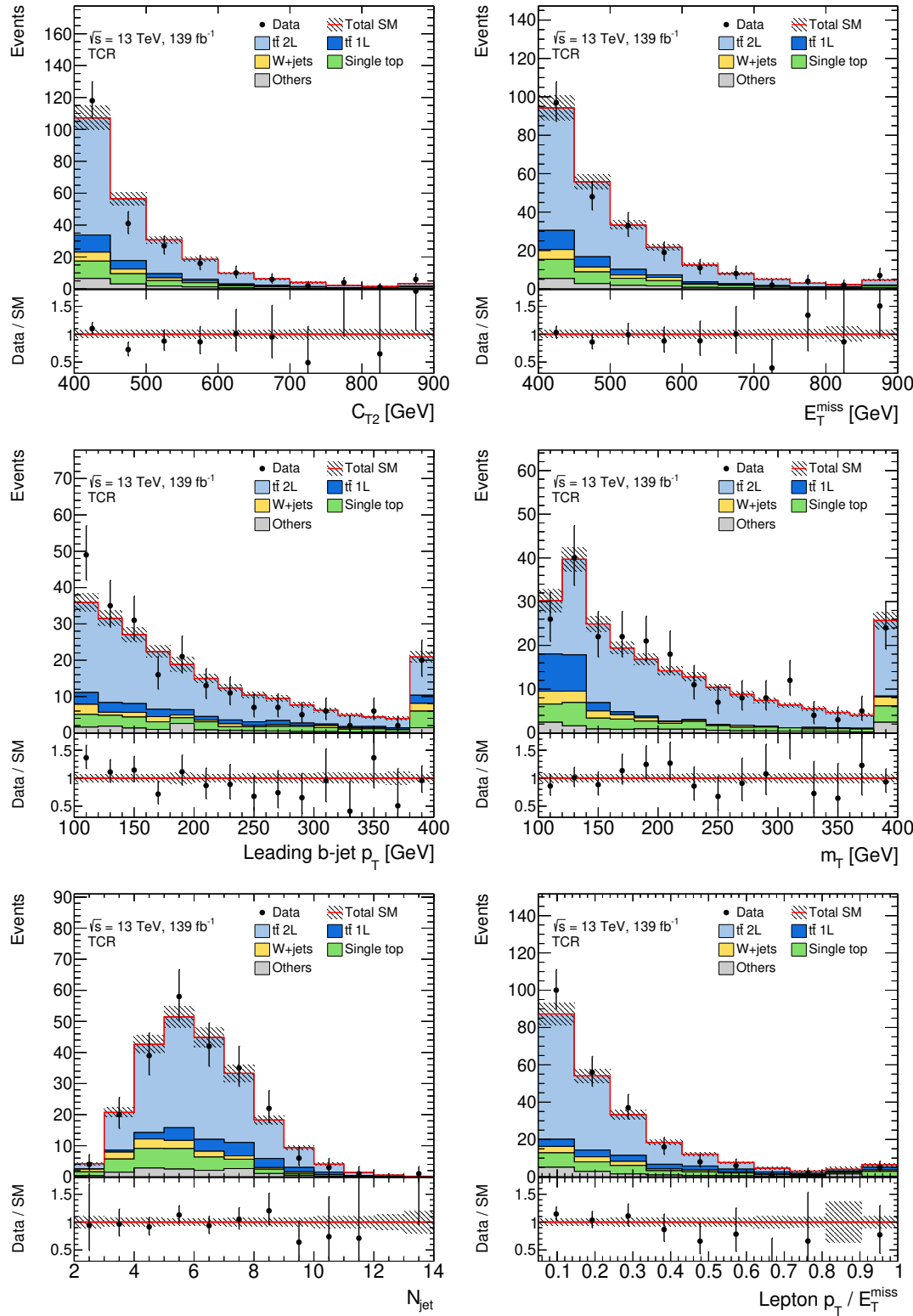


Figure 7.11.: Comparison of data and simulation for TCR after applying the normalization factors from Table 7.8. Statistical and experimental uncertainties are displayed. The last bin includes the overflow. The minor background processes are merged into the “Others” category.

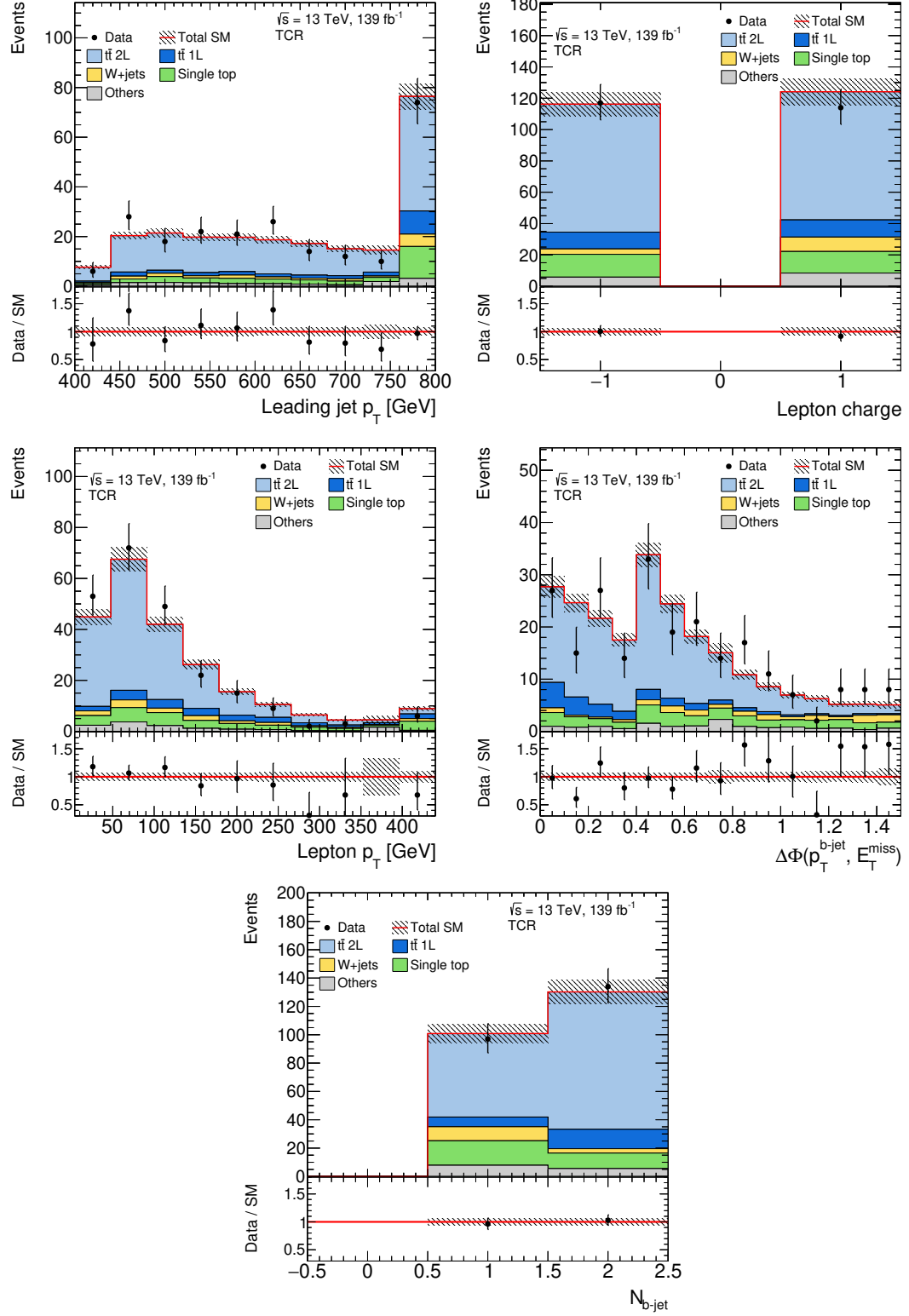


Figure 7.12.: Comparison of data and simulation for TCR after applying the normalization factors from Table 7.8. Statistical and experimental uncertainties are displayed. The last bin includes the overflow. The minor background processes are merged into the “Others” category.

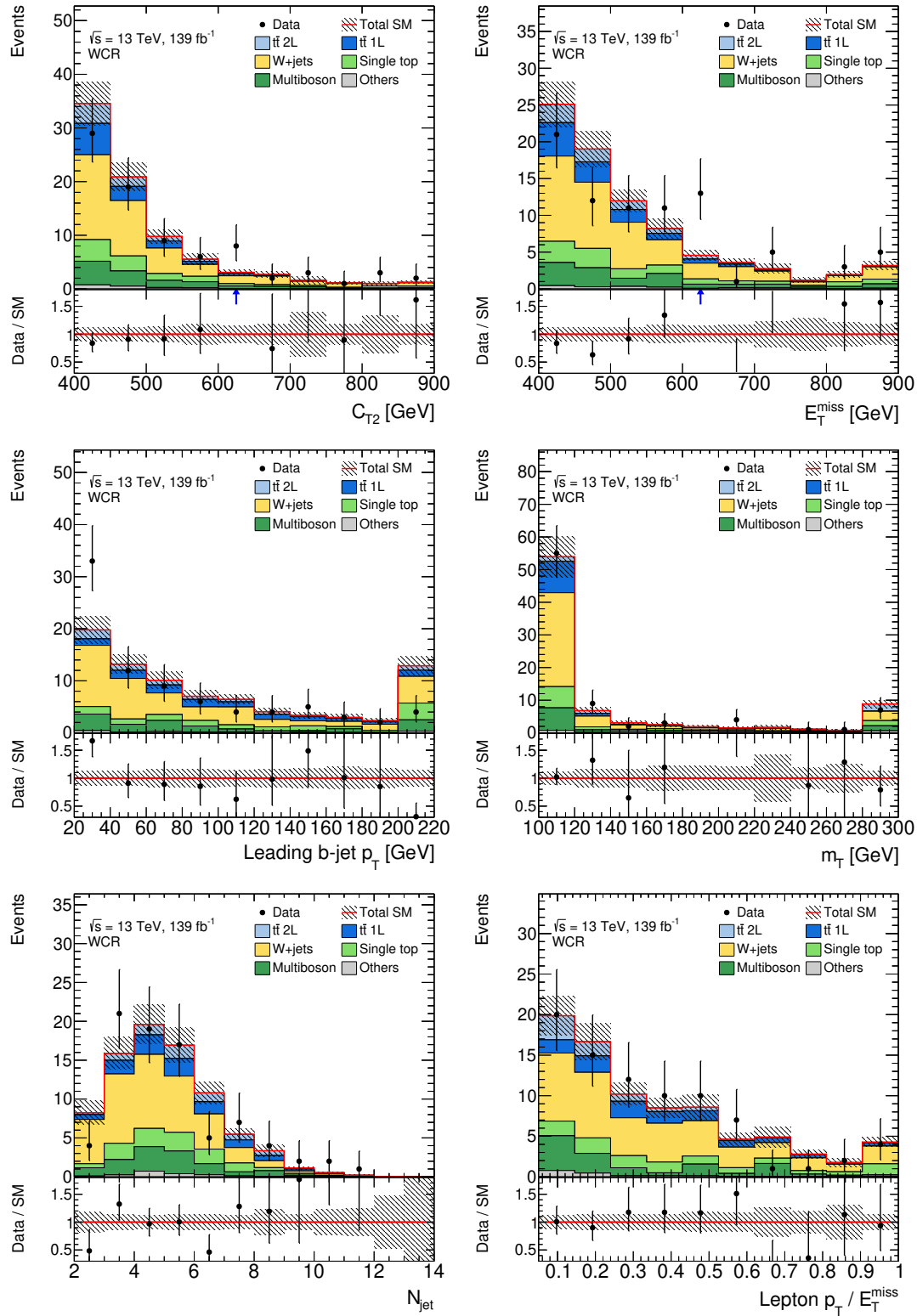


Figure 7.13.: Comparison of data and simulation for WCR after applying the normalization factors from Table 7.8. Statistical and experimental uncertainties are displayed. The last bin includes the overflow. The minor background processes are merged into the “Others” category.

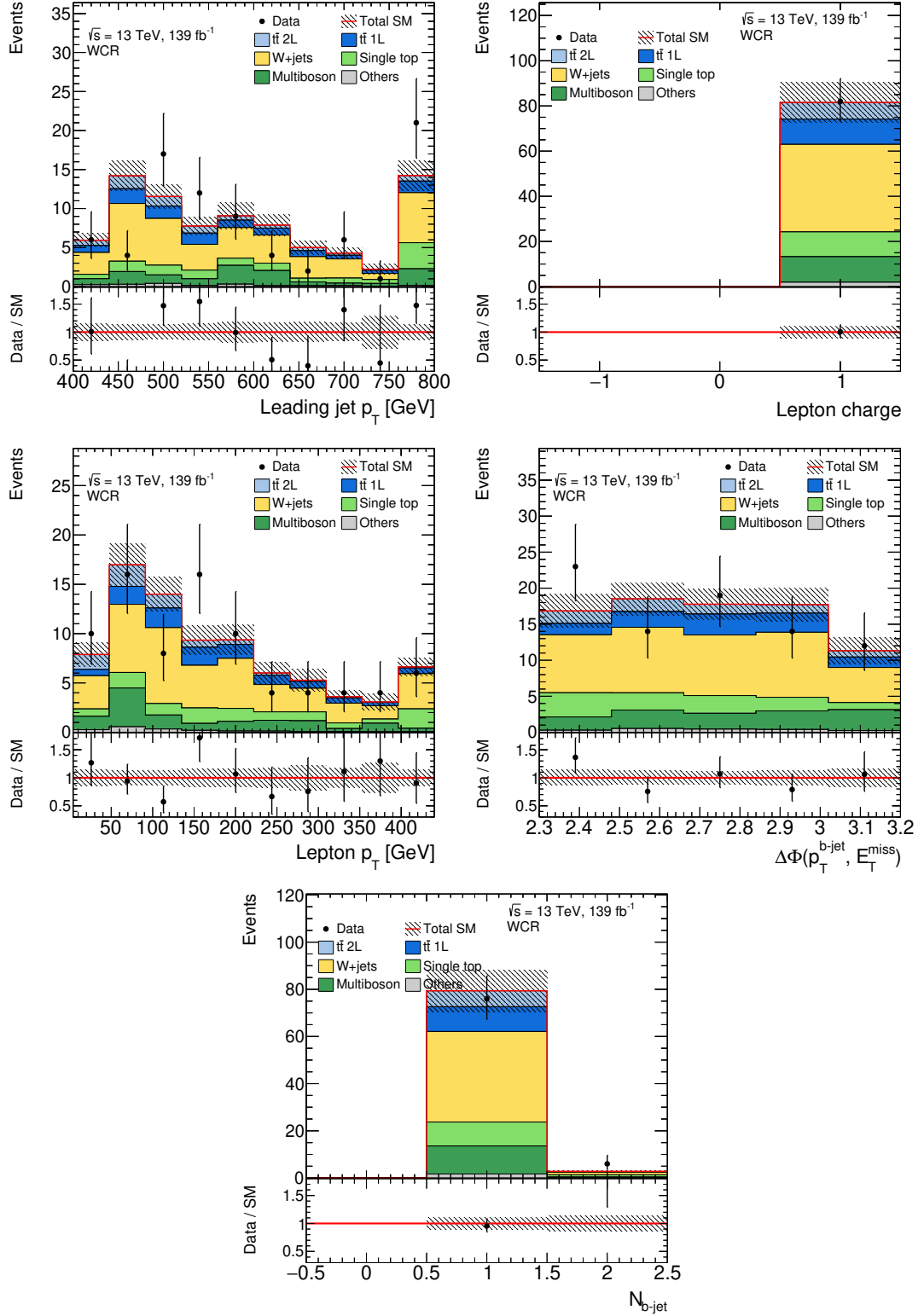


Figure 7.14.: Comparison of data and simulation for WCR after applying the normalization factors from Table 7.8. Statistical and experimental uncertainties are displayed. The last bin includes the overflow. The minor background processes are merged into the “Others” category.

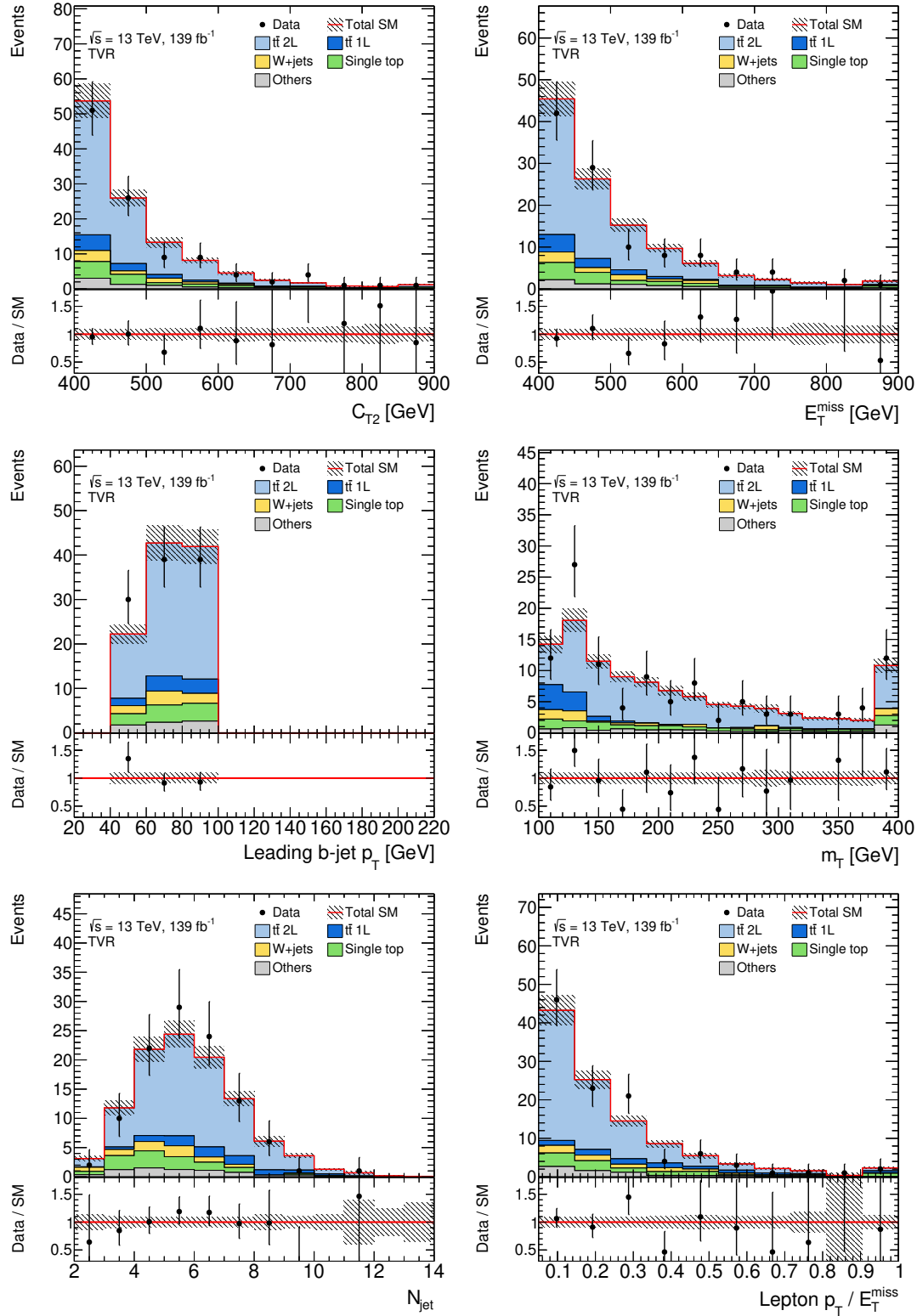


Figure 7.15.: Comparison of data and simulation for TVR after applying the normalization factors from Table 7.8. Statistical and experimental uncertainties are displayed. The last bin includes the overflow. The minor background processes are merged into the “Others” category.

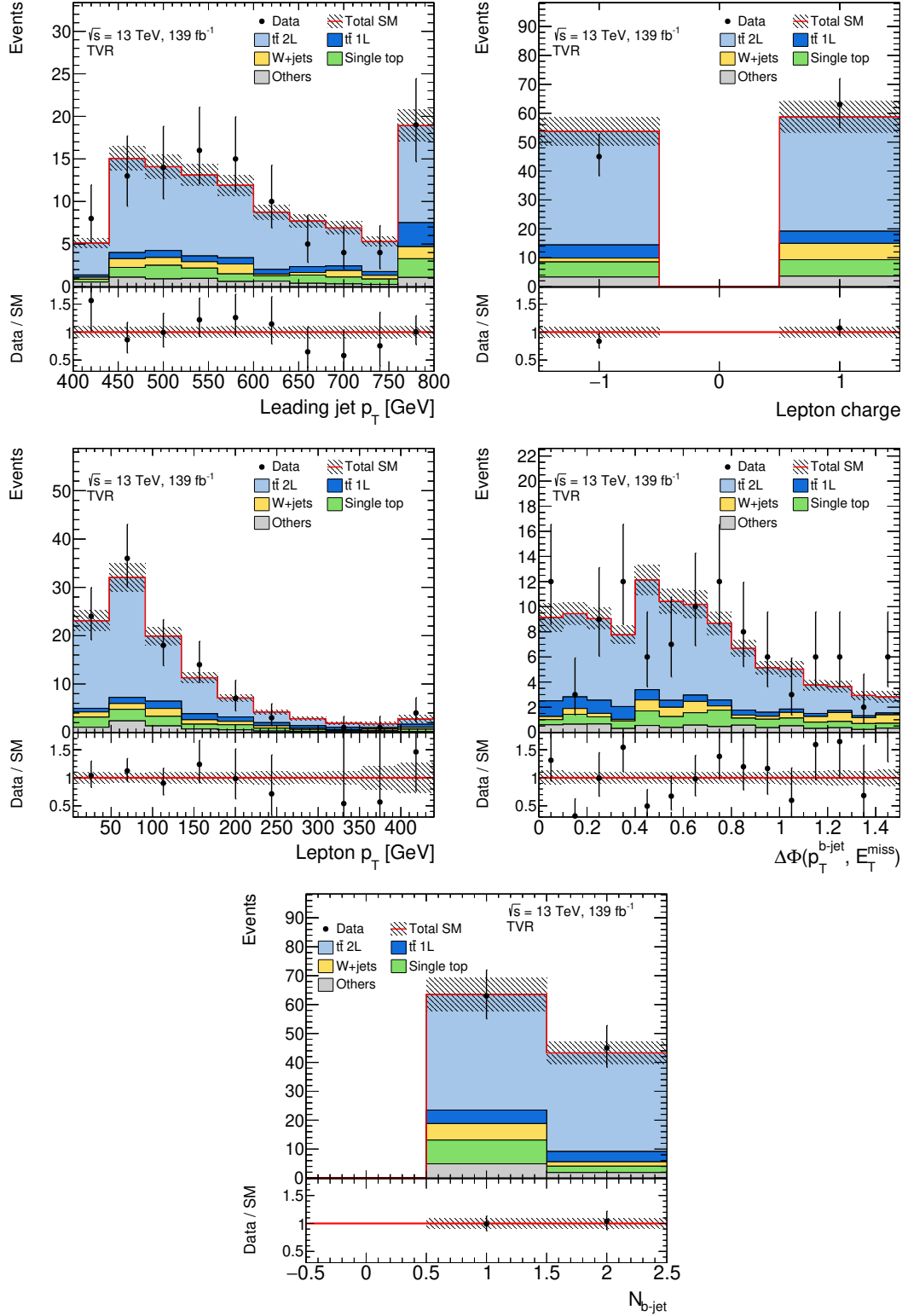


Figure 7.16.: Comparison of data and simulation for TVR after applying the normalization factors from Table 7.8. Statistical and experimental uncertainties are displayed. The last bin includes the overflow. The minor background processes are merged into the “Others” category.

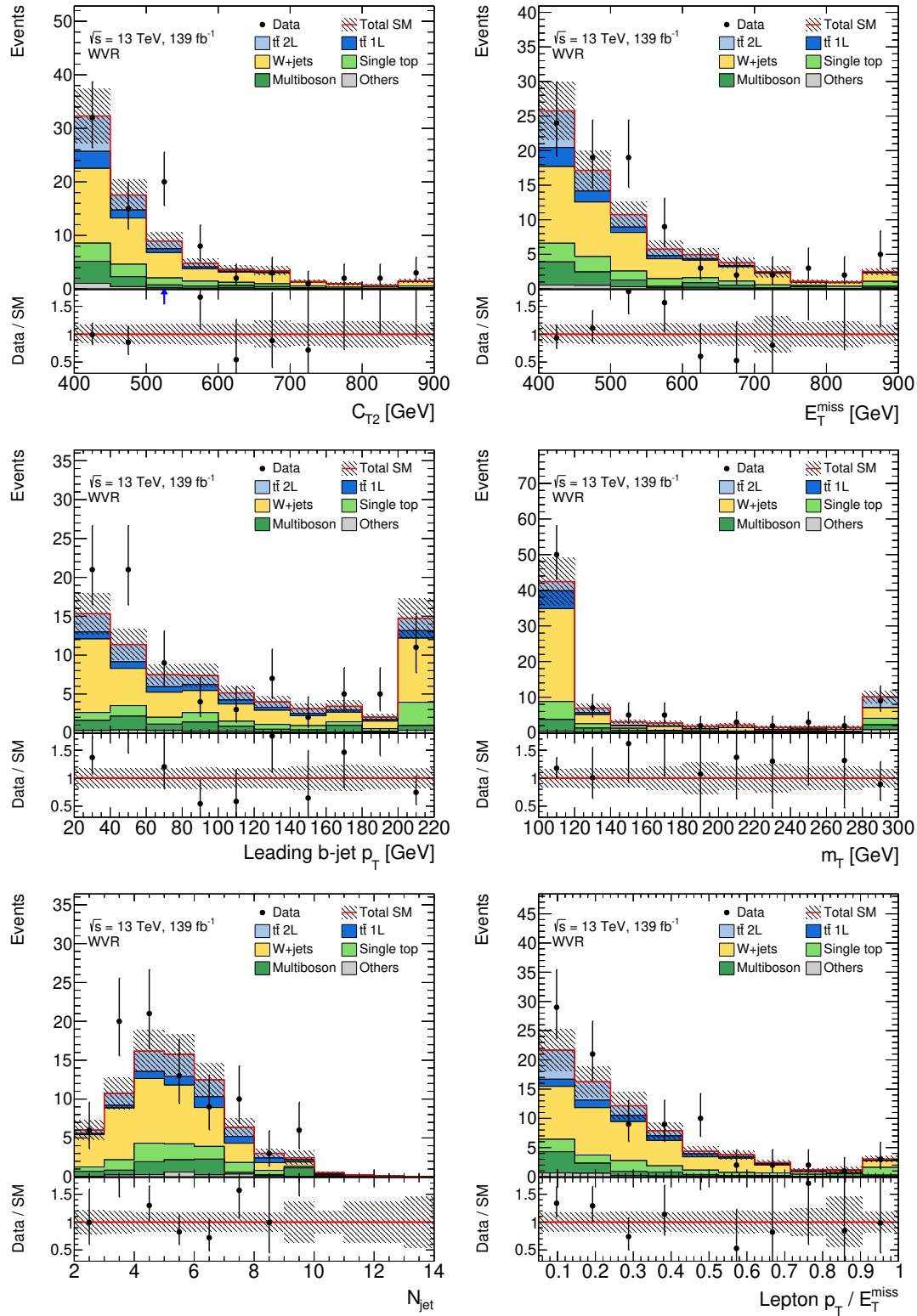


Figure 7.17.: Comparison of data and simulation for WVR after applying the normalization factors from Table 7.8. Statistical and experimental uncertainties are displayed. The last bin includes the overflow. The minor background processes are merged into the “Others” category.

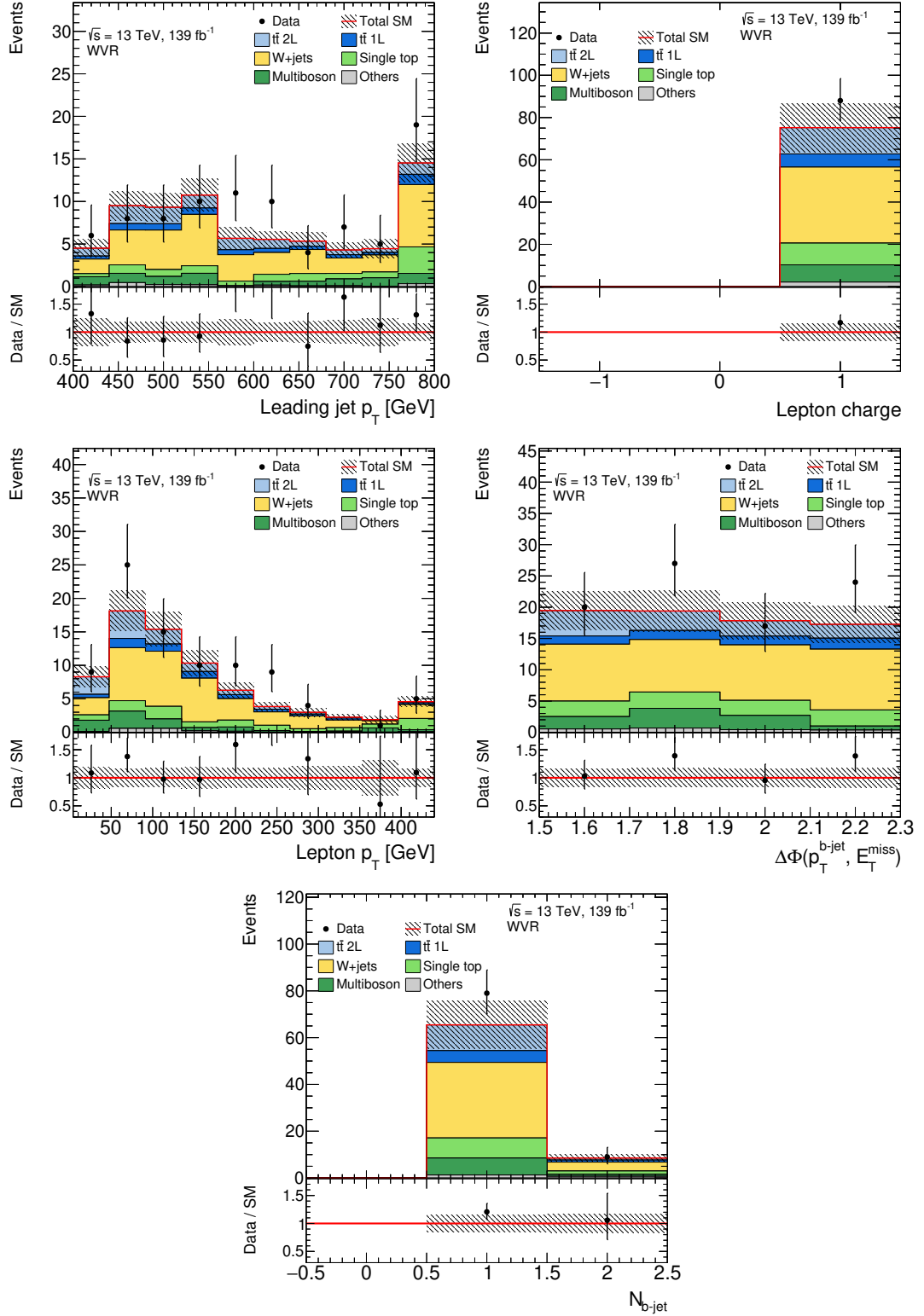


Figure 7.18.: Comparison of data and simulation for WVR after applying the normalization factors from Table 7.8. Statistical and experimental uncertainties are displayed. The last bin includes the overflow. The minor background processes are merged into the “Others” category.

7.4. Systematic uncertainties

An important point in the background estimation is to know how accurate the results are. Statistical fluctuations and systematic uncertainties influence in an increase the uncertainty in the result.

Systematic uncertainties are evaluated for all background and signal samples, using MC simulations. Since the yields from the dominant background sources, dileptonic $t\bar{t}$ and $W+jets$, are obtained in dedicated control regions, the modeling of uncertainties for these processes affect only the extrapolation from the CRs into the SR, but not the overall normalization. Systematic uncertainties are classified into two types: experimental and theoretical uncertainties. In Section 6.3.3 the details of the experimental uncertainties are explained and the method of the theoretical uncertainties estimation presented. In this chapter only the results are shown.

7.4.1. Theoretical uncertainties results

The theoretical uncertainties in each region are summarized in Table 7.10. The uncertainties in the transfer factors from the TCR or WCR to the other regions are estimated by the method as for the analysis described in Section 6.3.3. Due to the small contributions from the other minor background processes, a flat 30% uncertainty is included for the minor background processes which do not have a dedicated CR. For the $t\bar{t}$ background process, the main contributions come from the uncertainties in the parton shower and hard scattering. For the $W+jets$ background, the main contribution comes from the generator comparison with the alternative MadGraph +Pythia 8 sample. In the Appendix B the results for each theoretical systematic uncertainty, event yields, and region plots are shown.

The uncertainties of the background prediction in the SR are summarized in Table 7.11. The total statistical uncertainty is 30% for the expected SM events, and the systematic uncertainty is 12%. The total uncertainty is defined as the quadrature sum of the total systematic and the statistical uncertainties. Due to anti-correlations between the nuisance parameters, the total systematic uncertainties can be smaller than the quadrature sum over the individual sources. The sources of these uncertainties are explained in Section 6.3.3. The dominant systematic uncertainty comes from the $t\bar{t}$ normalization fit, arising from the statistical power of the $t\bar{t}$ events in the TCR. The number of events in the SR is also affected by the uncertainties originating from the jet energy scale (JES). The $W+jets$ normalization uncertainty is caused by the limited statistics in the WCR, and the $W+jets$ modeling uncertainty is the theoretical uncertainty as discussed above.

Table 7.10.: Theoretical uncertainties (%) in the signal $m(\tilde{t}_1, \tilde{\chi}_1^0) = (450, 400)$, $t\bar{t}$ and $W + \text{jets}$ processes. The relative uncertainties with respect to the number of events for the process in each region are shown. The uncertainties are calculated from the transfer factors as explained in more detail in Subsection 6.3.3 and Appendix B.

	$m(\tilde{t}_1, \tilde{\chi}_1^0) = (450, 400)$ GeV	$t\bar{t}$	$W + \text{jets}$
bffN	2.18	5.51	26.67
bffN1	2.61	6.28	26.52
bffN2	2.49	6.42	4.66
bffN3	12.46	14.75	22.60
bffN4	11.64	15.79	28.40
bffN5	14.02	7.29	30.27
bffN6	9.18	11.38	30.27
TCR	-	-	15.47
WCR	-	37.68	-
TVR	-	7.70	17.05
WVR	-	19.01	2.00

Table 7.11.: Summary of the dominant systematic uncertainties in the background prediction in the **bffN_btag** SR.

SR uncertainty[%]	bffN_btag
Statistical uncertainty $\sqrt{N_{\text{exp}}}$	30
Total systematic	12
$t\bar{t}$ normalization	6.6
JES experimental	6.1
$W + \text{jets}$ normalization	5.5
MC statistics	4.9
$W + \text{jets}$ modeling	4.3
Theory	3.8
$t\bar{t}$ modeling	3.1
$E_{\text{T}}^{\text{miss}}$ experimental	2.4
Leptons experimental	2.3
b -tagging experimental	1.9
JER experimental	1.8
Pile-up	1.0

Table 7.12.: Post fit yields in the `bf1N_btag` SRs. The “SR” is the single bin SR, while “SR1-6” are the bins `bf1N1-6` defined in Table 7.4 for the exclusion. The errors include statistical and systematic uncertainties.

	SR	SR1	SR2	SR3	SR4	SR5	SR6
Observed events	14	5	4	6	3	8	9
Predicted background events	11.26 ± 1.35	2.94 ± 0.40	4.94 ± 0.64	8.02 ± 0.94	2.38 ± 0.44	6.82 ± 3.66	6.36 ± 1.04
$t\bar{t}$	6.91 ± 1.05	1.83 ± 0.32	3.51 ± 0.56	5.09 ± 0.94	1.25 ± 0.28	2.10 ± 0.53	2.97 ± 0.56
$W+jets$	1.86 ± 0.84	$0.29^{+0.35}_{-0.29}$	0.30 ± 0.18	1.04 ± 0.47	0.53 ± 0.36	1.35 ± 0.68	1.53 ± 0.94
$Z+jets$	0.40 ± 0.13	0.19 ± 0.06	0.00 ± 0.00	0.00 ± 0.00	0.27 ± 0.09	0.00 ± 0.00	0.01 ± 0.00
Sigletop	0.82 ± 0.54	0.23 ± 0.14	0.44 ± 0.14	0.71 ± 0.25	0.10 ± 0.05	$2.99^{+3.88}_{-2.99}$	0.42 ± 0.17
Multiboson	1.07 ± 0.35	0.27 ± 0.09	0.68 ± 0.24	0.93 ± 0.31	0.17 ± 0.06	0.35 ± 0.11	1.21 ± 0.40
$t\bar{t}V$	0.21 ± 0.12	0.13 ± 0.08	0.02 ± 0.02	0.25 ± 0.15	0.05 ± 0.03	0.02 ± 0.01	0.22 ± 0.13

7.5. Results

The observed data in the SR is summarized in Table 7.12, together with the predicted background events. No significant excess was found in the discovery SR. The observed p -value for the background-only hypothesis is $p_0 = 0.20$, which corresponds to 0.84σ . The distributions of the key variables with the SR selection are shown in Figure 7.19 and Figure 7.20. Since no deviation from the estimated SM prediction was found, exclusion limits are derived from the shape-fit SR. For the exclusion, the SR with regular b -tagging (`bf1N_btag`) and another SR with the soft b -tagging reference [215, 217] are simultaneously fitted. The `bf1N_btag` is sensitive to higher $\Delta m(\tilde{t}_1, \tilde{\chi}_1^0)$, while the SR with the soft b -tagging has better sensitivity for low $\Delta m(\tilde{t}_1, \tilde{\chi}_1^0) < 40$ GeV. Figure 7.21 shows the gain of standard b -tagging comparing the expected exclusion limits with the soft b -tagging only and the combination of the two b -taggers. For $\Delta m(\tilde{t}_1, \tilde{\chi}_1^0) = 50$ GeV, the expected limit is improved from 400 GeV to ~ 640 GeV for the $m_{\tilde{t}_1}$.

In the exclusion limits, other signal regions are used for the 2-body and 3-body regions from reference [215]. Figure 7.22 shows the observed and expected exclusion limits at 95% CL in the $m_{\tilde{t}_1}$ versus $\tilde{\chi}_1^0$ plane, and Figure 7.23 shows the same limits with $\Delta m(\tilde{t}_1, \tilde{\chi}_1^0)$ on the vertical axis. In the four-body decay region $\Delta m(\tilde{t}_1, \tilde{\chi}_1^0) < (m_b + m_W)$, the limit reaches 640 GeV in the stop mass, and the limit is lowered to $\Delta m(\tilde{t}_1, \tilde{\chi}_1^0) \sim 20$ GeV with the `bf1N_btag` and `bf1N_softb` combination.

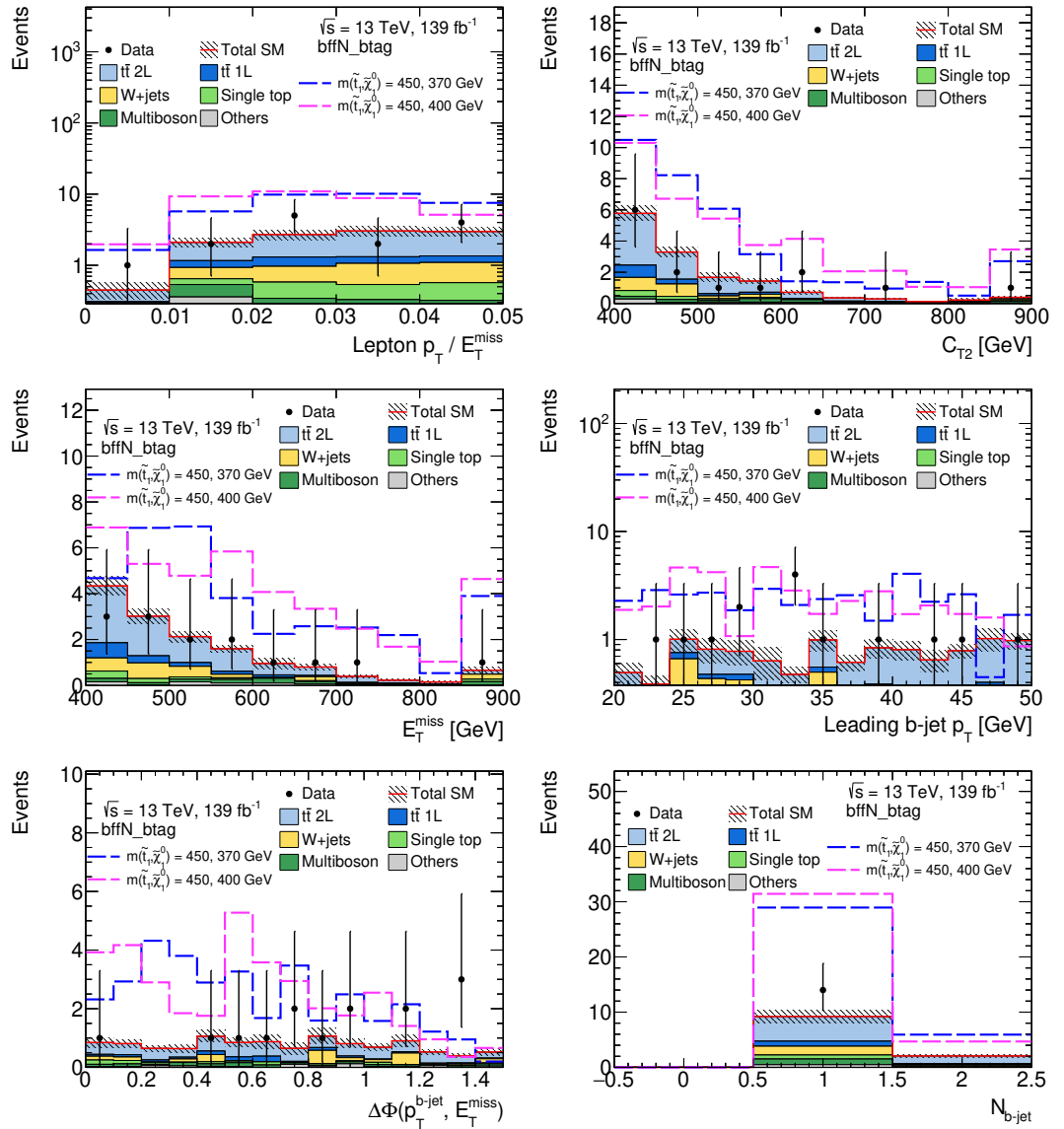


Figure 7.19.: Distribution of the variables used to define the `bffN_btag` discovery SR. The NFs are applied to the $t\bar{t}$ and $W+jets$ backgrounds. Statistical, theoretical, and experimental uncertainties are included. The last bin includes the overflow.

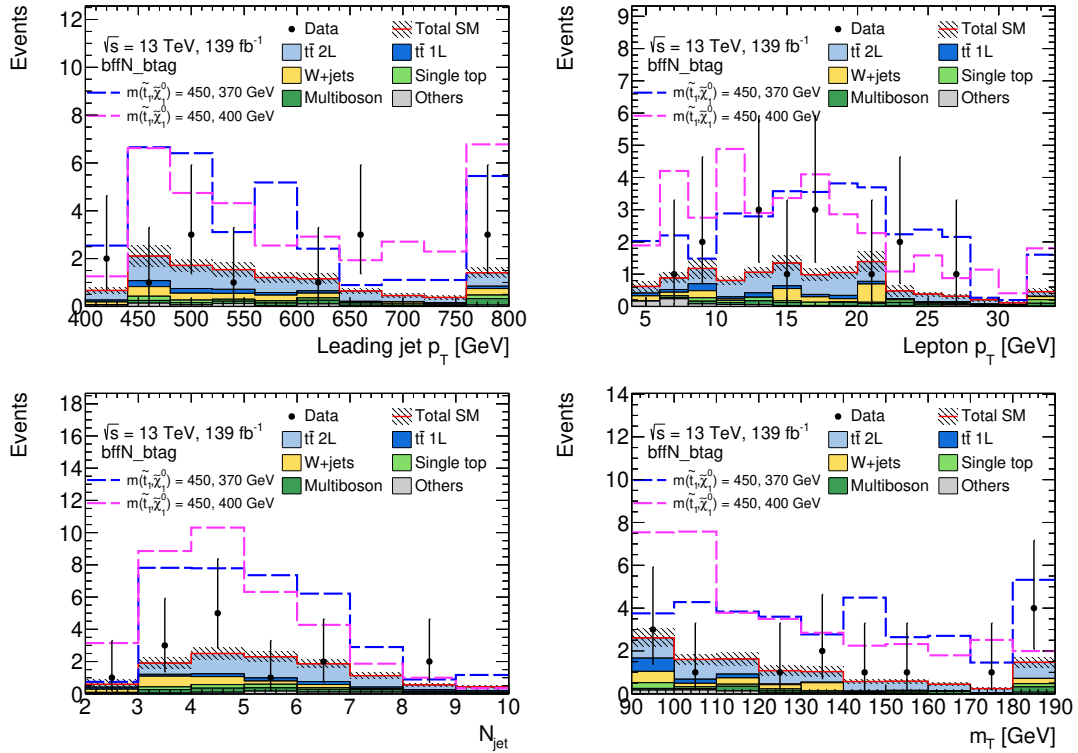


Figure 7.20.: Distribution of the variables used to define the `bffN_btag` discovery SR. The NFs are applied to the $t\bar{t}$ and $W+jets$ backgrounds. Statistical, theoretical, and experimental uncertainties are included. The last bin includes the overflow.

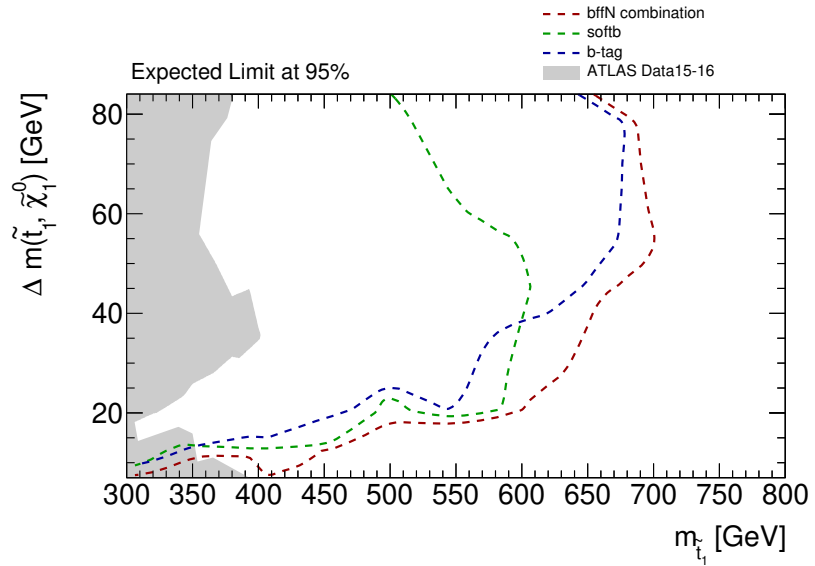


Figure 7.21.: Expected exclusion limits at 95% CL in the plane of $m_{\tilde{t}_1}$ versus $\Delta m(\tilde{t}_1, \tilde{\chi}_1^0)$. The blue line shows the limit obtained from the signal region with the standard b -tagging (`bffN_btag`). The green line shows the limit obtained from the signal region with the soft b -tagging. The red line shows the limit from the simultaneous exclusion fit using both soft b -tagging and standard b -tagging SRs. The gray region shows the previous ATLAS results with data collected in 2015–2016, which corresponds to 36 fb^{-1} [189, 218–220].

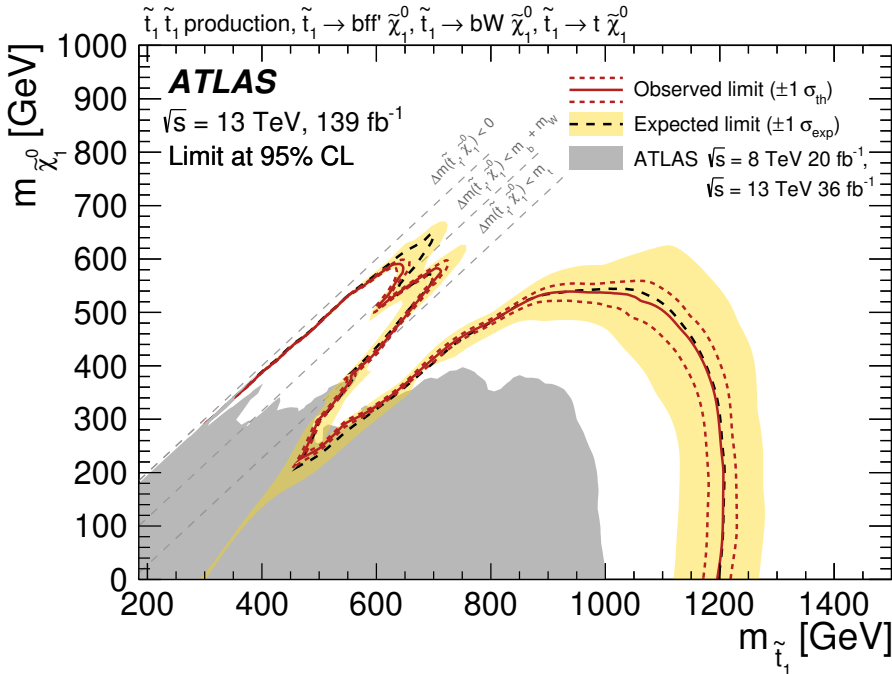


Figure 7.22.: Expected (black dashed) and observed (red solid) limits at 95% CL in the plane of $m_{\tilde{t}_1}$ $m_{\tilde{\chi}_1^0}$. The yellow band displays the $\pm 1 \sigma$ variation of the expected limit, and the red dotted lines along the observed line show the uncertainty in the cross section for pair production of top squarks. The gray dashed lines separate the \tilde{t}_1 decay modes: $t \tilde{\chi}_1^0$ (2-body), $bW \tilde{\chi}_1^0$ (3-body), and $bff' \tilde{\chi}_1^0$ (4-body) [25]. The gray region shows the previously excluded area from the ATLAS Run 1 and Run 2, which corresponds to 36 fb^{-1} [189, 218–220].

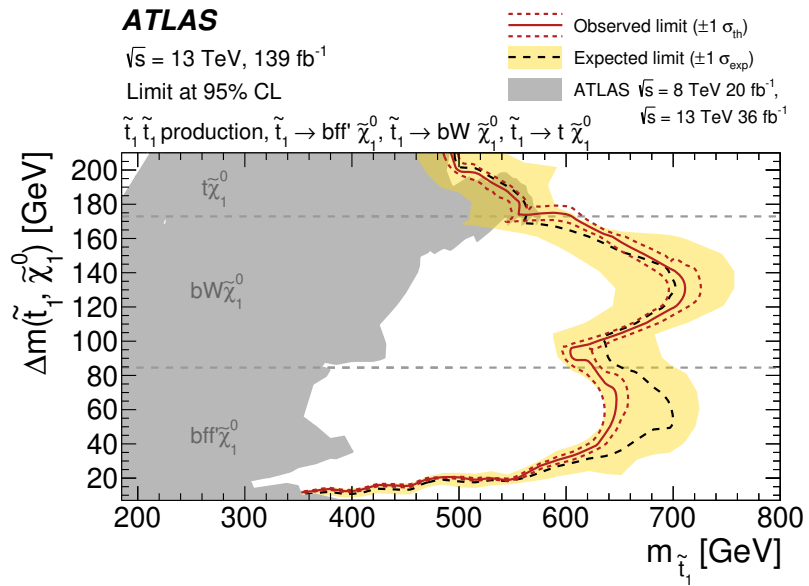


Figure 7.23.: Expected (black dashed) and observed (red solid) limits at 95% CL in the plane of $m_{\tilde{t}_1}$ versus $\Delta m(\tilde{t}_1, \tilde{\chi}_1^0)$. The yellow band displays the $\pm 1 \sigma$ variation of the expected limit, and the red dotted lines along the observed line show the uncertainty in the stop cross section. The gray dashed lines separate the \tilde{t}_1 decay modes: $t\tilde{\chi}_1^0$ (2-body), $bW\tilde{\chi}_1^0$ (3-body), and $bff'\tilde{\chi}_1^0$ (4-body) [25]. The gray region shows the previously excluded area from the ATLAS Run 1 and Run 2 results, which corresponds to 36 fb^{-1} [189, 218–220].

8. Search for R -parity violating supersymmetry in events with multiple jets and one lepton

The analysis presented in this chapter searched for new physics in final states characterized by high jet multiplicity and one isolated lepton. The model used 139 fb^{-1} of $\sqrt{s} = 13 \text{ TeV}$ proton-proton collision data collected by the ATLAS detector. The main target was a natural SUSY signal model with minimum flavor violation (MFV) [72], which predicts only the baryon-number-violating $\bar{u} \bar{d} \bar{d}$ coupling to be non-zero. In this way, the lightest supersymmetric particle decays promptly via a R -parity-violating (RPV) coupling to SM particles. Hence, this type of signal does not depend on a E_T^{miss} requirement, complementing the R -parity conserving SUSY searches. The results of this analysis are already public in [26].

This analysis extended the previous version [214] by including the full Run-2 dataset, aiming to improve the search sensitivity to access direct higgsino production. Getting sensitivity to higgsino production was extremely challenging due to its lower cross-section and mass range. For this reason, the higgsino signal was the main target of this analysis iteration.

8.1. Analysis Strategy

The signal model has been described in Chapter 6. This analysis searched for RPV SUSY in final states with at least one lepton and many jets and b -jets. An important feature of this type of analysis with many jets and b -jets in the final state is that a pure reliance on Monte Carlo (MC) is not possible. MC would not correctly describe events at such high jet-multiplicities. Therefore, a so-called *data-driven* method was applied, explained in more detail in Section 8.2.

For the analysis selection, at least one signal electron or muon was required in the event, at least four jets, and at least one b -jet. Up to 8 jets and 4 b -jets were expected in the higgsino model. Signal leptons were required to have a $p_T > 27 \text{ GeV}$ [26]. After a basic lepton selection, no additional cut were imposed on any kinematic variable, including E_T^{miss} and m_T . The only variables used to discriminate between SM and a potential SUSY signal were the number of leptons, jets, and b -jets. Apart from these objects'

multiplicities, a lower bound on the jet transverse momentum of 20 GeV was used to suppress background events. This strategy alone was not sufficient to reach sensitivity to higgsino production. For this reason, a new extension of the analysis named *shape analysis* was introduced and is explained in Section 8.3.

Besides the jet and b -jet multiplicities, the shape analysis introduced a third variable based on a neural network (NN) discriminant. To extract the shape of the b -jet multiplicity from data without relying on MC, dedicated techniques were implemented in the NN training to ensure a shape invariance with respect to a different number of b -jets.

8.2. Background Estimation

In the RPV higgsino scenario, a search for one lepton, multiple jets, and at least one b -jet in the final state was performed. For this reason, the main SM background was top-quark pair production with additional heavy flavor jets. The theoretical modeling of this background at high jet multiplicity suffers from large uncertainties. To overcome this, it was estimated from data by extrapolating the jet and b -jet multiplicity distributions at moderate jet multiplicities, to higher jet multiplicities where the signal was expected.

8.2.1. Jet Multiplicity Prediction

To estimate the contribution of the $t\bar{t}$ background a data-driven approach was used. The normalization estimate was based on a functional form describing the evolution of the number of background events as a function of jet multiplicity by

$$r(j) = N_{j+1}/N_j \quad (8.1)$$

with N_j as the number of jets in the $t\bar{t}$ event. As shown in Figure 8.1, above a certain number of jets, $r(j)$ can be assumed to be constant ($r(j) = c_0$) in a so-called *staircase-scaling* [222]. It implies a fixed probability of additional jet radiation. This behavior has also been observed by the ATLAS [223] and CMS [224] collaborations. For lower jet multiplicities a *poisson-scaling* was seen following $r(j) = c_1/(j+1)$ with c_1 as a constant. The transition between these scalings depends on the jet kinematic selections.

For this search, a superposition of both scaling parameters was used as

$$r(j) = c_0 + c_1/(j + c_2) \quad (8.2)$$

with the scaling constants c_0 and c_1 obtained from data. Formula 8.2 provides a good fit in the dedicated regions and in simulated MC samples.

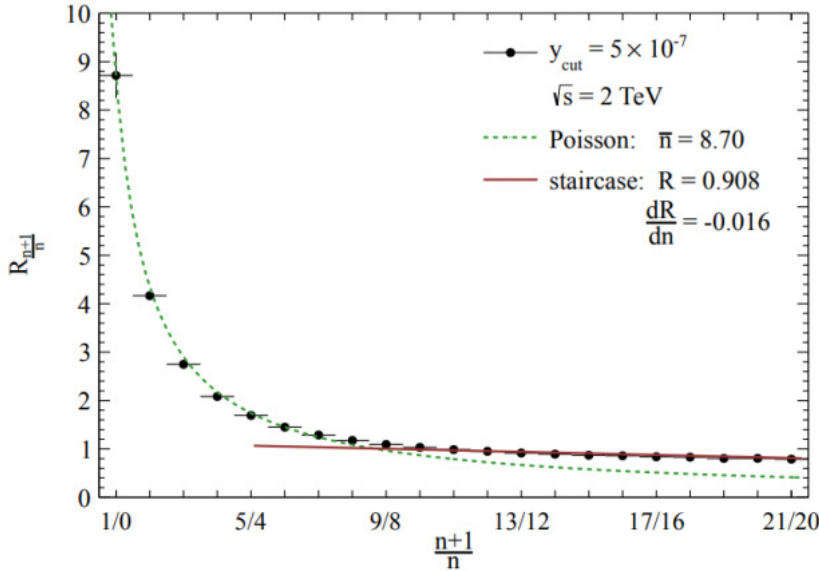


Figure 8.1.: Jet ratios $R_{n+1}^{(n+1)}$ in $e^-e^+ \rightarrow \text{jets}$ production at 2 TeV center-of-mass energy. They are shown as a function of the jet multiplicities [222]. The poisson-scaling is seen for low jet multiplicities in the green-dotted line. For higher jet multiplicities a staircase-scaling is shown in the dark red line.

The parameter c_2 takes into account the ambiguity in counting jets originating from the decay of $t\bar{t}$ with additional jets. The distinction between ‘extra’ jets and jets from the $t\bar{t}$ decay was not trivial. A four-jet event could have passed the jet selection by gaining jets via initial or final state radiation. The c_2 parameter was fixed to a value of -3 in case four jets from dileptonic $t\bar{t}$ events were reconstructed. Fits on simulated $t\bar{t}$ samples gave $c_2 = -2.8$ for a 20 GeV threshold, and $c_2 = -1$ for 100 GeV.

The number of background events with j jets was parameterized by

$$N_j = N_4 \cdot \prod_{j'=4}^{j'=j-1} r(j) \quad (8.3)$$

with the absolute number of jets in four-jet events N_4 . As the event selection required at least four jets, N_4 was the starting point for the scaling. The model was able to predict arbitrarily high jet multiplicities. The prediction of the inclusive number of events above a certain jet multiplicity was achieved by summing the predictions for all jet multiplicities above it. The four parameters (c_i, N_4) were extracted per process from data.

The jet scaling in equation 8.3 was validated in data using dileptonic $t\bar{t}$ events. The dileptonic $t\bar{t}$ data sample required an electron and muon candidate in the event with at least two jets of which at least one is a b -jet.

The scaling behavior in the dileptonic $t\bar{t}$ sample could be tested for up to thirteen jets, which corresponds to fifteen jets for a semileptonic MC $t\bar{t}$ + jets sample as seen in Figure 8.2. With the available statistics in the samples, the model provided a good description of the jet scaling for different jet p_T thresholds.

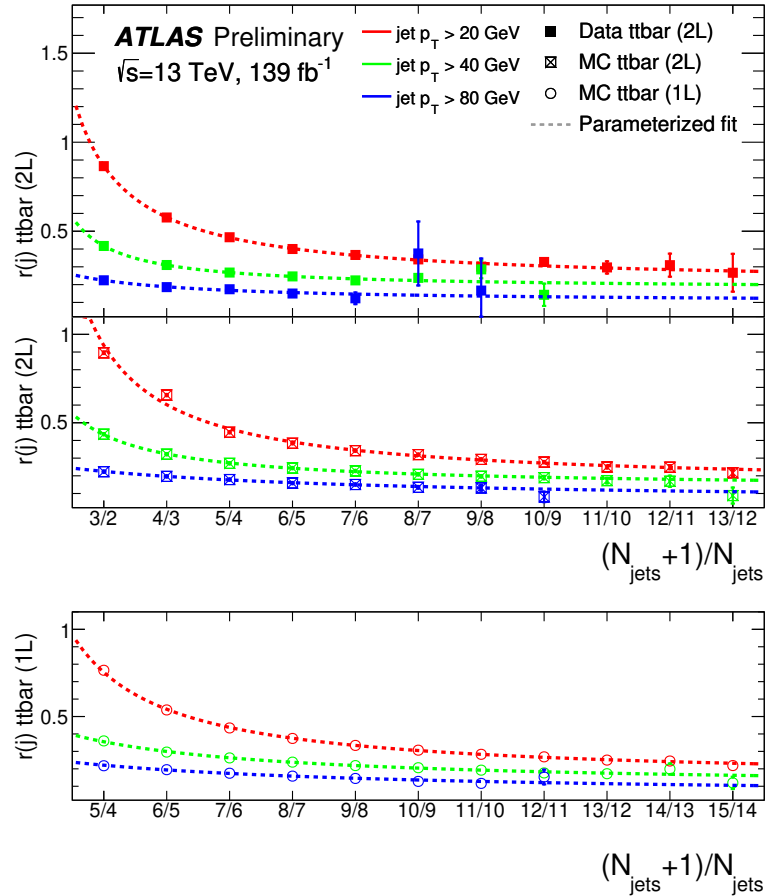


Figure 8.2.: Figure showing the ratio of the number of events with $(j + 1)$ jets to the number of events with j jets in different samples. This fit was performed to validate the jet-scaling parameterization. Each panel shows the ratio of data or MC with the fitted parameterization overlaid as a dashed line. The uncertainties shown are statistical. A good agreement between the the samples and the scaling parametrization is seen [26].

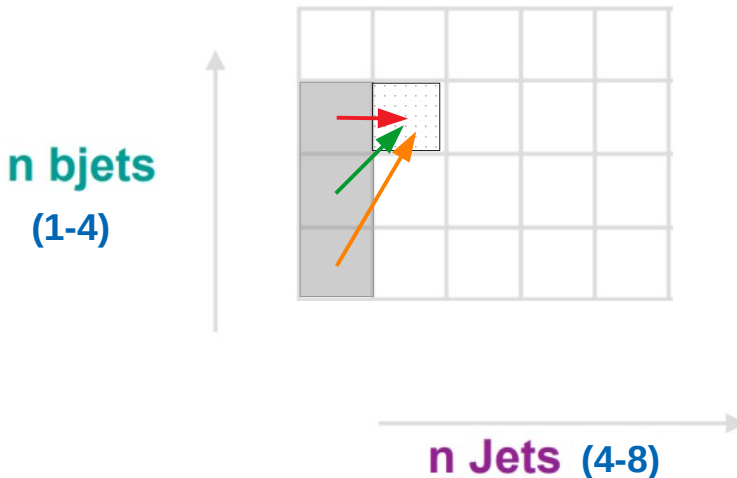


Figure 8.3.: Sketch representing the extraction of an initial template of the b -tag multiplicity spectrum in events with 4 jets, and its evolution. The main assumption is that the difference in the b -tag multiplicity spectrum with n and $n + 1$ jets arises from an additional jet production. The red arrow represents $f_{j,b} \cdot x_0$ as in equation 8.5. It is the fraction of b -tagged jets in the j jet slice times the probability of the additional jet not being b -tagged. For this reason, the arrow is horizontal, meaning that the number of b -tagged jets did not change. The green arrow illustrates $f_{j,(b-1)} \cdot x_1$, which is the fraction times the probability of being b -tagged. The orange arrow represents $f_{j,(b-2)} \cdot x_2$ which is the fraction times the probability of being b -tagged and causing a second b -tagged jet to move into acceptance.

8.2.2. b -Jet Multiplicity Prediction

A data-driven model was used to estimate the b -jet fraction in background processes containing top quarks. The basic concept was based on extracting an initial template of the b -jet fraction distribution in events with four jets. Then this template was parameterized for the evolution to higher jet multiplicities. In a given jet and b -jet multiplicity region, the number of background events was given by

$$N_{j,b} = f_{j,b} \cdot N_j \quad (8.4)$$

with $f_{j,b}$ the fraction of events with b number of b -jets in events with j jets. The extrapolation of the b -jet multiplicity distribution to higher jet multiplicities started assuming that the difference in the b -jet multiplicity distribution with n and $n + 1$ jets, arises from the production of additional jets.

This can be described by a fixed probability of the additional jet being b -tagged. The extrapolation to one additional jet was parameterized as

$$f_{(j+1),b} = f_{j,b} \cdot x_0 + f_{j,(b-1)} \cdot x_1 + f_{j,(b-2)} \cdot x_2 \quad (8.5)$$

where the parameter x_0 describes the probability of the additional jet not being b -tagged, x_1 of being b -tagged, and x_2 being b -tagged and causing a second b -tagged jet to move into acceptance. The x_2 parameter dominated cases where the extra jet was a b -jet influencing the kinematics such that the extra b -jet, previously below the jet p_T threshold, entered acceptance. As the x_i parameters describe probabilities, the sum $\sum_i x_i$ was normalized to unity. The extrapolation of the b -tag multiplicities to higher jet multiplicities is represented on the sketch in Figure 8.3. As a consequence, the application of this parameterization produces a b -jet template for arbitrarily high jet multiplicities.

MC simulated events showed the necessity of an extra fit parameter. The new parameter ρ_{11} was introduced to capture the correlation between b -jet pairs produced from gluon splittings. The initial b -tag multiplicity template was extracted from data events with 4 jets, represented by $f_{4,b}$ and scaled by the absolute number of events N_4 to obtain the model in the 4 jet bin:

$$N_{4,b} = N_4 \cdot f_{4,b} \quad (8.6)$$

where the sum $\sum_{b=0}^4 f_{4,b} = 1$, was normalized to unity.

8.3. Shape Analysis

8.3.1. Machine Learning

The essential concept of machine learning algorithms is that they can derive estimations from multi-variate data themselves, meaning that these algorithms “learn” from certain characteristics present in the data. The model needs to be trained to derive conclusive predictions from data. Therefore, the dataset is split into a dedicated *training set* and *test set*. The training set, as the name suggests, contains events on which the model is trained, while the events in the test set are used to assess the model’s performance and eventually tune the algorithm. A third set referred to as the *validation set* is completely independent from the training and test set. The validation set contains a collection of unseen events, from which the final model derives predictions while tuning the model’s *hyper-parameters* (i.e. parameters for the learning process). The hyper-parameters are constant parameters whose values are initialized before the learning takes place. They are like settings that can alter the algorithm’s behavior, and they are optimized in the course of training.

Neural networks (NNs) are one of the main tools used in machine learning. They are formed by input and output layers, as well as a hidden layer, consisting of units that

transform the input into something that the output layer can use. They are excellent tools for finding patterns which are far too complex from a regular analysis. The challenge for using NN discriminants in this analysis was the background estimation. To extract the shape of the NN output directly from data without relying on MC, the NN output shape was conditioned to be invariant with respect to the number of b -jets. The jet and b -jet counting analysis previously described, was not sufficient to reach direct higgsino sensitivity. For this reason, a third variable based on a NN discriminant was introduced to better separate signal from background. The NN was optimized to reach the low mass scale and cross-section of the higgsinos.

The background was fitted to data in each jet and b -jet bin. The higgsino signal was expected to be found in high b -jet multiplicities as shown in Figure 8.4. For this reason, the shape of the NN output for different b -jet multiplicities in the $t\bar{t}$ background needed to be invariant. If shape invariance was achieved, a $t\bar{t}$ template distribution could be obtained from data in background-dominated regions with a low number of b -jets (with 1 and 2 b -jets regions). Then, this template can be applied to higher b -tag multiplicity regions.

The NN was trained with dedicated techniques enforcing the invariance of the NN with respect to the number of b -jets. The technique presented in this dissertation makes use of a so-called *adversarial neural network*. In the RPV analysis team, another type of NN was tested in parallel using a distance correlation algorithm [225].

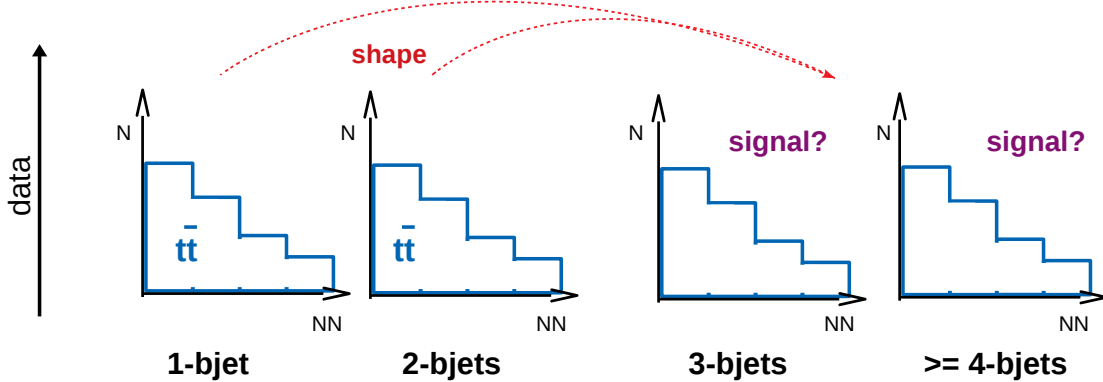


Figure 8.4.: Sketch showing the distribution of the NN output variable depending on the number of b -jets for the $t\bar{t}$ background. The $t\bar{t}$ background is normalized from data in each jet and b -jet bin. The higgsino signal is expected to be present at high number of b -jets (3 and 4). If the background shape is invariant, the $t\bar{t}$ template obtained in low b -jet multiplicities can be extrapolated to higher ones without the necessity of MC.

8.3.2. Adversarial Neural Network

The ML algorithm learns by means of a *loss function*. It is a method of evaluating how well the algorithm models the given data. A loss function is represented by the sum of squares of the difference between the actual and predicted value. If predictions deviate too much from actual results, the loss function would result in a large number. Gradually, with the help of some optimization function, the loss function learns to reduce the error in prediction. In a standard ML setup, the network is trained with a single objective: to separate SM background from SUSY signal. The motivation for introducing a NN was to find an observable providing good signal-background separation, but whose shape, under the background hypothesis, was invariant to b -jet multiplicities. This can be achieved using an adversarial neural network (ANN).

8.3.2.1. ANN Description

For two b -jet multiplicities, n_b and n'_b the distribution of the NN output score is set equal, $p_b(y|n_b) = p_b(y|n'_b)$, where $p_b(y|n_b)$ is the conditional probability density of the NN output score y for n_b b -jets. If invariance is achieved, a template of p_b can be obtained directly from data in low n_b regions and extrapolated to higher n_b . To achieve invariance an additional term L_{inv} to the NN loss function L is introduced as

$$L = L_{\text{main}} - \lambda L_{\text{inv}} \quad (8.7)$$

where λ is a parameter for tuning the strength of this additional contribution.

The ANN approach probes the difference between the distributions $p_b(y|n_b)$ and $p_b(y|n'_b)$ of a neural net f_{main} with output $y = f_{\text{main}}(x)$. This difference is achieved by training an additional NN (adversarial) f_{adv} with the discriminant y as an *input*, and the prediction of the b -jet multiplicity (n_b) as an *output*. The ANN is, in a sense, a model pitted against an adversary [226]. If the output y strongly informs about the shape of the distribution n_b , the task of the adversarial network is “easy” leading to a low value of L_{inv} and consequently a higher value of the total loss function L . On the contrary, if the distribution $p_b(y|n_b)$ does not depend on n_b , the task is difficult, leading to a high value of L_{inv} and consequently a lower value of the total Loss. So in this min-max “game”, L returned low values for good invariance.

A sketch depicting this process is shown in Figure 8.5. The first network can be defined as the discriminant $y = f_{\text{main}}(x|\theta_{\text{main}})$ (in orange) from x the discriminant, and the second network as the adversarial one $n_b = f_{\text{adv}}(y|\theta_{\text{adv}})$ (in purple). Given the two networks, a joint optimization of both parameters θ_{main} and θ_{adv} can be performed.

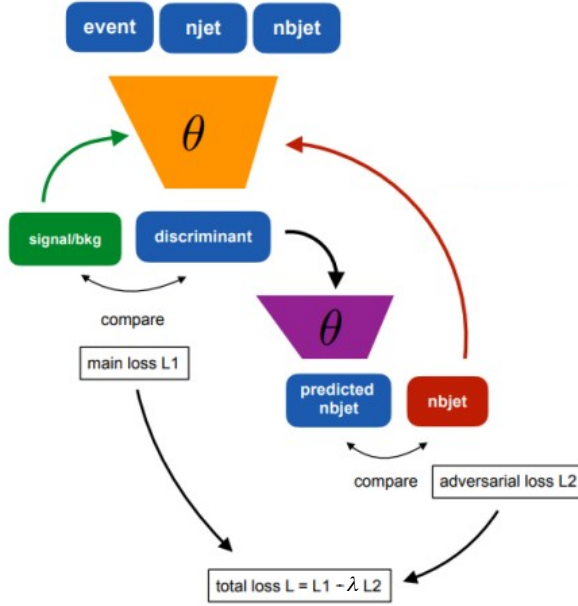


Figure 8.5.: Representation of the adversarial neural network (ANN) flow. A NN (in orange) was trained with the single objective of separating signal from background. The adversarial setup (in purple) analyzed the resulting discriminant with respect a secondary objective. This secondary objective describes the ability to predict the b -jet multiplicity purely from the discriminant input. The goal was to find a good signal-background discriminator, whose shape is invariant in different b -jet slices under the the background hypothesis. Sketch taken from Lukas Heinrich slides.

The total objective function can be written as

$$L = (1 - \lambda)L_{\text{main}} - \lambda L_{\text{adv}} \quad (8.8)$$

with L_{main} as the loss of the primary network f_{main} with respect to the signal-background separation. L_{adv} describes the adversarial network's ability to predict the b -jet multiplicity of the event purely from the discriminant input.

8.3.2.2. Training and Validation

The NN was trained with a mixture of $t\bar{t}$ samples for the background and a mixture of higgsino samples for signal. The $t\bar{t}$ sample was a mixture of 70% nominal $t\bar{t}$ and 30% of an alternative parton-shower $t\bar{t}$ as explained in Subsection 4.2.2. The signal samples used for the studies were a mixture of samples with $m_{\tilde{h}} = 250, 300, 350$ GeV (including the $\tilde{\chi}_1^0 \tilde{\chi}_1^\pm$, $\tilde{\chi}_1^0 \tilde{\chi}_2^0$, and $\tilde{\chi}_2^0 \tilde{\chi}_1^\pm$ signatures). To obtain an independent validation set, 10% of each sample was held out and did not enter any training procedure. The validation dataset had the same composition as the training dataset, with a fraction of the full

available MC statistics. For this reason, the validation set contained more statistics. The performance of the NN was then evaluated on the validation dataset.

The secondary goal of the training was to achieve invariance with respect to b -tag multiplicity. For this, the training data was prepared such that the training dataset had approximately the same number of events for each b -tag multiplicity slice to have equal statistics for validation.

The NN was only trained in jet multiplicities where a higgsino signal contribution was expected. The NN was trained on inputs based on the leading lepton and from 4 to 8 jets. The observable was constructed from a combination of low-level inputs, such as lepton and jet momenta, and high-level inputs corresponding to event-level variables such as missing transverse energy and jet invariant masses. The high-level variables consisted of

- jet and b -jet multiplicity of the event
- scalar p_T sum of all jets (H_T) and b -jets
- minimum distance between the leading lepton and any jet (ΔR)
- E_T^{miss} and E_T^{miss} angle ϕ
- invariant mass of the three-jet system with highest p_T
- invariant mass of the $3j + l + E_T^{\text{miss}}$ system with highest p_T
- $\min(\max m(\text{jets}))$ defined by having all the jets in the event split into two groups. Both groups have to contain at least one jet, and all possible combinations were tested. The higher invariant mass of the two groups was selected, and then the minimum across all possible groupings was taken. It had an endpoint for signal events below $m_{\tilde{\chi}_1^0}$, since the lepton and E_T^{miss} components were ignored. Background events however did not show such an endpoint. The shape of this variable had only a weak dependence on the number of b -tags, which helped the NN achieve separation while remaining invariant under the number of b -tags

The low-level variables were:

- jet and leading lepton four momentum: p_T , η , ϕ , and energy
- b -tag jet score defined by the pseudo-continuous working points [227]

The inputs were connected to a single output node via two fully connected hidden layers of 100 neurons. The NNs were trained using PyTorch [228] and the Adam optimizer [229].

8.3.2.3. Metrics

Different metrics were devised to track the training progress and select the NN with the best performance. The following were used for the ANN.

- Binary cross entropy [230–232]: used as a metric of signal-background separation. Lower values of this metric indicate better separation. Cross-entropy is a measure of the difference between two probability distributions for a given set of events.
- Invariance metrics across b -tag multiplicities:
 - KL mean: mean of the discretized Kullback-Leibler divergence of the NN shape between all off-diagonal pairs ($n_b \neq n'_b$). Explained in more detail in the following.
 - KL max: maximum of the discretized Kullback-Leibler divergence.
 - Distance correlation: dCorr [225] measuring the correlation between two variables.
- Expected CLs: this metric computed the expected signal and background yields using the pyhf [182, 233] package to compute the p -values and test the statistics. The uncertainty on the background shape was derived as the maximum deviation of each b -tag template with respect to the inclusive distribution. This metric was affected by the separation and invariance previously described by including the systematic uncertainty. Therefore the CLs metric was a combined measure of both goals that the training needs to achieve.
- Combined loss: is the sum of the binary cross-entropy and the adversarial main loss functions.

The Kullback Leibler divergence [234] $D_{KL}(p||q)$ is a measure of how one probability distribution is different from a second. It is computed as the expected log-likelihood ratio $\log p/q$ under one of the two distributions, resulting in an *asymmetric* measure. For this reason it cannot compute the *distance* between two distributions.

The NN was trained to predict $y = 0$ for the $t\bar{t}$ background, and $y = 1$ for the higgsino signal. The target domain of the NN was a continuous variable $x \in [0, 1]$. The discrete distributions p and q were estimated using training or validation set histograms with 4 bins. The discrete KL distance from q to p is computed as

$$D_{KL}(p||q) = \sum_{i=1}^N p(x_i) \cdot \log \frac{p(x_i)}{q(x_i)} \quad (8.9)$$

The distance correlation dCorr [225] measures the correlation between two variables estimated from a finite sample of events. The correlation between the neural network output y and the b -jet multiplicity n_b can be used as a measure of the invariance of the NN distribution with respect to the b -jet multiplicity $\text{dCorr}_{\text{bkg}}^2(y, n_b)$. This correlation measure is exactly zero if and only if n_b and y are independent.

8.4. Results

8.4.1. ANN

Different decision metrics and hyper-parameters were tested in order to select the best combination. In appendix C these studies are presented showing that the CLs metric was the best option by selecting the best CLs value reported during the trainings. The CLs value was the selected metric due to its sensitivity to the shape invariance. Trainings were performed separately for $n_{\text{jet}} = 4, 5, 6, 7, 8$ samples to discriminate the higgsino signal from the $t\bar{t}$ background. The full distribution of the NN output, binned in four bins with approximately equal signal fractions, was fitted in each of the regions with at least one b -jet.

The hyper-parameters on Table 8.1 were used, where the batch size is the number of samples processed before the model is updated. The number of epochs is the number of complete passes through the training dataset. The size of a batch must be less or equal to the number of samples in the training dataset. The learning rate is a tuning parameter that determines the step size at each iteration while moving toward a minimum of a loss function. It controls how quickly the model is adapted to the problem. The lambda hyper-parameter is a regularization parameter as shown in Equation 8.8. Setting lambda to 0 results in no regularization, while large values of lambda correspond to more regularization.

Hyper-parameter	Value
Training batch size	10 000
Validation batch size	500 000
Epochs	7 000
Steps per epoch	30
Learning rate	10^{-3}
Lambda	0.9

Table 8.1.: Hyper-parameter settings for the adversarial training.

In total, 10 million signal and background events were sampled for test and train categories. The training was performed for 7000 epochs. In each epoch, the loss function was evaluated 30 times on batches of 10 000 events sampled from the training set, and the network parameters were updated according to the gradient of the loss function with an initial learning rate of 10^{-3} . At the end of a training epoch the network was evaluated on a validation sample of 5×10^5 events, sampled once at the beginning of the training from the validation set. The adversarial parameter was optimized according to the expected CLs value in the training.

After completing the training on all epochs, the configuration that achieved the best CLs on the validation set was chosen, which was not necessarily the configuration after the last training epoch. The evolution of the CLs metric was computed from the signal and background event yields during the trainings.

Figure 8.6 shows the NN output distributions for the different jet multiplicities, where good shape invariance is seen in between the b -jet samples (colored lines) in all the jet slices, except in the 4-jet plot (top-left). The trainings were performed separately for each jet slice. The 4-jet ratio plot shows a significant discrepancy between the b -jet samples in the fourth bin, meaning that shape invariance was not achieved where more signal was expected. The 4-jet sample was trained again with the same hyper-parameters as in Table 8.1 but changing lambda to 0.95. This in order to look for a greater contribution of the adversarial network in the total loss. The result is seen in Figure 8.7 where the invariance in the 4-jet slice did not improve specially for the second bin.

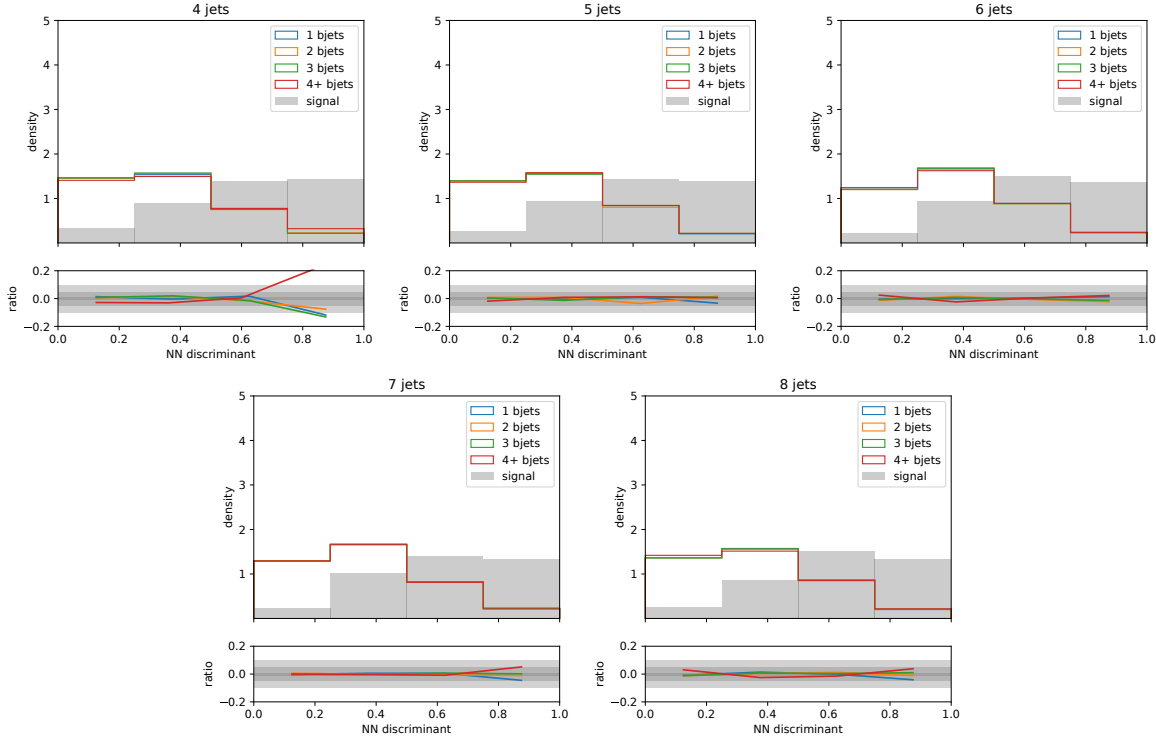


Figure 8.6.: Output distributions of the NN trained with the adversarial setup for $n_{\text{jet}} = 4, 5, 6, 7, 8$ $t\bar{t}$ background events in different b -tag multiplicities. The NNs were trained with $\lambda = 0.9$ and with all the hyper-parameters in Table 8.1. The ratio of each template is displayed with respect to the average of all the templates. The gray band in the ratio plot is a reference to 0.01, 0.05, 0.1 values.

The performance of each training according to the CLs and KLmean metrics is shown in Figure 8.8, where only trainings with $CLs < 0.2$ were considered. As it is seen, no $n_{jet} = 4$ (blue) passes the $CLs < 0.2$ selection, not even with $\lambda = 0.95$ (brown). The bad invariance in the 4-jet training leads to a large systematic which degrades the CLs metric, and the results were not contained in the range of the plot.

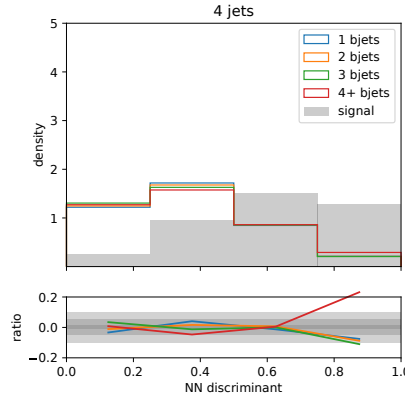


Figure 8.7.: Output of the NN trained with the adversarial setup, for $n_{jet} = 4$ $t\bar{t}$ background events in different b -tag multiplicity bins. The λ parameter was increased to 0.95 in an attempt to reach better invariance. The ratio of each template is displayed with respect to the average of the templates. The gray band in the ratio plot is a reference to 0.01, 0.05, 0.1 values.

Figure 8.9 shows the evolution of the metrics for the $n_{jet} = 6$ adversarial training comparing the training set (blue) and the validation sample (orange). The contributions of the signal, background, and the uncertainty for the CLs calculation in the fourth bin are shown. The bin uncertainty was derived in the CLs calculation as the maximum deviation of each b -tag template to the inclusive distribution. A large correlation between the CLs metric plot and the fourth-bin uncertainty was observed, since the highest signal contribution was expected in the fourth bin. The rest of the metric plots are shown in Appendix D.

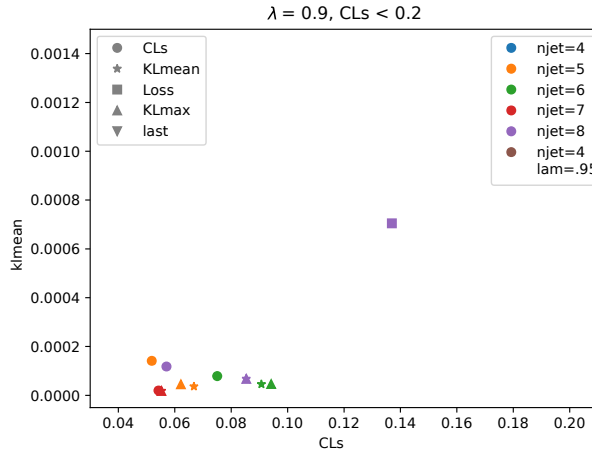


Figure 8.8.: Metric performance for the different jet slices and metrics according to which the best training was chosen. Only outputs with $CLs < 0.2$ are selected which removes all the 4-jet results, as the large non-invariance leads to a large systematic that degrades the CLs value.

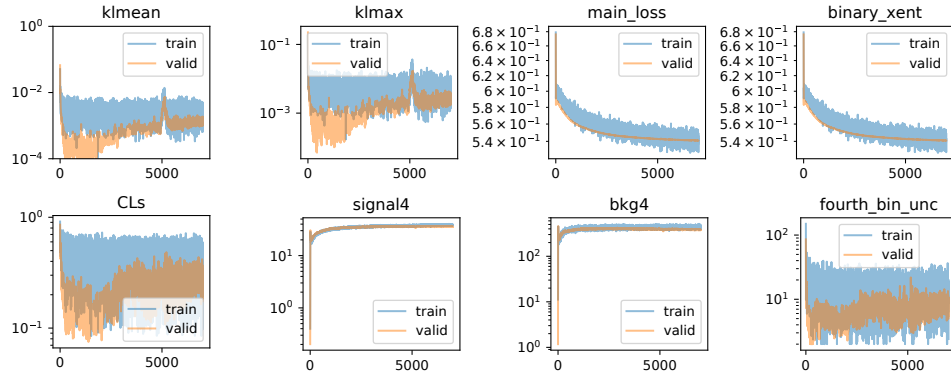


Figure 8.9.: Training metrics for the adversarial training with the $n_{jet} = 6$ sample. The training set (blue) and the validation sample (orange) are compared with respect to the training epoch. The title binary_xent refers to the binary cross entropy metric, and signal4 and bkg4 to the fourth bin tracking in signal and background.

8.4.2. Distance Correlation

The distance correlation was an alternative approach performed in the RPV analysis team where another type of NN was tested in parallel using a distance correlation algorithm [225]. In the distance correlation training, the correlation between the NN output y and the b -jet multiplicity n_b was used to measure the shape invariance of the NN

distribution with respect to the b -jet multiplicity. The distance correlation, denoted by $\text{dCorr}_{\text{bkg}}^2(y, n_b)$ is zero if and only if n_b and y are independent, that is [235–237]

$$p(y, n_b) = p(y|n_b)p(n_b) = p(y)p(n_b) \quad (8.10)$$

It follows that $p(y|n_b) = p(y)$ is invariant under $n_b \rightarrow n'_b$. The loss function in the distance correlation training was defined as

$$L = L_{\text{main}} + \lambda \cdot \text{dCorr}^2(y, n_b) \quad (8.11)$$

extending L with a second term penalizing the training for such a correlation.

The dCorr replaces the adversarial neural network term in equation 8.8. The dCorr training had the advantage that the set of hyper-parameters was only extended by one (λ dCorr), and no second network was trained.

The distance correlation training showed slightly better separation than the adversarial training, and it was less susceptible to sample variations. Therefore it was chosen as the final discriminant for the analysis results. Additional studies trying to combine both scores show no improvement in either separation or invariance. As shown in Figure 8.10, both NNs show a very similar classification of events, and therefore further combinations were not helpful.

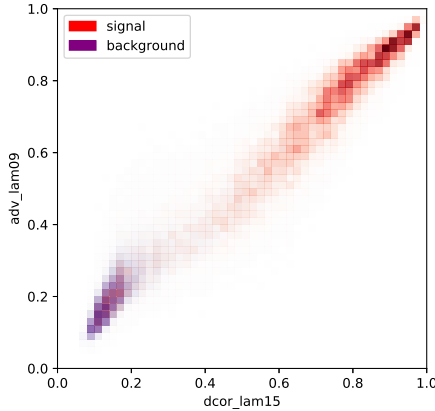


Figure 8.10.: Plot showing the event correlation between the adversarial and distance correlation neural network. Both featured a very similar classification of the events, suggesting that a combination would not yield to an improvement. Plot credits to Jan Kuechler.

Figure 8.11 shows the exclusion limits for the direct higgsino production with the dCorr results. It is seen that LSP masses between 200 GeV and 320 GeV are excluded

for the higgsino LSP. This results are already public in Ref. [26].

Even if the distance correlation setup showed slightly better results than the adversarial one, the studies were documented in our internal note. The ANN output was capable of maintaining a shape invariance with respect to the b -jet template. Only the lower n_{jet} region (4-jet) showed some problems, but besides it, the results were very promising. The second highest shape invariance in the ANN was seen in the sample with 7 jets with $\sim 6\%$. The dCorr output distribution maximum shape invariance was obtained from 4-jet sample with about 8%. Overall, ANN maintained a better shape invariance in the first 3 bins ($\sim 1\%$) than dCorr (max. $\sim 4\%$).

The ANN is a powerful tool capable of reaching sensitivity in difficult scenarios as the RPV higgsino. The ANN not only separates signals from the background but also performs an adversarial task. This interplay between the two setups can conditionalize the output distribution to optimize the desired results. Complex analyses can take advantage of this feature, for this reason, it is important to keep these studies for a future upgrade or models with similar characteristics.

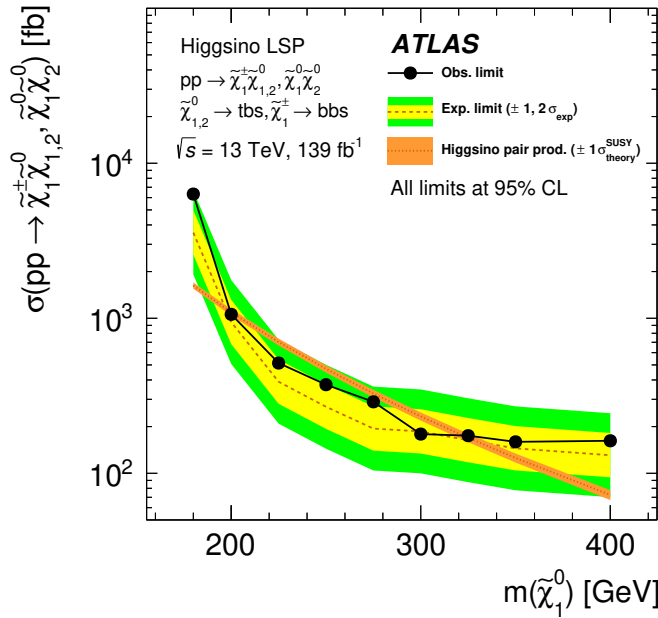


Figure 8.11.: Observed and expected upper limits for the RPV models with higgsino LSP hypotheses [26]. The yellow and green contours of the band around the expected limit are the $\pm 1\sigma$ and $\pm 2\sigma$ variations including all uncertainties. The theoretical prediction of the higgsino cross section is also shown in the red dotted line inside the orange band, with the colored band as the uncertainties on the prediction.

9. Search for Mono-Top Signatures in Compressed SUSY Scenarios

This chapter summarizes the SUSY mono-top feasibility studies results obtained in cooperation with Julius Ehrsam and Stephanie Steinmetz as part of their bachelor theses. It presents a completely new and unexplored SUSY signature with Julius' and Stephanie's remarkable optimization results. Although no analysis with ATLAS data has been published yet, these studies show a promising search strategy that is sensitive to this new signature.

A distinctive mono-top signature is present when the stop (\tilde{t}) and higgsinos (\tilde{h}) are almost mass degenerate $m_{\tilde{h}} \simeq m_{\tilde{t}}$. In this scenario, their decay products are too soft to be detected leading to a final state with a single top quark and missing transverse momentum (E_T^{miss}). The mono-top process is the SUSY counterpart of the $t\bar{t}H$ process, $t\tilde{t}\tilde{h}$, and it can have a measurable production rate due to the large top Yukawa coupling. Two different mono-top processes, namely the $pp \rightarrow t\tilde{\chi}_1^0\tilde{t}$ (TNT) and $pp \rightarrow t\tilde{g}\tilde{t}$ (TGT) are studied. In the TNT and TGT analyses, the search for the leptonic and hadronic final states are presented. Due to the mono-top signature, uncovered compressed regions in different SUSY grids are accessible as explained in the following.

9.1. Motivation

The higgsino-like LSP scenarios are favored by naturalness as discussed in Section 2.2.4. There are three higgsino states: two neutralinos ($\tilde{\chi}_2^0$, $\tilde{\chi}_1^0$) and a chargino ($\tilde{\chi}_1^\pm$). The SUSY mono-top signature is characterized by small mass-splittings among the higgsino states where they are almost mass degenerate $m_{\tilde{\chi}_1^0} \simeq m_{\tilde{\chi}_2^0} \simeq m_{\tilde{\chi}_1^\pm}$.

A very challenging region to target is the so-called *compressed region*, where the lighter stop \tilde{t}_1 is only slightly heavier than the lightest supersymmetric particle (LSP) $\tilde{\chi}_1^0$. This chapter presents the possibility of observing the stop-top-neutralino production process, $pp \rightarrow \tilde{t}_1^* t\tilde{\chi}_1^0$ ¹ (TNT), providing an additional handle for the compressed stop-higgsino region. This process is the supersymmetric counterpart of the $t\bar{t}H$ process and crucial to probe the interaction between stops and higgsinos.

¹ $\tilde{t}_1^* t\tilde{\chi}_1^0$ is considered as well.

The TNT signature has been studied in [238–240]. Because the \tilde{t}_1 is essentially invisible as its decay products are too soft to be detected, the process leads to a distinctive mono-top signature as shown in the left Feynman diagram of Figure 9.1. The production rate of this process for the TGT should be high enough due to the top Yukawa coupling Y_t . The QCD multijet background in the mono-top can be controlled by requiring an isolated lepton from the top-quark decay [238, 239] for the leptonic channel or by reconstructing a full hadronic top quark with a top tagger algorithm [241].

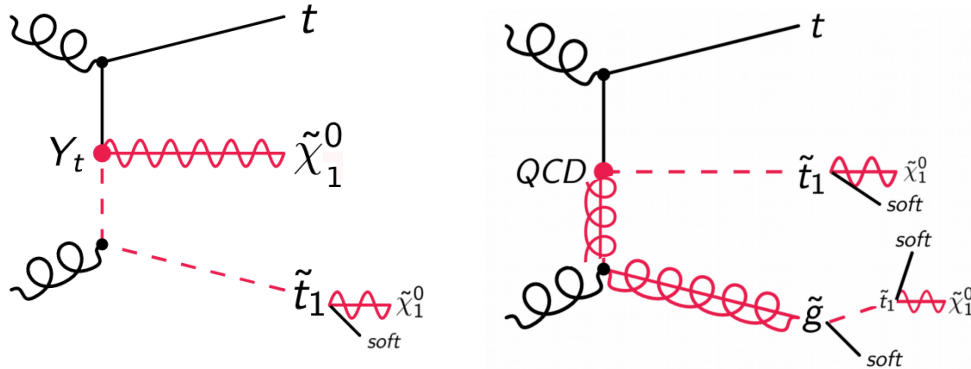


Figure 9.1.: Representative Feynman diagrams for the supersymmetric mono-top processes. The left diagram shows the $pp \rightarrow \tilde{t}_1 t\tilde{\chi}_1^0$ (TNT) where the $\Delta m(\tilde{t}_1, \tilde{\chi}_1^0)$ is very small. The right diagram represents a completely new SUSY signature $pp \rightarrow \tilde{t}_1 t\tilde{g}$ (TGT) with a compressed $\Delta m(\tilde{g}, \tilde{t}_1)$. The red dots denote the interactions Y_t for the stop-top-neutralino, and QCD for stop-top-gluino.

A completely new SUSY signature is presented defined by the $pp \rightarrow t\tilde{g}\tilde{t}$ (TGT) process seen on Figure 9.1 right. In this mono-top process instead of a neutralino, a gluino is produced together with a top quark and a stop. The study of TGT is highly motivated because it has a stronger QCD coupling and a higher cross-section due to the 8 degrees of freedom in the gluon.

9.1.1. Region to Target

The studies presented in the following assume the mass differences of $\Delta m(\tilde{t}_1, \tilde{\chi}_1^0) = 10$ GeV, and in the case of TGT $\Delta m(\tilde{g}, \tilde{t}_1) = 10$ GeV. These small mass differences between the SUSY particles offer the opportunity to reach unexplored regions in some existing SUSY analyses with phase space not excluded. The main target of the mono-top analysis is to reach the most compressed region which is possible due to the fully reconstructed top quark.

A previous search for a gluino pair production decaying into $\tilde{g} \rightarrow t\tilde{t}_1 \rightarrow t\tilde{\chi}_1^0 + \text{soft}$ was carried out by the ATLAS Collaboration [242]. Figure 9.2 shows the exclusion limits

of this search in terms of the stop and gluino masses. It is seen that the sensitivity of this search degrades towards the $m_{\tilde{g}} - m_{\tilde{t}_1} < m_t$ line. The TGT model is expected to be sensitive in the compressed region above the diagonal indicated with the gray dotted line, where the gluino cannot decay into top-stop anymore. The forbidden region in this plot is delimited by $m_{\tilde{g}} - m_{\tilde{t}_1} < m_t$, and the TGT is constructed by $m_{\tilde{g}} - m_{\tilde{t}_1} < 10$ GeV.

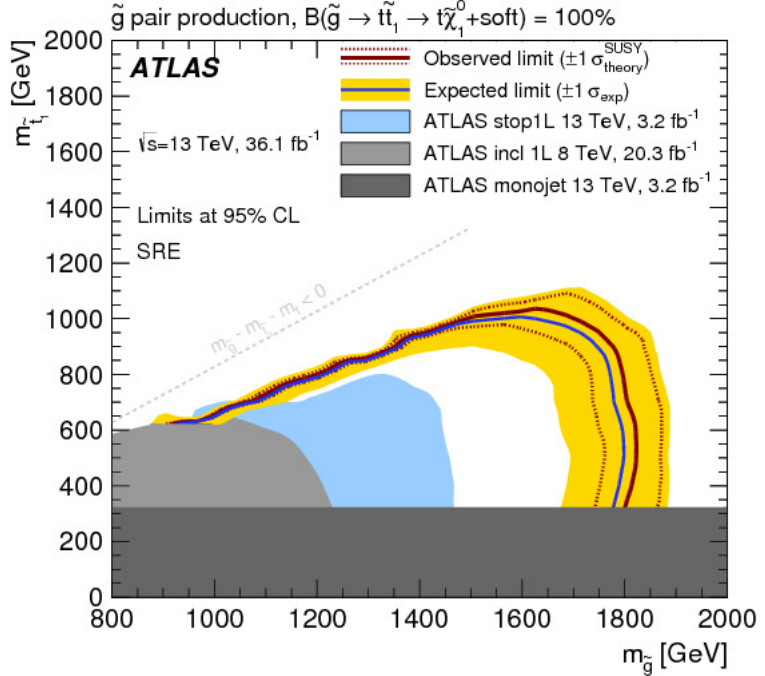


Figure 9.2.: Observed (red solid line) and expected (blue solid line) exclusion contours at 95% CL as a function of \tilde{g} and \tilde{t}_1 masses in the scenario where both gluinos decay via $\tilde{g} \rightarrow t\tilde{t}_1 \rightarrow t\tilde{\chi}_1^0 + \text{soft}$ and $\Delta m(\tilde{t}_1, \tilde{\chi}_1^0) = 5$ GeV [242]. Observed limits from previous searches with the ATLAS detector at $\sqrt{s} = 8$ and $\sqrt{s} = 13$ TeV are overlaid in gray and blue [243–245].

Another example in terms of the gluino and neutralino masses is seen in Figure 9.3 left. The $g \rightarrow t\bar{t}\tilde{\chi}_1^0$ (Gtt) exclusion limits are seen where a pair of gluinos decays promptly via off-shell top squarks to four top quarks and two lightest neutralinos. Exclusion limits from analyses with different jet and b -jet multiplicities are seen. The analysis with same-sign leptons (SS) in the final state is denoted with the blue curve. This analysis overpasses the dotted line delimiting the forbidden area given by $m_{\tilde{g}} - m_{\tilde{\chi}_1^0} < t\bar{t}$. To have a better picture of the range of the SS analysis, the exclusion limits are shown separately in Figure 9.3 right. Notably, the forbidden area limits of the SS analysis are given by $m_{\tilde{g}} - m_{\tilde{\chi}_1^0} < 2m_W$. The TGT analysis expects to have sensitivity in regions up to $m_{\tilde{g}} - m_{\tilde{\chi}_1^0} = 20$ GeV, being able to access this unexplored phase space.

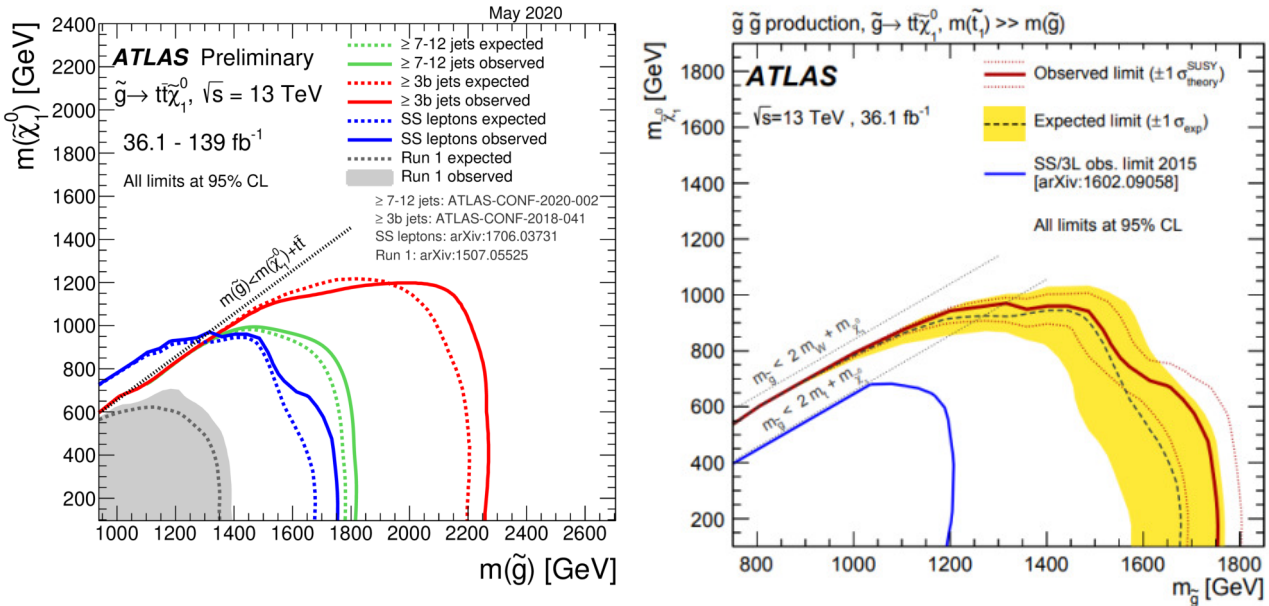


Figure 9.3.: Exclusion limits at 95% CL based on 13 TeV data in the \tilde{g} and $\tilde{\chi}_1^0$ mass plane for the Gtt simplified model where a pair of gluinos decays promptly via off-shell top squarks to four top quarks and two lightest neutralinos. All limits are computed at 95% CL. The diagonal lines indicate the kinematic limit for the decays. The left plot shows the full Gtt analyses combination [246]. The blue curve corresponds to the same-sign (SS) analysis and it passes the kinematic limit ($m_{\tilde{g}} < m_{\tilde{\chi}_1^0} + t\bar{t}$), the plot on the right shows the exclusions only for the SS analysis showing another kinematic limit ($m_{\tilde{g}} < 2m_W + m_{\tilde{\chi}_1^0}$) [247].

9.1.2. Mono-top Cross-sections

Phenomenological references [238–240] predict the cross section of $t\tilde{t}_1\tilde{\chi}_i^0$ as seen in the plot in Figure 9.4. The red curves show the Leading Order (LO) cross sections of the $t\tilde{t}_1\tilde{\chi}_i^0$ production ($i = 1$ and 2 are combined) at 8 (dashed), 13 (solid) and 14 TeV (dashed-dotted) LHC. The fixed parameters were $\Delta m_{\tilde{t}_1-\tilde{\chi}_1^0} = 10$ GeV, $m_{\tilde{\chi}_2^0} = m_{\tilde{\chi}_1^0} + 5$ GeV. The 13 TeV cross-section varies from 105 to 0.53 fb^{-1} as $m_{\tilde{t}_1}$ increases from 200 to 600 GeV.

The LO cross section of $t\tilde{t}_1\tilde{\chi}_i^0$ is compared with the Next-to-Leading Order (NLO) cross sections of the \tilde{t}_1 pair production (blue solid) [248, 249] and the Standard Model $t\bar{t}H$ production (black solid) [250] at the 13 TeV LHC. The NLO cross section of the \tilde{t}_1 pair production is ~ 700 times larger than the LO cross section of the $t\tilde{t}_1\tilde{\chi}_i^0$ production at $m_{\tilde{t}_1} = 200$ GeV. This ratio decreases for larger stop masses and becomes ~ 400 at $m_{\tilde{t}_1} = 600$ GeV. This is because for larger $m_{\tilde{t}_1}$ (and $m_{\tilde{\chi}_i^0}$), the relative importance of the top quark mass decreases and the price to produce an extra top quark diminishes. The $t\tilde{t}_1\tilde{\chi}_i^0$ production at lower stop masses has a comparable cross section with that of the

Standard Model $t\bar{t}H$ process.

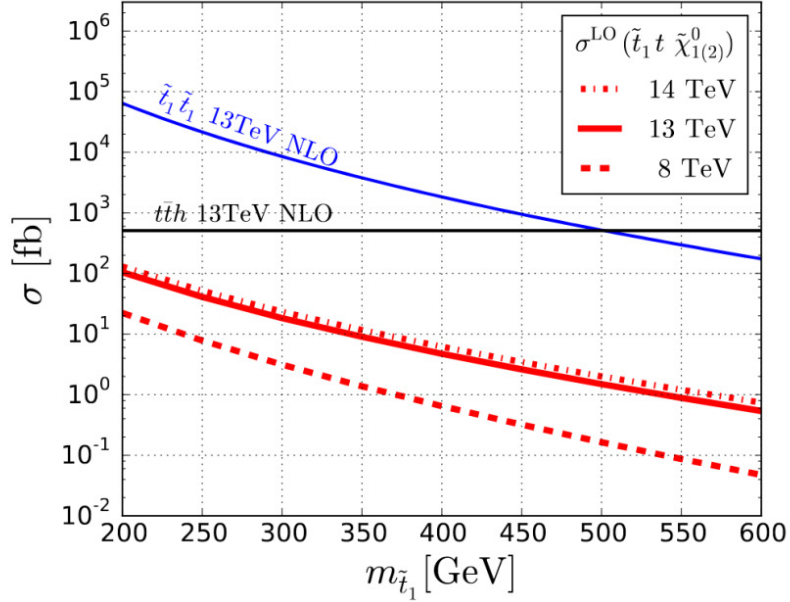


Figure 9.4.: LO cross-section of the supersymmetric equivalent to the $t\bar{t}H$ process ($pp \rightarrow \tilde{t}_1 t \tilde{\chi}_i^0$) in the pure higgsino limit at the 8 (red dashed), 13 (red solid) and 14 TeV (red dashed-dotted) LHC [239]. These LO are compared with the NLO cross-sections of the \tilde{t}_1 pair production (blue solid) [248, 249], and the Standard Model $t\bar{t}H$ production (black solid) [250] at the 13 TeV LHC.

Cross-section studies at LO were performed for the mono-top processes presented in this chapter. MadGraph 2.6.1 [251, 252] was used as an event generator to calculate the $t\tilde{t}_1\tilde{\chi}_1^0$ (TNT) and $t\tilde{t}_1\tilde{g}$ (TGT) cross-sections. Both charge conjugated top-stop process were taken into account, for example, $pp \rightarrow t\tilde{t}_1\tilde{g}$ and $pp \rightarrow t\tilde{t}_1^*\tilde{g}$, with $*$ denoting the anti-stop. Figure 9.5 shows the cross-section results where the blue, black and red curves are the same cross-sections previously shown in Figure 9.4, for $\tilde{t}_1\tilde{t}_1$, $t\bar{t}H$, and $t\tilde{t}_1\tilde{\chi}_i^0$, respectively.

The parameters used for TNT cross-section studies were $m_{\tilde{t}_1} - m_{\tilde{\chi}_1^0}$ (denoted in Figure 9.5 left as Δm), $\Delta m(\tilde{\chi}_2^0, \tilde{\chi}_1^0) = 5$ GeV, and $\Delta m(\tilde{\chi}_1^\pm, \tilde{\chi}_2^0) = 1$ GeV as in reference [239]. It is seen in Figure 9.5 left that MadGraph cross-sections reproduce the results previously shown in Figure 9.4. The calculated cross section in [239] is slightly higher (red curve), since the authors combined the cross-sections from $\tilde{t}_1\tilde{t}_1\tilde{\chi}_1^0$ and $\tilde{t}_1\tilde{t}_1\tilde{\chi}_2^0$.

The TGT is an entirely new SUSY process where the $\tilde{\chi}_1^0$ is substituted by a \tilde{g} . The SUSY particles involved in this new process were also expected to be almost mass degenerate, $m_{\tilde{g}} \simeq m_{\tilde{t}} \simeq m_{\tilde{\chi}_1^0}$, to keep the distinctive mono-top signature. In this way, a higher cross section is expected due the gluon's 8 degrees of freedom. MadGraph was again

used to estimate the TGT LO cross-sections. The results are shown in the right plot in Figure 9.5, where different values of $\Delta m = (\tilde{g}, \tilde{t}_1)$ were taken into account. It is nicely seen that, in fact, the TGT cross-section is in the order of 30 times higher than for TNT.

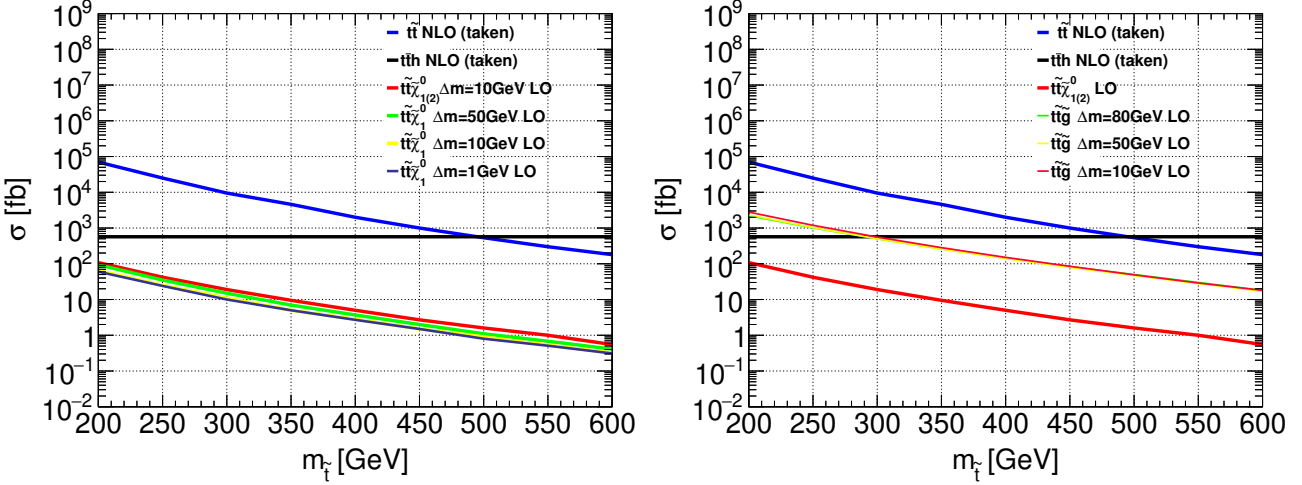


Figure 9.5.: Expected cross-sections produced with MadGraph in terms of the top-squark mass. The blue lines show the $t\bar{t}$ cross-section taken from [248, 249], and the black line the SM $t\bar{t}H$ cross-section [250]. The red lines show the combined $\tilde{t}_1 t\tilde{\chi}_1^{0,1}$ cross-section from reference [239]. The left plot shows the expected cross-sections for different $\Delta m = (\tilde{t}_1, \tilde{\chi}_1^0)$ in the TNT process, and the right plot the cross-sections for the TGT process for different $\Delta m(\tilde{g}, \tilde{t}_1)$. It is clearly visible that the TGT cross-section is in the order of 30 times higher than TNT.

9.2. Signal Regions Optimization

The mono-top signal samples were generated with MadGraph interfaced with Pythia 8 [101], while the background samples were the same as in Section 4.2.2 Table 4.2. Optimization studies were then performed to define a mono-top signal region. This section presents J. Ehrsam's and S. Steinmetz's results for the mono-top quark decaying into one lepton or hadrons.

As mentioned before, as the SUSY particles are almost mass degenerate, a distinctive mono-top signature is expected. The mono-top kinematics are represented for TGT in Figure 9.6. In the mono-top scenario, the masses of the \tilde{t}_1 and \tilde{g} are similar and not significantly larger than the mass of the $\tilde{\chi}_1^0$, such that additional SM objects produced during the SUSY decays are soft and invisible. Large E_T^{miss} is expected in the final state accounting for the two $\tilde{\chi}_1^0$'s. This E_T^{miss} will recoil against the fully reconstructed top

quark characterizing the kinematics of the process.

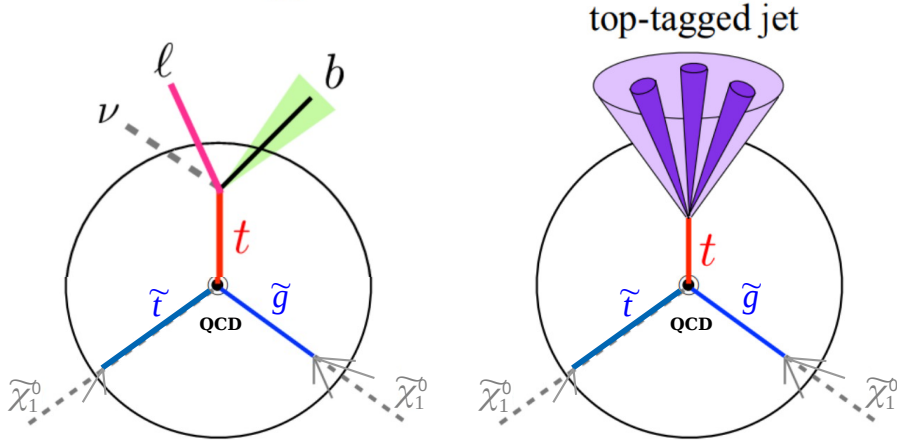


Figure 9.6.: Visualization of the kinematics of the TGT process decaying leptonically on the left plot, and hadronically on the right plot. The high E_T^{miss} expected in the right sketch from the SUSY decays will recoil against a fully reconstructed top quark.

The expected significance (Z) is a measure that quantifies how sensitive the analysis is to a potential discovery. There are different approaches to estimate it and in the SUSY mono-top analysis, Z was calculated using RooStats, a package with statistical tools built on top of RooFit [253] and distributed in ROOT [254]. The leptonic final state used a function named Binomial significance [255, 256], while the hadronic final state the Asimov significance [255, 257]. To calculate Z , the number of signal event yields, background event yields, and a relative error including the statistical uncertainty of the background and a systematic uncertainty were used. For the leptonic channel the relative background uncertainty was taken to be 25% and 30% for the hadronic channel.

The benchmark signal point of TGT was $m(\tilde{g}, \tilde{t}_1) = (600, 590)$ GeV. For TNT in the leptonic channel was $m(\tilde{t}_1, \tilde{\chi}_1^0) = (100, 90)$ GeV, and in the hadronic one was $m(\tilde{t}_1, \tilde{\chi}_1^0) = (300, 290)$ GeV.

9.2.1. Leptonic Final State

Julius [258] optimized the SUSY mono-top leptonic final state for TNT and TGT scaling his results to 140 fb^{-1} . The preselection of events possibly containing a leptonically decaying monotop signal has been directly designed from the expected final-state particle content. As such, the presence of exactly one lepton (e or μ) candidate with a $p_T > 30$ GeV was required, and one b -jet with a $p_T > 30$ GeV selected. The E_T^{miss} trigger was

used where for all samples the trigger was fully efficient above 230 GeV.

After these basic requirements a number of additional selection steps were implemented to increase the sensitivity. Different kinematic variables were defined to separate the SM background from the SUSY mono-top signal, explained in more detail in appendix E. After the preselection, the remaining larger background was $W+jets$. To reduce it, m_T was selected above the W boson mass, and the invariant mass of the lepton and the b -jet (m_{bl}) was required to be less than the top quark mass < 170 GeV. This in order to reduce the number of background events in which the identified lepton and b -jet do not originate from a single top quark. After this selection, the main background was dileptonic $t\bar{t}$ with one miss-reconstructed lepton.

The asymmetric stransverse mass am_{T2} [259–262] is a kinematic variable targeting dileptonic $t\bar{t}$ events with a missing lepton. It has a boundary at the top quark mass for the SM background, while the SUSY signals can exceed this limit. This variable was used for the TNT and TGT optimization studies, with a selection higher than the top mass (> 180 GeV). Small distances in terms of the ΔR variable between the highest b -jet p_T and the lepton were expected, because they are assumed to originate from the decay of the same top quark.

A high E_T^{miss} cut was imposed to account for the two $\tilde{\chi}_1^0$'s. The mono-top signal was expected in values of $\Delta\phi(E_T^{\text{miss}}, l)$ closer to π because the lepton was a decay product of the top quark while the E_T^{miss} originates from the SUSY decays, recoiling at each other as shown in Figure 9.6. The negative vectorial sum of the p_T of all jets, H_T was only useful in the TNT optimization.

The optimal selection for TNT and TGT is seen in Table 9.1. The main background was dileptonic $t\bar{t}$ with a contribution higher than 90%. The significances calculated with the Binomial function function are shown. Two plots showing the am_{T2} distribution with the optimal selection except the am_{T2} cut are seen in Figure 9.7.

9.2.2. Hadronic Final State

The mono-top hadronic final state was optimized by Stephanie [263]. These studies were performed a year and a half later than the leptonic ones, for this reason new variables were introduced. The optimization for TNT was performed for higher mass points than in the leptonic channel. The TNT and TGT results were scaled to 139 fb^{-1} . As a preselection, a E_T^{miss} trigger, events with high E_T^{miss} value (> 300) GeV, and no leptons were selected. After the preselection, the main backgrounds were $t\bar{t}$ and $W+jets$.

The reconstruction of the hadronic top quark was not an easy task in the hadronic channel. A top tagger algorithm (TopTag) was introduced [241, 264] that reconstructed high- p_T “fat-jets” (or large radius jets) as a hadronic top quark, depicted in Figure 9.6.

Table 9.1.: Summary of the event selections defining the optimal results for TNT and TGT with one lepton in the final state. The yields for the total SM background and the mono-top signal are shown with statistical uncertainties. The significance was calculated with the Binomial significance function.

Variable	TNT	TGT
Preselection		
E_T^{miss} [GeV]	> 270	> 380
1st b -jet p_T [GeV]	> 220	> 170
m_T [GeV]	> 200	> 300
m_{bl} [GeV]	< 170	
am_{T2} [GeV]	> 180	
$\Delta R(b, l)$	< 1.2	
$\Delta\phi(E_T^{\text{miss}}, l)$	> 2.2	> 2.6
H_T [GeV]	< 350	–
Yields		
Total SM	17.70 ± 2.39	7.65 ± 0.81
$m(\tilde{t}_1, \tilde{\chi}_1^0) = (100, 90)$ GeV	31.76 ± 7.23	–
$m(\tilde{g}, \tilde{t}_1) = (600, 590)$ GeV	–	4.78 ± 0.46
Significance Z	3.38	1.04

A description of the algorithm is found in the appendix E.

The m_T variable definition was different from the one described in Section 6.3.1. It used E_T^{miss} and the first jet p_T (1st jet), see appendix E. This variable utilized the signal kinematics assuming that the highest jet- p_T came from the hadronic top quark, and the high E_T^{miss} from the SUSY decays. The min $\Delta\phi(E_T^{\text{miss}}, j)$ followed the same principle. To reflect the topology of signal events, the reconstructed top quark must be well separated from the E_T^{miss} with a high difference in the azimuthal angle.

After the optimal selection, the main backgrounds still were $t\bar{t}$ and $W+\text{jets}$. The optimal selections for the hadronic channel of TGT and TNT are listed in Table 9.2. The total SM background and signal yields are also shown. The significance was calculated using the Asimov significance function with a 30% of uncertainty. Figure 9.8 shows the distribution with the optimal selection applied except for min $\Delta\phi(E_T^{\text{miss}}, j)$.

Preliminary studies were performed to optimize higher mass points with larger Δm (30 and 50 GeV). The same cuts were selected as in Table 9.2 except for min $\Delta\phi(E_T^{\text{miss}}, j)$.

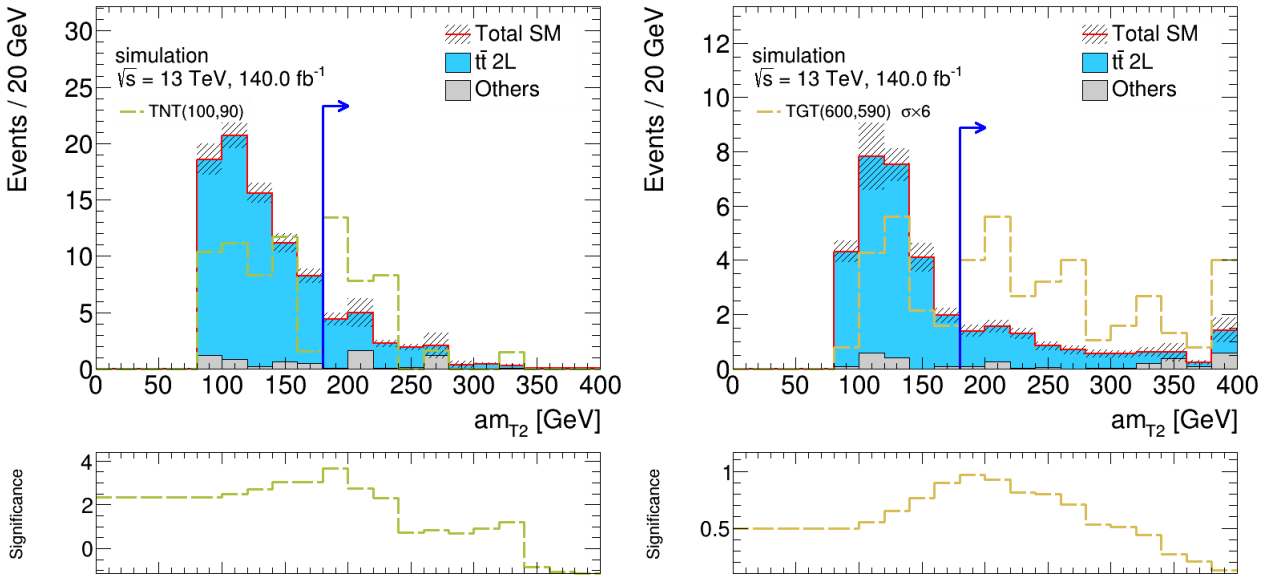


Figure 9.7.: Plots defining the optimal mono-top selection in the leptonic channel applying the Table 9.1 cuts except the am_{T2} . The bottom plot shows the significance calculated in each bin following the Binomial significance function. The left plot shows the distribution for the TNT process, while the right one for TGT. The TGT signal is scaled up by six so the shape is visible. Only the statistical uncertainty is displayed. The last bin includes the overflow. The arrow indicates the selection boundary and points towards the region of accepted events. The minor background processes are merged into the “Others” category. The plots are taken from Julius Ehrsam thesis [258].

For higher Δm , the decays of the SUSY particles are not as invisible anymore shifting the distribution of $\min \Delta\phi(E_T^{\text{miss}}, j)$ to smaller angles.

9.3. Conclusions

In this chapter, two different supersymmetric mono-top signatures have been studied. The first one, the $t\tilde{t}_1\tilde{\chi}_1^0$ (TNT), has already been presented in [238–240]. The TNT LO cross-sections were calculated with different $\Delta m(\tilde{t}_1, \tilde{\chi}_1^0)$. The results reproduced the cross-section in [239] and checked that the TNT cross-section is in the order of 10^2 times lower than the direct stop pair production. For this reason, a completely new SUSY process was introduced, the $t\tilde{t}_1\tilde{g}$ (TGT). It was motivated to have a higher cross-section due to the gluon 8 degrees of freedom. Its cross-section was also calculated, and seen that the TGT cross-section was in the order of 30 times higher than TNT.

The SUSY mono-top may access unexplored regions because it has almost mass de-

generate SUSY particles and a fully reconstructed top quark. Julius and Stephanie optimized the TNT and TGT processes in their bachelor theses. The studies were separated in leptonic and hadronic channels. Sensitivity was achieved in both channels for the TNT and TGT scenarios.

Table 9.2.: Summary of the event selections defining the optimal results for TNT and TGT with a hadronic top quark. The yields for the total SM background and the mono-top signal are shown with statistical uncertainties. The significance was calculated with the Asimov significance function.

Variable	TNT	TGT
Preselection		
E_T^{miss} [GeV]	> 550	> 600
TopTag	$= 1$	
m_T (1st jet) [GeV]	> 1100	> 1150
$\min \Delta\phi(E_T^{\text{miss}}, j)$	> 1.5	> 0.9
Yields		
Total SM	5.60 ± 1.05	6.27 ± 0.98
$m(\tilde{t}_1, \tilde{\chi}_1^0) = (300, 290)$ GeV	4.31 ± 0.76	–
$m(\tilde{g}, \tilde{t}_1) = (600, 590)$ GeV	–	6.48 ± 0.53
Significance Z	1.62	2.25

The leptonic channel reached sensitivity for TNT of 3.38 with $\Delta m(\tilde{t}_1, \tilde{\chi}_1^0) = (100, 90)$ GeV mass point. This signal point has already been excluded by several analyses. Nevertheless, these are preliminary results to be followed up in future studies. It seemed that more complex variables are needed because the sensitivity on higher mass points dropped dramatically. The TGT scenario with a lepton in the final state reached a sensitivity of 1.04 with $\Delta m(\tilde{g}, \tilde{t}_1) = (600, 590)$ GeV.

In the hadronic channel, the TopTag was introduced. It was a top tagging algorithm that reconstructed hadronically decaying top quarks from “fat jets” and high jet p_T . The achieved sensitivity for TGT with $\Delta m(\tilde{g}, \tilde{t}_1) = (600, 590)$ GeV was high enough with a value of 2.25. TNT was optimized with higher mass points than in the leptonic channel. The mass point used as a benchmark point was $\Delta m(\tilde{t}_1, \tilde{\chi}_1^0) = (300, 290)$ GeV. The reached sensitivity was 1.62.

It was nicely shown that sensitivity can be reached for TNT and the newly introduced TGT, even at a preliminary stage. These results leave a good motivation and starting point for future studies. The SUSY mono-top is a powerful model capable of reaching

unexplored compressed SUSY regions. Usually, they are difficult to access due to the mass degeneracy of the SUSY particles. These results show that the SUSY mono-top signature provides a powerful benchmark model for designing a new search strategy. With the monotop analyses shown, the diagonal in Figure 9.3 right ($m_{\tilde{g}} < 2m_W + m_{\tilde{\chi}_1^0}$) can be surpassed and that unexplored phase space could be reached.

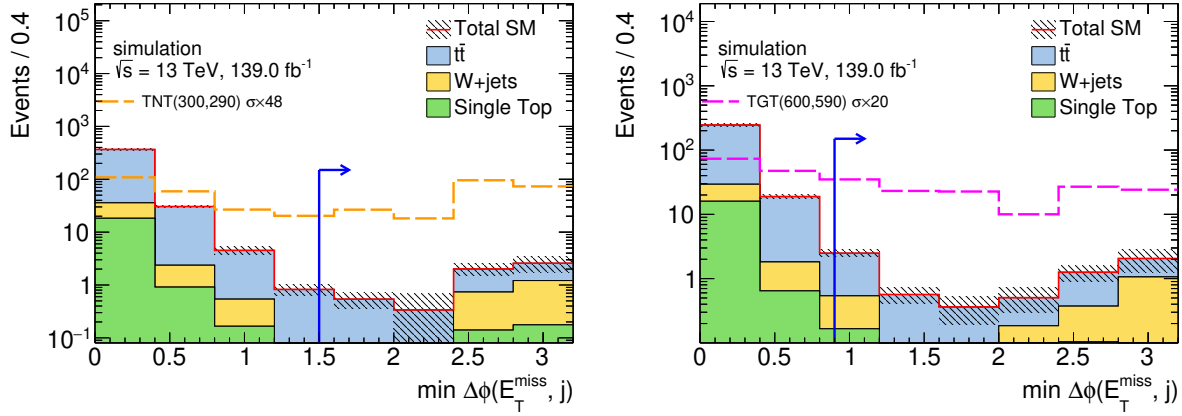


Figure 9.8.: Plots for defining the optimal mono-top selection in the hadronic channel applying the selection from Table 9.2 except the $\min \Delta\phi(E_T^{\text{miss}}, j)$. The distribution for the TNT and TGT processes are shown in the left and right plots, respectively. The signals are scaled to show the shape of the events. Only statistical uncertainty is displayed. The last bin includes the overflow. The arrow indicates the value and points to the direction of the selection criteria. The minor background processes are merged into the “Others” category.

10. Discussion

In Chapter 7 and 8, the results of the RPC stops and RPV higgsinos are presented. In the following, the results are evaluated in terms of the exclusion limits. The RPC stops results are compared with the results from a search performed by the CMS collaboration. The RPV results are then compared to the last electroweakino limit defined by LEP.

The simplified model used in the RPC stops analysis for the small $\Delta m(\tilde{t}_1, \tilde{\chi}_1^0)$ presented in Chapter 7 is also used in the CMS stop searches. The latest results of searches for the stop four-body signature from CMS is based on the partial Run-2 data collected in 2015–2016, which corresponds to an integrated luminosity of 35.9 fb^{-1} [265]. Two different approaches were used in the CMS analysis. The first one was a cut-and-count analysis (CC) using a signal selection based on applying requirements on several discriminating variables as in Section 7.2. The second approach used a multivariate analysis (MVA) followed by a counting experiment approach in the signal selection. The MVA approach exploited the correlations between discriminating variables for different $\Delta m(\tilde{t}_1, \tilde{\chi}_1^0)$ kinematic regions, improving the sensitivity of the CC approach. Both approaches were based on a nearly identical preselection.

Figure 10.1 shows the expected and observed exclusion limits at 95% confidence level from the CMS analysis. The results obtained from the one-lepton analysis with the CC approach are shown on the left, and the MVA results in the plot on the right. The CC search reached its highest mass exclusion of 500 GeV for $\Delta m \sim 30 \text{ GeV}$, for the MVA search the maximum sensitivity was reached for the highest Δm of 80 GeV excluding top squark masses up to 560 GeV. Comparing the limit with the one presented in Section 7.5 (up to 640 GeV), it is concluded that the most stringent limit is derived by the analysis in this dissertation. Nevertheless, upcoming results should be expected soon with the full Run 2 dataset for the CMS 4-body model. From the CMS direct stop pair production exclusion limits with one lepton in the final state in [266] with 137 fb^{-1} , the authors did not present the four-body region and their results are only shown for other decay modes. The same could be expected for the four-body model.

In Section 6.3.5, it was mentioned that no higgsino results were achieved for the previous SUSY RPV paper publication [214]. This is why reaching higgsino sensitivity was one of the main goals in this iteration [26] and explained in Chapter 8. Searches for pair-production of SUSY particles under the assumption of non-conservation of R -parity with a dominant $\bar{u}u\bar{d}\bar{d}$ term were performed using the data collected at LEP in e^+e^- collisions at center-of-mass energies from 192 up to 208 GeV [167–169]. The last paper published dates back to 2004 [167] and its authors performed an analysis looking for direct decays

of neutralinos and charginos separately, assuming their gaugino component only. They first defined a hadronic preselection and then the analysis was based on neural network techniques since the optimization of the signal selection was performed on variables which were extensively correlated. Their neural network performed trainings in a standard manner with one hidden layer on simulated signal and background events. Their main kinematic variables were based on reconstructing different jet masses. The RPV higgsinos result presented in Chapter 8 are the first limits on electroweakino production with RPV decay to quarks since LEP [26].

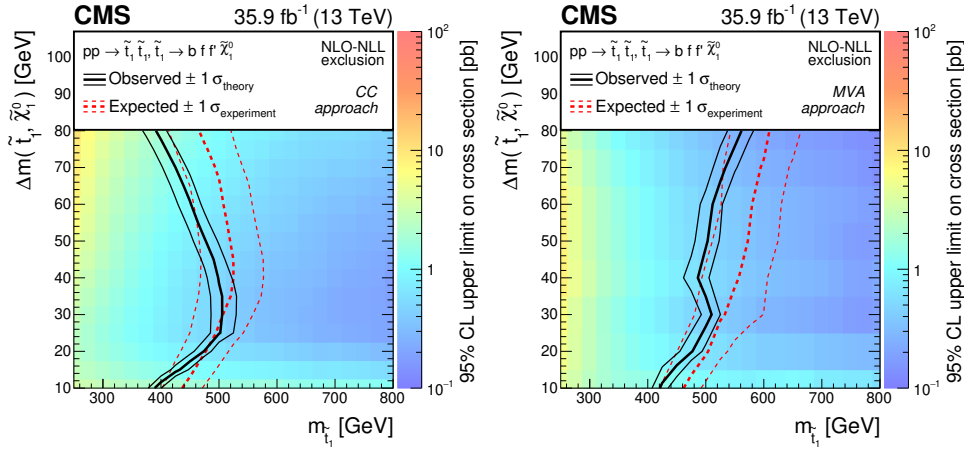


Figure 10.1.: Latest observed and expected exclusion limits for the simplified model with the stop four-body decay from the CMS collaboration [265]. The plots are as a function of $m_{\tilde{t}_1}$ and Δm . The plot on the left shows the exclusion limit using a multivariate analysis (MVA). On the right a cut-and-count analysis was used. The color shading corresponds to the observed limit on the cross section. The solid black (dashed red) lines represent the observed (expected) limits, derived using the expected top squark pair production cross section. The thick lines represent the central values and the thin lines the variations due to the theoretical or experimental uncertainties.

11. Conclusion

This dissertation presented models searching for Supersymmetry using data collected with the ATLAS detector at the LHC, using pp collisions at a center-of-mass energy of $\sqrt{s} = 13$ TeV. Two searches were described, one for direct stop production and another with direct higgsino production with an isolated electron or muon in the final state using the full Run 2 dataset with 139 fb^{-1} .

The first search assumes R -parity conservation (RPC) and thus a stable lightest supersymmetric particle (LSP) taken to be the lightest neutralino $\tilde{\chi}_1^0$. The model presented a direct stop pair production where the mass difference of the stop and the LSP is smaller than the W boson mass plus the mass of the b quark. In this compressed scenario, each stop decayed via a 4-body process to a b quark, an electron or muon, two different fermions, and a LSP. The signature of the four-body stops was characterized by a low p_T electron or muon, low p_T b -jets, and large E_T^{miss} from the two LSPs. The signal region was defined using discriminating variables such as $p_T^\ell/E_T^{\text{miss}}$, number of b -tagged jets, and $\Delta\phi(p_T^{b\text{-jet}}, E_T^{\text{miss}})$. The SM background prediction was estimated by normalizing the main background processes ($t\bar{t}$ and $W+\text{jets}$) in CRs. Since no significant excess in data over the SM prediction was found, exclusion limits at 95% confidence level for the targeted simplified model were determined by a shape-fit approach in $p_T^\ell/E_T^{\text{miss}}$ and $\Delta\phi(p_T^{b\text{-jet}}, E_T^{\text{miss}})$ variables. For the shape-fit configuration, six disjoint signal regions in the interval of $p_T^\ell/E_T^{\text{miss}}$ from 0 to 0.1 and $\Delta\phi(p_T^{b\text{-jet}}, E_T^{\text{miss}})$ from 0 to 1.5 were included. By exploiting the different shapes of the signal and background distribution in the shape-fit, the background was further constrained resulting in a better exclusion sensitivity. For a $\Delta m(\tilde{t}_1, \tilde{\chi}_1^0) = 50$ GeV, the stop mass was excluded up to 640 GeV. This result optimized the previous paper findings by 240 GeV [189].

The second analysis searched for direct higgsino production in a R -parity violating scenario characterized by one isolated electron or muon, and many jets and b -jets in the final state. Getting sensitivity to the higgsino signal was extremely challenging due to its lower mass-scale and cross-section. For this reason, an adversarial neural network (ANN) was tested and presented in this thesis trying to separate the SM background from the higgsino signal. Data-based techniques were used to estimate the dominant $t\bar{t}$ background production plus the invariance. Although another NN (dCorr) performed slightly better than the ANN, the ANN results were documented as it showed to be a powerful discriminating algorithm. Using the dCorr method, the direct higgsino production from 200 GeV up to 320 GeV at 95% confidence level. The results on the higgsino production model improved the limits on RPV decays from LEP [167–169].

Unfortunately, no sign of SUSY has been found in the searches. The full Run 2 dataset is still under investigation and new exciting results are yet to come. In this thesis, only a small fraction of the total expected delivered data by the LHC has been analyzed. A third data-taking period for proton-proton collisions at the LHC is currently in preparation, which will presumably start in 2022 and deliver about 350 fb^{-1} of data [267, 268]. The High Luminosity Large Hadron Collider (HL-LHC) [267] is an upgrade that already started in 2018 and is expected to boost the accelerator’s potential for a new physics discovery starting at 2027. With the HL-LHC upgrade, about 3000 fb^{-1} of data are planned to be collected during the total lifetime of the LHC [268, 269]. For these reasons, searches for phenomena beyond the Standard Model are still very exciting. With the incredible amount of data lying ahead, the opportunity for exotic and advanced analysis strategies are open, such as shape fit analyses and machine learning algorithms. The increased data statistics together with improved analysis techniques will allow to extend the reach of our searches considerably, hopefully revealing an exciting result in the near future.

Acknowledgments

It is funny just writing this part because so many people have been involved in this crazy process, so here it goes. To start, thanks to Dorothee, who was not only the Chair of our department, but my interest in particle physics arise from attending her lecture. I always felt very welcomed and involved in our group. Thanks to my first supervisor Jeannine, who guided me so well and close during my Master's and the first part of my PhD. To Alexander, thank you so so much for everything. He was an excellent and supportive supervisor who got fully involved in the projects I was in. He did not only view for my professional status, but also for my well-being. As a foreigner with a scholarship, I represented so much extra work for Alex (paperwork, reports, visa, ...), but he never hesitated on helping me. I have learned so much from him, and I could not finish expressing all my gratitude towards him. Thanks to Clara, Michi Holzbock (Holzie), and David for all the years sharing an office and the great times. Thanks to Holzie for everything! Even though he was no longer part of our Chair, he helped me correcting my thesis. Big big thanks to David. He was the person that I bothered the most with any issue, and he was always so patient with all the questions/problems I had. And to all of our Chair in general: Jeanette, Sascha, Dani, Adam Samara, Balthi, Thomas, Michi A, Ana, Christoph, Kyong, Daniel, Bernhard, Andrea, Eric, and Ferdinando, I take with me the best memories with you in our summer and Christmas parties, DPGs, congresses, ping pong games, barbecues, Wiesn, biergartens, or simply going to Mensa. Special thanks to Nikolai and Philipp for checking some chapters of my thesis too. And, of course, to our hardware group. I had the great opportunity to work with them as a HiWi and then as part of my PhD. Thanks to big and small Ralph, both Maxes, Otmar, and Christoph, for the amazing time, I learned so much from you.

I spent most and the of my PhD working with the Stop1L team. Thank you to Keisuke, Michaela, Christoph, Frederik, and Sara for guiding our results to a publication. In particular to Keisuke. I had the opportunity to met him several times and he was (and is) a great support with all of his knowledge and experience. He was always aware on keeping our group together. Thank you deeply for the advice and chats regarding my future career. And to my colleagues/friends Laura, Yosse, and Prim, I always found support in you and you made things more fun. It was amazing meeting at the congresses and be able to spend some quality time. Special thanks to Tomohiro (big big ones). Not long ago, I commented with Prim that I should dedicate a whole paragraph to him. Tomohiro is that kind of person who always has a solution for any problem. Even when he moved to the U.S., I kept bothering him. He was my savior repeatedly times, and he always found the time to help me. Thank you, Tomohiro. To close, at the end of my PhD I worked with the RPV1L group. It was an amazing experience in which

I learned so much in just a few months. Thanks to Javier for welcoming me and being so patient when I started. He always encouraged me to present our work even when I was new. I really appreciate all the support.

And last but not least, to my Pato, who has always supported me, and I know he will keep on doing it for the rest of our lives. I cannot wait to start this journey with him. Y para terminar, a mi familia. Mi papá Manolo que siempre se preocupó por darmelo todo, y nunca ha dejado de apoyarme y presumirme. Mi mamá Ale, que aunque yo se que le pesa que estemos lejos, hablamos seguido y me hace sentir más cerca de casa. Y a mis hermanos Manolito y Gerar, que son las personas que mas quiero y extraño. No sé dónde estaría sin ustedes. Me han apoyado ciegamente desde el día uno en esta decisión tan loca de irme al otro lado del mundo. Les debo todo y espero hacerlos orgullosos.

Appendices

A. bffN b -tag High Negative Event Weights in WCR Selection

High negative event weights were found in the WCR selection which affected the data/MC agreement. Figure A.1 shows the distributions with the high event weights included. The WCR and WVR selections differ only by a cut on the $\min \Delta\phi(p_T^{b\text{-jet}}, E_T^{\text{miss}})$ variable, where WCR: $2.5 < \min \Delta\phi(p_T^{b\text{-jet}}, E_T^{\text{miss}})$ and WVR: $\min \Delta\phi(p_T^{b\text{-jet}}, E_T^{\text{miss}}) \in [1.5, 2.5]$. For this reason the events with negative weights were not visible on the WVR. The complete distribution of the $\min \Delta\phi(p_T^{b\text{-jet}}, E_T^{\text{miss}})$ variable is shown in Figure A.2, where in the higher bins (> 2.5) where the WCR is defined, the data/MC agreement gets worse.

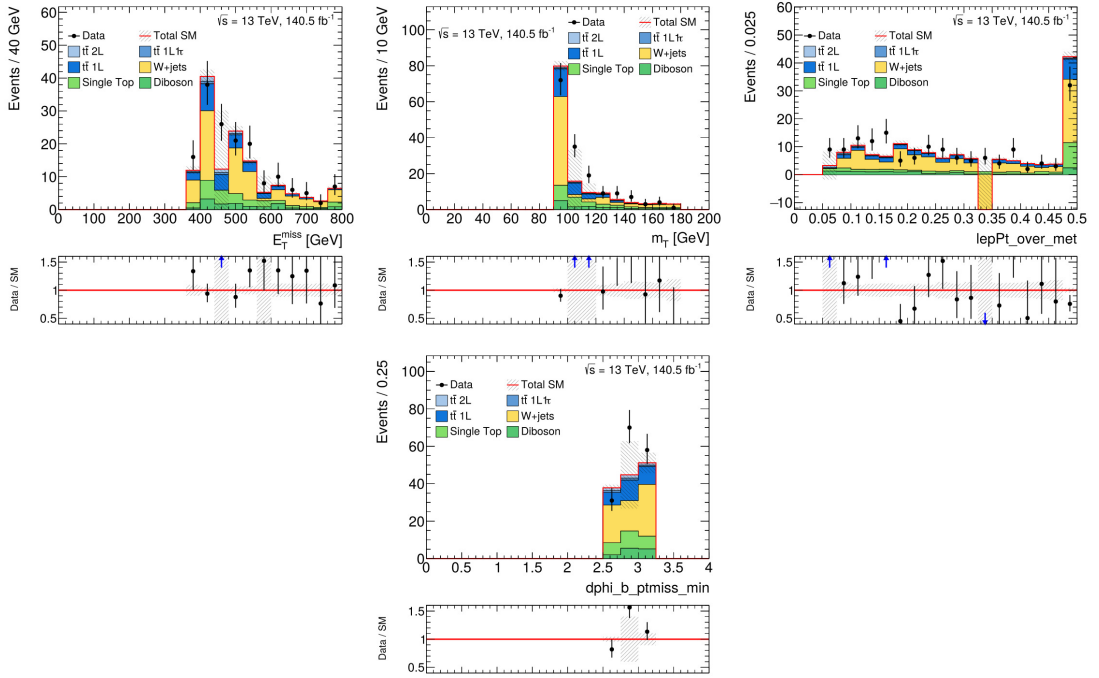


Figure A.1.: Distribution of the WCR discriminating variables before removing the highly negative events weights.

After applying a scan over the generator-weighted events using the WCR selection, two high negative event weights were found in $W+jets$ (Sherpa) samples. One with a weight of -204 and the other with -60. The recommendation in the Twiki page from the Physics Modelling Group for V+jets [221] for treating pathological high-weight events in Sherpa samples, says that these weights can be set to 1. The explanation is that

these events correspond to a phase space with differential cross sections larger than the maximal weight estimated during the optimization phase. In order to follow this they need to be just a few of them and cause spikes in the distributions. As we only have 2 and they do cause disagreement between data and MC, we set the weight to 1 of these two events. Figure A.3 shows the $\min \Delta\phi(p_T^{b\text{-jet}}, E_T^{\text{miss}})$ distribution, in the middle setting the highest-weight to 1 and in the right setting the highest and the second highest event weights to 1. Note that the agreement between data/MC is highly improved and all of the discriminating variables distribution now look reasonable as shown in Figure 7.13.

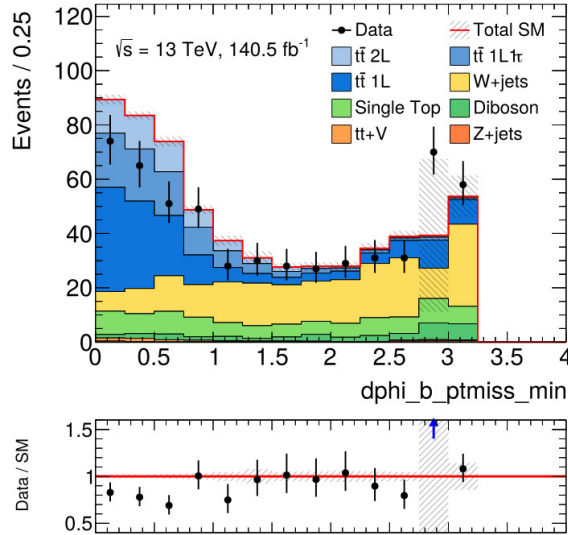


Figure A.2.: Complete distribution of the $\min \Delta\phi(p_T^{b\text{-jet}}, E_T^{\text{miss}})$ variable with the WCR selection applied except for the $\min \Delta\phi(p_T^{b\text{-jet}}, E_T^{\text{miss}})$ selection.

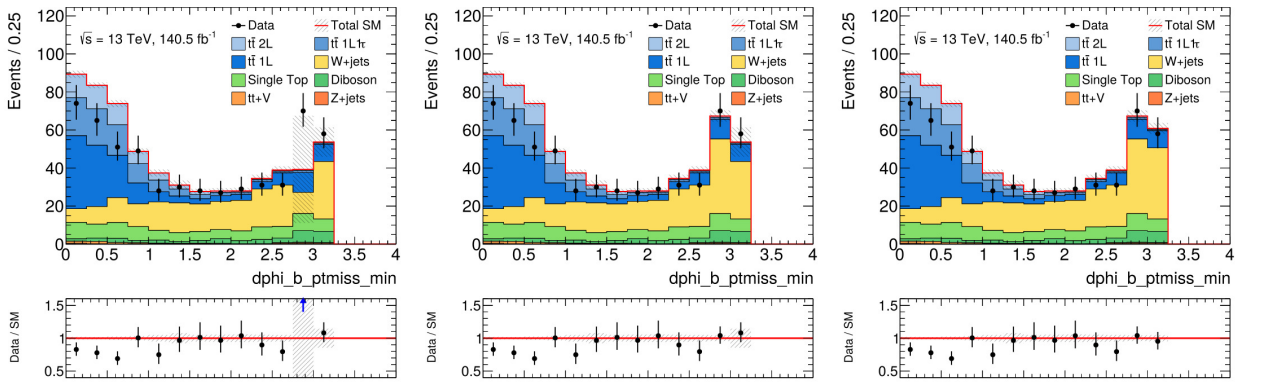


Figure A.3.: Complete distribution of the $\min \Delta\phi(p_T^{b\text{-jet}}, E_T^{\text{miss}})$ variable with the WCR selection applied except for the variable shown. On the left the distribution including the negative weighted events, in the middle without the highest negative event weight and in the right without the highest and the second highest negative weights.

B. Additional plots for the theoretical systematic uncertainties

B.1. Signal

Table B.1 summarizes the theoretical systematic uncertainties from the signal model with $m(\tilde{t}_1, \tilde{\chi}_1^0) = (450, 400)$ GeV explained in more detail on Chapter 7. They are measured in the `bfN_btag` discovery (bfN) and exclusion (bfN1, bfN2 ...) regions. Figure B.1 shows the comparison of the event yields in the `bfN_btag` signal region and the bins used in the shape-fit analysis, between the nominal and the variations.

Table B.1.: Summary of the theoretical systematic uncertainties for the signal samples in the in `bfN_btag` discovery and exclusion regions.

	Preselection	bfN	bfN1	bfN2	bfN3	bfN4	bfN5	bfN6
PartonShower Up	10.53 ± 0.09	5.45 ± 0.2	7.12 ± 0.36	8.33 ± 0.55	20.93 ± 2.25	-1.15 ± 0.1	7.47 ± 0.73	-1.57 ± 0.22
PartonShower Down	-8.29 ± 0.07	-9.21 ± 0.33	-11.9 ± 0.61	-5.44 ± 0.35	-10.26 ± 1.13	-8.74 ± 0.74	1.65 ± 0.16	-2.88 ± 0.38
Merging scale Up	1.77 ± 0.01	-2.6 ± 0.09	-0.38 ± 0.02	-9.04 ± 0.61	8.86 ± 0.96	-7.0 ± 0.61	-2.81 ± 0.28	-10.49 ± 1.46
Merging scale Down	4.49 ± 0.04	2.69 ± 0.09	2.45 ± 0.12	3.7 ± 0.24	7.46 ± 0.8	2.64 ± 0.22	-0.1 ± 0.01	15.34 ± 1.97
Fact./ ren. Up	3.55 ± 0.03	6.18 ± 0.22	2.95 ± 0.15	10.73 ± 0.7	-9.34 ± 1.07	10.41 ± 0.87	6.87 ± 0.67	6.18 ± 0.83
Fact./ ren. Down	-2.73 ± 0.02	-0.1 ± 0.0	-2.6 ± 0.13	-5.49 ± 0.36	3.25 ± 0.35	16.48 ± 1.32	2.02 ± 0.19	3.98 ± 0.52

B.2. $t\bar{t}$

On Section 6.3.3 the calculation of the $t\bar{t}$ theoretical systematic uncertainties in `bfN_btag` was described.

Table B.2 summarizes the $t\bar{t}$ theoretical systematic uncertainties measured in `bfN_btag` discovery and exclusion regions and in the control and validation regions. Figure B.2 shows the comparison of the event yields in the `bfN_btag` signal region as well as the bins used in the shape-fit analysis, between the nominal $t\bar{t}$ sample and the events from alternative $t\bar{t}$ samples. This determines the systematics due to initial state radiation, hard scatter effects and hadronization and fragmentation scale variation in all of the defined regions.

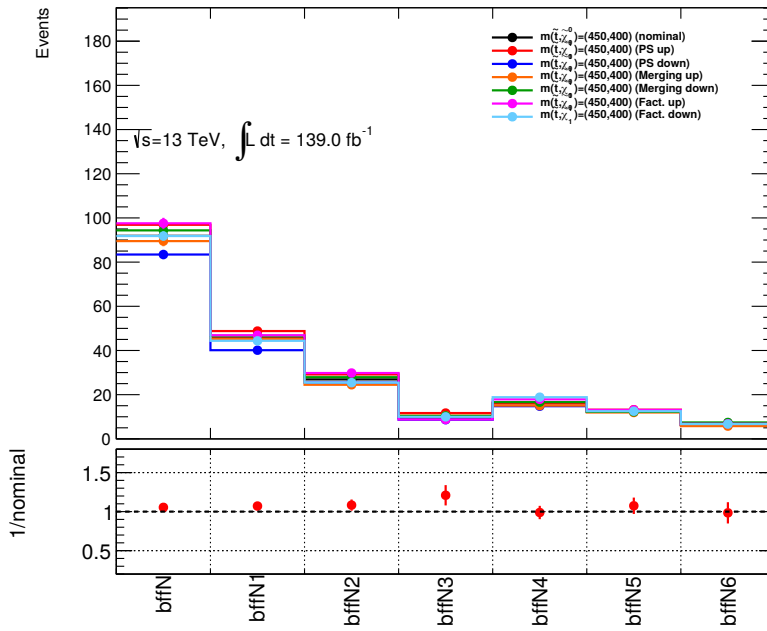


Figure B.1.: Comparison of the event yields in the `bfN_btag` signal region as well in the bins used for the shape-fit analysis. The contrast between the nominal signal sample $m(\tilde{t}, \tilde{\chi}_1^0) = (450, 400)$ GeV and the events from alternative signal samples to determine systematic uncertainties due to parton shower or radiation, factorization and renormalization are shown.

Table B.2.: Summary of the theoretical systematic uncertainties for $t\bar{t}$ in the `bfN_btag` discovery and exclusion regions, also in the corresponding control and validation regions.

	Uncertainties of the systematic $t\bar{t}$ theory effects [%]									
	bfN_btag	bfN1	bfN2	bfN3	bfN4	bfN5	bfN6	T2LVR	WVR	WCR
Radiation down	-4.62±0.15	-4.95±0.36	-3.91±0.24	-3.73±0.2	-4.77±0.27	-3.17±0.16	-5.43±0.17	-2.74±0.15	-3.74±0.14	-18.17±0.31
Radiation up	3.99±0.11	3.99±0.17	3.92±0.14	3.56±0.09	4.56±0.22	2.28±0.21	4.42±0.14	2.34±0.01	3.38±0.08	17.26±0.02
Hard scatter	0.24±1.13	1.51±1.98	-3.72±1.75	3.53±1.52	-8.59±2.46	17.98±1.85	4.31±1.9	-2.31±0.5	18.54±0.88	33.44±1.28
Had./Frag.	3.8±0.02	4.62±0.11	3.48±0.04	13.88±0.11	12.44±0.2	5.13±0.04	9.56±0.03	6.97±0.02	2.51±0.06	-1.96±0.09
Total	5.51±0.09	6.28±0.5	6.42±1.02	14.75±0.38	15.79±1.35	18.83±1.77	11.38±0.72	7.7±0.15	19.01±0.86	37.68±1.14

B.3. $W + \text{jets}$

On Section 6.3.3 the calculation of the $W + \text{jets}$ theoretical systematic uncertainties in `bfN_btag` was described. Table B.3 summarizes the $W + \text{jets}$ theoretical systematic uncertainties measured in `bfN_btag` discovery and exclusion regions and in the corresponding control and validation regions. For each variation type, there was an up and down variation. MadGraph samples differ in the number of events with the nominal Sherpa samples. To work around this statistical limitation, the generator comparison is calculated using the *variable-by-variable* method explained in more detail on Section 6.3.3. Figure B.3 shows the comparison of the event yields in the `bfN_btag` signal

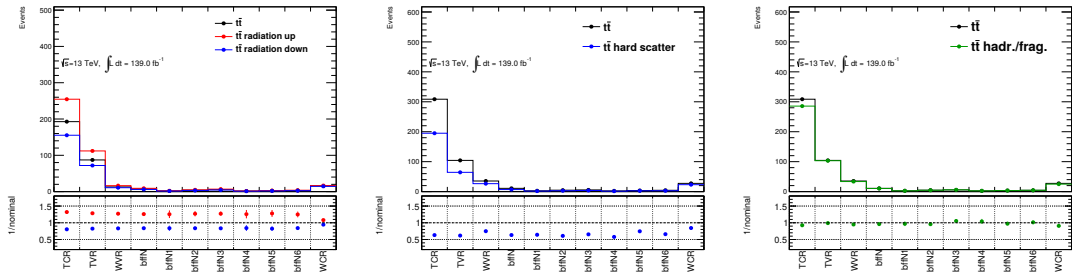


Figure B.2.: Comparison of the event yields, in the `bf1N_btag` signal region as well as the bins used in the shape-fit analysis, between the nominal $t\bar{t}$ sample and the events from alternative $t\bar{t}$ samples to determine systematic uncertainties due to initial state radiation (left), hard scatter effects (middle) and hadronization and fragmentation scale variation (right).

region as well as the bins used in the shape-fit analysis, between the nominal W +jets sample and the alternative W +jets samples.

Table B.3.: Summary of the theoretical systematic uncertainties for $W+jets$ in the in **bffN_btag** discovery and exclusion regions, and also in the corresponding control and validation regions.

Uncertainties of the systematic $W+jets$ theory effects [%]										
	bffN	bffN1	bffN2	bffN3	bffN4	bffN5	bffN6	WVR	TCR	TVR
ckkw	-0.96±0.13	-2.43±0.25	-2.65±0.24	-3.41±0.29	-0.43±0.22	0.36±0.31	-0.86±0.29	-1.95±0.11	-5.42±0.28	-5.61±0.09
fac	-0.68±0.1	-1.47±0.12	-2.19±0.21	-1.99±0.23	-0.4±0.11	0.46±0.25	-0.43±0.22	-1.22±0.09	-3.43±0.2	-4.23±0.07
renorm	-1.6±0.22	-3.33±0.35	-4.86±0.4	-3.97±0.46	-1.05±0.25	0.28±0.54	-1.13±0.51	-2.24±0.2	-6.9±0.4	-6.71±0.14
qsf	-0.87±0.12	-1.98±0.2	-2.74±0.25	-2.68±0.3	-0.56±0.15	0.67±0.31	-0.52±0.3	-1.58±0.12	-4.45±0.24	-4.99±0.08
MadGraph	-26.64±1.05	-26.44±2.36	-3.59±2.28	-22.45±2.19	-28.39±1.81	-30.24±2.29	-19.12±2.32	-15.07±0.2	16.55±0.95	-1.69±0.46
Total	26.67±1.05	26.52±2.36	4.66±1.77	22.6±2.18	28.4±1.81	30.27±2.29	30.27±2.29	2.0±0.39	15.47±0.2	17.05±0.92

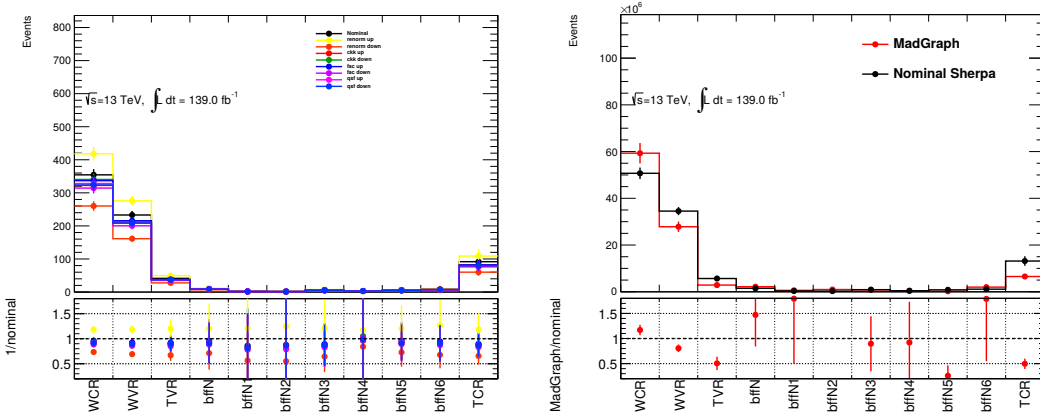


Figure B.3.: Comparison of the event yields, in the `bffN_btag` signal region as well as the bins used in the shape-fit analysis, between the nominal $W + \text{jets}$ sample and the events from alternative $W + \text{jets}$ samples to determine systematic uncertainties due to variations (left) and generator comparison (right).

C. Choice of the ANN Decision Metric Parameters

Different decision metrics were studied to select the one with the best performance. Figure C.1 is an example showing the NN output for different decisions metrics with $n_{jet} = 6$ sample. It is appreciated that the plot on the bottom right achieves the best shape invariance with respect to the b -jet templates. The decision metric selected with this plot was CLs.

Figure C.2 compares the performance of the NN configurations chosen according to different criteria during one training. The comparison is repeated for 5 different trainings, differing only on the initial random seed. In general, the configurations chosen according to the best CLs value reported during the training (orange markers) show the best performance. For these reasons, the CLs were chosen as the decision metric of the ANN.

Studies using different hyper-parameters listed on Table C.1 were performed to select an optimal combination. The best trainings output with respect 4 different hyper-parameters combination is seen on Figure C.3 left. Option 3 (green) achieved the smallest CLs and KLmean values, and therefore it was selected for the ANN training.

With option 3, different lambda scans were performed as seen on Figure C.3 right with CLs as the selecting metric. It shows the metrics performance for these different lambda scans in terms of KL-mean and CLs, selecting outputs with CLs values < 0.2 .

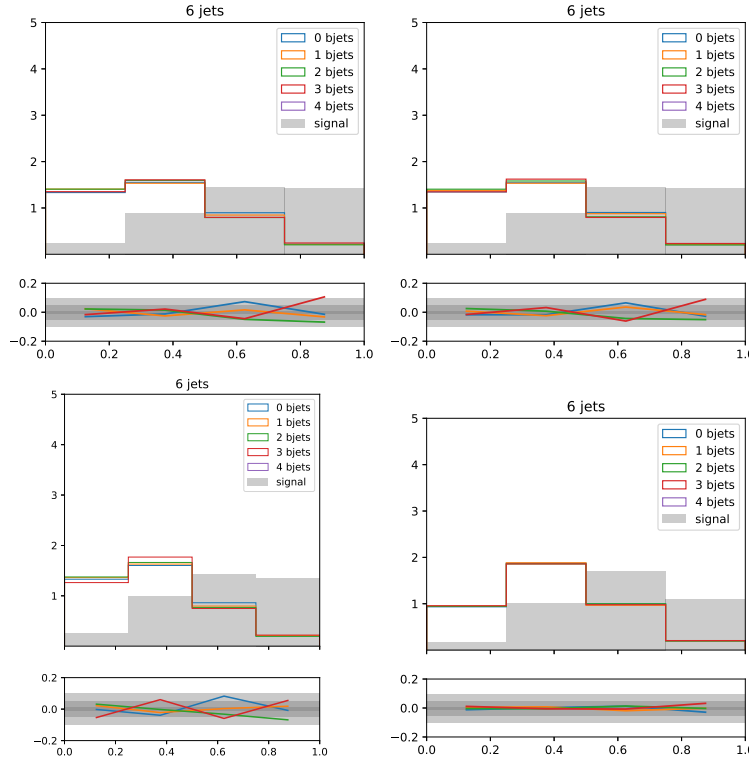


Figure C.1.: Output of the NN trained with the adversarial setup for $n_{\text{jet}} = 6$ $t\bar{t}$ background events in different b -tag multiplicity bins. Different decision metrics are displayed. Top left the KLmean decision metric was chosen, top right the KLmax, bottom left the total loss, and bottom right the CLs. The ratio of each template is displayed with respect to the average of the templates where the shape invariance is appreciated. The best shape invariance is achieved by the CLs decision metric. These were first study-plots and it was decided to drop the 0- b -tag due to its $t\bar{t}$ impurity.

Hyper-parameter	Option 1	Option 2	Option 3	Option 4
Training batch size	1 000	10 000	10 000	10 000
Validation batch size	300 000	300 000	500 000	300 000
Epochs	20 000	10 000	7 000	10 000
Steps per epoch	20	20	30	20
Learning rate	10^{-3}	10^{-4}	10^{-3}	10^{-3}
Lambda	0.9	0.9	0.9	0.9

Table C.1.: Hyper-parameter scans performed with the $t\bar{t}$ 6 jets sample. Option 3 showed the best performance.

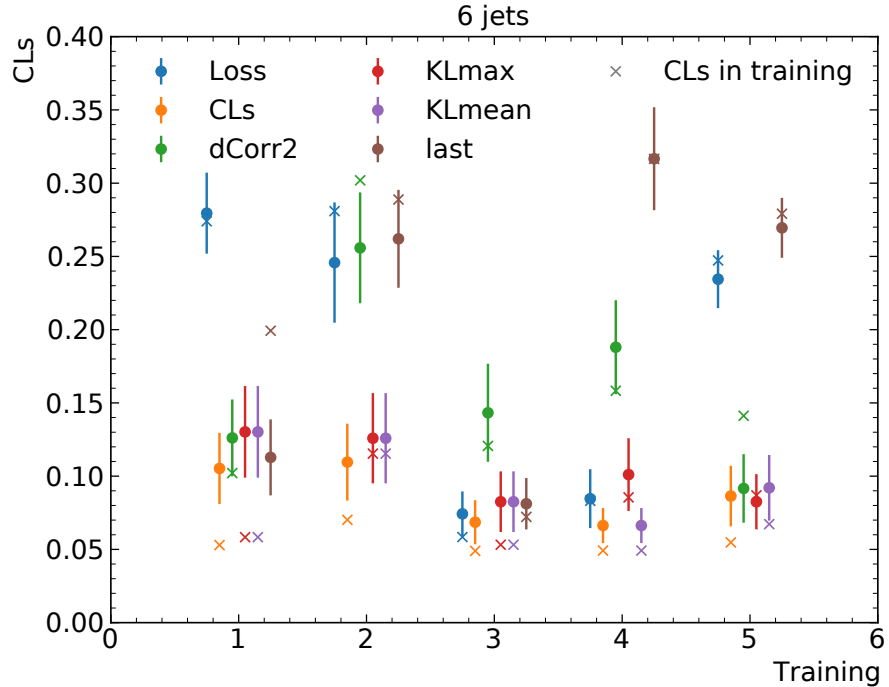


Figure C.2.: Expected CLs value from different NNs evaluation on 100 samples of 300 000 events from the validation set with $n_{\text{jet}} = 6$ sample. The ‘x’ markers show the CLs value obtained in the validation set with the different decision metrics. The NN decision metrics are represented by CLs (orange), KLmax (red), KLmean (purple), dCorr (green), total loss (blue), and last epoch (brown). The training was repeated 5 times with independent training and validation sets, as indicated by the ‘Training’ number on the x-axis. Plot credits to Jan Kuechler.

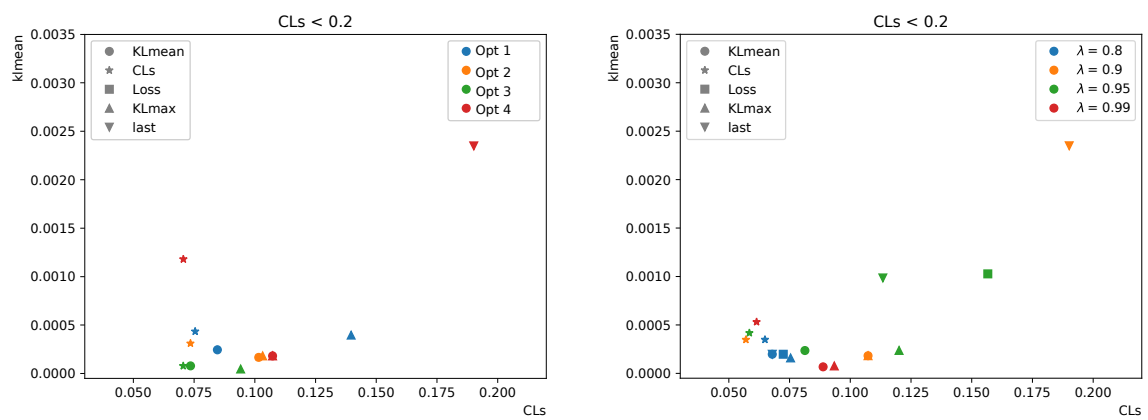


Figure C.3.: The plot on the left shows the different hyper-parameter scans from Table C.1. Option 3 (green) gave the best performance with smaller results for CLs and KLmean. The plot on the right shows different lamda scans using hyper-parameter option 3.

D. Metric Plots

Figures D.1 to D.5 show the evolution of the training metrics for the adversarial neural network trainings with $n_j = 4 - 8$. The plots are shown with respect to the training epoch, in comparison of the training set (blue) and the validation sample (orange).

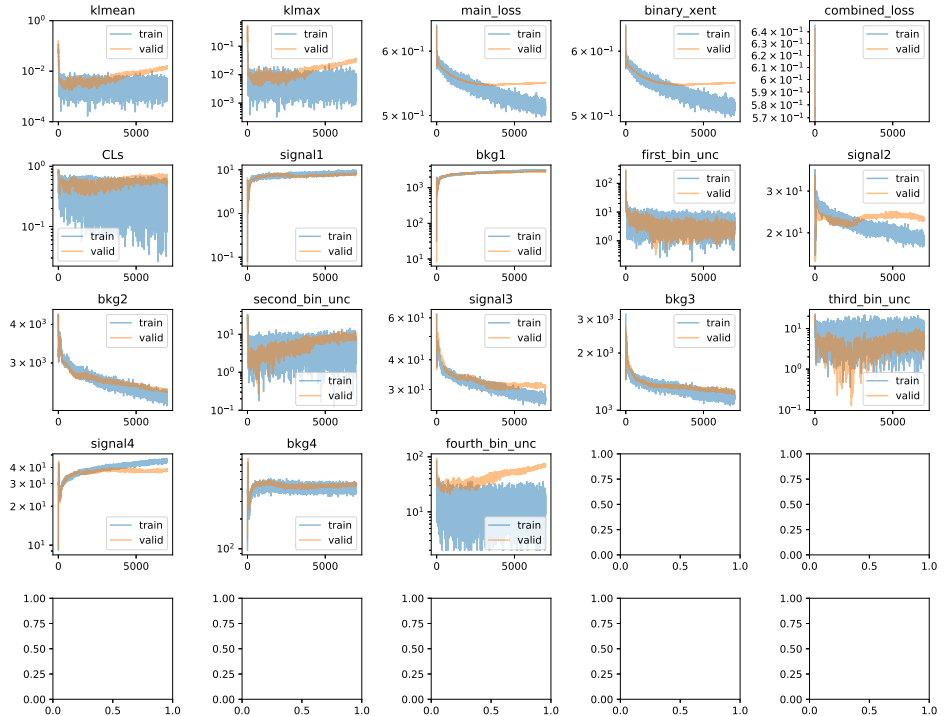


Figure D.1.: Training metrics fro the adversarial neural network with $n_j = 4$.

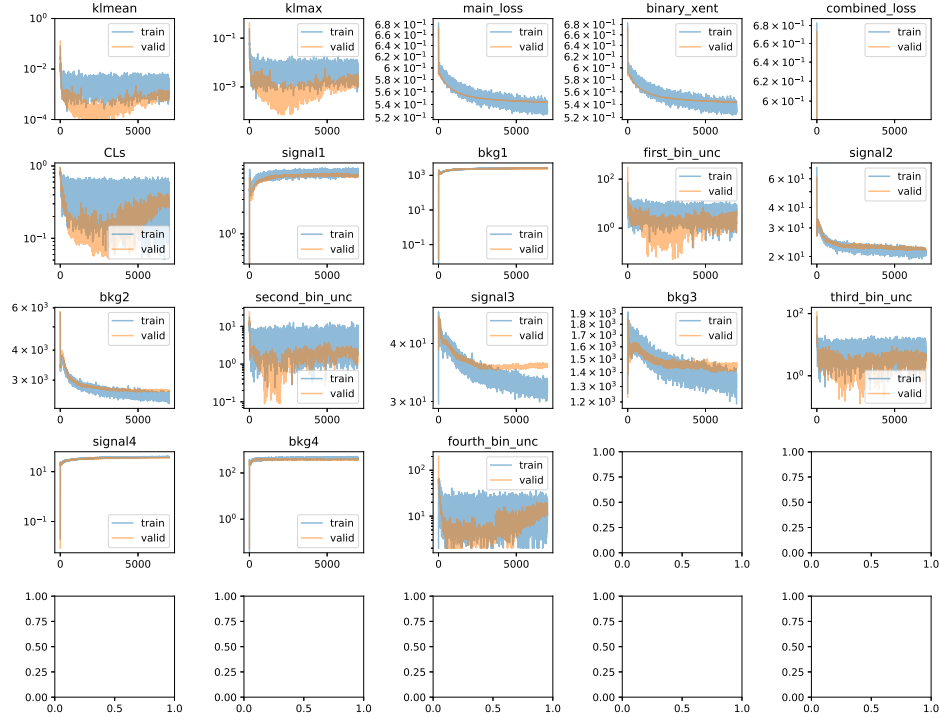


Figure D.2.: Training metrics fro the adversarial neural network with $n_j = 5$.

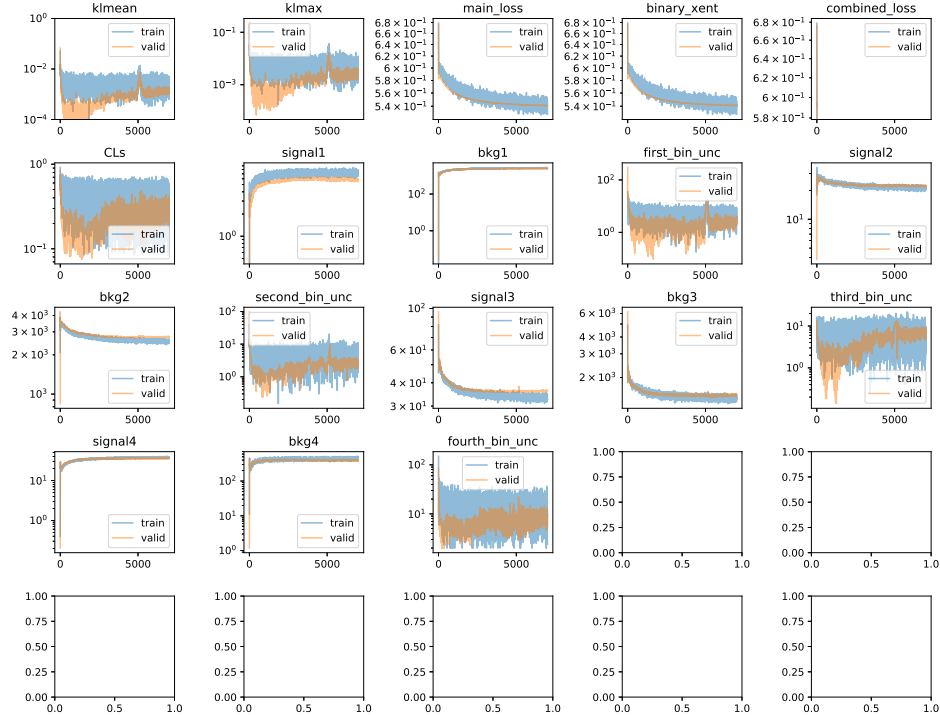
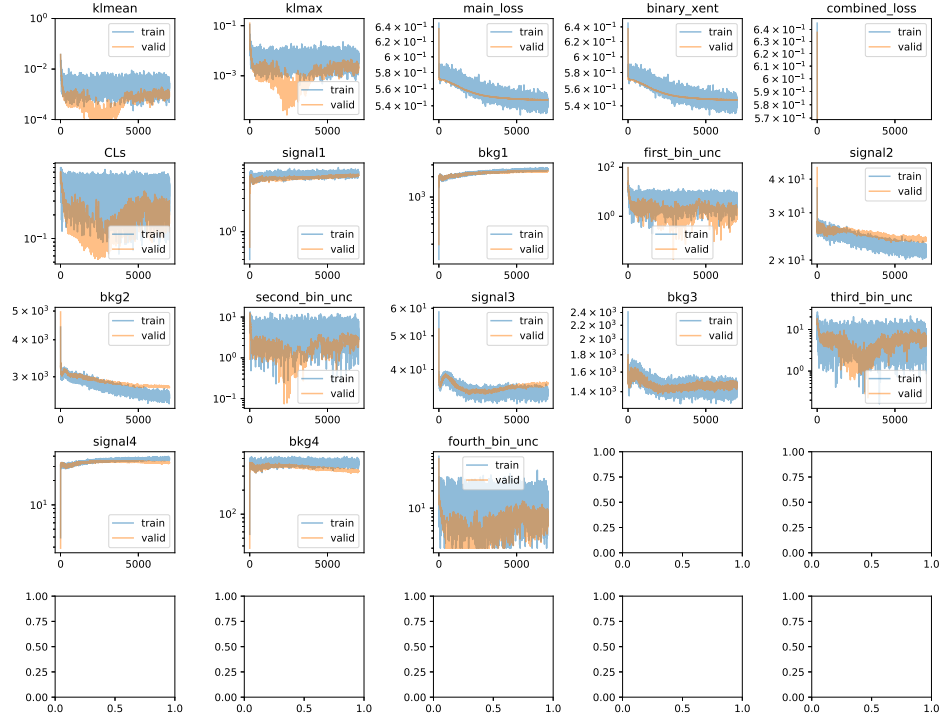
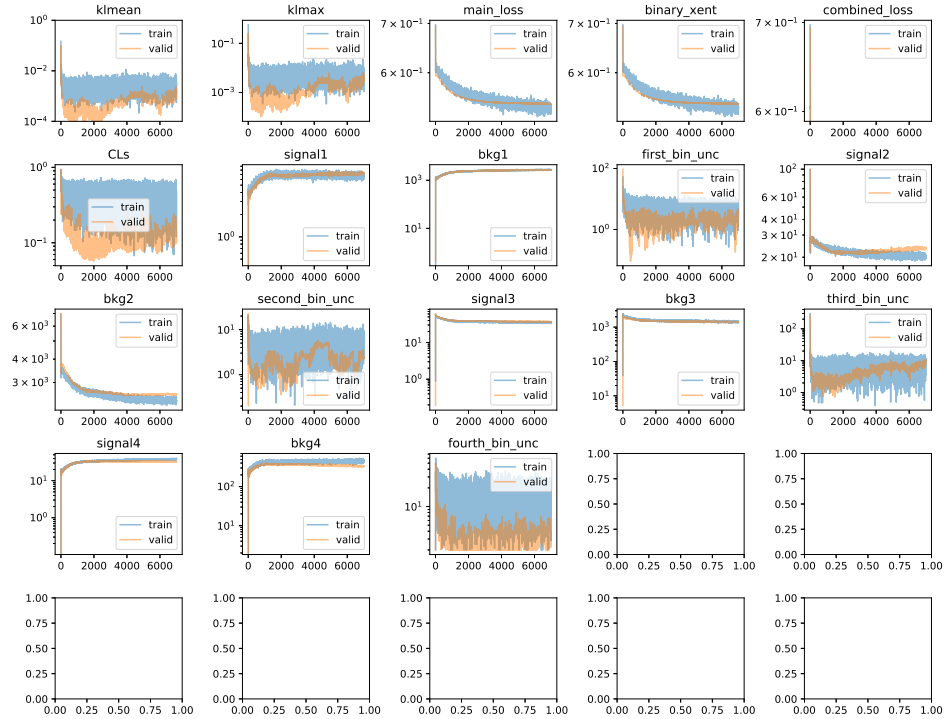


Figure D.3.: Training metrics fro the adversarial neural network with $n_j = 6$.

Figure D.4.: Training metrics fro the adversarial neural network with $n_j = 7$.Figure D.5.: Training metrics fro the adversarial neural network with $n_j = 8$.

E. Mono-Top Discriminating Variables

This appendix presents a brief description of the discriminating variables used for the SUSY mono-top searches.

Leptonic Final State:

- m_{bl} : The invariant mass of the lepton and a b -tagged jet, referred to as m_{bl} , was found to have discriminating power in SUSY mono-top searches. For the reconstruction of this variable the leading b -tagged jet is used unless the event has a second b -tagged jet. In that case the minimum of the invariant mass computed with the first or the second b -tagged jet is used ($m_{bl} = \min(m_{b_1l}, m_{b_2l})$). Signals are bounded from above by the full reconstructed top quark mass as the decays of the SUSY particles are expected to be very soft. Hence, the SM backgrounds can exceed this limit making it a good discriminating variable.
- $\Delta R(b, l)$: is the opening angle in $\eta - \phi$ space between the highest transverse momentum b -jet and the lepton. Small distances in terms of the ΔR variable between the highest b -jet p_T and the lepton were expected, because they are assumed to originate from the decay of the same top quark.
- $\Delta\phi(E_T^{\text{miss}}, l)$: is the azimuthal angle between the missing transverse energy vector and the isolated lepton. SM backgrounds are expected to have a lower value of this variable because their E_T^{miss} only comes from the neutrinos which are closely produced with the leptons. On the contrary, the SUSY mono-top decays result in high E_T^{miss} value, recoiling against the lepton coming from the top quark.
- am_{T2} : m_{T2} [260–262] is the stransverse mass which is used for decay topology with two branches (a and b in the following); both branches are not fully reconstructed due to an invisible particle or particles. The measured four-momentum is referred to as $\vec{p} = (E_i, \vec{p}_{T_i}, p_{z_i})$, while the unmeasured momentum is referred to as $\vec{q} = (F_i, \vec{q}_{T_i}, q_{z_i})$). For each branch $i \in (a, b)$,

$$m_{T_i}^2 = \left(\sqrt{p_{T_i}^2 + m_{p_i}^2} + \sqrt{q_{T_i}^2 + m_{q_i}^2} \right)^2 - (\vec{p}_{T_i} + \vec{q}_{T_i})^2 \quad (\text{E.1})$$

with $m_{p_i}^2 = E_i^2 - \vec{p}_i^2$. If the invisible momentum and the masses of the particles are correctly assigned, the m_{T_i} must be smaller than the mass of the pair-produced parent. The observed missing momentum E_T^{miss} is split into \vec{q}_{T_a} and \vec{q}_{T_b} , and then the stransverse mass is defined as

$$m_{T_2} = \min_{\vec{q}_{T_a} + \vec{q}_{T_b} = \vec{E}_T^{\text{miss}}} \{ \max(m_{T_a}, m_{T_b}) \} \quad (\text{E.2})$$

The asymmetric transverse mass (am_{T_2}) is a variation of a variable targeting dileptonic $t\bar{t}$ with a missing lepton, as shown in Figure E.1. For chain 1), the measured particle is the b -jet from the top quark decay, and the unmeasured particle is the W boson with a missing lepton. For chain 2), the measured particles are the b -jet and charged lepton, while the neutrino is the unmeasured particle. For the masses of the particles needed for the calculation above, $m_{qa} = m_W = 80.4$ GeV and $m_{qb} = m_\nu = 0$ GeV are used. According to the discussion above, the distribution of the am_{T_2} in the dileptonic $t\bar{t}$ events has a boundary at the mass of the top quark while our supersymmetric events can exceed this limit.

- H_T : is the negative scalar sum of the momenta of the signal jets. Its variant $H_{T,\text{sig}}$ takes also into account the p_T values of the lepton. It provides additional suppression against backgrounds with miss-measured missing momentum, arising from miss-measured jets.

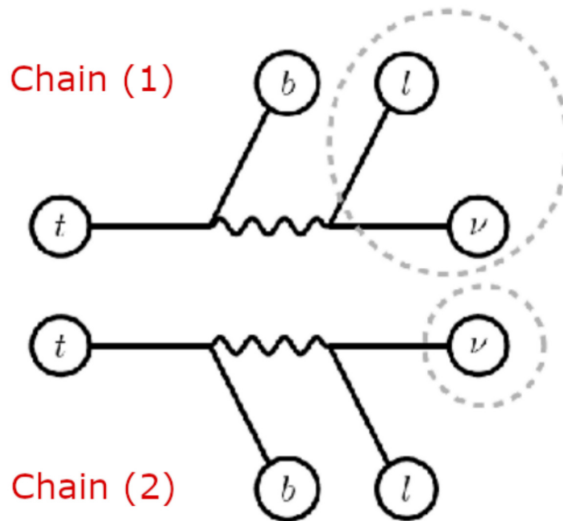


Figure E.1.: An illustration of a dileptonic $t\bar{t}$ event for the am_{T_2} calculation. The unmeasured particles on the top branch (chain 1) form a W boson, i.e., a missing lepton and a neutrino, while the one in the bottom branch (chain 2) is a neutrino. The assignment of the measured b -jets to either chain 1) or 2) is unknown, so both assumptions are tested.

Hadronic Final State:

- $\min \Delta\phi(E_T^{\text{miss}}, j)$: it is the smallest calculated angle between the missing transverse momentum and the vectorial sum of the p_T of all jets. The hadronic top quark

is expected to decay into the highest p_T jets. The SUSY particle decays are too soft to be detected, instead a large amount of E_T^{miss} is expected. In the SUSY mono-top signals the values of this variable are expected to be high, closer to π . This happens because the reconstructed top quark is estimated to recoil against the high E_T^{miss} .

- m_T (1st jet): the transverse mass is calculated in terms of the E_T^{miss} and the first jet p_T . It is defined as:

$$m_T = \sqrt{2p_T^{\text{jet}1}E_T^{\text{miss}}(1 - \cos \Delta\phi(E_T^{\text{miss}}, p_T^{\text{jet}1}))} \quad (\text{E.3})$$

Here, again, the jet is produced by the top quark decay, and the E_T^{miss} by the SUSY particles.

- TopTag: this variable represents the top tagging algorithm described in [264]. The implementation followed the the SM mono-top analysis [241] framework. It was set to reconstruct hadronically decaying top quarks by selecting large R jets (“fat jets”) with a p_T higher than 200 GeV. The algorithm is based on a deep neural network (DNN) with a designed efficiency of 50%.

Bibliography

- [1] ATLAS Collaboration. “Observation of a new particle in the search for the Standard Model Higgs boson with the ATLAS detector at the LHC”. *Phys.Lett. B* **716** (2012) 1–29. [arXiv:1207.7214 \[hep-ex\]](https://arxiv.org/abs/1207.7214)
- [2] CMS Collaboration. “Observation of a new boson at a mass of 125 GeV with the CMS experiment at the LHC”. *Phys. Lett. B* **716** (2012) 30. [arXiv:1207.7235 \[hep-ex\]](https://arxiv.org/abs/1207.7235)
- [3] S. L. Glashow. “Partial-symmetries of weak interactions”. *Nucl. Phys.* **22** (1961) 579–588.
- [4] A. Salam and J. C. Ward. “Electromagnetic and weak interactions”. *Phys. Lett.* **13** (1964) 168–171.
- [5] S. Weinberg. “A Model of Leptons”. *Phys. Rev. Lett.* **19** (1967) 1264–1266.
- [6] G. ‘t Hooft and M. Veltman. “Regularization and renormalization of gauge fields”. *Nucl. Phys. B* **44** (1972) 189–213
- [7] G. Hinshaw, D. Larson, E. Komatsu, D. N. Spergel, C. Bennett, J. Dunkley, M. Nolta, M. Halpern, R. Hill, N. Odegard, et al. “Nine-year Wilkinson Microwave Anisotropy Probe (WMAP) observations: cosmological parameter results”. *Astrophys. J., Suppl. Ser.* **208** (2013) 19. [arXiv:1212.5226 \[astro-ph.CO\]](https://arxiv.org/abs/1212.5226)
- [8] Planck Collaboration. “Planck 2018 results. I. Overview and the cosmological legacy of Planck”. *A&A* **641**, A1 (2020). [arXiv:1807.06205 \[astro-ph.CO\]](https://arxiv.org/abs/1807.06205)
- [9] V. Trimble. “Existence and Nature of Dark Matter in the Universe”. *Annu. Rev. Astron. Astrophys.* **25** (1987) 425–472.
- [10] G. Bertoni et al. “Particle dark matter: evidence, candidates and constraints”. *Phys. Rep.* **405** (2005) 279–390.
- [11] J. L. Feng. “Dark matter candidates from particle physics and methods of detection”. *Ann. Rev. Astron. Astrophys.* **48** (2010) 495–545. [arXiv:1003.0904 \[astro-ph.CO\]](https://arxiv.org/abs/1003.0904)
- [12] D. Volkov and V. Akulov. “Is the neutrino a goldstone particle?”. *Phys. Lett. B* **46** (1973) 109.
- [13] J. Wess and B. Zumino. “Supergauge transformations in four dimensions”. *Nucl. Phys. B* **70** (1974) 39.

[14] J. Wess and B. Zumino. “Supergauge invariant extension of quantum electrodynamics”. *Nucl. Phys. B* **78** (1974) 1.

[15] S. Ferrara and B. Zumino. “Supergauge invariant Yang-Mills theories”. *Nucl. Phys. B* **79** (1974) 413.

[16] A. Salam and J. Strathdee, “Super-symmetry and non-Abelian gauges”. *Phys. Lett. B* **51** (1974) 353.

[17] S. P. Martin. “A Supersymmetry Primer”. *Adv. Ser. Direct. High Energy Phys.* **18** (1998) 1. [arXiv:hep-ph/9709356](https://arxiv.org/abs/hep-ph/9709356)

[18] N. Sakai. “Naturalness in supersymmetric GUTS”. *Z. Phys. C* **11** (1981) 153.

[19] J. L. Feng. “Naturalness and the Status of Supersymmetry”. *Ann. Rev. Nucl. Part. Sci.* **63** (2013) 351–382. [arXiv:1302.6587 \[hep-ph\]](https://arxiv.org/abs/1302.6587)

[20] G. R. Farrar and P. Fayet. “Phenomenology of the production, decay, and detection of new hadronic states associated with supersymmetry”. *Phys. Lett. B* **76** (1978) 575.

[21] H. Goldberg. “Constraint on the Photino Mass from Cosmology”. *Phys. Rev. Lett.* **50** (1983) 1419. Erratum: *Phys. Rev. Lett.* **103** (2009) 099905.

[22] J. Ellis, J. Hagelin, D. V. Nanopoulos, K. A. Olive and M. Srednicki. “Supersymmetric relics from the big bang”. *Nucl. Phys. B* **238** (1984) 453.

[23] J. A. Evans, Y. Kats, D. Shih and M. J. Strassler. “Toward Full LHC Coverage of Natural Supersymmetry”. *JHEP* **07** (2014) 101. [arXiv: 1310.5758 \[hep-ph\]](https://arxiv.org/abs/1310.5758)

[24] B. Batell, T. Lin and L.-T. Wang. “Flavored Dark Matter and R-Parity Violation”. *JHEP* **01** (2014) 075. [arXiv:1309.4462 \[hep-ph\]](https://arxiv.org/abs/1309.4462)

[25] ATLAS Collaboration. “Search for new phenomena with top quark pairs in final states with one lepton, jets, and missing transverse momentum in pp collisions at $\sqrt{s} = 13$ TeV with the ATLAS detector”. *JHEP* **04** (2021) 174. [arXiv:2012.03799 \[hep-ex\]](https://arxiv.org/abs/2012.03799)

[26] ATLAS Collaboration. “Search for R -parity violating supersymmetry in a final state containing leptons and many jets with the ATLAS experiment using $\sqrt{s} = 13$ TeV proton-proton collision data”. [ATLAS-CONF-2021-007](https://cds.cern.ch/record/2607207).

[27] Rayleigh. “Joseph John Thomson. 1856–1940”. *Obituary Notices of Fellows of the Royal Society*, **3** (1941) 586–609. <http://www.jstor.org/stable/769169>

[28] S. F. Novaes. “Standard Model: An Introduction”. [arXiv:hep-ph/0001283](https://arxiv.org/abs/hep-ph/0001283)

[29] S. L. Glashow. “Partial-symmetries of weak interactions”. *Nucl. Phys.*, **22** *4* 579–588 (1961). doi: [10.1016/0029-5582\(61\)90469-2](https://doi.org/10.1016/0029-5582(61)90469-2).

[30] S. Weinberg. “A Model of Leptons”. *Phys. Rev. Lett.* **19** (1967) 1264–1266. doi: [10.1103/PhysRevLett.19.1264](https://doi.org/10.1103/PhysRevLett.19.1264)

[31] A. Salam and J. C. Ward. “Electromagnetic and weak interactions”. *Phys. Lett.* **13** (1964) 168–171. doi: [10.1016/0031-9163\(64\)90711-5](https://doi.org/10.1016/0031-9163(64)90711-5)

[32] P.A. Zyla et al. Particle Data Group Collaboration. “The Review of Particle Physics (2020)”. *Prog. Theor. Exp. Phys.* **2020**, 083C01 (2020). doi: [10.1093/ptep/ptaa104](https://doi.org/10.1093/ptep/ptaa104)

[33] D. Griffiths. “Introduction to Elementary Particle Physics”. Wiley-VCH, 2008. Section 2.3 Quantumchromodynamics (QCD).

[34] P. W. Higgs. “Broken Symmetries and the Masses of Gauge Bosons”. *Phys. Rev. Lett.* **13** (1964) 508–509. doi: [10.1103/PhysRevLett.13.508](https://doi.org/10.1103/PhysRevLett.13.508)

[35] F. Englert and R. Brout. “Broken Symmetry and the Mass of Gauge Vector Mesons”. *Phys. Rev. Lett.* **13** (1964) 321–323. doi: [10.1103/PhysRevLett.13.321](https://doi.org/10.1103/PhysRevLett.13.321)

[36] D. Griffiths. “Introduction to Quantum Mechanics”. Pearson Prentice Hall, 2005. Second edition.

[37] D. Griffiths. “Introduction to Elementary Particle Physics”. Wiley-VCH, 2008.

[38] M. Thomson. “Modern particle physics”. Cambridge University Press. 2013.

[39] E. Noether. “Invariante Variationsprobleme”. *Nachr. Ges. Wiss. Gött., Math. Phys. Kl.* **II** 235 (1918).

[40] F. Mandl and G. Shaw. “Quantum Field Theory”. John Wiley & Sons Ltd. Second edition. 2010.

[41] C.R. Nave. “HyperPhysics: The Color Force” (2011). url: <http://hyperphysics.phy-astr.gsu.edu/hbase/Forces/color.html>

[42] G.'t Hooft. “Naturalness, Chiral Symmetry and Spontaneous Chiral Symmetry Breaking”. *NATO Sci. Ser. B* **59** (1980) 135-157 PRINT-80-0083 (UTRECHT). doi: [10.1007/978-1-4684-7571-59](https://doi.org/10.1007/978-1-4684-7571-59)

[43] C. S. Wu, E. Ambler, R. W. Hayward, D. D. Hoppes, and R. P. Hudson. “Experimental Test of Parity Conservation in Beta Decay”. *Phys. Rev.* **105**, 1413. doi: [10.1103/PhysRev.105.1413](https://doi.org/10.1103/PhysRev.105.1413)

[44] H. Frauenfelder, J. D. Jackson, and H. W. Wyld, Jr. “Polarization Effects following Beta Decay”. *Phys. Rev.* **110** (1958) 451. doi: [10.1103/PhysRev.110.451](https://doi.org/10.1103/PhysRev.110.451)

[45] R. D. Klauber. “Electroweak Symmetry Breaking”. University notes. url: <http://www.quantumfieldtheory.info/ElectroweakSymbreaking.pdf>

[46] T. Ritbergen, R. Stuart. “Complete 2-loop Quantum Electrodynamical Contributions to the Muon Lifetime in the Fermi Model”. *Phys. Rev. Lett.* **82** (1999) 488–491. [arXiv:hep-ph/9808283](https://arxiv.org/abs/hep-ph/9808283)

[47] M. Steinhauser, T. Seidensticker. “Second Order Corrections to the Muon Lifetime and the Semileptonic B Decay”. *Phys. Lett. B* **467** (1999) 271–278. [arXiv:hep-ph/9909436](https://arxiv.org/abs/hep-ph/9909436)

[48] T. Ritbergen, R. Stuart. “On the Precise Determination of the Fermi Coupling Constant from the Muon Lifetime”. *Nucl. Phys. B* **564** (2000) 343–390. [arXiv:hep-ph/9904240](https://arxiv.org/abs/hep-ph/9904240)

[49] D. Griffiths. “Introduction to Elementary Particle Physics”. Wiley-VCH, 2008. Section 10.7.3 Electro-Weak Mixing. pp. 336.

[50] W. de Boer. “The Discovery of the Higgs Boson with the CMS Detector and its Implications for Supersymmetry and Cosmology”. *Time and Matter 2013 (TAM2013)*. Italy. [arXiv:1309.0721 \[hep-ph\]](https://arxiv.org/abs/1309.0721)

[51] J. Goldstone, A. Salam, and S. Weinberg. “Broken Symmetries”. *Phys. Rev.* **127** (1962) 965. doi: [10.1103/PhysRev.127.965](https://doi.org/10.1103/PhysRev.127.965)

[52] N. Cabibbo. “Unitary Symmetry and Leptonic Decays”. *Phys. Rev. Lett.* **10** (1963) 531. doi: [10.1103/PhysRevLett.10.531](https://doi.org/10.1103/PhysRevLett.10.531)

[53] M. Kobayashi and T. Maskawa. “CP Violation in the Renormalizable Theory of Weak Interaction”. *Prog. Theor. Phys.* **49** (1973) 652. doi: [10.1143/PTP.49.652](https://doi.org/10.1143/PTP.49.652)

[54] F. Zwicky, “Die Rotverschiebung von extragalaktischen Nebeln”, *Helv. Phys. Acta* **6**, 110–127 (1933). Published online in 2008. doi: [10.1007/s10714-008-0707-4](https://doi.org/10.1007/s10714-008-0707-4)

[55] E. Corbelli and P. Salucci. “The Extended Rotation Curve and the Dark Matter Halo of M33”, *Monthly Notices of the Royal Astronomical Society*, **311** (2000) 441–447. url: <http://mnras.oxfordjournals.org/content/311/2/441.abstract>

[56] K. Garrett and G. Duda. “Dark Matter: A Primer”. *Adv. Astron.* 2011 (2011), p. 968283. [arXiv:1006.2483 \[hep-ph\]](https://arxiv.org/abs/1006.2483)

[57] F. Dyson, A. Eddington and C. Davidson. “A Determination of the Deflection of Light by the Sun’s Gravitational Field from Observations Made at the Total Eclipse of May 29, 1919”. *Phil. Trans. Roy. Soc.* **220** 291. doi: [10.1098/rsta.1920.0009](https://doi.org/10.1098/rsta.1920.0009)

[58] R. Massey, T. Kitching, and J. Richard. “The Dark Matter of Gravitational Lensing”. [arXiv:1001.1739](https://arxiv.org/abs/1001.1739)

[59] D. J. Gross, H. D. Politzer, F. Wilczek. The Nobel Prize in Physics 2004. Popular Information. url: <https://www.nobelprize.org/prizes/physics/2004/popular-information/>

[60] M. Bustamante, L. Cieri, and J. Ellis. “Beyond the Standard Model for Montaneros”. CERN Yellow Report CERN-2010-001, pp. 145–228. [arXiv:0911.4409 \[hep-ph\]](https://arxiv.org/abs/0911.4409)

[61] K. Inoue et al. “Aspects of Grand Unified Models with Softly Broken Supersymmetry”. *Prog. Theor. Phys.* **68** (1982) 927. doi: [10.1143/PTP.68.927](https://doi.org/10.1143/PTP.68.927)

[62] P. Fayet. “The Supersymmetric Standard Model”. *Eur. Phys. J. C* **74** (2014) 2837. doi: [10.1140/epjc/s10052-014-2837-z](https://doi.org/10.1140/epjc/s10052-014-2837-z)

[63] I. J. R. Aitchison. “Supersymmetry and the MSSM: An Elementary Introduction”. Notes of Lectures for Graduate Students, Oxford (2004). [arXiv:hep-ph/0505105](https://arxiv.org/abs/hep-ph/0505105)

[64] S. Y. Choi, J. Kalinowski, G. Moortgat-Pick, and P. M. Zerwas. “Analysis of the neutralino system in supersymmetric theories”. *Eur. Phys. J. C* **22** (2001) 563–579. [arXiv:hep-ph/0108117](https://arxiv.org/abs/hep-ph/0108117)

[65] R. Kitano and Y. Nomura. “Supersymmetry, naturalness, and signatures at the LHC”. *Phys. Rev. D* **73** (2006) 095004. [arXiv:hep-ph/0602096 \[hep-ph\]](https://arxiv.org/abs/hep-ph/0602096)

[66] M. Papucci, J. T. Ruderman, and A. Weiler. “Natural SUSY Endures”. *JHEP* **09** (2012) 035. [arXiv:1110.6926 \[hep-ph\]](https://arxiv.org/abs/1110.6926)

[67] A. Djouadi, J. L. Kneur, and G. Moultaka. “SuSpect: A Fortran code for the supersymmetric and Higgs particle spectrum in the MSSM”. *Comput. Phys. Commun.* **176** (2007) 426–455. [arXiv:hep-ph/0211331 \[hep-ph\]](https://arxiv.org/abs/hep-ph/0211331)

[68] S. Heinemeyer, W. Hollik, and G. Weiglein. “FeynHiggs: A Program for the calculation of the masses of the neutral CP even Higgs bosons in the MSSM”. *Comput. Phys. Commun.* **124** (2000) 76–89. [arXiv:hep-ph/9812320 \[hep-ph\]](https://arxiv.org/abs/hep-ph/9812320)

[69] L. J. Hall, D. Pinner, and J. T. Ruderman. “A Natural SUSY Higgs Near 125 GeV”. *JHEP* **04** (2012) 131. [arXiv:1112.2703 \[hep-ph\]](https://arxiv.org/abs/1112.2703)

[70] R. Barbier et al. “ R -parity violating supersymmetry”. *Phys. Rept.* **420** (2005) 1. [arXiv:hep-ph/0406039 \[hep-ph\]](https://arxiv.org/abs/hep-ph/0406039)

[71] B. C. Allanach, A. Dedes, and H. K. Dreiner. “Bounds on R -parity violating couplings at the weak scale and at the GUT scale”. *Phys. Rev. D* **60** (1999) 075014. [arXiv:hep-ph/9906209](https://arxiv.org/abs/hep-ph/9906209)

[72] C. Csáki, Y. Grossman, B. Heidenreich. “MFV SUSY: A Natural Theory for R-parity Violation”. *Phys. Rev. D* **85**, 095009 (2012). [arXiv:1111.1239 \[hep-ph\]](https://arxiv.org/abs/1111.1239)

[73] B. S. Chivukula, H. Georgi. “Composite-technicolor standard model”. *Phys. Lett. B* **188** (1987) 59. doi: [10.1016/0370-2693\(87\)90713-1](https://doi.org/10.1016/0370-2693(87)90713-1)

[74] G. D’Ambrosio, G.F. Giudice, G. Isidori, A. Strumia. “Minimal Flavour Violation: an effective field theory approach”. *Nucl. Phys. B* **645** (2002) 155–187. [arXiv:hep-ph/0207036](https://arxiv.org/abs/hep-ph/0207036)

[75] J. Bernon and C. Smith. “Baryonic R-parity violation and its running”. *JHEP* **07** (2014) 038. [arXiv:1404.5496 \[hep-ph\]](https://arxiv.org/abs/1404.5496)

[76] E. Nikolidakis, C. Smith. “Minimal Flavor Violation, Seesaw, and R-parity”. *Phys. Rev. D* **77** (2008) 015021. [arXiv:0710.3129 \[hep-ph\]](https://arxiv.org/abs/0710.3129)

[77] M. Gell-Mann. “A schematic model of baryons and mesons”. *Phys. Lett. B* **8** (1964) 214–215. doi: [10.1016/S0031-9163\(64\)92001-3](https://doi.org/10.1016/S0031-9163(64)92001-3)

[78] A. D. Sakharov. “Violation of CP Invariance, C asymmetry, and baryon asymmetry of the universe”. *Sov. Phys. Usp.* **34** **392** (1991). doi: [10.1070/PU1991v03n05ABEH002497](https://doi.org/10.1070/PU1991v03n05ABEH002497)

[79] K.S. Babu, et. al. “Baryon Number Violation”. Report of the Community Summer Study (Snowmass 2013). [arXiv:1311.5285 \[hep-ph\]](https://arxiv.org/abs/1311.5285)

[80] CERN Homepage. url: <https://home.cern/about>

[81] The Large Hadron Collider Homepage. url: home.cern/science/accelerators/large-hadron-collider

[82] F. Marcastel. CERN’s Accelerator Complex. General Photo. url: <https://cds.cern.ch/record/1621583>

[83] ATLAS Collaboration. “The ATLAS Experiment at the CERN Large Hadron Collider”. *2008 JINST* **3** S08003

[84] E. Daw. “Lecture 7. Rapidity and Pseudorapidity”. The University of Sheffield. 2012. url: <http://www.hep.shef.ac.uk/edaw/PHY206/Site/2012coursefiles/phy206rlec7.pdf>

[85] Y. Abulati. “Search for Pair-Produced Supersymmetric Top Quark Partners with the ATLAS Experiment”. Stockholm University, Department of Physics. 2016. url: <https://cds.cern.ch/record/2225221/files/FULLTEXT01.pdf>

[86] The ATLAS TRT collaboration. “The ATLAS Transition Radiation Tracker (TRT) proportional drift tube: design and performance”. *J. Instrum.* **3** (2008) P02013–P02013

[87] G. Avoni et al. “The new LUCID-2 detector for luminosity measurement and monitoring in ATLAS”. *J. Instrum.* **13** (2018) P07017

[88] ATLAS Collaboration. “Performance of the ATLAS trigger system in 2015”. *Eur. Phys. J. C* **77** (2017) 317. [arXiv:1611.09661 \[hep-ex\]](https://arxiv.org/abs/1611.09661)

[89] ATLAS Collaboration. “Luminosity determination in pp collisions at $\sqrt{s} = 13$ TeV using the ATLAS detector at the LHC”. ATLAS-CONF-2019-021, 2019. url: <https://cds.cern.ch/record/2677054>

[90] ATLAS Collaboration. “Luminosity Public Results Run 2”. url: <https://twiki.cern.ch/twiki/bin/view/AtlasPublic/LuminosityPublicResultsRun2>

[91] S. van der Meer. “Calibration of the effective beam height in the ISR”. Tech. Rep. CERN-ISR-PO-68-31. ISR-PO-68-31, CERN, Geneva, 1968. <https://cds.cern.ch/record/296752>

[92] C. Barschel. “Precision luminosity measurement at LHCb with beam-gas imaging”. 2014. <https://cds.cern.ch/record/1693671>

[93] ATLAS Collaboration. “Performance of the ATLAS muon triggers in Run 2”. JINST **15** (2020) P09015. [arXiv:2004.13447 \[hep-ex\]](https://arxiv.org/abs/2004.13447)

[94] ATLAS Collaboration. “Performance of electron and photon triggers in ATLAS during LHC Run 2”. Eur. Phys. J. C **80** (2020) 47. [arXiv:1909.00761 \[hep-ex\]](https://arxiv.org/abs/1909.00761)

[95] A. Buckley et al. “General-purpose event generators for LHC physics”. Phys. Rept. **504** (2011). [arXiv:1101.2599 \[hep-ph\]](https://arxiv.org/abs/1101.2599)

[96] NNPDF Collaboration. “Parton distributions from high-precision collider data”. Eur. Phys. J. C **77** (2017) 663. [arXiv:1706.00428 \[hep-ph\]](https://arxiv.org/abs/1706.00428)

[97] A. Buckley and H. Schulz. “Tuning of MC generator MPI models”. Adv. Ser. Direct. High Energy Phys. **29** (2018) 281. [arXiv:1806.11182 \[hep-ph\]](https://arxiv.org/abs/1806.11182)

[98] A. Buckley, H. Hoeth, H. Lacker, H. Schulz, and J. E. von Seggern. “Systematic event generator tuning for the LHC”. Eur. Phys. J. C **65** (2010) 331. [arXiv:0907.2973 \[hep-ph\]](https://arxiv.org/abs/0907.2973)

[99] The Particle Data Group Collaboration. “Review of particle physics”. Phys. Rev. D **98** 030001 (2018). doi: [10.1103/PhysRevD.98.030001](https://doi.org/10.1103/PhysRevD.98.030001)

[100] S. Alioli, P. Nason, C. Oleari and E. Re. “A general framework for implementing NLO calculations in shower Monte Carlo programs: the POWHEG BOX”. JHEP **06** (2010) 043. [arXiv:1002.2581 \[hep-ph\]](https://arxiv.org/abs/1002.2581)

[101] T. Sjöstrand, S. Mrenna, and P. Z. Skands. “A Brief Introduction to PYTHIA 8.1”. Comput. Phys. Commun. **178** (2008) 852. [arXiv:0710.3820 \[hep-ph\]](https://arxiv.org/abs/0710.3820)

[102] J. Alwall et al. “The automated computation of tree-level and next-to-leading order differential cross sections, and their matching to parton shower simulations”. JHEP **07** (2014) 079. [arXiv:1405.0301 \[hep-ph\]](https://arxiv.org/abs/1405.0301)

[103] M. Bähr et al. “Herwig++ physics and manual”. Eur. Phys. J. C **58** (2008) 639. [arXiv:0803.0883 \[hep-ph\]](https://arxiv.org/abs/0803.0883)

[104] L. Harland-Lang, A. Martin, P. Motylinski and R. Thorne. “Parton distributions in the LHC era: MMHT 2014 PDFs”. Eur. Phys. J. C **75** (2015) 204. [arXiv: 1412.3989 \[hep-ph\]](https://arxiv.org/abs/1412.3989)

[105] S. Catani, L. Cieri, G. Ferrera, D. de Florian, and M. Grazzini. “Vector boson production at hadron colliders: a fully exclusive QCD calculation at NNLO”. *Phys. Rev. Lett.* **103** (2009) 082001. [arXiv:0903.2120 \[hep-ph\]](https://arxiv.org/abs/0903.2120)

[106] S. Schumann and F. Krauss. “A Parton shower algorithm based on Catani-Seymour dipole factorisation”. *JHEP* **03** (2008) 038. [arXiv:0709.1027 \[hep-ph\]](https://arxiv.org/abs/0709.1027)

[107] T. Gleisberg and S. Höche. “COMIX, a new matrix element generator”. *JHEP* **12** (2008) 039. [arXiv:0808.3674 \[hep-ph\]](https://arxiv.org/abs/0808.3674)

[108] F. Cascioli, P. Maierhofer, and S. Pozzorini. “Scattering Amplitudes with Open Loops”. *Phys. Rev. Lett.* **108** (2012) 111601. [arXiv:1111.5206 \[hep-ph\]](https://arxiv.org/abs/1111.5206)

[109] S. Höche, F. Krauss, M. Schönherr, and F. Siegert. “QCD matrix elements + parton showers: The NLO case”. *JHEP* **04** (2013) 027. [arXiv:1207.5030 \[hep-ph\]](https://arxiv.org/abs/1207.5030)

[110] T. Gleisberg, S. Hoeche, F. Krauss, M. Schonherr, S. Schumann, F. Siegert, and J. Winter. “Event generation with SHERPA 1.1”. *JHEP* **02** (2009) 007. [arXiv:0811.4622 \[hep-ph\]](https://arxiv.org/abs/0811.4622)

[111] P. Artoisenet, R. Frederix, O. Mattelaer, and R. Rietkerk. “Automatic spin-entangled decays of heavy resonances in Monte Carlo simulations”. *JHEP* **03** (2013) 015. [arXiv:1212.3460 \[hep-ph\]](https://arxiv.org/abs/1212.3460)

[112] P. Z. Skands. “Tuning Monte Carlo Generators: The Perugia Tunes”. *Phys. Rev. D* **82** (2010) 074018. [arXiv:1005.3457 \[hep-ph\]](https://arxiv.org/abs/1005.3457)

[113] ATLAS Collaboration. “ATLAS Pythia 8 tunes to 7 TeV data”. ATL-PHYS-PUB-2014-021. 2014. <https://cds.cern.ch/record/1966419>

[114] J. Bellm et al. “Herwig 7.0/Herwig++ 3.0 release note”. *Eur. Phys. J. C* **76** (2016) 196. [arXiv:1512.01178 \[hep-ph\]](https://arxiv.org/abs/1512.01178)

[115] GEANT4 Collaboration. S. Agostinelli et al. “GEANT4: A Simulation toolkit”. *Nucl. Instrum. Meth. A* **506** (2003) 250. doi: [10.1016/S0168-9002\(03\)01368-8](https://doi.org/10.1016/S0168-9002(03)01368-8)

[116] ATLAS Collaboration. “The ATLAS Simulation Infrastructure”. *Eur. Phys. J. C* **70** (2010) 823. [arXiv:1005.4568 \[physics.ins-det\]](https://arxiv.org/abs/1005.4568)

[117] M. Czakon, P. Fiedler, and A. Mitov. “Total Top-Quark Pair-Production Cross Section at Hadron Colliders Through $O(\alpha_S^4)$ ”. *Phys. Rev. Lett.* **110** (2013) 252004. [arXiv:1303.6254 \[hep-ph\]](https://arxiv.org/abs/1303.6254)

[118] M. Czakon and A. Mitov. “NNLO corrections to top pair production at hadron colliders: the quark-gluon reaction”. *JHEP* **01** (2013) 080. [arXiv:1210.6832 \[hep-ph\]](https://arxiv.org/abs/1210.6832)

[119] M. Czakon and A. Mitov. “NNLO corrections to top-pair production at hadron colliders: the all-fermionic scattering channels”. *JHEP* **12** (2012) 054. [arXiv:1207.0236 \[hep-ph\]](https://arxiv.org/abs/1207.0236)

[120] P. Bärnreuther, M. Czakon, and A. Mitov. “Percent Level Precision Physics at the Tevatron: First Genuine NNLO QCD Corrections to $q\bar{q} \rightarrow t\bar{t} + X$ ”. *Phys. Rev. Lett.* **109** (2012) 132001. [arXiv:1204.5201 \[hep-ph\]](https://arxiv.org/abs/1204.5201)

[121] M. Cacciari, M. Czakon, M. Mangano, A. Mitov, and P. Nason. “Top-pair production at hadron colliders with next-to-next-to-leading logarithmic soft-gluon resummation”. *Phys. Lett. B* **710** (2012) 612. [arXiv:1111.5869 \[hep-ph\]](https://arxiv.org/abs/1111.5869)

[122] M. Czakon and A. Mitov. “Top++: A Program for the Calculation of the Top-Pair Cross-Section at Hadron Colliders”. *Comput. Phys. Commun.* **185** (2014) 2930. [arXiv:1112.5675 \[hep-ph\]](https://arxiv.org/abs/1112.5675)

[123] N. Kidonakis. “Next-to-next-to-leading-order collinear and soft gluon corrections for t-channel single top quark production”. *Phys. Rev. D* **83** (2011) 091503. [arXiv:1103.2792 \[hep-ph\]](https://arxiv.org/abs/1103.2792)

[124] N. Kidonakis. “Two-loop soft anomalous dimensions for single top quark associated production with a W^- or H^- ”. *Phys. Rev. D* **82** (2010) 054018. [arXiv:1005.4451 \[hep-ph\]](https://arxiv.org/abs/1005.4451)

[125] N. Kidonakis. “NNLL resummation for s-channel single top quark production”. *Phys. Rev. D* **81** (2010) 054028. [arXiv:1001.5034 \[hep-ph\]](https://arxiv.org/abs/1001.5034)

[126] M. Beneke, M. Czakon, P. Falgari, A. Mitov, and C. Schwinn. “Threshold expansion of the $gg(q\bar{q}) \rightarrow Q\bar{Q} + X$ cross section at $O(\alpha_S^4)$ ”. *Phys. Lett. B* **690** (2010) 483. [arXiv:0911.5166 \[hep-ph\]](https://arxiv.org/abs/0911.5166)

[127] W. Beenakker, C. Borschensky, M. Krämer, A. Kulesza, and E. Laenen. “NNLLfast: predictions for coloured supersymmetric particle production at the LHC with threshold and Coulomb resummation”. *JHEP* **12** (2016) 133. [arXiv:1607.07741 \[hep-ph\]](https://arxiv.org/abs/1607.07741)

[128] S. Frixione, P. Nason and C. Oleari. “Matching NLO QCD computations with Parton Shower simulations: the POWHEG method”. *JHEP* **11** (2007) 070. [arXiv:0709.2092 \[hep-ph\]](https://arxiv.org/abs/0709.2092)

[129] M. Beneke, P. Falgari, S. Klein and C. Schwinn. “Hadronic top-quark pair production with NNLL threshold resummation”. *Nucl. Phys. B* **855** (2012) 695. [arXiv:1109.1536 \[hep-ph\]](https://arxiv.org/abs/1109.1536)

[130] W. Beenakker, R. Höpker, M. Spira and P. Zerwas. “Squark and gluino production at hadron colliders”. *Nucl. Phys. B* **492** (1997) 51. [arXiv:hep-ph/9610490](https://arxiv.org/abs/hep-ph/9610490)

[131] A. Kulesza and L. Motyka. “Threshold Resummation for Squark-Antisquark and Gluino-Pair Production at the LHC”. *Phys. Rev. Lett.* **102** (2009) 111802. [arXiv:0807.2405 \[hep-ph\]](https://arxiv.org/abs/0807.2405)

[132] A. Kulesza and L. Motyka. “Soft gluon resummation for the production of gluino-gluino and squark-antisquark pairs at the LHC”. *Phys. Rev. D* **80** (2009) 095004. [arXiv:0905.4749 \[hep-ph\]](https://arxiv.org/abs/0905.4749)

[133] W. Beenakker et al. “Soft-gluon resummation for squark and gluino hadroproduction”. *JHEP* **12** (2009) 041. [arXiv:0909.4418 \[hep-ph\]](https://arxiv.org/abs/0909.4418)

[134] W. Beenakker et al. “Squark and gluino hadroproduction”. *Int. J. Mod. Phys. A* **26** (2011) 2637. [arXiv:1105.1110 \[hep-ph\]](https://arxiv.org/abs/1105.1110)

[135] M. Krämer et al. “Supersymmetry production cross sections in pp collisions at $\sqrt{s} = 7$ TeV”. (2012). [arXiv:1206.2892 \[hep-ph\]](https://arxiv.org/abs/1206.2892)

[136] ATLAS Collaboration. “Performance of the ATLAS track reconstruction algorithms in dense environments in LHC Run 2”. *Eur. Phys. J. C* **77** (2017) 673. [arXiv:1704.07983 \[hep-ex\]](https://arxiv.org/abs/1704.07983)

[137] R. E. Kalman. “A new approach to linear filtering and prediction problems”. *J. Basic Eng.* **82** *1* (1960) 35–45. doi: [10.1115/1.3662552](https://doi.org/10.1115/1.3662552)

[138] R. Frühwirth. “Application of Kalman filtering to track and vertex fitting”. *Nucl. Instrum. Methods Phys. Res., A* **262** (1987) 444. HEPHY-PUB-87-503. doi: [10.1016/0168-9002\(87\)90887-4](https://doi.org/10.1016/0168-9002(87)90887-4)

[139] ATLAS Collaboration. “Reconstruction of primary vertices at the ATLAS experiment in Run 1 proton-proton collisions at the LHC”. *Eur. Phys. J. C* **77** (2017) 332. [arXiv:1611.10235 \[hep-ex\]](https://arxiv.org/abs/1611.10235)

[140] ATLAS Collaboration. “Vertex Reconstruction Performance of the ATLAS Detector at $\sqrt{s} = 13$ TeV”. ATL-PHYS-PUB-2015-026, 2015. <https://cds.cern.ch/record/2037717>

[141] W. Waltenberger, R. Frühwirth, and P. Vanlaer. “Adaptive vertex fitting”. *J. Phys. G: Nucl. Part. Phys.* **34** (2007) N343–N356. doi: [10.1088/0954-3899/34/12/N01](https://doi.org/10.1088/0954-3899/34/12/N01)

[142] ATLAS Collaboration. “Topological cell clustering in the ATLAS calorimeters and its performance in LHC Run 1”. *Eur. Phys. J. C* **77** (2017) 490. [arXiv:1603.02934 \[hep-ex\]](https://arxiv.org/abs/1603.02934)

[143] ATLAS Collaboration. “Jet energy measurement with the ATLAS detector in proton-proton collisions at $\sqrt{s} = 7$ TeV”. *Eur. Phys. J. C* **73** (2013) 2304. [arXiv:1112.6426 \[hep-ex\]](https://arxiv.org/abs/1112.6426)

[144] ATLAS Collaboration. “Electron reconstruction and identification in the ATLAS experiment using the 2015 and 2016 LHC proton-proton collision data at $\sqrt{s} = 13$ TeV”. *Eur. Phys. J. C* **79** (2019) 639. [arXiv:1902.04655 \[hep-ex\]](https://arxiv.org/abs/1902.04655)

[145] ATLAS Collaboration. “Improved electron reconstruction in ATLAS using the Gaussian Sum Filter-based model for bremsstrahlung”. ATLAS-CONF-2012-047. 2012. <https://cds.cern.ch/record/1449796>

[146] C. Anastopoulos et al. “Electron Efficiency Measurements with the ATLAS Detector Using the 2015 LHC Proton-Proton Collision Data”. Tech. Rep. ATLAS-COM-CONF-2016-028. CERN. 2016. url: <https://cds.cern.ch/record/21428316>

[147] ATLAS Collaboration. “Electron and photon performance measurements with the ATLAS detector using the 2015–2017 LHC proton-proton collision data”. JINST **14** (2019) P12006. CERN-EP-2019-145. [arXiv:1908.00005 \[hep-ex\]](https://arxiv.org/abs/1908.00005)

[148] ATLAS Collaboration. “Search for doubly charged Higgs boson production in multi-lepton final states with the ATLAS detector using proton–proton collisions at $\sqrt{s} = 13$ TeV”. Eur. Phys. J. C **78** (2018) 199. [arXiv:1710.09748 \[hep-ex\]](https://arxiv.org/abs/1710.09748)

[149] ATLAS Collaboration. “Muon Reconstruction Performance of the ATLAS Detector in Proton-Proton Collision Data at $\sqrt{s}=13$ TeV”. Eur. Phys. J. C **76**. CERN-EP-2016-033, (2016) 292. [arXiv:1603.05598 \[hep-ex\]](https://arxiv.org/abs/1603.05598)

[150] ATLAS Collaboration. “Muon reconstruction and identification efficiency in ATLAS using the full Run 2 pp collision data set at $\sqrt{s} = 13$ TeV”. CERN-EP-2020-199. [arXiv:2012.00578 \[hep-ex\]](https://arxiv.org/abs/2012.00578)

[151] M. Cacciari, G. P. Salam, and G. Soyez. “The Anti- $k(t)$ Jet Clustering Algorithm”. JHEP **0804** (2008) 063. [arXiv:0802.1189 \[hep-ph\]](https://arxiv.org/abs/0802.1189)

[152] A. Schwartzman. “Jet Energy Calibration at the LHC”. Int. J. Mod. Phys. A **30** no. 31, (2015) 1546002. [arXiv:1509.05459 \[hep-ex\]](https://arxiv.org/abs/1509.05459)

[153] ATLAS Collaboration. “Expected Performance of the ATLAS b -tagging Algorithms in Run-2”. ATL-PHYS-PUB-2015-022. CERN. 2015. url: [http://cds.cern.ch/record/2037697](https://cds.cern.ch/record/2037697)

[154] ATLAS Collaboration. “Optimisation and performance studies of the ATLAS b -tagging algorithms for the 2017-18 LHC run”. ATL-PHYS-PUB-2017-013 (2017). url: <https://cds.cern.ch/record/2273281>

[155] ATLAS Collaboration. “Soft b -hadron tagging for compressed SUSY scenarios”. ATLAS-CONF-2019-027 (2019). url: <https://cds.cern.ch/record/2682131>

[156] D. Adams et al. “Recommendations of the Physics Objects and Analysis Harmonisation Study Groups 2014”. Tech. Rep. ATL-PHYS-INT-2014-018, CERN (2014). url: <https://cds.cern.ch/record/1743654>

[157] J. Gallicchio and Y. Chien. “Quit Using Pseudorapidity, Transverse Energy, and Massless Constituents”. (2018). [arXiv: 1802.05356 \[hep-ph\]](https://arxiv.org/abs/1802.05356)

[158] ATLAS Collaboration. “Measurements of b -jet tagging efficiency with the ATLAS detector using $t\bar{t}$ events at $\sqrt{s} = 13$ TeV”. *JHEP* **08** (2018) 089. [arXiv:1805.01845](https://arxiv.org/abs/1805.01845) [hep-ex]

[159] M. Cacciari, G. P. Salam, and G. Soyez. “The Catchment Area of Jets”. *JHEP* **04** (2008) 005. [arXiv:0802.1188](https://arxiv.org/abs/0802.1188) [hep-ph]

[160] ATLAS Collaboration. “Performance of Missing Transverse Momentum Reconstruction With the ATLAS Detector in the First Proton-Proton Collisions at $\sqrt{s}=13\text{TeV}$ ”. ATL-PHYS-PUB-2015-027. 2015. url: <https://cds.cern.ch/record/2037904>

[161] ATLAS Collaboration. “Performance of missing transverse momentum reconstruction with the ATLAS detector using proton-proton collisions at $\sqrt{s} = 13$ TeV”. *Eur. Phys. J. C* **78** (2018) 903. [arXiv:1802.08168](https://arxiv.org/abs/1802.08168) [hep-ex]

[162] P. J. Laycock et al. “ATLAS data preparation in run 2”. *J. Phys. Conf. Ser.* **898** (2017) 042050.

[163] ATLAS Collaboration. “Selection of Jets Produced in 13 TeV Proton-Proton Collisions with ATLAS Detector”. Tech. Rep. ATLAS-CONF-2015-029. CERN 2015. url: <https://cds.cern.ch/record/2037702>

[164] J. Alwall, P. Schuster, and N. Toro. “Simplified Models for a First Characterization of New Physics at the LHC”. *Phys. Rev. D*, **79** (2009) 075020. doi: [10.1103/PhysRevD.79.075020](https://doi.org/10.1103/PhysRevD.79.075020)

[165] D. Alves et al. “Simplified Models for LHC New Physics Searches”. *J. Phys. G*, **39** (2012) 105005. doi: [10.1088/0954-3899/39/10/105005](https://doi.org/10.1088/0954-3899/39/10/105005)

[166] LHC SUSY Cross Section Working Group. url: <https://twiki.cern.ch/twiki/bin/view/LHCPhysics/SUSYCrossSections>

[167] DELPHI Collaboration. “Search for supersymmetric particles assuming R -parity non-conservation in e^+e^- collisions at $\sqrt{s} = 192$ GeV to 208 GeV”. *Eur. Phys. J. C* **36** (2004) 1.

[168] A. Heister et al. “Search for supersymmetric particles with R parity violating decays in e^+e^- collisions at \sqrt{s} up to 209-GeV”. *Eur. Phys. J. C* **31** (2003) 1. [arXiv:hep-ex/0210014](https://arxiv.org/abs/hep-ex/0210014)

[169] P. Achard et al. “Search for R parity violating decays of supersymmetric particles in e^+e^- collisions at LEP”. *Phys. Lett. B* **524** (2002) 65. [arXiv:hep-ex/0110057](https://arxiv.org/abs/hep-ex/0110057)

[170] ATLAS Collaboration. “Measurement of the $t\bar{t}$ production cross-section using $e\mu$ events with b -tagged jets in pp collisions at $\sqrt{s} = 13$ TeV with the ATLAS detector”. *Phys. Lett. B* **761** (2016) 136. [arXiv:1606.02699](https://arxiv.org/abs/1606.02699) [hep-ex]

[171] ATLAS Collaboration. “Measurement of W^\pm and Z -boson production cross sections in pp collisions at $\sqrt{s} = 13$ TeV with the ATLAS detector”. *Phys. Lett. B* **759** (2016) 601. [arXiv:1603.09222 \[hep-ex\]](https://arxiv.org/abs/1603.09222)

[172] ATLAS Collaboration. “Measurement of the cross-section for producing a W boson in association with a single top quark in pp collisions at $\sqrt{s} = 13$ TeV with ATLAS”. *JHEP* **01** (2018) 063. [arXiv:1612.07231 \[hep-ex\]](https://arxiv.org/abs/1612.07231)

[173] CMS Collaboration. “Search for top squarks decaying via four-body or chargino-mediated modes in single-lepton final states in proton-proton collisions at $\sqrt{s} = 13$ TeV”. *JHEP* **09** (2018) 065. [arXiv:1805.05784 \[hep-ex\]](https://arxiv.org/abs/1805.05784)

[174] ATLAS Collaboration. “Jet Energy Measurement and its Systematic Uncertainty in Proton-Proton Collisions at $\sqrt{s}=7$ TeV with the ATLAS Detector”. *Eur. Phys. J. C* **75** (2015) 17. [arXiv:1406.0076 \[hep-ex\]](https://arxiv.org/abs/1406.0076)

[175] ATLAS Collaboration. “Performance of Jet Substructure Techniques for Large-R Jets in Proton-Proton Collisions at $\sqrt{s} = 7$ TeV Using the ATLAS Detector”. *JHEP* **1309** (2013) 076. [arXiv:1306.4945 \[hep-ex\]](https://arxiv.org/abs/1306.4945)

[176] ATLAS Collaboration. “Calibration of b -tagging Using Dileptonic Top Pair Events in a Combinatorial Likelihood Approach with the ATLAS Experiment”. ATLAS-CONF-2014-004. 2014. LAS Detector”. *JHEP* **1309** (2013) 076. url: <http://cdsweb.cern.ch/record/1664335>

[177] ATLAS Collaboration. “Calibration of the Performance of b –tagging for c and Light-Flavour Jets in the 2012 ATLAS Data”. ATLAS-CONF-2014-046, 2014. url: <http://cdsweb.cern.ch/record/1741020>

[178] ATLAS Collaboration. “Performance of missing transverse momentum reconstruction with the ATLAS detector using proton-proton collisions at $\sqrt{s} = 13$ TeV”. *Eur. Phys. J. C* **78** (2018) 903. [arXiv:1802.08168 \[hep-ex\]](https://arxiv.org/abs/1802.08168)

[179] ATLAS Collaboration. “Measurement of the Inelastic Proton-Proton Cross-Section at $\sqrt{s} = 7$ TeV with the ATLAS Detector”. *Nature Commun.* **2** (2011) 463. [arXiv:1104.0326 \[hep-ex\]](https://arxiv.org/abs/1104.0326)

[180] ATLAS Collaboration. “Luminosity determination in pp collisions at $\sqrt{s} = 13$ TeV using the ATLAS detector at the LHC”. ATLAS-CONF-2019-021. url: <https://cds.cern.ch/record/2677054>

[181] M. Baak, G.J. Besjes, et.al. “HistFitter Software Framework for Statistical Data Analysis”. 2014. [arXiv:1410.1280 \[hep-ex\]](https://arxiv.org/abs/1410.1280)

[182] G. Cowan, K. Cranmer, E. Gross, O. Vitells. “Asymptotic formulae for likelihood-based tests of new physics”. *Eur. Phys. J. C* **71** (2011) 1554. [arXiv:1007.1727 \[physics.data-an\]](https://arxiv.org/abs/1007.1727)

[183] R. J. Barlow. “A Guide to the Use of Statistical Methods in the Physical Sciences”. WILEY-VCH, 1989.

[184] K. Cranmer, G. Lewis, L. Moneta, A. Shibata and W. Verkerke. “HistFactory: A tool for creating statistical models for use with RooFit and RooStats”. Technical Report CERN-OPEN-2012-016, (2012). url: <https://cds.cern.ch/record/1456844>

[185] G. Cowan “Statistical Data Analysis”. Oxford University Press Inc. New York. 1998.

[186] E. Gross G. Cowan, K. Cranmer and O. Vitells. “Asymptotic Formulae for Likelihood-based Tests of New Physics”. *Eur. Phys. J. C* **71** (2011) 554. [arXiv:1007.1727 \[physics.data-an\]](https://arxiv.org/abs/1007.1727)

[187] A. L. Read. “Presentation of search results: The CL(s) technique”. *J. Phys. G* **28** (2002) 2693-2704. doi: [10.1088/0954-3899/28/10/313](https://doi.org/10.1088/0954-3899/28/10/313)

[188] G. Cowan. “Statistics for Searches at LHC”. Lectures presented at the 69th Scottish Universities Summer School in Physics, St. Andrews, 2012. [arXiv:1307.2487 \[hep-ex\]](https://arxiv.org/abs/1307.2487)

[189] ATLAS Collaboration. “Search for top-squark pair production in final states with one lepton, jets, and missing transverse momentum using 36 fb^{-1} of $\sqrt{s} = 13 \text{ TeV}$ pp collision data with the ATLAS detector”. *JHEP* **06** (2018) 108. [arXiv:1711.11520 \[hep-ex\]](https://arxiv.org/abs/1711.11520)

[190] ATLAS Collaboration. “ATLAS Run 1 searches for direct pair production of third-generation squarks at the Large Hadron Collider”. *Eur. Phys. J. C* **75** (2015) 510. [arXiv:1506.08616 \[hep-ex\]](https://arxiv.org/abs/1506.08616)

[191] ATLAS Collaboration. “Search for a scalar partner of the top quark in the jets plus missing transverse momentum final state at $\sqrt{s} = 13 \text{ TeV}$ with the ATLAS detector”. *JHEP* **12** (2017) 085. [arXiv:1709.04183 \[hep-ex\]](https://arxiv.org/abs/1709.04183)

[192] ATLAS Collaboration. “Search for direct top squark pair production in final states with two leptons in $\sqrt{s} = 13 \text{ TeV}$ pp collisions with the ATLAS detector”. *Eur. Phys. J. C* **77** (2017) 898. [arXiv:1708.03247 \[hep-ex\]](https://arxiv.org/abs/1708.03247)

[193] ATLAS Collaboration. “Search for dark matter and other new phenomena in events with an energetic jet and large missing transverse momentum using the ATLAS detector”. *JHEP* **01** (2018) 126. [arXiv:1711.03301 \[hep-ex\]](https://arxiv.org/abs/1711.03301)

[194] ATLAS Collaboration. “Search for top squarks in final states with one isolated lepton, jets, and missing transverse momentum in $\sqrt{s} = 13 \text{ TeV}$ pp collisions with the ATLAS detector”. *Phys. Rev. D* **94** (2016) 052009. [arXiv:1606.03903 \[hep-ex\]](https://arxiv.org/abs/1606.03903)

[195] ATLAS Collaboration. “Search for top squark pair production in final states with one isolated lepton, jets, and missing transverse momentum in $\sqrt{s} = 8 \text{ TeV}$ pp collisions with the ATLAS detector”. *JHEP* **11** (2014) 118. [arXiv:1407.0583 \[hep-ex\]](https://arxiv.org/abs/1407.0583)

[196] ATLAS Collaboration. “Search for direct pair production of the top squark in all-hadronic final states in proton-proton collisions at $\sqrt{s} = 8$ TeV with the ATLAS detector”. *JHEP* **09** (2014) 015. [arXiv:1406.1122 \[hep-ex\]](https://arxiv.org/abs/1406.1122)

[197] ATLAS Collaboration. “Search for direct top-squark pair production in final states with two leptons in pp collisions at $\sqrt{s} = 8$ TeV with the ATLAS detector”. *JHEP* **06** (2014) 124. [arXiv:1403.4853 \[hep-ex\]](https://arxiv.org/abs/1403.4853)

[198] ATLAS Collaboration. “Search for a heavy top-quark partner in final states with two leptons with the ATLAS detector at the LHC”. *JHEP* **11** (2012) 094. [arXiv:1209.4186 \[hep-ex\]](https://arxiv.org/abs/1209.4186)

[199] ATLAS Collaboration. “Search for direct top squark pair production in final states with one isolated lepton, jets, and missing transverse momentum in $\sqrt{s} = 7$ TeV pp collisions using 4.7 fb^{-1} of ATLAS data”. *Phys. Rev. Lett.* **109** (2012) 211803. [arXiv:1208.2590 \[hep-ex\]](https://arxiv.org/abs/1208.2590)

[200] ATLAS Collaboration. “Search for a supersymmetric partner to the top quark in final states with jets and missing transverse momentum at $\sqrt{s} = 7$ TeV with the ATLAS detector”. *Phys. Rev. Lett.* **109** (2012) 211802. [arXiv:1208.1447 \[hep-ex\]](https://arxiv.org/abs/1208.1447)

[201] CMS Collaboration. “Search for direct production of supersymmetric partners of the top quark in the all-jets final state in proton-proton collisions at $\sqrt{s} = 13$ TeV”. *JHEP* **10** (2017) 005. [arXiv:1707.03316 \[hep-ex\]](https://arxiv.org/abs/1707.03316)

[202] CMS Collaboration. “Search for top squark pair production in pp collisions at $\sqrt{s} = 13$ TeV using single lepton events”. *JHEP* **10** (2017) 019. [arXiv:1706.04402 \[hep-ex\]](https://arxiv.org/abs/1706.04402)

[203] CMS Collaboration. “Search for top squarks and dark matter particles in opposite-charge dilepton final states at $\sqrt{s} = 13$ TeV”. *Phys. Rev. D* **97** (2018) 032009. [arXiv:1711.00752 \[hep-ex\]](https://arxiv.org/abs/1711.00752)

[204] CMS Collaboration. “Search for top squarks decaying via four-body or chargino-mediated modes in single-lepton final states in proton-proton collisions at $\sqrt{s} = 13$ TeV”. *JHEP* **09** (2018) 065. [arXiv:1805.05784 \[hep-ex\]](https://arxiv.org/abs/1805.05784)

[205] CMS Collaboration. “Search for top-squark pair production in the single-lepton final state in pp collisions at $\sqrt{s} = 8$ TeV”. *Eur. Phys. J. C* **73** (2013) 2677. [arXiv:1308.1586 \[hep-ex\]](https://arxiv.org/abs/1308.1586)

[206] CMS Collaboration. “Search for direct pair production of supersymmetric top quarks decaying to all-hadronic final states in pp collisions at $\sqrt{s} = 8$ TeV”. *Eur. Phys. J. C* **76** (2016) 460. [arXiv:1603.00765 \[hep-ex\]](https://arxiv.org/abs/1603.00765)

[207] CMS Collaboration. “Search for direct pair production of scalar top quarks in the single- and dilepton channels in proton-proton collisions at $\sqrt{s} = 8$ TeV”. *JHEP* **07** (2016) 027. [arXiv:1602.03169 \[hep-ex\]](https://arxiv.org/abs/1602.03169)

[208] CMS Collaboration. “Searches for third-generation squark production in fully hadronic final states in proton-proton collisions at $\sqrt{s} = 8$ TeV”. *JHEP* **06** (2015) 116. [arXiv:1503.08037 \[hep-ex\]](https://arxiv.org/abs/1503.08037)

[209] CMS Collaboration. “Search for supersymmetry in events with soft leptons, low jet multiplicity, and missing transverse energy in proton-proton collisions at $\sqrt{s} = 8$ TeV”. *Phys. Lett. B* **759** (2016) 9. [arXiv:1512.08002 \[hep-ex\]](https://arxiv.org/abs/1512.08002)

[210] CMS Collaboration. “Search for supersymmetry in final states with missing transverse energy and 0, 1, 2, or ≤ 3 b -quark jets in 7 TeV pp collisions using the variable αT ”. *JHEP* **01** (2013) 077. [arXiv:1210.8115 \[hep-ex\]](https://arxiv.org/abs/1210.8115)

[211] CMS Collaboration. “Inclusive search for supersymmetry using razor variables in pp collisions at $\sqrt{s} = 7$ TeV”. *Phys. Rev. Lett.* **111** (2013) 081802. [arXiv:1212.6961 \[hep-ex\]](https://arxiv.org/abs/1212.6961)

[212] Summary plots from the ATLAS Supersymmetry physics group. url: <https://atlas.web.cern.ch/Atlas/GROUPS/PHYSICS/CombinedSummaryPlots/SUSY/>

[213] ATLAS Collaboration. “Search for supersymmetry in final states with charm jets and missing transverse momentum in 13 TeV pp collisions with the ATLAS detector”. *JHEP* **09** (2018) 050. [arXiv:1805.01649 \[hep-ex\]](https://arxiv.org/abs/1805.01649)

[214] ATLAS Collaboration. “Search for new phenomena in a lepton plus high jet multiplicity final state with the ATLAS experiment using $\sqrt{s} = 13$ TeV proton-proton collision data”. *JHEP* **88** (2017). [arXiv:1704.08493 \[hep-ex\]](https://arxiv.org/abs/1704.08493)

[215] ATLAS Collaboration. “Search for new phenomena with top quark pairs in final states with one lepton, jets, and missing transverse momentum in pp collisions at $\sqrt{s}=13$ TeV with the ATLAS detector”. *JHEP* **04** (2021) 174. [arXiv:2012.03799 \[hep-ph\]](https://arxiv.org/abs/2012.03799)

[216] M. Cacciari, G. P. Salam, and G. Soyez. “The Anti- $k(t)$ Jet Clustering Algorithm”. *JHEP* **04** (2008) 063. [arXiv:0802.1189 \[hep-ph\]](https://arxiv.org/abs/0802.1189)

[217] ATLAS Collaboration. “Soft b -hadron tagging for compressed SUSY scenarios”. ATLAS-CONF-2019-027 (2019). url: <https://cds.cern.ch/record/2682131>.

[218] ATLAS Collaboration. “Search for a scalar partner of the top quark in the jets plus missing transverse momentum final state at $\sqrt{s} = 13$ TeV with the ATLAS detector”. *JHEP* **12** (2017) 085. [arXiv:1709.04183 \[hep-ex\]](https://arxiv.org/abs/1709.04183)

[219] ATLAS Collaboration. “Search for direct top squark pair production in final states with two leptons in $\sqrt{s} = 13$ TeV pp collisions with the ATLAS detector”. *Eur. Phys. J. C* **77** (2017) 898. [arXiv:1708.03247 \[hep-ex\]](https://arxiv.org/abs/1708.03247)

[220] ATLAS Collaboration. “Search for dark matter and other new phenomena in events with an energetic jet and large missing transverse momentum using the ATLAS detector”. *JHEP* **01** (2018) 126. [arXiv:1711.03301 \[hep-ex\]](https://arxiv.org/abs/1711.03301)

[221] ATLAS Protected web page. ATLAS Physics Modeling Group. url: <https://twiki.cern.ch/twiki/bin/viewauth/AtlasProtected/PmgWeakBosonProcesses>

[222] E. Gerwick, T. Plehn, S. Schumann and P. Schichtel. “Scaling Patterns for QCD Jets”. *JHEP* **10** (2012) 162. [arXiv:1208.3676 \[hep-ph\]](https://arxiv.org/abs/1208.3676)

[223] ATLAS Collaboration. “Measurements of the production cross section of a Z boson in association with jets in pp collisions at $\sqrt{s} = 13$ TeV with the ATLAS detector”. *Eur. Phys. J. C* **77** (2017) 361. [arXiv: 1702.05725 \[hep-ex\]](https://arxiv.org/abs/1702.05725)

[224] CMS Collaboration. “Jet Production Rates in Association with W and Z Bosons in pp Collisions at $\sqrt{s} = 7$ TeV”. *JHEP* **01** (2012) 010. [arXiv:1110.3226 \[hep-ex\]](https://arxiv.org/abs/1110.3226)

[225] G. J. Székely, M. L. Rizzo and N. K. Bakirov. “Measuring and testing dependence by correlation of distances”. *Ann. Statist.* **35** (2007) 2769. url: [doi: 10.1214/009053607000000505](https://doi.org/10.1214/009053607000000505)

[226] Goodfellow, I., Pouget-Abadie, J., Mirza, M., Xu, B., Warde-Farley, D., Ozair, S., Courville, A., and Bengio, Y. “Generative adversarial nets. In Advances in Neural Information Processing Systems”. (2014). [arXiv:1406.2661 \[stat.ML\]](https://arxiv.org/abs/1406.2661)

[227] ATLAS Collaboration. “Jet reconstruction and performance using particle flow with the ATLAS Detector”. *Eur. Phys. J. C* **77** (2017) 466. [arXiv:1703.10485 \[hep-ex\]](https://arxiv.org/abs/1703.10485)

[228] A. Paszke et al. “PyTorch: An Imperative Style, High-Performance Deep Learning Library”. Curran Associates, Inc. (2019). url: <https://proceedings.neurips.cc/paper/2019/file/bdbca288fee7f92f2bfa9f7012727740-Paper.pdf>

[229] D. P. Kingma and J. Ba. “Adam: A Method for Stochastic Optimization”. (2017). [arXiv: 1412.6980 \[cs.LG\]](https://arxiv.org/abs/1412.6980)

[230] Loss Functions. url: https://ml-cheatsheet.readthedocs.io/en/latest/loss_functions.html

[231] D. Godoy. “Understanding binary cross-entropy / log loss: a visual explanation”. (2018). url: <https://towardsdatascience.com/understanding-binary-cross-entropy-log-loss-a-visual-explanation-a3ac6025181a>

[232] C. Olah. “Visual Information Theory”. (2015). url: <http://colah.github.io/posts/2015-09-Visual-Information/>

[233] L. Heinrich, M. Feickert and G. Stark. “pyhf: v0.6.1, hypotest”. url: <https://scikit-hep.org/pyhf/>

[234] S. Kullback, R. A. Leibler “On Information and Sufficiency”. *Ann. Math. Statist.* **22** *1* (1951) 79–86. doi: [10.1214/aoms/1177729694](https://doi.org/10.1214/aoms/1177729694)

[235] G. Kasieczka and D. Shih. “Robust Jet Classifiers through Distance Correlation”. *Phys. Rev. Lett.* **125** (2020) 122001. arXiv: [2001.05310](https://arxiv.org/abs/2001.05310) [hep-ph]

[236] C. R. Carreño. “dcor: distance correlation and related E-statistics in Python”. url: <https://github.com/vnmabus/dcor>

[237] G. Kasieczka and D. Shih. url: <https://github.com/gkasieczka/DisCo>

[238] D. Goncalves, K. Sakurai, M. Takeuchi. “Tagging a mono-top signature in Natural SUSY”. *Phys. Rev. D* **95**, 015030 (2017). arXiv: [1610.06179](https://arxiv.org/abs/1610.06179) [hep-ph]

[239] D. Goncalves, K. Sakurai, M. Takeuchi. “Mono-top Signature from Supersymmetric $t\bar{t}H$ Channel”. *Phys. Rev. D* **94**, 075009 (2016). arXiv: [1604.03938](https://arxiv.org/abs/1604.03938) [hep-ph]

[240] B. Fuks, P. Richardson, A. Wilcock. “Studying the sensitivity of monotop probes to compressed supersymmetric scenarios at the LHC”. *Eur. Phys. J. C* **75** (2015) 7, 308. arXiv: [1408.3634](https://arxiv.org/abs/1408.3634) [hep-ph]

[241] ATLAS Collaboration. “Search for large missing transverse momentum in association with one top-quark in proton-proton collisions at $\sqrt{s} = 13$ TeV with the ATLAS detector”. *JHEP* **05** (2019) 41. arXiv: [1812.09743](https://arxiv.org/abs/1812.09743) [hep-ex]

[242] ATLAS Collaboration. “Search for a scalar partner of the top quark in the jets plus missing transverse momentum final state at $\sqrt{s} = 13$ TeV with the ATLAS detector”. *JHEP* **12** (2017) 085. arXiv: [1709.04183](https://arxiv.org/abs/1709.04183) [hep-ex]

[243] ATLAS Collaboration. “Search for top squarks in final states with one isolated lepton, jets, and missing transverse momentum in $\sqrt{s} = 13$ TeV pp collisions with the ATLAS detector”. *Phys. Rev. D* **94** (2016) 052009. arXiv: [1606.03903](https://arxiv.org/abs/1606.03903) [hep-ex]

[244] ATLAS Collaboration. “Search for squarks and gluinos in events with isolated leptons, jets and missing transverse momentum at $\sqrt{s} = 8$ TeV with the ATLAS detector”. *JHEP* **04** (2015) 116. arXiv: [1501.03555](https://arxiv.org/abs/1501.03555) [hep-ex]

[245] ATLAS Collaboration. “Search for new phenomena in final states with an energetic jet and large missing transverse momentum in pp collisions at $\sqrt{s} = 13$ TeV using the ATLAS detector”. *Phys. Rev. D* **94** (2016) 032005. arXiv: [1604.07773](https://arxiv.org/abs/1604.07773) [hep-ex]

[246] “Summary plots from the ATLAS Supersymmetry physics group”. url: <https://atlas.web.cern.ch/Atlas/GROUPS/PHYSICS/CombinedSummaryPlots/SUSY>

[247] ATLAS Collaboration. “Search for supersymmetry in final states with two same-sign or three leptons and jets using 36 fb^{-1} of $\sqrt{s} = 13 \text{ TeV}$ pp collision data with the ATLAS detector”. *JHEP* **09** (2017) 084. [arXiv:1706.03731 \[hep-ex\]](https://arxiv.org/abs/1706.03731)

[248] U. Langenfeld. “Threshold Improved QCD Corrections for Stop-Antistop production at Hadron colliders”. *JHEP* **1107** (2011) 052. [arXiv:1011.3341 \[hep-ph\]](https://arxiv.org/abs/1011.3341)

[249] W. Beenakker, S. Bremsing, M. Kramer, A. Kulesza, E. Laenen, and I. Niessen. “Supersymmetric top and bottom squark production at hadron colliders”. *JHEP* **1008** (2010) 098. [arXiv:1006.4771 \[hep-ph\]](https://arxiv.org/abs/1006.4771)

[250] LHC Higgs Working Group. url: <https://twiki.cern.ch/twiki/bin/view/LHCPhysics>

[251] J. Alwall, R. Frederix, S. Frixione, V. Hirschi, F. Maltoni, O. Mattelaer, H.-S. Shao, T. Stelzer, P. Torrielli, M. Zaro. “The automated computation of tree-level and next-to-leading order differential cross sections, and their matching to parton shower simulations”. *JHEP* **07** (2014) 079. [arXiv:1405.0301 \[hep-ph\]](https://arxiv.org/abs/1405.0301)

[252] MadGraph Generator Homepage. url: <http://madgraph.phys.ucl.ac.be>

[253] G. Moneta, S. Lorenzo and K. Cranmer. “The RooStats project”. PoS (2011) ACAT2010 057. [arXiv:1009.1003 \[physics.data-an\]](https://arxiv.org/abs/1009.1003)

[254] ROOT Data Analysis Framework. url: <https://root.cern/>

[255] R. Cousins, J. Linnemann, J. Tucker. “Evaluation of three methods for calculating statistical significance when incorporating a systematic uncertainty into a test of the background-only hypothesis for a Poisson process”. *Nucl. Instrum. Methods Phys. Res. A* **595** (2008) 480–501. [arXiv:physics/0702156 \[physics.data-an\]](https://arxiv.org/abs/physics/0702156)

[256] ROOT web page. Number Counting Utils Detailed Description. url: https://root.cern/doc/v610/rs_numbercountingutils_8C.html

[257] ROOT web page. RooStats Namespace Reference. url: <https://root.cern/doc/v614/namespaceroostats.html>

[258] J. Ehrsam. “Search for a Monotop Signature in Compressed SUSY Scenarios with One-Lepton Final States”. LMU Bachelor Thesis. (2019). url: <https://www.etp.physik.uni-muenchen.de/publications/bachelor/download-authetp/Bachelorarbeit-2019-JuliusEhrsam.pdf>

[259] ATLAS Collaboration. “Search for top squark pair production in final states with one isolated lepton, jets, and missing transverse momentum in $\sqrt{s} = 8 \text{ TeV}$ pp collisions with the ATLAS detector”. *JHEP* **11** (2014) 118. [arXiv:1407.0583 \[hep-ex\]](https://arxiv.org/abs/1407.0583)

[260] A. J. Barr, B. Gripaios, and C. G. Lester. “Transverse masses and kinematic constraints: from the boundary to the crease”. *JHEP* **11** (2009) 096. [arXiv:0908.3779 \[hep-ph\]](https://arxiv.org/abs/0908.3779)

[261] Y. Bai, H.-C. Cheng, J. Gallicchio and J. Gu. “Stop the top background of the stop search”. *JHEP* **07** (2012) 110. [arXiv:1203.4813 \[hep-ph\]](https://arxiv.org/abs/1203.4813)

[262] P. Konar, K. Kong, K.T. Matchev and M. Park. “Dark matter particle spectroscopy at the LHC: generalizing M_{T2} to asymmetric event topologies”. *JHEP* **04** (2010) 086. [arXiv:0911.4126 \[hep-ph\]](https://arxiv.org/abs/0911.4126)

[263] S. Steinmetz. “Suche nach Mono-Top-Signaturen mit einem 0-Lepton-Endzustand in komprimierten SUSY-Szenarien in pp -Kollisionen bei $\sqrt{s} = 13$ TeV mit dem ATLAS-Detektor”. LMU Bachelor Thesis. (2021). [To be uploaded](#)

[264] ATLAS Collaboration. “Boosted hadronic top identification at ATLAS for early 13 TeV data”. (2015). [ATL-PHYS-PUB-2015-053](#)

[265] CMS Collaboration. “Search for top squarks decaying via four-body or chargino-mediated modes in single-lepton final states in proton-proton collisions at $\sqrt{s} = 13$ TeV”. *JHEP* **09** (2018) 065. [arXiv:1805.05784 \[hep-ex\]](https://arxiv.org/abs/1805.05784)

[266] CMS Collaboration. “Search for direct top squark pair production in events with one lepton, jets, and missing transverse momentum at 13 TeV with the CMS experiment”. *JHEP* **05** (2020) 032. [arXiv:1912.08887 \[hep-ex\]](https://arxiv.org/abs/1912.08887)

[267] CERN webpage, Accessed: April 2021. url: <https://home.cern/news/news/accelerators/ls2-report-new-schedule>

[268] Webpage of the HL-LHC Project. Accessed: April 2021. url: <https://project-hl-lhc-industry.web.cern.ch/sites/project-hl-lhcindustry.web.cern.ch/files/inline-images/HL-LHC-plan-2020-Plan-2.pdf>

[269] G. Apollinari, O. Brüning, T. Nakamoto and L. Rossi. “High Luminosity Large Hadron Collider HL-LHC”. CERN Yellow Rep. (2015) 1. [arXiv:1705.08830 \[physics.acc-ph\]](https://arxiv.org/abs/1705.08830)